The validity of the dipole approximation in the simulation of X-ray absorption spectroscopy

Martin van Horn

To cite this version:

Martin van Horn. The validity of the dipole approximation in the simulation of X-ray absorption spectroscopy. Quantum Physics [quant-ph]. Université Paul Sabatier - Toulouse III, 2023. English. NNT : 2023TOU30204 . tel-04449587

HAL Id: tel-04449587
https://theses.hal.science/tel-04449587

Submitted on 9 Feb 2024

THÈSE

En vue de l'obtention du
DOCTORAT DE L'UNIVERSITÉ DE TOULOUSE
Délivré par l'Université Toulouse 3 - Paul Sabatier

Présentée et soutenue par
Martin VAN HORN

Le 24 novembre 2023

THE VALIDITY OF THE DIPOLE APPROXIMATION IN THE SIMULATION OF X-RAY ABSORPTION SPECTROSCOPY

École doctorale : **SDM - SCIENCES DE LA MATIÈRE - Toulouse**

Spécialité : **Physico-Chimie Théorique**

Unité de recherche :
LCPQ - Laboratoire de Chimie et Physique Quantiques

Thèse dirigée par
Trond SAUE et Nanna Holmgaard LIST

Jury
Prof. Christoph JACOB, *Technical University of Braunschweig*, Rapporteur
Prof. Roland LINDH, *University of Uppsala,* Rapporteur
Prof. Phuong Mai DINH, *Université Toulouse 3 - Paul Sabatier,* Examinatrice
Prof. Sonia CORIANI, *Technical University of Denmark,* Examinatrice
DR1-CNRS Trond SAUE, *Université Toulouse 3 - Paul Sabatier,* Directeur de thèse
Asst. Prof. Nanna Holmgaard LIST, *Royal Institute of Technology (KTH),* Co-directrice de thèse
Prof. Patrick Norman, *Royal Institute of Technology (KTH),* Invité

Abstract

In the simulation of UV-Vis spectroscopy, multipole expansions are an indispensable tool to calculate absorption intensities, justified by the vast difference in scale between the wave length of light and the spatial extent of the molecular system. Depending on the type of spectroscopy, conventional or electronic circular dichroism, this expansion yields the electric-dipole approximation or the rotational strength, respectively, at first order. I will use the term *dipole approximation* throughout this thesis as a single descriptor encompassing both schemes. However, in the X-ray regime, where the wave length can reach molecular dimensions, this approximation comes into question. The main goal of this thesis is to assess the validity of the dipole approximation in the simulation of X-ray absorption spectroscopy. In the pursuit of this goal, a fully relativistic approach is employed to correctly describe the core electrons. Furthermore, this approach allows us to reach the far ends of the hard X-ray regime, typically probing core electrons of heavy elements.

In general, there are two methods to include non-dipolar effects: either the semi-classical light–matter interaction is treated exactly, or the multipole expansion is truncated beyond first order. For the truncated approach there are two possible representations that are equivalent in the complete basis set limit: the generalized length- and velocity representation. Imposing former representation yields multipole moments in their conventional form known from classical electrodynamics. Both of these schemes have been implemented in DIRAC, a quantum chemistry code capable of two- and four-component relativistic calculations. In this thesis, the implementation of this code is discussed, together with four applications.

Based on the core- and valence transitions of the radium atom, the convergence with respect to the multipole expansion and the choice of basis set is assessed. For extremely high excitation energies ($\sim$ 3728 eV), it follows that the absorption cross-section converges extremely slowly with respect to the multipole expansion. Subsequent analysis reveals that this slow convergence is introduced at the property integral level. The basis set studies on the same system indicate that the basis set convergence is generally more difficult at high orders and for core transitions. The magnetic- and velocity representation electric-multipole moments were most difficult to converge, due to linear dependence problems associated with the small component function. The full interaction, however, does not suffer from the aforementioned problems.

However, even for the core transitions, non-dipolar corrections are rather modest, at most 20%, due to the compactness of the radium $1s_{1/2}$ orbital. For that reason, additional calculations were performed on the Cl K-edge of $\mathrm{TiCl_4}$, whose symmetry equivalent centers delocalise the core orbitals. Even though the corrections were significant in individual transitions (a factor around 5), this effect was difficult to perceive due to spectral broadening. Further investigations on systems of this type may require wave function methods beyond SCF.

Additionally, the electronic circular dichroism of the H_2S_2 molecule was calculated across the electromagnetic spectrum, using the full- and truncated interaction operator. Interestingly, non-dipolar effects seem to be much more relevant for electronic circular dichroism, inducing corrections of roughly a factor of 2 for the relatively light H_2S_2 molecule. Even with spectral broadening, these effects are visible due to the signed nature of circular dichroism. Further calculations demonstrate that these effects are even more pronounced for the heaver analogues, i.e. H_2Se_2 and H_2Te_2.

Taking these points into considerations, the electric-dipole approximation seems to describe the overall characteristics of the core spectra well, although it is mandatory to go beyond this approximation to capture dipole-forbidden transitions. For electronic circular dichroism, however, it seems much more relevant to include non-dipolar effects, with effects already appearing for relatively light elements. Furthermore, for this type of spectroscopy, it can be argued that a first-order truncated approach does not make sense for heavier elements, due to the strong non-dipolar effects. Based on its favourable convergence behaviour with respect to basis set choice and the multipole expansion, the full interaction operator is the most robust method to include non-dipolar effects.

Preface

This Ph.D thesis has been submitted in partial fulfilment of the requirements for obtaining a Ph.D degree in the subject of theoretical chemistry at the University of Toulouse III - Paul Sabatier. The work presented herein was carried out from October 2020 to October 2023 at the Laboratoire de Chimie et Physique Quantiques under the supervision of Trond Saue and co-supervision of Nanna Holmgaard List. However, I was first introduced to this line of research during my Master's internship between May 2019 and December 2019, where I worked on the same project as the one presented in this thesis. The research output of this project, forming the main inspiration of this thesis, is hereafter listed in chronological order of publication date:

* 1. Nanna Holmgaard List, Timothé Romain Léo Melin, Martin van Horn, and Trond Saue. Beyond the electric-dipole approximation in simulations of x-ray absorption spectroscopy: Lessons from relativistic theory. *The Journal of chemical physics*, 152 (18):184110, 2020. doi:10.1063/5.0003103

2. Martin van Horn, Trond Saue, and Nanna Holmgaard List. Probing chirality across the electromagnetic spectrum with the full semi-classical light–matter interaction. *The Journal of Chemical Physics*, 156(5):054113, 2022. doi:10.1063/5.0077502

3. Martin van Horn, Nanna Holmgaard List, and Trond Saue. Transition moments beyond the electric-dipole approximation: Visualization and basis set requirements. *The Journal of Chemical Physics*, 158(18):184103, 05 2023. doi:10.1063/5.0147105.

The first article in this list is marked with an asterisk, because it is based on work from my Master's internship. I have included it to this list regardless, due to its high relevance to current work

As can be inferred from the above list, several authors have contributed to these articles, so in the following, I will explicitly state my own contributions: I provided the analysis to conclude that schemes bases on truncated light–matter interactions converge extremely slowly in the hard X-ray regime; furthermore, I performed the calculations and analyses related to the basis set studies; I derived the equations- and implemented all the code related to electronic circular dichroism and lastly I implemented the calculation of oscillator strengths in the generalized velocity representation with explicit separation between electric- and magnetic components.

Acknowledgments

Homo sapiens is a storytelling animal that thinks in stories rather than in numbers or graphs, and believes that the universe itself works like a story, replete with heroes and villains, conflicts and resolutions, climaxes and happy endings.

Yuval Noah Harari[4]

First and foremost, I would like to thank my supervisor, Trond Saue, for his excellent mentorship that has elevated this work beyond any of my expectations. From the many things I learned from Trond, I will always remember his emphasis on precise language and story-telling in science. To the best of my abilities, I have written my thesis in this spirit. Secondly, I would like to express my honest gratitude towards my co-supervisor, Nanna Holmgaard List, whose unique scientific style and perspectives have proven to be crucial for my thesis. I also want to thank her for the foundational work she has done before the start of my Ph.D.

In addition, I want to show appreciation to several other people who have either directly or indirectly influenced my work in a positive manner:

- Luuk Visscher, for introducing me to the fascinating field of relativistic quantum chemistry
- Stefan Knecht for teaching me MCSCF theory
- Hans Jørgen Aagaard Jensen, for the rewarding stay in Odense, Denmark
- Patrick Norman, Ruud Kenneth (and Trond Saue) for allowing me to be a teaching assistant at the Molecular Response Properties Summer School 2023
- the Relativistic Group: Maen Salman, Jan Brandejs, Johann Pototschnig, Ryan Benazzouk and Gabriele Fabbro, I thank you all for the synergistic effects we had on each others research and I'm sure we'll meet again.
- Gabriele Riva, Raul Quintero, Miguel Escobar Azor, for being great friends
- Huib van Drooge for being an encouraging teacher and recommending me ref. 5
- my family for their support and providing an intellectually stimulating environment

and a special thanks to you, Anna, for all your emotional support and patience.

Contents

Introduction

Over the centuries, the evolution of chemistry is characterized by the emergence of distinct sub-disciplines whose boundaries gradually eroded over time. One notable example is the rise of organic chemistry during the nineteenth century.[5, Chapter 8] In its early days, this field was mainly preoccupied with the chemistry of living matter, whereas its more developed and older cousin, inorganic chemistry, was rather centered around inorganic salts and mineral acids. For that reason, a dichotomous division of chemistry was prevalent, according to which organic chemistry is based on fundamentally different principles than inorganic chemistry. However, one key discovery that challenged this paradigm is the synthesis of urea from inorganic matter by Wöhler in 1828.[6] Combined with the further improvements in the characterization techniques of organic compounds, a unification of both fields was inevitable. The chemists at the heart of these developments can be likened to detectives, meticulously deducing structural features using minimalistic resources, such as decomposition analysis and chemical reactivity.[5, Chapter 9]

In modern-day chemistry, the resolution of molecular structure has become a routine task due to the advent of spectroscopy. Spectroscopy generally measures light–matter interactions in terms of absorption, emission or scattering as a function of the wave length. However, the utility of spectroscopy extends beyond mere structural characterization, since it also serves as a technique to gauge molecular properties, whose nature generally depends on the wave length of light.[7, Chapter 8] For example, in the lower energy range of the spectrum, i.e. microwave and IR, the radiation induces molecular rotations and vibrations, whereas the UV-Vis regime is associated with electronic excitations.[8, Chapters 10 and 11] Further decreasing the wave length gives rise to X-rays, whose application in molecular spectroscopy has been pioneered by de Broglie[9], Moseley[10], Siegbahn[11, 12] and Stenström.[13] X-rays have sufficient energy to reveal the shell structure of the inner electrons, which are buried deep inside the core and otherwise unaffected by UV-Vis radiation. Furthermore, above a certain threshold, X-rays may even ionize the system, which manifests itself as sudden vertical jumps in the absorption spectrum, also referred to as the edges. The edges form a particularly useful tool in structural analysis, as they are centered at the ionization energies of core electrons, thus being element-specific and well-separated.

However, the more interesting structural features are not easily deduced from the edges alone, but rather from its neighbouring regions.[14, 15] In the region beyond the edge, subtle oscillations can be observed, caused by interferences of photoelectrons that are back-scattered from their local surroundings. The technique to measure these oscillations, also referred to as extended X-ray absorption fine structure (EXAFS), provides us with information about the crystal structure of the sample.[16] However, this thesis will rather be devoted to the opposite side of the edge, which can be probed using near-edge X-ray absorption fine structure (NEXAFS).[15] In this energy range, the X-rays are still energetic enough to interact with core electrons, although they are excited to bound, empty levels. Since core orbitals tend to be localized around the nuclei, NEXAFS provides site-specific information about the system under consideration, thus forming a complement to UV-Vis spectroscopy which involves valence excitations that are delocalized over the entire molecule. In its simplest form, NEXAFS is based on linearly polarized light, although this procedure has one critical blind spot: it does not distinguish between the members of an enantiomeric pair.

Such a pair consists of two molecules that are related by mirror symmetry, while at the same time being non-superimposable. This situation generally occurs for molecules that lack any mirror plane, inversion center or axis of improper rotation, e.g. chiral point-groups: C_n or D_n. Historically, the existence of enantiomerism formed the decisive evidence to conclude that molecules are three-dimensional objects characterized by their particular constellation of atoms.[5, Chapter 11] In the modern day, enantiomerism has not lost any of its relevance, being a crucial factor to consider in medicinal chemistry, since only a specific enantiomer may fit in the highly asymmetric pocket of a protein molecule.

In addition, enantiomers have the same bulk physical properties and, as alluded to before, the same spectra if the experiment is based on linearly polarized light. To make a distinction, one posibility is to measure its electronic circular dichroism (ECD), which is defined as the difference in absorption between left- and right-handed circularly polarized light. Typically, this quantity is measured in the UV-Vis range, although it manifests itself in the X-ray regime as well, where it is called X-ray natural circular dichroism (XNCD) by convention. XNCD comes with the same benefits as ordinary NEXAFS in the sense that it provides more local information compared to ECD in the UV-Vis range.

However, creating circularly polarized light at elevated frequencies can be quite challenging, as X-rays are notoriously difficult to manipulate using conventional optical elements. In present day, this technical feat can be routinely carried out due to the recent developments of synchrotron radiation. Originally being a by-product of particle physics, these devices are circular particle accelerators that use magnetic fields to constrain electrons to circular orbits in their hollow interior.[17, 18, 19] X-rays can be extracted from these electrons by applying an additional alternating magnetic field that is perpendicular to the trajectory of the electrons. The induced oscillations of the electrons give rise to a coherent X-ray source that allows for full polarization control. This makes synchrotron radiation particularly useful to carry out NEXAFS experiments. Alternative techniques that have gained much traction are based on free electron lasers[20] or high harmonic generation.[21]

Even though much useful information can be extracted from these experiment alone, assignment and interpretation of the spectra require input from theory and simulation. For example, the absolute stereochemistry of chiral molecules can only be determined when ECD (or XNCD) is compared to equivalent results from quantum chemical simulations. Furthermore, in conjunction with theory, NEXAFS can be used to determine the oxidation state and local coordination environment of metal complexes.[22] Therefore, the advances in experimental techniques should go hand-in-hand with the development of theory and implementation thereof.

To simulate X-ray spectroscopy, it seems only natural to apply the well-established theory developed for the UV-Vis regime. However, a large discrepancy with experiment is observed if we blindly transfer this theory to the X-ray domain. To correct this discrepancy, it is thus necessary to include several effects beyond what is typically required for UV-Vis spectroscopy. First of all, since relativistic effects are generated in the core region, they need consideration in the simulation of core excitations already for quite light elements.[23, 24] Secondly, after exciting the core electron, the system is left with a core-hole that reduces the screening of the nuclear charge. As a result, the effective nuclear charge increases, which amounts to an additional stabilization of the excited state, referred to as core-hole relaxation.[25, 26] Third, in the UV-Vis regime, the wavelength is considerably larger than the extent of the molecule, suggesting that the fields appear to be uniform from the perspective of the molecule. Due to this difference in scale, the light–matter interaction can effectively be described by the first terms of a multipole expansion, yielding the electric-dipole approximation for linearly polarized light and the rotational strength for circular dichroism, the latter of which depends on both the electric- and magnetic-dipole moment. Considering that in both cases only dipolar contributions are needed, it seems natural to use *dipole approximation* as an umbrella term to designate both of these schemes. In the X-ray regime, however, the dipole approximation come into question.

In this thesis, it will be assessed whether the dipole approximation holds in the simulation of X-ray absorption spectroscopy.

In general, there are two possible approaches to include non-dipolar effects: either the semi-classical light–matter interaction is treated exactly, or the multipole expansion is truncated beyond zeroth order. However, truncated expansions inherently introduce gauge-origin dependency in the calculation, a problem which Bernadotte *et al.*[27] solved by expanding the absorption cross-section rather than the light–matter interaction itself. Furthermore, schemes of this type may also suffer from negative absorption cross-sections[28] and appearant divergences, which are, in principle, both alleviated if enough terms are included in the multipole expansion, although the latter problem may require an unreasonably large amount.[1] There are several other examples of implementations, besides the ones from the abovementioned references, that are capable to compute absorption intensities using either a truncated interaction,[29, 30] or the full interaction.[31, 32, 33] Some of these schemes have even been extended to model more complicated phenomena such as X-ray magnetic circular dichroism,[34] X-ray scattering[35] or transient absorption.[36] However, all of these implementations have a limited spectral range of applicability, since they are derived from a non-relativistic framework, having at most perturbative relativistic corrections. In the hard X-ray regime, where non-dipolar effects are most relevant, the light typically excites core orbitals of heavy elements, which demand a fully relativistic treatment. To answer the main question in a way that also holds for the hard X-ray regime, it is thus mandatory to work within such a framework.

In this thesis, I will present an implementation to simulate light–matter interactions using both the full- and truncated interaction in a four-component relativistic framework. This implementation is a part of Dirac,[37] a quantum chemical code specialized in relativistic molecular calculations either at the two- or four-component level. However, it should be noted that even this level of theory has a limited range of validity. At extreme energy scales, such as the ones encountered in highly charged cations, the effects of quantum electrodynamics may play a role in X-ray absorption spectra, either affecting the core electron through vacuum polarization/self-energy effects, or pair-creation stemming from high-energy photons. In addition, I have not included the effects of the core hole, the importance of which has been alluded to in previous paragraph. However, the treatment of these effects is beyond the scope of this thesis and will not be further pursued.

This thesis will be divided into four chapters. The first three discuss the required theory, whereas the fourth chapter discusses the Dirac implementation itself together with some applications. In particular, each chapter contains the following subjects:

- In Chapter 1, I will discuss the conventional methodology to calculate UV-Vis absorption spectra.
- Chapter 2 will be devoted to the basic principles of relativistic quantum chemistry.
- Subsequently, in Chapter 3, it will be discussed how light–matter interactions can be treated beyond the dipole approximation.
- Using the results from previous three chapters, I will discuss the implementation in Dirac and apply it to various examples in Chapter 4.
- The last section is devoted to the conclusion and outlook.

The various quantities appearing throughout this work are expressed in SI units and unless stated otherwise, the Einstein summation convention will be applied.

Chapter 1

Conventional Methods to Simulate UV-Vis Absorption Spectroscopy

1.1 Introduction

In this chapter, I will illustrate conventional quantum chemical methods to calculate UV-Vis absorption spectra. The ideas and derivations expressed in this chapter generally follow the book *Principles and Practices of Molecular Properties*[7], which should be consulted for further details. To classify the type of approximations typically made in the simulation of UV-Vis spectroscopy, I will divide the calculation of absorption intensities into three main components: the ground state calculation, excited-state calculation and the treatment of the light–matter interaction.

To simplify the ground state calculation, approximations can be applied to either the electronic-structure method or the Hamiltonian. For example, the valence orbitals typically involved in UV-Vis spectroscopy are the least susceptible to relativistic effects, suggesting that a non-relativistic Hamiltonian, such as the Schrödinger- or Pauli Hamiltonian, is usually sufficient. After having decided which Hamiltonians to use, an electronic structure method has to be chosen to approximate the complexity of the many-body wave function. There is a plethora of electronic structure methods to choose from, each of which having a distinct cost-to-accuracy ratio. For example, the ground state can most reliably be obtained using wave function methods such as coupled cluster (CC) or configuration interaction (CI), albeit at the expense of computational costs. The computational costs are less for the Hartree-Fock (HF), although its accuracy is rather low as well. An improved cost to accuracy ratio can be obtained by employing density-functional theory (DFT), which roughly comes at the cost of a HF calculation and can even approach the accuracy of wave function methods in some cases. In this thesis, HF and DFT will be the methods of choice to describe the ground state. Hereafter, I will use the term self-consistent-field methods to encompass both approaches.

Using the ground-state as a starting point, there is a variety of methods available to treat excited states, as will become more clear in this chapter. For exact states, and CI wave functions, this procedure is rather straightforward, because excited states can be obtained directly from diagonalization of the Hamiltonian. Following this route at the SCF level is more cumbersome, because HF and DFT are essentially ground state theories. However, explicit calculation of excited states can be avoided by applying linear response theory. In this chapter, it will be shown how the poles and residues of the linear response functions can be related to excitation energies and transition moments, which in turn, can be used to obtain absorption intensities. As a main drawback, this method does not take core-hole effects into consideration, which should not matter too much in the UV-Vis regime.

What thus remains is to find a suitable description of the light–matter interaction. In this work, a semi–classical description will be pursued, although there are examples in literature in which the quantum mechanical nature of light is taken into account.[38, 39] A particular feature of the UV-Vis regime is the large size of the wavelength compared to the molecular system, which allows for the application of the dipole approximation.

To better understand the origins of this approximation, let us consider the following example. Suppose we want to model the absorption of linearly polarized red light ($\lambda = 700$ nm) by a benzene molecule. The electromagnetic fields describing this type of light are shown below

$$\mathbf{E}\left(\mathbf{r},t\right) = E_\omega \boldsymbol{\epsilon} \sin\left[\mathbf{k}\cdot\mathbf{r} - \omega t + \delta\right]; \quad \mathbf{B}\left(\mathbf{r},t\right) = \frac{E_\omega}{\omega}\left(\mathbf{k}\times\boldsymbol{\epsilon}\right)\sin\left[\mathbf{k}\cdot\mathbf{r} - \omega t + \delta\right], \tag{1.1}$$

where appears the wave vector $\mathbf{k}$ with length

$$k = \frac{\omega}{c} = \frac{2\pi}{\lambda}, \tag{1.2}$$

the polarization vector $\boldsymbol{\epsilon}$ and the phase δ.[40, Chapter 9][41, Chapter 7] Light can be polarized in other forms than the one shown above, but that discussion will be postponed to Chapter 3.

For dilute solutions, the absorption of light is given by the Lambert-Beer law

$$\frac{I}{I_0} = e^{-\mathcal{N}\sigma(\omega)\ell}. \tag{1.3}$$

In this expression, I and I_0 are the out- and ingoing intensities, whereas the exponent gives the effective number of absorbing molecules, expressed in terms of the number density of absorbing molecules, $\mathcal{N}$, the length traversed by the light, ℓ, and the absorption cross-section, $\sigma(\omega)$. The latter can be regarded as a surface spanned by all molecules that have successfully absorbed the incoming light, hence forming a measure of the absorption intensity. The quantities expressed in the Lambert-Beer law are macroscopic in nature and are in principle, only available from experiment, whereas quantum chemical simulations typically provide microscopic quantities. In the context of light absorption, the two scales can be connected by the following relation

$$I\sigma(\omega_{fi}) = \hbar\omega_{fi} w_{i\rightarrow f}, \tag{1.4}$$

where $w_{i \to f}$ is the transition rate and $\hbar\omega_{fi}$ the energy difference between the initial- and final state. Both sides of this equation give a measure of the energy that is absorbed by the system. The transition rate can be calculated using quantum mechanical methods, thus avoiding the need to directly calculate the absorption cross-section. Before we proceed to calculate this quantity, let us first take a step back and examine the system under consideration (Figure 1.1).

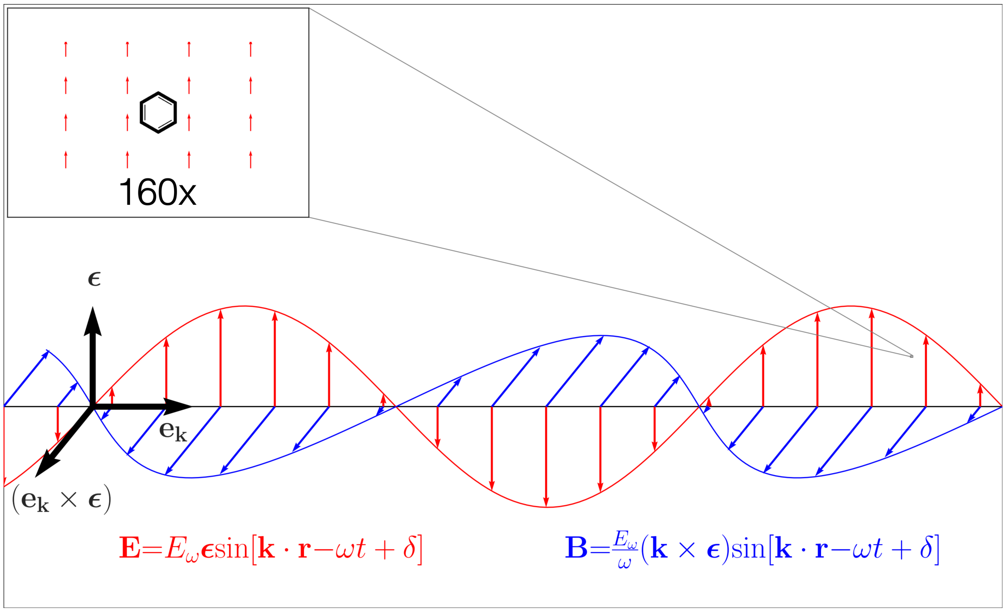

Figure 1.1: schematic representation of a benzene molecule interacting with linearly polarized red light (λ = 700 nm) consisting of an electric (red) and magnetic (blue) component. To make the magnetic field amplitude visible in this picture, it is not depicted at its true relative scale with respect to the electric field. The benzene molecule is only visible after zooming into a small region of space and in this region, the molecule effectively experiences a uniform field, which is dominated by its electric component. The mathematical expressions describing the electromagnetic fields are given at the bottom of the box. The propagation- and polarization direction are described by the unit vectors $\boldsymbol{e}_k$ and $\boldsymbol{\epsilon}$, respectively, with the latter being defined by the relation $\boldsymbol{e}_k = \frac{c}{\omega}\boldsymbol{k}$.

What stands out is the vast difference in scale between the wavelength and the benzene molecule, the latter of which can only be perceived in a zoomed-in frame. In this frame, most of the curvature of the plane wave is lost, implying that the molecule effectively experiences a uniform field, whose magnetic component can safely be neglected due to its prefactor of $1/c$. Formulated more mathematically, the light–matter interaction is expanded in orders of the wave vector and truncated at first order, justified by the limit $kr \ll 1$. At this order, our interaction is given by the electric-dipole operator, corresponding to a uniform electric field. These considerations form the basis of the electric-dipole approximation, which is widely used in UV-Vis spectroscopy. To describe ECD, however, the electric-dipole approximation is not sufficient, since this interaction also depends on the magnetic-dipole operator, appearing an order higher in our expansion.

Let us now direct our attention to the Hamiltonian that describes this system. Without the loss of generality, our Hamiltonian can be separated into a static part (given by a non-relativistic Hamiltonian) and a time-dependent interaction operator

$$\hat{H} = \hat{H}_0 + \hat{V}(t); \quad \hat{V}(t) = \int_{-\infty}^{\infty} dt e^{-i\omega t} \hat{V}(\omega), \tag{1.5}$$

the latter of which is conveniently expressed as a Fourier transform. Furthermore, hermiticity of the interaction operator implies the following relation in the frequency domain

$$\hat{V}^{\dagger}(t) = \hat{V}(t) \rightarrow \hat{V}^{\dagger}(\omega) = \hat{V}(-\omega). \tag{1.6}$$

I will postpone the explicit construction of this operator to Chapter 3, as it suffices for now to assume that this operator is periodic. In turn, this implies that the Fourier transform of the interaction operator is discretized into frequency components that are integer multiples of a fundamental frequency

$$\hat{V}(t) = \hat{V}(t+T) \rightarrow \omega = n\omega_T; \quad \omega_T = \frac{2\pi}{T}, \quad n \in \mathbb{N}. \tag{1.7}$$

Therefore, the interaction operator can be expressed as

$$\hat{V}(t) = \sum_{y=-N}^{N} \lambda_{\alpha}^{\omega_y} \hat{V}_{\alpha}(\omega_y) e^{-i\omega_y t + \epsilon t}, \tag{1.8}$$

where the indices y and α represent the Fourier- and Cartesian components. For the Cartesian components, the Einstein summation convention is applied, whereas the sum over frequency components is written explicitly. As can be concluded from the hermiticity of the overall operator, the summation over the frequency components contains positive- and negative indices, corresponding to equal but opposite pairs of frequencies

$$\omega_0, (\omega_1, -\omega_1), (\omega_2, -\omega_2), (\omega_3, -\omega_3), \cdots . \tag{1.9}$$

Here, the zeroth frequency is zero ($\omega_0 = 0$), thus allowing for the possibility of static contributions to our perturbation. Furthermore, in this expression, ϵ is an infinitesimal number ensuring that the perturbation is switched on slowly, i.e. an adiabatic switch.

Within the electric-dipole approximation, the frequency components are given by the electric-dipole moment operator

$$\hat{V}_{\alpha}(\omega_y) = \hat{Q}_{\alpha}^{[1]} = -er_{\alpha}; \quad \lambda_{\alpha}^{\omega_y} = \frac{1}{2} E^{\omega} \epsilon_{\alpha}, \tag{1.10}$$

where $-e$ is the electron charge. In our particular case of monochromatic light, only one pair of frequencies contributes, allowing us to express our interaction operator in a more simple form

$$\hat{V}(t) = E^{\omega}\epsilon_{\alpha}\hat{Q}_{\alpha}^{[1]}\cos(\omega t)e^{\epsilon t}. \tag{1.11}$$

However, in the following, the representation from Eqn. (E.8) is preferred to preserve generality of the formalism.

1.2 Exact-State Formalism

1.2.1 Absorption Intensities

Using our Hamiltonian as a starting point, the time evolution of the wave function can be found by solving the time-dependent Schrödinger equation

$$i\hbar\frac{\partial}{\partial t}|\psi(t)\rangle = \hat{H}|\psi(t)\rangle. \tag{1.12}$$

Approximative schemes are needed to find a solution to this equation, because in general it is not analytically solvable. To keep our analysis simple, it will be assumed for now that the exact eigenfunctions of the time-independent Hamiltonian are known

$$\hat{H}_0|n\rangle = E_n|n\rangle. \tag{1.13}$$

This set of functions is complete and can thus form a basis for the time-dependent wave function

$$|\psi(t)\rangle = \sum_n c_n(t)e^{-\frac{iE_nt}{\hbar}}|n\rangle, \tag{1.14}$$

where the time-dependent phase factors of each eigenfunction is included in the expansion. Equations of motion can be obtained for these coefficients by inserting this ansatz into the time-dependent Schrödinger equation

$$i\hbar\sum_n\frac{\partial}{\partial t}(c_n(t)e^{-\frac{iE_nt}{\hbar}})|n\rangle = \sum_n c_n(t)e^{-\frac{iE_nt}{\hbar}}\hat{H}|n\rangle \tag{1.15}$$

and projecting with $\langle m|$

$$\frac{\partial c_m(t)}{\partial t} = \sum_n\frac{1}{i\hbar}e^{i\omega_{mn}t}V_{mn}(t)c_n(t); \quad \omega_{mn} = \frac{1}{\hbar}(E_m - E_n) \tag{1.16}$$

$$V_{mn}(t) = \langle m|\hat{V}(t)|n\rangle. \tag{1.17}$$

However, solving this equation still forms a major obstacle. The problem can be simplified by expanding the coefficients, and thus the wave function, in orders of $\lambda = \{\lambda_{\alpha}^{\omega_y}\}$

$$c_n(t) = c_n^{(0)} + c_n^{(1)}(t) + c_n^{(2)}(t) + \cdots; \quad |\psi(t)\rangle = |\psi^{(0)}\rangle + |\psi^{(1)}\rangle + |\psi^{(2)}\rangle + \cdots. \tag{1.18}$$

This expansion is the essence of perturbation theory and it is valid provided that $\lambda \ll 1$. At $t = -\infty$, before the perturbation has been switched on, the wave function is in the ground state, which translates to the following boundary condition $c_n^{(0)} = \delta_{n0}$.

To first order in the perturbation, the equation of motion reads

$$\frac{\partial c_m^{(1)}(t)}{\partial t} = \sum_n \frac{1}{i\hbar} e^{i\omega_{mn}t} V_{mn}(t) c_n^{(0)}(t) \tag{1.19}$$

from which the first-order coefficients can be isolated upon integration

$$c_m^{(1)}(t) = \frac{1}{i\hbar}\int_{-\infty}^{t} dt' e^{i\omega_{mn}t'} V_{mn}(t') c_n^{(0)} = -\frac{1}{\hbar}\sum_{y=-N}^{N} \frac{\langle m|\lambda_\alpha^{\omega_y}\hat{V}_\alpha(\omega_y)|0\rangle}{\omega_y - \omega_{m0} + i\epsilon} e^{(-i\omega_y + i\omega_{m0} + \epsilon)t}. \tag{1.20}$$

In the integration step, the adiabatic switch shows its true virtue, because the lower bound of this integral would be ill-defined without its presence. Furthermore, due to its infinitesimal nature, it can be neglected in the final expression. To arbitrary order, the coefficients can be obtained by applying this procedure recursively

$$c_m^{(N)}(t) = \frac{1}{i\hbar}\int_{-\infty}^{t} dt' e^{i\omega_{mn}t'} V_{mn}(t') c_n^{(N-1)}(t). \tag{1.21}$$

However, for the purposes of this thesis, the first-order equations are sufficient, as the light intensity of conventional spectrometers is typically too small to evoke high-order effects. We thus arrive at the following expression for the first-order perturbed wave function

$$|\psi^{(1)}\rangle = \sum_n \sum_{y=-N}^{N} \left[-\frac{\lambda_\alpha^{\omega_y}}{\hbar} \frac{\langle n|\hat{V}_\alpha(\omega_y)|0\rangle}{\omega_{n0} - \omega_y} e^{-i\omega_y t} \right] e^{-i\frac{E_0 t}{\hbar}} |n\rangle, \tag{1.22}$$

in which the adiabatic switch is neglected. Turning back our attention to Eqn. (E.4), the absorption rate from the ground state to a final state, $|f\rangle$, can be found using the first-order coefficients

$$w_{0\to f} = \frac{d|c_f^{(1)}(t)|^2}{dt} = \frac{d}{dt}\left| -\sum_{y=-N}^{N} \frac{\lambda_\alpha^{\omega_y}}{\hbar} \frac{\langle f|\hat{V}_\alpha(\omega_y)|0\rangle}{\omega_y - \omega_{f0} + i\epsilon} e^{(-i\omega_y + \epsilon)t} \right|^2 \tag{1.23}$$

If we assume resonance conditions, i.e. $\omega_y = \omega_{f0}$, and let the adiabatic switch go to zero, then the y^{th} term in the summation diverges. Evidently, an infinite transition rate does not make physical sense. However, for now, let us tolerate the presence of this divergence and use it to our advantage. The fact that one term in this summation is infinite, implies that all other terms can be neglected. From further manipulations of the above expression, we arrive at the following result

$$w_{0\to f} = \frac{2\pi}{\hbar^2} |\langle f|\lambda_\alpha^{\omega_{f0}}\hat{V}_\alpha(\omega_{f0})|0\rangle|^2 f(\omega;\omega_{f0},\epsilon) e^{2\epsilon t}; \quad f(\omega;\omega_{f0},\epsilon) = \frac{1}{\pi}\frac{\epsilon}{(\omega_{f0} - \omega)^2 + \epsilon^2}. \tag{1.24}$$

As the adiabatic switch approaches zero, the frequency-dependent factor reduces to a Dirac-delta function

$$\lim_{\epsilon\to 0} f(\omega;\omega_{f0},\epsilon) = \delta(\omega_{f0}-\omega), \tag{1.25}$$

which confirms the presence of a divergence, as expected from previous analysis. Strictly speaking, the delta function is a distribution rather than an actual function, implying that it can only be properly defined inside of an integral: $f(a) = \int dx\delta(x-a)f(x)$. In section 1.2.2, it will be illustrated how divergences of this type can be useful in the calculation of excitation energies and transition moments. However, before we arrive there, I will first demonstrate how to avoid these divergences altogether.

The origin of this problem can be traced back to the lack of essential physics in our model. The perturbing operator in the Hamiltonian only allows for stimulated emission, whereas in more realistic systems, emission can also occur spontaneously under the influence of environmental factors such as thermal collisions or vacuum fluctuations.[42] These effects can be taken into account phenomenologically by the following change of variables $\omega_{n0} \to \omega_{n0} + i\gamma_{n0}$ in the denominator

$$c_f^{(1)}(t) = -\sum_{y=-N}^{N} \frac{\lambda_\alpha^{\omega_y}}{\hbar}\left[\frac{\langle f|\hat{V}_\alpha(\omega_y)|0\rangle}{\omega_{f0}-\omega_y+i\gamma_{f0}} e^{(-i\omega_y+i\omega_{f0})t}\right] e^{\epsilon t}. \tag{1.26}$$

Here, γ_{n0} represents a damping factor that introduces exponential decay. The damping factor pushes the poles into the complex plane, thus making the coefficient well-defined on the real line. Using these adjusted coefficients, the transition rate can be expressed as

$$\lim_{\epsilon\to 0} w_{0\to f} = \frac{2\pi}{\hbar^2}|\langle f|\lambda_\alpha^{\omega_{f0}}\hat{V}_\alpha(\omega_{f0})|0\rangle|^2 f(\omega;\omega_{f0},\gamma_{f0}); \quad f(\omega;\omega_{f0},\gamma_{f0}) = \frac{1}{\pi}\frac{\gamma_{f0}}{(\omega_{f0}-\omega)^2+\gamma_{f0}^2}. \tag{1.27}$$

Due to the finite value of the damping factor, $f(\omega,\omega_{f0},\gamma_{f0})$ becomes a Lorentzian linewidth function. By comparing with Eqn. (E.4), we find the following expression for the absorption cross-section

$$\sigma(\omega) = \frac{\omega}{\hbar I}|V_{f0}^{\omega_{f0}}|^2 f(\omega;\omega_{f0},\gamma_{f0}) \tag{1.28}$$

The above result is referred to as Fermi's golden rule and it will be the central equation in this thesis to evaluate absorption intensities.[43, 44] In practice, the auxiliary quantity $\frac{\omega}{\hbar I}|V_{f0}^{\omega}|^2$ is calculated first, giving rise to discrete peaks, which are then broadened according to the Lorentzian distribution. Alternatively, absorption intensities can be calculated using response functions, which will be discussed in the next section.

1.2.2 Response Functions

Having established the time-dependence of the first-order perturbed wave function, we can proceed to express the time evolution of expectation values. Let us in this example study the time evolution of the αth component of the electric-dipole moment of our system

$$Q_\alpha^{[1]}(t) = \langle \psi(t) | \hat{Q}_\alpha^{[1]} | \psi(t) \rangle. \tag{1.29}$$

This expression will be simplified by developing it in orders of the perturbation

$$Q_\alpha^{[1]}(t) = \langle \psi^{(0)} | \hat{Q}_\alpha^{[1]} | \psi^{(0)} \rangle + \langle \psi^{(1)} | \hat{Q}_\alpha^{[1]} | \psi^{(0)} \rangle + \langle \psi^{(0)} | \hat{Q}_\alpha^{[1]} | \psi^{(1)} \rangle + \cdots . \tag{1.30}$$

To describe linear absorption processes, it suffices to only keep the first few terms in this expansion

$$Q_\alpha^{[1]}(t) = Q_{0;\alpha}^{[1]} + \sum_{y=-N}^{N} \lambda_\beta^{\omega_y} \langle\langle \hat{Q}_\alpha^{[1]}; \hat{V}_\beta(\omega_y) \rangle\rangle e^{-i\omega_y t}, \tag{1.31}$$

where appears the permanent electric-dipole moment

$$Q_{0;\alpha}^{[1]} = \langle \psi^{(0)} | \hat{Q}_\alpha^{[1]} | \psi^{(0)} \rangle \tag{1.32}$$

and the linear response function

$$\langle\langle \hat{Q}_\alpha^{[1]}; \hat{V}_\beta(\omega) \rangle\rangle = -\frac{1}{\hbar} \sum_n \left[\frac{\langle 0 | \hat{V}_\beta(\omega) | n \rangle \langle n | \hat{Q}_\alpha^{[1]} | 0 \rangle}{\omega_{n0} + \omega} + \frac{\langle 0 | \hat{Q}_\alpha^{[1]} | n \rangle \langle n | \hat{V}_\beta(\omega) | 0 \rangle}{\omega_{n0} - \omega} \right]. \tag{1.33}$$

In this expression, I have dropped the frequency index y, since the response function only depends on one frequency component of the interaction operator. For a given perturbation frequency, the linear response function tells us how the electric-dipole moment changes under the influence of the external perturbation. More generally, the response function $\langle\langle \hat{A}; \hat{B} \rangle\rangle$ gauges the response of the expectation value of $\hat{A}$ under the influence of $\hat{B}$ as a perturbation, or the other way around due to their symmetric nature. Furthermore, by only considering the zeroth frequency mode of a perturbation, i.e. $\omega_0 = 0$, response functions can also be used to describe static perturbations. In the following I will denote static response functions as $\langle\langle \hat{A}; \hat{B} \rangle\rangle_0$.

Similar to the findings of previous section, response function diverges under resonance conditions, i.e. $\omega_{n0} = \pm\omega_y$. However, this artifact should not be seen as a nuisance, but rather as a useful tool that provides us with excitation energies and transition moments.[45][46, Section 6.4] From response functions, we can assert whether a certain frequency is a transition frequency, because a divergence appears in this case. Therefore, the poles serve as a diagnostic that can be used to find transition frequencies. Once this pole has been identified, transition moments can be extracted from the residues of the response functions.

$$\lim_{\omega \to \omega_{n0}} (\omega_{n0} - \omega) \langle\langle \hat{Q}_\alpha^{[1]}; \hat{V}_\beta(\omega) \rangle\rangle = -\frac{1}{\hbar} \langle 0 | \hat{Q}_\alpha^{[1]} | n \rangle \langle n | \hat{V}_\beta(\omega) | 0 \rangle. \tag{1.34}$$

These transition moments can then be inserted into Fermi's golden rule to obtain the absorption cross-section. Although these relations seem obvious in an exact-state-formalism, they prove to be essential to calculate excitation energies and transition moments in approximate theories.

Alternatively, the divergences can be eliminated by introducing an imaginary damping factor

$$\langle\langle \hat{Q}_\alpha^{[1]}; \hat{V}_\beta(\omega)\rangle\rangle = -\frac{1}{\hbar}\sum_n \left[\frac{\langle 0|\hat{V}_\beta(\omega)|n\rangle\langle n|\hat{Q}_\alpha^{[1]}|0\rangle}{\omega_{n0}+\omega+i\gamma_{n0}} + \frac{\langle 0|\hat{Q}_\alpha^{[1]}|n\rangle\langle n|\hat{V}_\beta(\omega)|0\rangle}{\omega_{n0}-\omega-i\gamma_{n0}}\right] \tag{1.35}$$

that push the poles into the imaginary plane. This response function is thus valid over the entire spectral range.[47, 48] Due to their general structure, damped response functions can provide information on a plethora of molecular properties such as the refractive index,[47] electronic circular dichroism[49, 50] and absorption spectra.[51, 52] An absorption spectrum can be obtained from this response function by tracing its imaginary part over the spectral range of interest. To facilitate this calculation, it is often assumed that there is a universal damping factor for all terms in the response function

$$Im[\langle\langle \hat{Q}_\alpha^{[1]}; \hat{V}_\beta^\omega\rangle\rangle] = \frac{\gamma}{\hbar}\sum_n \left[\frac{\langle 0|\hat{Q}_\alpha^{[1]}|n\rangle\langle n|\hat{V}_\beta(\omega)|0\rangle}{(\omega_{n0}-\omega)^2+\gamma^2} - \frac{\langle 0|\hat{V}_\beta(\omega)|n\rangle\langle n|\hat{Q}_\alpha^{[1]}|0\rangle}{(\omega_{n0}+\omega)^2+\gamma^2}\right] \tag{1.36}$$

In this work, we will pursue the former method that uses the poles and residues of the response functions to calculate absorption intensities, which will be generalized to SCF methods in the next section.

1.3 SCF Theory

1.3.1 Energy Optimization

In the previous section, it was assumed that the exact eigenstates of the time-independent Hamiltonian are known. However, in practice, this is seldom the case due to the sheer complexity of the many-body wave function. To perform calculations, it is thus necessary to resort to approximative schemes. I recall that this work is based on SCF methods, i.e. HF and DFT, both of which essentially involve the optimization of a single Slater determinant

$$\frac{1}{\sqrt{N!}}\begin{vmatrix} \phi_1(\boldsymbol{r}_1) & \phi_2(\boldsymbol{r}_1) & \cdots & \phi_N(\boldsymbol{r}_1) \\ \phi_1(\boldsymbol{r}_2) & \phi_2(\boldsymbol{r}_2) & \cdots & \phi_N(\boldsymbol{r}_2) \\ \vdots & \vdots & \ddots & \vdots \\ \phi_1(\boldsymbol{r}_N) & \phi_2(\boldsymbol{r}_N) & \cdots & \phi_N(\boldsymbol{r}_N) \end{vmatrix}, \tag{1.37}$$

where $\{\phi_i\}$ are one-electron functions, $\boldsymbol{r}_i$ the coordinates of electron i and N the number of electrons in the system. At first glance, HF and DFT seem to resemble quite a lot, although the physical origins of the two theories differ significantly.

The foundations of DFT are given by the two Hohenberg-Kohn theorems.[53] The theorem states that all properties of the wave function can be obtained from the electron density alone. In particular, the energy can be expressed as a functional of the density

$$E[\rho] = T[\rho] + V_{en}[\rho] + V_{ee}[\rho], \tag{1.38}$$

where $T[\rho]$, $V_{en}[\rho]$ and $V_{ee}[\rho]$ are the kinetic energy, electron-nucleus attraction and the electron-electron repulsion functionals, respectively. The second theorem states that this functional obeys a variational principle

$$E_0 \leq E[\tilde{\rho}], \tag{1.39}$$

where $\tilde{\rho}$ is some trial density. If the density functional is known, it thus becomes possible to obtain the ground state density using optimization schemes. However, the first theorem is an existence proof and thus neither prescribes how the exact functional should be constructed, nor how approximate functionals can be systematically improved. Notably, the kinetic energy functional is difficult to construct.

Kohn and Sham made a huge leap forward with their follow-up paper, in which they represented the problem as a fictitious non-interacting system.[54] This fictitious system partially eliminates the complications associated with the kinetic energy functional, since the kinetic energy of this system can be obtained exactly. To compensate for this drastic approximation, the system is subjected to an effective one-electron potential ensuring that the non-interacting one-electron density is equivalent to the density of the exact many-body wave function. More specifically, this potential corrects for exchange and correlation effects and the approximative nature of the kinetic energy. The one-particle functions that constitute the determinant can be obtained by solving

$$\left[\hat{T} + v_H[\rho] + v_{xc}[\rho]\right]\phi_i = \epsilon\phi_i, \tag{1.40}$$

where appears the kinetic energy operator, $\hat{T}$, the exchange-correlation potential, $v_{xc}[\rho]$, and the Hartree potential, $v_H[\rho] = \int d^3\boldsymbol{r}'\rho(\boldsymbol{r}')/|\boldsymbol{r}' - \boldsymbol{r}|$. Using this fictitious system, the exact energy can be obtained from the functional

$$E[\rho] = T_s[\rho] + V_{en}[\rho] + J[\rho] + E_{xc}[\rho], \tag{1.41}$$

where $T_s[\rho]$ is the kinetic energy of the fictitious system, $J[\rho]$ the energy associated with the Hartree potential and $E_{xc}[\rho]$ the exchange-correlation energy. To this day, the main challenge associated with DFT is to find approximative exchange-correlation potentials, since there is no systematic method to improve this potential.

HF theory, however, is much more simple in nature. In this theory, the wave function is approximated by a single determinant, while the Hamiltonian is exact. Given that the exact many-body wave function is an infinite expansion of such determinants, the HF determinant is in some cases the dominant contribution to the wave function. Therefore, the HF determinant can be understood as an effective one-determinantal wave function. It should be stressed, however, that the Kohn-Sham determinant does not share this interpretation, because in this case the density is physically meaningful and not the determinant on its own.

Regardless of the applied method, it is convenient to represent SCF methods using the second-quantization formalism.[55] In this formalism, the occupation numbers of each orbital are contained in a vector. Electrons can be added or removed from orbitals by the action of creation and annihilation operators

$$a_p|\boldsymbol{k}\rangle = a_p|i_1, i_2, \cdots i_p, \cdots, i_N\rangle = \begin{cases} 0 & \text{if } i_p = 0 \\ \Gamma_p^k|i_1, i_2, \cdots 0, \cdots, i_N\rangle & \text{if } i_p = 1 \end{cases} \tag{1.42}$$

$$a_p^\dagger|\boldsymbol{k}\rangle = a_p^\dagger|i_1, i_2, \cdots i_p, \cdots, i_N\rangle = \begin{cases} \Gamma_p^k|i_1, i_2, \cdots 1, \cdots, i_N\rangle & \text{if } i_p = 0 \\ 0 & \text{if } i_p = 1 \end{cases},$$

where $\{i_p\}$ are occupation numbers of orbitals and Γ_p^k is a phase factor depending both on the index p and the overall occupation, represented by the the label k. It can be shown that this phase factor is required to correctly reproduce the Slater-Condon rules. In the Slater determinant representation, the fermionic nature of electrons is taken into account by the anti-symmetry of determinants upon exchange of rows. The second-quantization formalism, however, naturally incorporates this feature into its algebraic properties. The algebra of these operators can be summarized as

$$\{a_p, a_q\} = 0; \quad \{a_p^\dagger, a_q\} = \delta_{pq} \quad \{a_p^\dagger, a_q^\dagger\} = 0, \tag{1.43}$$

from which we can derive the relation

$$|1_p, 1_q\rangle = a_p^\dagger a_q^\dagger|vac\rangle = -a_q^\dagger a_p^\dagger|vac\rangle = -|1_q, 1_p\rangle. \tag{1.44}$$

In the following, it will be assumed that the indices $(pqrs)$ represent general orbitals, $(ijkl)$ occupied orbitals and $(abcd)$ virtual orbitals.

In this convention, the second-quantized electronic Hamiltonian assumes the form

$$\hat{H}_0 = h_{pq}a_p^\dagger a_q + \frac{1}{2}(pq|rs)a_p^\dagger a_r^\dagger a_s a_q, \tag{1.45}$$

where appears the one-electron integrals

$$h_{pq} = \int d^3\boldsymbol{r}\phi_p^\dagger(\boldsymbol{r})\left[\hat{T} + V_{en}\right]\phi_q(\boldsymbol{r}); \quad h_{pq}^* = h_{qp} \tag{1.46}$$

and the two-electron integrals

$$(pq|rs) = \int d^3\boldsymbol{r}_1 \int d^3\boldsymbol{r}_2 \frac{\phi_p^\dagger(\boldsymbol{r}_1)\phi_q(\boldsymbol{r}_1)\phi_r^\dagger(\boldsymbol{r}_2)\phi_s(\boldsymbol{r}_2)}{r_{12}}. \tag{1.47}$$

For some generic wave function, ψ, the energy can be obtained from the expectation value of the Hamiltonian

$$E = \langle\psi|\hat{H}_0|\psi\rangle = h_{pq}D_{pq} + \frac{1}{2}(pq|rs)d_{pq,rs}, \tag{1.48}$$

where in the second equality, I have introduced the one-body

$$D_{pq} = \langle\psi|a_p^\dagger a_q|\psi\rangle \tag{1.49}$$

and two-body density matrix

$$d_{pq,rs} = \langle\psi|a_p^\dagger a_r^\dagger a_s a_q|\psi\rangle. \tag{1.50}$$

In the special case of Hartree-Fock theory, which is based on a *single* determinant state, the two-body density matrix can be expressed in terms of the one-body density matrix, yielding the following expression for the Hartree-Fock energy

$$E_{HF} = h_{pq}D_{pq} + \frac{1}{2}\big((pq|rs) - (ps|rq)\big)D_{pq}D_{rs}. \tag{1.51}$$

A similar expression can be found for DFT by relating the one-body density matrix to its corresponding density function[56]

$$\rho(\boldsymbol{r}) = D_{pq}\phi_p^\dagger(\boldsymbol{r})\phi_q(\boldsymbol{r}) \tag{1.52}$$

and inserting it in Eqn. (1.41)

$$E_{DFT} = h_{pq}D_{pq} + \frac{1}{2}\big((pq|rs) - \gamma(ps|rq)\big)D_{pq}D_{rs} + E_{xc}[\rho]. \tag{1.53}$$

To allow for the possibility of hybrid functionals, the factor γ is included which mixes in Hartree-Fock exchange.[57]

Both SCF theories are variational, so the orbitals can be obtained by minimizing the energy. For this procedure, it is convenient to express the determinant in a set of parameters. In this work, an exponential parametrization will be chosen to describe the SCF determinant

$$|\tilde{0}\rangle = \exp[-\hat{\kappa}]|0\rangle; \quad \hat{\kappa} = \kappa_{pq}\hat{a}_p^\dagger\hat{a}_q. \tag{1.54}$$

Here, $|0\rangle$ is a reference state which, in current context, is the wave function from previous SCF iteration. As a starting guess, orbitals are typically given as linear combinations of atomic orbitals, which may be obtained from equivalent basis set calculations,[58] the extended Huckel approach[59] or numerical calculations.[60] The action of the exponential operator is to rotate between orbitals. Unitarity is ensured in this operator by imposing anti-hermiticity in the parameter matrix: $\kappa_{pq}^* = -\kappa_{qp}$. Using the properties of this operator, it can be shown that orbitals transform according to

$$\tilde{a}_p = U_{pq}\hat{a}_q^\dagger; \quad U_{pq} = \big(\exp[-\hat{\kappa}]\big)_{pq}. \tag{1.55}$$

Written in this form, the wave function parameters can assume any value without breaking orthonormality. Alternatively, a constrained optimization can be applied using the method of Lagrange multipliers,[61][62, p. 407] but this will not be further pursued in this work. Using the exponential parametrization, the one-body density matrix assumes the form

$$\tilde{D}_{pq} = \langle \tilde{0} | a_p^\dagger a_q | \tilde{0} \rangle = \langle 0 | \exp[\hat{\kappa}] a_p^\dagger a_q \exp[-\hat{\kappa}] | 0 \rangle. \tag{1.56}$$

The energy can thus be expressed as a function of the parameters by inserting this definition into the energies provided by Eqs. (1.51) and (1.53). At the minimum of the energy, the partial derivatives of the energy with respect to the parameters vanish, hence forming a condition of convergence. By extension, this condition is determined by the first partial derivatives of the one-body density matrix.

However, before proceeding to further analyse this condition, it should be stressed that for a certain subset of parameters, the density matrix does not change, hence fulfilling the variational condition trivially. To understand this better, let us apply a Baker-Campbell-Hausdorff expansion to the one-body density matrix

$$\langle 0 | \exp[\hat{\kappa}] a_p^\dagger a_q \exp[-\hat{\kappa}] | 0 \rangle = \langle 0 | a_p^\dagger a_q + [\hat{\kappa}, a_p^\dagger a_q] + \frac{1}{2} \left[\hat{\kappa}, [\hat{\kappa}, a_p^\dagger a_q] \right] + \cdots | 0 \rangle. \tag{1.57}$$

When evaluated at the reference point, only the linear commutator terms can contribute to the first derivative with respect to the parameters. For the occupied-occupied and virtual-virtual block, these derivatives thus assume the form

$$\begin{aligned} \frac{\partial \tilde{D}_{pq}}{\partial \kappa_{ij}} \Big|_{\kappa=0} &= \langle 0 | \left[a_i^\dagger a_j, a_p^\dagger a_q \right] | 0 \rangle = 0 \\ \frac{\partial \tilde{D}_{pq}}{\partial \kappa_{ab}} \Big|_{\kappa=0} &= \langle 0 | \left[a_a^\dagger a_b, a_p^\dagger a_q \right] | 0 \rangle = 0. \end{aligned} \tag{1.58}$$

The non-redundant parameters are given by the occupied-virtual and virtual-occupied blocks

$$\begin{aligned} \frac{\partial \tilde{D}_{pq}}{\partial \kappa_{ai}} \bigg|_{\kappa=0} &= \langle 0 | [a_a^\dagger a_i, a_p^\dagger a_q] | 0 \rangle = \langle 0 | a_p^\dagger a_q | \Phi_i^a \rangle = \delta_{pi} \delta_{qa} \\ \frac{\partial \tilde{D}_{pq}}{\partial \kappa_{ai}^*} \bigg|_{\kappa=0} &= \langle 0 | [a_i^\dagger a_a, a_p^\dagger a_q] | 0 \rangle = \langle \Phi_i^a | a_p^\dagger a_q | 0 \rangle = \delta_{qi} \delta_{pa}. \end{aligned} \tag{1.59}$$

The variational condition can thus be expressed as

$$\frac{\partial E}{\partial \kappa_{ai}} \bigg|_{\kappa=0} = \frac{\partial E_0}{\partial \kappa_{ai}^*} \bigg|_{\kappa=0} = 0; \quad \forall \kappa_{ai}, \kappa_{ai}^*, \tag{1.60}$$

In case of DFT, the energy derivatives also depend on derivatives of the exchange-correlation energy. These derivatives can most conveniently be expressed in terms of the exchange-correlation density,

$$\left.\frac{\partial e_{xc}(\rho,\zeta)}{\partial \kappa_{ai}}\right|_{\kappa=0} = \frac{\partial e_{xc}}{\partial \rho}\frac{\partial \rho}{\partial \kappa_{ai}} + \frac{\partial e_{xc}}{\partial \zeta}\frac{\partial \zeta}{\partial \kappa_{ai}}; \quad E_{xc}[\rho] = \int d^3\boldsymbol{r} e_{xc}(\rho,\zeta). \tag{1.61}$$

As a general feature of GGA functionals, the exchange-correlation density is also a function of $\zeta = \boldsymbol{\nabla}\rho\cdot\boldsymbol{\nabla}\rho$.[56] For DFT, it can be shown that the variational condition can be expressed in terms of the Kohn-Sham Fock matrix

$$\left.\frac{\partial E_{DFT}}{\partial \kappa_{ai}}\right|_{\kappa=0} = -F^{KS}_{ai} = 0 \tag{1.62}$$

$$\left.\frac{\partial E_{DFT}}{\partial \kappa^*_{ai}}\right|_{\kappa=0} = -F^{KS}_{ia} = 0$$

$$F^{KS}_{pq} = h_{pq} + (pq|ii) - \gamma(pi|iq) + v_{xc;pq}, \tag{1.63}$$

whereas in HF theory, we obtain the closely related Fock matrix

$$\left.\frac{\partial E_{HF}}{\partial \kappa_{ai}}\right|_{\kappa=0} = -F_{ai} = 0 \tag{1.64}$$

$$\left.\frac{\partial E_{HF}}{\partial \kappa^*_{ai}}\right|_{\kappa=0} = -F_{ia} = 0$$

$$F_{pq} = h_{pq} + (pq|ii) - (pi|iq). \tag{1.65}$$

Therefore, the optimal wave function can be obtained by finding a set of parameters that put the secondary-inactive/inactive-secondary block of the (Kohn-Sham) Fock matrix to zero. Alternatively, the orbitals can be found by solving the pseudo-eigenvalue problem of the (Kohn-Sham) Fock operator

$$\hat{F}^{(KS)}\phi_i = \epsilon_i\phi_i, \tag{1.66}$$

which amounts to a diagonalization of the Fock matrix. By extension, the variational condition is met in a diagonal basis, although this procedure is somewhat excessive, as it also sets the off-diagonal of the inactive-inactive and secondary-secondary blocks to zero, corresponding to redundant parameters.

Nevertheless, the pseudo-eigenvalue problem is particularly useful in atomic physics, where spherical symmetry renders the problem one-dimensional, thus allowing the problem to be solved on a numerical grid.[63, Chapter 3] Using the grid-based methods, it is possible to nearly approach the complete basis set limit and it is thus very suitable for benchmark calculations. However, like any method, it does have significant drawbacks. For instance, the finite-difference methods is less applicable for molecules, generally requiring three dimensional grids. Furthermore, using a finite-difference method it is only possible to compute occupied orbitals, which complicates its extension to correlated- or excited-state methods. Therefore, a basis set expansion is the preferred method for the purposes of this thesis.

However, before proceeding it should be noted that Eqs. (1.62) and (1.64) do not guarantee a global minimum, because they can also mark a local minimum, a saddle point, or even a local maximum. By using second-order optimization schemes, the possibility of maxima and saddle points can be ruled out. However, even second-order schemes are not capable of finding a global minimum with absolute certainty.

Besides its utility in energy optimization, the variational condition can also be used to determine static molecular properties. To arrive at this point, the Helmann-Feynman theorem needs to be invoked,[64, 65] which is an exact-state theorem that can be reproduced for variational, approximate theories, such as SCF theory

$$\frac{dE(\lambda,\kappa,\kappa^*)}{d\lambda_\alpha^0} = \frac{\partial E}{\partial \lambda_\alpha^0} + \sum_{ai} \frac{\partial E}{\partial \kappa_{ai}} \frac{\partial \kappa_{ai}}{\partial \lambda_\alpha^0} + \sum_{ai} \frac{\partial E}{\partial \kappa_{ai}^*} \frac{\partial \kappa_{ai}^*}{\partial \lambda_\alpha^0} = \frac{\partial E}{\partial \lambda_\alpha^0} = \langle \Phi_0 | \hat{V}_\alpha^0 | \Phi_0 \rangle, \tag{1.67}$$

where $\hat{V}_\alpha^0$ is a static perturbation with λ_α^0 being its associated coupling strength. In the above equation, it is assumed that the variational condition holds at every field strength and the orbitals do not explicitly depend on the perturbation, the latter of which does not hold for geometric distortion or magnetic properties with the use of London atomic orbitals.[66] Further differentiation of this condition yields the static response function

$$\left.\frac{d^2E}{d\lambda_\alpha^0 d\lambda_\beta^0}\right|_{\lambda=0} = \langle\langle \hat{V}_\alpha^0; \hat{V}_\beta^0 \rangle\rangle_0. \tag{1.68}$$

However, in current context, we are interested in light–matter interactions, thus implying that the static response functions have limited interest. In the following, I will generalize above findings to the time-dependent domain.

1.3.2 Quasi-Energy

We start of with our SCF wave function and subject it to the influences of a time-dependent interaction operator. However, by introducing time-dependence into our Hamiltonian, we bump into the immediate problem that the energy is not a conserved quantity. Without the energy and a variational condition, it is not straightforward how to apply Eqn. (1.68) and find time-dependent response functions. Notwithstanding, in the presence of a periodic perturbation, the perturbed state does share some similarities with stationary states. If the system is exposed sufficiently long to a time-periodic perturbation, the influences of the adiabatic switch can be neglected and after this point, the wave function will continue oscillating periodically. This steady-state behaviour can be inferred from Eqn. (1.22) and it holds more generally by virtue of Floquet's theorem.[67, 68, 69] The existence of such steady-states suggest that there might be other conserved quantities apart from the energy.

To further investigate this idea, I will draw inspiration from the static problem, hence assuming that only the zeroth frequency component in Eqn. (E.8) contributes. However, the perturbation is strictly speaking quasi-static, as it is turned on using an adiabatic switch. Using the adiabatic theorem, it can thus be shown that in the limit $t \to \infty$, the wave function becomes

$$|\psi\rangle = \sum_n c_n(t)e^{-iE_n t/\hbar}|n\rangle \to |\psi\rangle = e^{-iE' t/\hbar}\sum_n c_n'(t)|n\rangle, \tag{1.69}$$

where E' is the exact energy of the full Hamiltonian, including the perturbation. It can be shown that the coefficients, c_n, are related to c_n' by

$$c_n(t) = c_n'(t)e^{-i\left(E'-E_n\right)t/\hbar}. \tag{1.70}$$

The perturbative expansion of these coefficients is complicated because the exact perturbed energy appearing in the exponent needs to be expanded as well. Furthermore, the additional terms arising from this exponent diverge. Therefore, it seems to be more practical to isolate the exponential phase from our ansatz

$$|\psi\rangle = e^{-iE' t/\hbar}|\bar{\psi}\rangle \tag{1.71}$$

and apply a perturbative series based on the phase-isolated wave function. However, if one insists, expression (1.70) can be used, because the diverging terms do not contribute to expectation values, as pointed out by Langhoff *et al.*[70] Therefore, the divergences introduced by the exponential phase are secular in nature, meaning that they can be removed with the proper mathematical manipulations.

Besides its capability to isolate secular divergences, the phase-isolated ansatz is also particularly useful when defining time-dependent molecular properties. The time-dependent generalization of the phase-isolated ansatz can be expressed as

$$|\psi\rangle = e^{i\phi(t)/\hbar}|\bar{\psi}\rangle, \tag{1.72}$$

where the phase, $\phi(t)$, is now a general time-dependent function. This decomposition is made unique by imposing that $\phi(t)$ is real and that the projection of phase-isolated wave function onto the unperturbed wave function is zero. The following equation can be obtained by inserting our ansatz in the time-dependent Schrödinger equation

$$\left(\hat{H} - i\hbar\frac{\partial}{\partial t}\right)|\bar{\psi}\rangle = Q(t)|\bar{\psi}\rangle; \quad Q(t) = \frac{\partial\phi(t)}{\partial t}, \tag{1.73}$$

where the second equation defines the quasi-energy. However, this equation is seldom used, as it is much more convenient to obtain the quasi-energy from projection with the phase-isolated wave function

$$Q(t) = \langle\bar{\psi}|\left(\hat{H} - i\hbar\frac{\partial}{\partial t}\right)|\bar{\psi}\rangle. \tag{1.74}$$

The quasi-energy deserves its name due to its connection to the energy in the static limit $Q(t) \to E$.

Due to this connection, the quasi-energy seems like a suitable candidate for the generalization of Eqn. (1.68) to the time-dependent domain. However, considering that Eqn. (1.67) is derived from the variational properties of the energy, it should be assessed whether the quasi-energy is variational as well before making this connection. I will thus apply the following variations to the wave function

$$|\bar{\psi}\rangle \rightarrow |\bar{\psi}\rangle + |\delta\bar{\psi}\rangle, \tag{1.75}$$

which should preserve the norm of the wave function

$$(\langle\delta\bar{\psi}|+\langle\bar{\psi}|)(|\bar{\psi}\rangle + |\delta\bar{\psi}\rangle) = \langle\bar{\psi}|\bar{\psi}\rangle + \langle\delta\bar{\psi}|\bar{\psi}\rangle + \langle\bar{\psi}|\delta\bar{\psi}\rangle. \tag{1.76}$$

Therefore, the allowed variations assume the form

$$|\delta\bar{\psi}\rangle = |\bar{\psi}_{\perp}\rangle + i\epsilon|\bar{\psi}_{\parallel}\rangle; \quad \epsilon \in \mathbb{R}, \tag{1.77}$$

where $|\bar{\psi}_{\perp}\rangle$ and $|\bar{\psi}_{\parallel}\rangle$ are parallel and perpendicular to the phase isolated wave function. Applying these variations to the quasi-energy yields the result

$$\delta Q(t) = -i\hbar\frac{\partial}{\partial t}\langle\bar{\psi}|\delta\bar{\psi}\rangle, \tag{1.78}$$

suggesting that the quasi-energy is not variational. Furthermore, differentiation with respect to the field strength gives the time-dependent generalization of the Helmann-Feynman theorem

$$\frac{dQ}{d\lambda_{\alpha}^{\omega_y}} = \langle\bar{\psi}|\hat{V}_{\alpha}^{\omega_y}|\bar{\psi}\rangle - i\hbar\frac{\partial}{\partial t}\langle\bar{\psi}|\frac{d\bar{\psi}}{d\lambda_{\alpha}^{\omega_y}}\rangle. \tag{1.79}$$

However, we would like to connect quasi-energy derivatives with expectation values, and by extension to time-dependent response functions.

Fortunately, the time-periodicity of the system can be used to our advantage. Due to this property, the time derivative term is periodic, suggesting it vanishes upon time-averaging over a full period

$$\frac{1}{T}\int_{-T/2}^{T/2} dt\dot{f}(t) = 0; \quad f(t+T) = f(t). \tag{1.80}$$

Using these relation we can retrieve a variational condition for the time-averaged quasi-energy

$$\delta Q_T = 0 \tag{1.81}$$

and a more useful expression for the time-dependent Helmann-Feynman theorem[71]

$$\frac{dQ_T}{d\lambda_{\alpha}^{\omega_y}} = \frac{1}{T}\int_{t-T/2}^{t+T/2} dt\langle\bar{\psi}|\hat{V}_{\alpha}^{\omega_y}|\bar{\psi}\rangle - i\hbar\frac{1}{T}\int_{t-T/2}^{t+T/2} dt\frac{\partial}{\partial t}\langle\bar{\psi}|\delta\bar{\psi}\rangle = \langle\Phi_0|\hat{V}_{\alpha}^{\omega_y}|\Phi_0\rangle\delta_{\omega_y}, \tag{1.82}$$

where δ_{ω_y} is a generalized Kronecker delta that equals 1 if $\omega_y = 0$ and 0 otherwise.

In analogy with the static case, the time-dependent Helmann-Feynman theorem can be exploited to compute response functions. For these purposes, I will further differentiate Eqn. (1.82)

$$\left.\frac{d^2 Q_T}{d\lambda_\alpha^{\omega_y} d\lambda_\beta^{\omega_z}}\right|_{\lambda=0} = \frac{1}{T}\int_{t-T/2}^{t+T/2} dt \langle \frac{d\bar{\psi}}{d\lambda_\beta^{\omega_z}}|\hat{V}_\alpha(\omega_y)e^{-i\omega_y t}|\bar{\psi}\rangle\Big|_{\lambda=0} + \frac{1}{T}\int_{t-T/2}^{t+T/2} dt \langle \bar{\psi}|\hat{V}_\alpha(\omega_y)e^{-i\omega_y t}|\frac{d\bar{\psi}}{d\lambda_\beta^{\omega_z}}\rangle\Big|_{\lambda=0}, \tag{1.83}$$

which indeed gives the time-dependent response functions upon insertion of the first-order perturbed wave function.

$$\left.\frac{d^2 Q_T}{d\lambda_\alpha^{\omega_y} d\lambda_\beta^{\omega_z}}\right|_{\lambda=0} = \langle\langle \hat{V}_\alpha(\omega_y); \hat{V}_\beta(\omega_z)\rangle\rangle \delta_{\omega_y+\omega_z} \tag{1.84}$$

Response functions can thus be computed by evaluating field strength derivatives of the quasi-energy.

1.3.3 Response Theory

To evaluate the quasi-energy derivatives, it is necessary to expand SCF theory to the time-dependent domain. For HF theory, this is a straightforward exercise, because the HF determinant directly represents the wave function. In exponentially parametrized form, the time-dependent generalization of the HF wave function can be expressed as

$$|\bar{\psi}(t)\rangle = \exp[-\hat{\kappa}(t)]|\Phi_0\rangle; \quad \hat{\kappa}(t) = \kappa_{ai}(t)a_a^\dagger a_i - \kappa_{ai}^*(t)a_i^\dagger a_a, \tag{1.85}$$

where the generator is given by non-redundant rotations. Contrary to Eqn. (1.54), the reference state in this ansatz is the optimized HF ground state, while the parameters are time-dependent to accommodate the influences of the perturbing operator. The action of the generator is to (de-)excite orbitals, thus including contributions from excited determinants. Using this ansatz, the quasi-energy can be expressed as

$$Q_T = Q_{0:HF} + \sum_{y=-N}^{N} \lambda_\alpha^{\omega_y} Q_\alpha(\omega_y), \tag{1.86}$$

in terms of the two quantities

$$Q_{0;HF} = \{E_{HF}\}_T - \langle\bar{\psi}|i\hbar\frac{\partial}{\partial t}|\bar{\psi}\rangle_T; \quad Q_\alpha(\omega_y) = \langle\bar{\psi}|\hat{V}_\alpha(\omega_y)e^{-i\omega_y t}|\bar{\psi}\rangle_T, \tag{1.87}$$

where the subscript T denotes time-averaging.

Due to previously established similarities between HF and DFT, it is tempting to assume that a time-dependent generalization of the latter (TDDFT) is based on a similar ansatz. However, demonstrating the validity of this assumption turns out to be a non-trivial task.

After all, the Hohenberg-Kohn theorems makes use of a variational principle of the energy, thus only applying to the ground state. A major breakthrough was provided in a seminal article by Runge and Gross, where they generalized the Hohenberg-Kohn theorems to the time-dependent domain by formulating the problem as an action integral.[72] However, this formulation can be rather cumbersome, as the initial state needs to be known to establish a one-to-one correspondence between the density and potentials. Here, I will rather follow a procedure based on the variational properties of the time-averaged quasi-energy, which avoids problems associated with boundary conditions due to the assumed periodicity of the system.[73, 74] Using the variational properties of the time-averaged quasi-energy, it can be demonstrated that it can be expressed as a functional of the density, in analogy with the Hohenberg-Kohn theorems. Furthermore, this density can be expressed using fictitious system of non-interacting particles, thus yielding the following functional

$$Q_T[\rho] = Q_{0;DFT}[\rho] + \sum_{y=-N}^{N} \lambda_\alpha^{\omega_y} \Big\{ \int d^3\boldsymbol{r}\hat{V}_\alpha(\omega_y)\rho(\boldsymbol{r},\boldsymbol{\kappa}) \Big\}_T \tag{1.88}$$

$$Q_{0;DFT}[\rho] = \{T_s[\rho] + V_{en}[\rho] + J[\rho] + Q_{xc}[\rho]\}_T - \langle\bar{\psi}|i\hbar\frac{\partial}{\partial t}|\bar{\psi}\rangle_T. \tag{1.89}$$

It seems tempting to identify the first four terms in $Q_{0:DFT}$ with the time-averaged DFT energy (Eqn. (1.41)). However, the observant reader should have noticed that the exchange correlation functional is different. Indeed, in the time-dependent case, this functional does not only correct for the lack of exchange, correlation and the approximate nature of the kinetic energy, but also for the approximate nature of the time-derivative term.[75] In general, the time-dependent exchange-correlation functional is difficult to obtain. For that reason, the adiabatic approximation is often applied, where the general exchange correlation potential is approximated by the time-independent one,[76] i.e. $Q_{xc}[\rho] \rightarrow \{E_{xc}[\rho]\}_T$. Within this approximation, the quasi-energy thus becomes

$$Q_T[\rho] = \{E_{DFT}[\rho]\}_T - \langle\bar{\psi}|i\hbar\frac{\partial}{\partial t}|\bar{\psi}\rangle_T + \sum_{y=-N}^{N} \lambda_\alpha^{\omega_y} \Big\{ \int d^3\boldsymbol{r}\hat{V}_\alpha(\omega_y)\rho(\boldsymbol{r},\boldsymbol{\kappa}) \Big\}_T. \tag{1.90}$$

Having derived expressions for the quasi-energy at the SCF level, the most difficult theoretical step has been taken, with the remainder of the derivation leaning on the general properties of the quasi-energy, thus being mostly equivalent for both HF and DFT. In the following, I will closer inspect the dependency of the quasi-energy on the rotation parameters to derive working equations for its field strength derivatives.

Due to time-periodicity, the parameters in our ansatz can be expanded in Fourier components that are integer multiples of a fundamental frequency[67, 68, 69]

$$\begin{aligned}\kappa_{ai}(t) &= \sum_{k=-N}^{N} \kappa_{ai}^{(1)}(\omega_k) e^{-i\omega_k t} + \sum_{k,l=-N}^{N} \kappa_{ai}^{(2)}(\omega_k, \omega_l) e^{-i(\omega_k+\omega_l)t} + \cdots \\ \kappa_{ai}^{*}(t) &= \sum_{k=-N}^{N} \kappa_{ai}^{(1)*}(-\omega_k) e^{-i\omega_k t} + \sum_{k,l=-N}^{N} \kappa_{ai}^{(2)*}(-\omega_k, -\omega_l) e^{-i(\omega_k+\omega_l)t} + \cdots .\end{aligned} \tag{1.91}$$

Here, the superscripts on the parameters denote the order of the response. To distinguish the frequency components of the response with the ones of the interaction, I have labelled the former using the indices k, l and the latter using y, z. Within this parametrization, the time averaged quasi-energy becomes a function of the field strengths and the Fourier amplitudes

$$Q_T(\lambda_\alpha^{\omega_k}, \kappa_n^{(1)}(\omega_k), \kappa_n^{(1)*}(\omega_k), \kappa_n^{(2)}(\omega_k, \omega_l), \kappa_n^{(2)*}(-\omega_k, -\omega_l), \cdots), \tag{1.92}$$

where the index pair ai is now represented as a super index n. In linear response, only the first-order response parameters are considered, which can be conveniently represented in vector form

$$\boldsymbol{K}(\omega_k) = \begin{pmatrix} \boldsymbol{\kappa}^{(1)}(\omega_k) \\ \boldsymbol{\kappa}^{(1)*}(-\omega_k) \end{pmatrix}; \quad K_m(\omega_k) = \begin{cases} \kappa_m^{(1)}(\omega_k) & \text{if } m > 0 \\ \kappa_m^{(1)*}(-\omega_k) & \text{if } m < 0 \end{cases}, \tag{1.93}$$

where the indices of this vector are positive for the upper half and negative for the lower half. The quasi-energy derivatives can now be found using the chain rule

$$\begin{aligned}\left.\frac{d^2 Q_T}{d\lambda_\alpha^{\omega_y} d\lambda_\beta^{\omega_z}}\right|_{\lambda=0} &= \left.\left[\frac{\partial^2 Q_T}{\partial\lambda_\alpha^{\omega_y}\partial\lambda_\beta^{\omega_z}}\right]\right|_{\lambda=0} \\ &+ \sum_{k=-N}^{N} \left.\left[\frac{\partial^2 Q_T}{\partial\lambda_\beta^{\omega_z}\partial K_n(\omega_k)} \frac{\partial K_n(\omega_k)}{\partial\lambda_\alpha^{\omega_y}}\right]\right|_{\lambda=0} + \sum_{k=-N}^{N} \left.\left[\frac{\partial Q_T}{\partial K_n(\omega_k)} \frac{\partial^2 K_n(\omega_k)}{\partial\lambda_\alpha^{\omega_y}\partial\lambda_\beta^{\omega_z}}\right]\right|_{\lambda=0} \\ &+ \sum_{k,l=-N}^{N} \left.\left[\frac{\partial K_n(\omega_k)}{\partial\lambda_\beta^{\omega_z}} \left(\frac{\partial^2 Q_T}{\partial K_n(\omega_k)\partial K_m(\omega_l)} \frac{\partial K_m(\omega_l)}{\partial\lambda_\alpha^{\omega_y}} + \frac{\partial^2 Q_T}{\partial\lambda_\alpha^{\omega_y}\partial K_n(\omega_k)}\right)\right]\right|_{\lambda=0} .\end{aligned} \tag{1.94}$$

Several simplifications can be applied to above results. Firstly, the perturbation only appears linear in the Hamiltonian, implying that the first term in Eqn. (1.94) vanishes. Secondly, as demonstrated in previous section, the time averaged quasi-energy is variational for all field strengths

$$\left.\frac{\partial Q_T}{\partial K_n(\omega_k)}\right|_{\lambda} = 0; \quad \forall\lambda, \tag{1.95}$$

rendering the third term zero as well. Further simplifications can be made by differentiation of the variational condition with respect to the field strength

$$\left[\frac{\partial^2 Q_T}{\partial K_n(\omega_k)\partial\lambda_\alpha^{\omega_y}}\right]\Bigg|_{\lambda=0} + \sum_{l=-N}^{N}\left[\frac{\partial^2 Q_T}{\partial K_n(\omega_k)\partial K_m(\omega_l)}\frac{\partial K_m(\omega_l)}{\partial\lambda_\alpha^{\omega_y}}\right]\Bigg|_{\lambda=0} = 0. \tag{1.96}$$

This expression necessarily equals zero because the variational condition holds for all field strengths. Upon inspection of Eqn. (1.94), the differentiated variational condition can be recognized in the last two terms. Therefore, Eqn. (1.94) simplifies to

$$\frac{d^2 Q_T}{d\lambda_\alpha^{\omega_y} d\lambda_\beta^{\omega_z}}\Bigg|_{\lambda=0} = \sum_{k=-N}^{N}\left[\frac{\partial^2 Q_T}{\partial\lambda_\beta^{\omega_z}\partial K_n(\omega_k)}\frac{\partial K_n(\omega_k)}{\partial\lambda_\alpha^{\omega_y}}\right]\Bigg|_{\lambda=0}. \tag{1.97}$$

To evaluate the double derivatives of the quasi-energy, and hence response functions, it is required to evaluate the property gradient

$$\boldsymbol{E}_{V_\beta^{\omega_y}}\delta_{\omega_k+\omega_y} = \begin{pmatrix} \frac{\partial^2 Q_T}{\partial\lambda_\beta^{\omega_y}\partial\kappa_n^{(1)}(\omega_k)}\Big|_{\lambda=0} \\ \frac{\partial^2 Q_T}{\partial\lambda_\beta^{\omega_y}\partial\kappa_n^{(1)*}(-\omega_k)}\Big|_{\lambda=0} \end{pmatrix} \tag{1.98}$$

and the solution vectors

$$\boldsymbol{X}_{V_\alpha^{\omega_y}}(\omega_k) = \begin{pmatrix} \boldsymbol{Z} \\ \boldsymbol{Y}^* \end{pmatrix} = \begin{pmatrix} \frac{\partial\kappa_n^{(1)}(\omega_k)}{\partial\lambda_\alpha^{\omega_y}}\Big|_{\lambda=0} \\ \frac{\partial\kappa_n^{(1)*}(-\omega_k)}{\partial\lambda_\alpha^{\omega_y}}\Big|_{\lambda=0} \end{pmatrix}. \tag{1.99}$$

Note that both of these quantities are stored in vector format for convenience. Using this notation, the response functions can be expressed in the elegant form below

$$\langle\langle\hat{A};\hat{B}\rangle\rangle = \boldsymbol{E}_A^\dagger\boldsymbol{X}_B. \tag{1.100}$$

The solution vectors can be obtained by inverting the differentiated variational condition. However, solving this equation requires the property gradient and the double derivative of the quasi-energy with respect to the first-order Fourier components. Therefore, I will first proceed to calculate these quantities. To evaluate the property gradient, I will exploit the fact that its evaluated at zero field strength, implying that only the linear terms with respect to the field strength and first-order response parameters are non-vanishing. To gather contributions to the quasi-energy in a transparent manner, it proves to be useful to apply a Baker-Campbell-Hausdorff expansion to the perturbed density matrix and the time-derivative term

$$\langle\Phi_0|\exp[\hat{\kappa}]a_p^\dagger a_q\exp[-\hat{\kappa}]|\Phi_0\rangle = \langle\Phi_0|a_p^\dagger a_q|\Phi_0\rangle + \langle\Phi_0|[\hat{\kappa},a_p^\dagger a_q]|\Phi_0\rangle + \frac{1}{2}\langle\Phi_0|\big[\hat{\kappa},[\hat{\kappa},a_p^\dagger a_q]\big]|\Phi_0\rangle + \cdots \tag{1.101}$$

$$\langle\Phi_0|\exp[\hat{\kappa}]i\hbar\partial_t\exp[-\hat{\kappa}]|\Phi_0\rangle = \langle\Phi_0|i\hbar\partial_t|\Phi_0\rangle + \langle\Phi_0|[\hat{\kappa},i\hbar\partial_t]|\Phi_0\rangle + \frac{1}{2}\langle\Phi_0|\big[\hat{\kappa},[\hat{\kappa},i\hbar\partial_t]\big]|\Phi_0\rangle + \cdots.$$

Note that unlike the expansion from Eqn. (1.57), these expressions are defined with respect to the SCF ground state and the response parameters. The property gradient can be evaluated by first inserting these terms into the quasi-energy and then gathering the terms of the right order. Therefore, the gradient reads

$$\left.\frac{\partial^2 Q_T}{\partial K_m(\omega_k)\partial\lambda_\alpha^{\omega_y}}\right|_{\lambda=0} = \begin{cases} -\langle\Phi_0|\left[\hat{V}_\alpha^{\omega_y}, a_a^\dagger a_i\right]|\Phi_0\rangle\delta_{\omega_k+\omega_y} & m > 0 \\ \langle\Phi_0|\left[\hat{V}_\alpha^{\omega_y}, a_i^\dagger a_a\right]|\Phi_0\rangle\delta_{\omega_k+\omega_y} & m < 0 \end{cases}, \tag{1.102}$$

which has inherited the overall vector structure from Eqn. (1.93). In vector notation, it can be rewritten as

$$\boldsymbol{E}_{V_\alpha^{\omega_y}} = \begin{pmatrix} \boldsymbol{g}_{V_\alpha^{\omega_y}} \\ \boldsymbol{g}^*_{V_\alpha^{\omega_y}} \end{pmatrix}; \quad g_{V_\alpha^{\omega_y};ai} = -\langle\Phi_0|\hat{V}_\alpha^{\omega_y}|\Phi_i^a\rangle = -\int d^3\boldsymbol{r}\,\phi_i^*(\boldsymbol{r})\hat{V}_\alpha^{\omega_y}\phi_a(\boldsymbol{r}). \tag{1.103}$$

We now proceed to calculate the double derivative of the quasi-energy with respect to the response parameters. This quantity is ideally represented as a matrix having the following block-structure

$$Q_T^{[2]} = \begin{bmatrix} \frac{\partial^2 Q_T}{\partial\kappa_n^*(-\omega_k)\partial\kappa_m(\omega_l)} & \frac{\partial^2 Q_T}{\partial\kappa_n^*(-\omega_k)\partial\kappa_m^*(-\omega_l)} \\ \frac{\partial^2 Q_T}{\partial\kappa_n(\omega_k)\partial\kappa_m(\omega_l)} & \frac{\partial^2 Q_T}{\partial\kappa_n(\omega_k)\partial\kappa_m^*(-\omega_l)} \end{bmatrix}. \tag{1.104}$$

To evaluate these derivatives, we can follow a similar approach as the one for the property gradient, although the situation is somewhat more complicated for DFT, due to the additional burden to evaluate the double derivatives of the exchange-correlation density. The evaluation of these terms boil down to calculating the exchange-correlation kernel (see ref. 75 for more detail)

$$\begin{aligned} W_{xc;pq,rs} = \int d^3\boldsymbol{r}\Bigg(&\left.\frac{\partial^2 e_{xc}}{\partial\rho^2}\right|_{\lambda=0}\Omega_{pq}\Omega_{rs} + 2\left.\frac{\partial^2 e_{xc}}{\partial\rho\partial\zeta}\right|_{\lambda=0}\left[(\boldsymbol{\nabla}\rho_0\cdot\boldsymbol{\nabla}\Omega_{pq})\Omega_{rs} + \Omega_{pq}(\boldsymbol{\nabla}\rho_0\cdot\boldsymbol{\nabla}\Omega_{rs})\right. \\ &+ 4\left.\frac{\partial^2 e_{xc}}{\partial\zeta^2}\right|_{\lambda=0}(\boldsymbol{\nabla}\rho_0\cdot\boldsymbol{\nabla}\Omega_{pq})(\boldsymbol{\nabla}\rho_0\cdot\boldsymbol{\nabla}\Omega_{rs}) + 2\left.\frac{\partial e_{xc}}{\partial\zeta}\right|_{\lambda=0}(\boldsymbol{\nabla}\Omega_{pq}\cdot\boldsymbol{\nabla}\Omega_{rs})\Bigg) \end{aligned} \tag{1.105}$$

$$\Omega_{pq} = \phi_p^\dagger(\boldsymbol{r})\phi_q(\boldsymbol{r}).$$

Therefore, we end up with the following general structure

$$Q_T^{[2]} = (E_0^{[2]} - \hbar\omega_l S^{[2]})\delta_{\omega_k+\omega_l}, \tag{1.106}$$

where appears the generalized metric

$$S^{[2]} = \begin{bmatrix} \Sigma & \Delta \\ -\Delta^* & -\Sigma^* \end{bmatrix} \begin{cases} \Sigma_{ai,bj} = \langle 0 | \big[-a_i^\dagger a_a, a_b^\dagger a_j \big] | 0 \rangle = \delta_{ab}\delta_{ij} \\ \Delta_{ai,bj} = \langle 0 | \big[a_i a_a, a_j^\dagger a_b \big] | 0 \rangle = 0 \end{cases} \tag{1.107}$$

and the electronic Hessian, $E_0^{[2]}$. Depending on the level of theory, the Hessian assumes different forms. In Hartree-Fock theory,[77] the Hessian reads

$$E_0^{[2]} = \begin{bmatrix} A & B \\ B^* & A^* \end{bmatrix} \begin{cases} A_{ai,bj} = \langle 0 | \big[-a_i^\dagger a_a, [a_b^\dagger a_j, \hat{H}_0] \big] | 0 \rangle = \delta_{ij} F_{ab} - \delta_{ab} F_{ji} + (ai|jb) - (ab|ji) \\ B_{ai,bj} = \langle 0 | \big[a_i^\dagger a_a, [a_j^\dagger a_b, \hat{H}_0] \big] | 0 \rangle = (ai|bj) - (aj|bi) \end{cases} \tag{1.108}$$

whereas in DFT it assumes the form[78]

$$E_0^{[2]} = \begin{bmatrix} A & B \\ B^* & A^* \end{bmatrix} \begin{cases} A_{ai,bj} = \delta_{ij} F_{ab}^{KS} - \delta_{ab} F_{ji}^{KS} + (ai|jb) - \gamma (ab|ji) + W_{xc;ai,jb} \\ B_{ai,bj} = (ai|bj) - \gamma (aj|bi) + W_{xc;ai,bj}. \end{cases} \tag{1.109}$$

Using these quantities, Eqn. (1.96) can be written in its conventional form

$$\big(E_0^{[2]} - \hbar\omega S^{[2]} \big) \boldsymbol{X}_{V_\alpha^\omega}(\omega) = -\boldsymbol{E}_{V_\alpha^\omega}, \tag{1.110}$$

which is also referred to as the response equation. Note that in this equation, the action of the Kronecker symbol ensures that all different frequency components stemming from various sources are the same. For ease of notation, this index has thus been dropped. As eluded to before, the solution vectors can be obtained by inverting the matrix expression

$$\boldsymbol{X}_{V_\alpha^\omega}(\omega) = -\big(E_0^{[2]} - \hbar\omega S^{[2]} \big)^{-1} \boldsymbol{E}_{V_\alpha^\omega}. \tag{1.111}$$

In practice, however, such a matrix inversion is rarely performed explicitly due to the sheer size of the electronic Hessian. Instead, the Hessian is projected in a basis of trial vectors and solved iteratively, which is explained more thoroughly in Appendix A.1.

With the explicit form of the solution vectors, the response functions can be expressed as

$$\langle\langle \hat{A}; \hat{B} \rangle\rangle = -\boldsymbol{E}_A^\dagger (E_0^{[2]} - \hbar\omega S^{[2]})^{-1} \boldsymbol{E}_B. \tag{1.112}$$

However, I recall that we started this venture in response theory to find transition moments and excitation energies at the SCF level. In the exact-state case, it is a straightforward exercise to identify the poles and hence find these quantities. From expression (1.112), however, it is less clear where the poles are located. From elementary linear algebra, it is known that the inverse of any matrix is inversely proportional to its determinant. It thus follows that the resolvent matrix in Eqn. (1.112) induces divergences if

$$\det \big(E_0^{[2]} - \hbar\omega S^{[2]} \big) = 0. \tag{1.113}$$

This condition is nothing more than the characteristic equation of the generalized eigenvalue problem

$$E_0^{[2]}\boldsymbol{X}_n = \hbar\omega_{n0}S^{[2]}\boldsymbol{X}_n. \tag{1.114}$$

In above expression ω_{n0} should be understood as the specific value of ω that induces a divergence, i.e. the transition frequency. From the structure of the electronic Hessian and the generalized metric, it can be shown that the eigenvectors come in pairs having equal but opposite frequencies

$$\left\{\omega_+ = +\left|\omega_n\right|, \boldsymbol{X}_{n,+} = \begin{bmatrix} \boldsymbol{Z}_n \\ \boldsymbol{Y}_n^* \end{bmatrix}\right\} \cup \left\{\omega_- = -\left|\omega_n\right|, \boldsymbol{X}_{n,-} = \begin{bmatrix} \boldsymbol{Y}_n \\ \boldsymbol{Z}_n^* \end{bmatrix}\right\}. \tag{1.115}$$

Expressing the response function in the set of these eigenvectors thus allows us the identify the poles. To further pursue this idea, I define a unitary matrix

$$X = \left(\boldsymbol{X}_1, \boldsymbol{X}_2, \cdots, \boldsymbol{X}_N\right); \quad X^\dagger X = I \tag{1.116}$$

which has the eigenvectors as columns.[79] The response functions can be transformed by inserting the identity matrix

$$-\boldsymbol{E}_A^\dagger XX^\dagger(E_0^{[2]} - \hbar\omega S^{[2]})^{-1}XX^\dagger\boldsymbol{E}_B = -\boldsymbol{E}_A^\dagger X(XE_0^{[2]}X^\dagger - \hbar\omega XS^{[2]}X^\dagger)^{-1}X^\dagger\boldsymbol{E}_B \tag{1.117}$$

Brought in diagonal form, the resolvent can be expressed as

$$(XE_0^{[2]}X^\dagger - \hbar\omega XS^{[2]}X^\dagger)^{-1} = \begin{bmatrix} \frac{1}{\hbar\omega_{1,0}-\hbar\omega} & 0 & 0 & \cdots & 0 \\ 0 & \frac{1}{\hbar\omega_{2,0}-\hbar\omega} & 0 & \cdots & 0 \\ 0 & 0 & \ddots & \ddots & 0 \\ \vdots & \vdots & \ddots & \frac{1}{\hbar\omega_{N-1,0}+\hbar\omega} & \vdots \\ 0 & 0 & 0 & \cdots & \frac{1}{\hbar\omega_{N,0}+\hbar\omega} \end{bmatrix}, \tag{1.118}$$

which further establishes the analogy between the resolvent and the frequency denominators in the exact response functions (Eqn. (1.33)). Written in this diagonal representation, the approximate response functions become

$$\langle\langle\hat{A};\hat{B}\rangle\rangle = -\sideset{}{'}\sum_n \left[\frac{(\boldsymbol{E}_A^\dagger\boldsymbol{X}_n)(\boldsymbol{X}_n^\dagger\boldsymbol{E}_B)}{\hbar\omega_{n0} - \hbar\omega} + \frac{(\boldsymbol{E}_A^\dagger\boldsymbol{X}_n)(\boldsymbol{X}_n^\dagger\boldsymbol{E}_B)}{\hbar\omega_{n0} + \hbar\omega}\right]. \tag{1.119}$$

In this form, the residues can be readily evaluated

$$\lim_{\omega_B\to\omega_{n0}}(\omega_B - \omega_n)\langle\langle\hat{A};\hat{B}\rangle\rangle = -\frac{1}{\hbar}(\boldsymbol{E}_A^\dagger\boldsymbol{X}_n)(\boldsymbol{X}_n^\dagger\boldsymbol{E}_B), \tag{1.120}$$

implying that the transition moments can be written as

$$\langle f|\hat{A}|i\rangle^{SCF} = \boldsymbol{E}_A^\dagger \boldsymbol{X}_n = -Z_{ai}\langle\Phi_i^a|\hat{A}|\Phi_0\rangle - Y_{ai}^*\langle\Phi_0|\hat{A}|\Phi_i^a\rangle. \tag{1.121}$$

Using the well-defined hermiticity of the interaction operator, the transition moments can be further simplified by utilizing the paired structure of the solution vectors

$$\boldsymbol{X}_h = \frac{1}{2}\left(\boldsymbol{X}_{m,+} + \boldsymbol{X}_{m,-}\right) = \frac{1}{2}\begin{bmatrix} \boldsymbol{Z}+\boldsymbol{Y} \\ (\boldsymbol{Z}+\boldsymbol{Y})^* \end{bmatrix}; \quad \boldsymbol{X}_a = \frac{1}{2}\left(\boldsymbol{X}_{m,+} - \boldsymbol{X}_{m,-}\right) = \frac{1}{2}\begin{bmatrix} \boldsymbol{Z}-\boldsymbol{Y} \\ -(\boldsymbol{Z}-\boldsymbol{Y})^* \end{bmatrix}, \tag{1.122}$$

which makes the transition moment either purely real or imaginary

$$\boldsymbol{X}_h^\dagger \boldsymbol{E}_A^{[1]} = \mathrm{Re}\left[(\boldsymbol{Z}+\boldsymbol{Y})^\dagger \boldsymbol{g}_A\right]; \quad \boldsymbol{X}_a^\dagger \boldsymbol{E}_A^{[1]} = i\mathrm{Im}\left[(\boldsymbol{Z}-\boldsymbol{Y})^\dagger \boldsymbol{g}_A\right]. \tag{1.123}$$

To calculate absorption intensities, the eigenvalue problem from Eqn. (1.114) is first solved, yielding the transition frequencies and the solution vectors. The transition moments, which may be frequency-dependent, are then constructed from relation (1.121). Absorption intensities are then calculated by inserting these transition moments into Fermi's golden rule.

By comparison with exact-state theory, it is tempting to associate the solution vectors with excited states

$$\hat{X}_n|\Phi_0\rangle = \left(Y_{ai}a_i^\dagger a_a + Z_{ai}^* a_a^\dagger a_i\right)|\Phi_0\rangle. \tag{1.124}$$

However, this comparison does not hold, because $|X_n\rangle$ does not obey the so-called killer-condition.[77, 80] This condition applies to excited states

$$|n\rangle = \hat{O}_n|0\rangle, \tag{1.125}$$

generated from the ground state by the operator $\hat{O}$. According to the killer-condition, the Hermitian conjugate of $\hat{O}$ should annihilate the ground-state

$$\hat{O}_n^\dagger|0\rangle = 0. \tag{1.126}$$

However, when applying $\hat{X}_n^\dagger$ to the ground state, this condition is violated

$$\hat{X}_n^\dagger|\Phi_0\rangle = Y_{ai}|\Phi_i^a\rangle. \tag{1.127}$$

Therefore, the approximate methods describes in this section can only provide transition moments and excitation energies.

Using the techniques developed in this chapter, we are now in a position to calculate UV-Vis absorption spectra at the SCF level of theory. In principle, these techniques can also be used to calculate X-ray absorption intensities, although the results differ severely from experiment. These discrepancies can be explained by the limitations of the models that we have been using throughout this chapter. The next two chapters will describe the theory required to adapt our model for the simulation of X-ray absorption spectroscopy.

Chapter 2

Relativistic Quantum Chemistry

2.1 Introduction

In the formation of bonds, the core electrons typically do not need special considerations, since they are not easily polarized and thus largely retain their atomic character. Notwithstanding, the core electrons take center stage in X-ray spectroscopy, which operates at high enough energies to probe these electrons. The simulation of X-ray spectroscopy is met with difficulties, because the conventional theory from UV-Vis spectroscopy (see Chapter 1) cannot accurately reproduce X-ray experiments. At least some of these shortcomings are rooted in the special characteristics of core electrons. Due to their close proximity to the nucleus, core electrons experience a much stronger attraction than valence electrons, thus significantly increasing their velocities (see Fig. 2.1). An analogous effect occurs in the solar system, where the planet Mercury orbits the sun at much higher velocities than the more distant planets. In general, the velocity of the electrons increases with higher atom number. Already for elements of moderate size, the core electrons move so fast that classical quantum mechanics fails to properly account for their motion. However, for elements in the lower half of the periodic table, the influences of relativistic effects extend beyond the core, since the orbitals of all other electrons need to remain orthogonal to the core orbitals, hence effectively contracting the valence shell. To even obtain a qualitatively correct wave function of molecules that contain such elements, relativistic effects must be included.[23]

Together with quantum mechanics, special relativity has revolutionized the paradigm of modern physics. The latter theory requires a drastic re-evaluation of the concepts of space and time, although it only gains relevance at extremely high energy scales. However, this theory is classical in the sense that it concerns the deterministic motion of point particles, whereas quantum mechanics is fundamentally probabilistic in nature. To include the effects of relativity in our calculations, it has to be extended to the quantum mechanical realm. Fortunately, this work has already been done for us by Paul Dirac, who formulated a relativistic extension of the Schrödinger equation.[81] The merits of the Dirac equation are its more accurate energy values, its natural description of spin and spin-orbit coupling and its prediction of anti-matter. As alluded to before, the Dirac equation is particularly useful when describing properties that depend on the core electrons, such as NMR-,[82, 83, 84] Mössbauer-[85, 86, 87] or X-ray spectroscopy.[25] In this work, a relativistic approach will be pursued to properly describe the core electrons. Therefore, this chapter will be devoted to the methods of relativistic quantum chemistry.

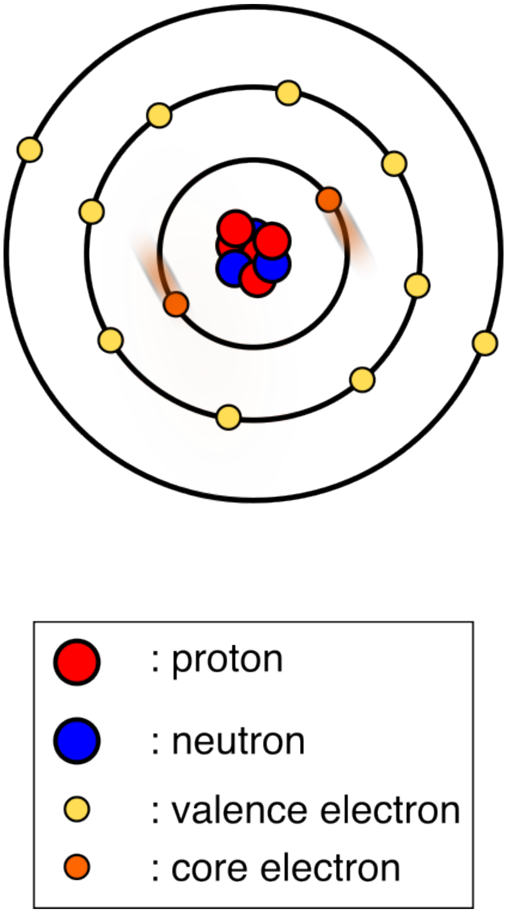

Figure 2.1: schematic representation of the atomic shell model. Compared to the valence electrons (yellow) the core electrons (orange) move at an elevated speed, thus inducing relativistic effects.

2.2 Special Relativity

2.2.1 The Postulates of Special Relativity

As a point of departure, I will first discuss the theory of special relativity, thus illustrating the basic principles to understand the more advanced topics that are introduced later in this chapter. The foundations of this theory are given by the two postulates of special relativity, the first of which, originally formulated by Galileo, states that the laws of physics are the same regardless of the inertial frame from which it is described. Here, an inertial frame is any frame that does not undergo accelerated motion. Therefore, the axis of two inertial frames may be oriented differently and move at a constant relative speed. Suppose that we have two of such frames S and S' that are described by parallel axes, where the former is stationary and the latter is moving with a speed of v in the direction of the positive part of the x-axis. In the framework of classical mechanics, the coordinates of both systems are related by the transformation rules

$$\begin{aligned} t' &= t \\ x' &= x - vt \\ y' &= y \\ z' &= z, \end{aligned} \tag{2.1}$$

where it has further been assumed that both frames coincide at $t = 0$. In transformations of this type, referred to as Galilean transformations, time enters as a parameter that is universally agreed on. It can be shown straightforwardly that Newton's second law is indeed invariant with respect to transformations of this type $\boldsymbol{F} = m\frac{d^2\boldsymbol{r}'}{dt'^2} = m\frac{d^2}{dt^2}(\boldsymbol{r} - \boldsymbol{v}t) = m\frac{d^2\boldsymbol{r}}{dt^2}$.

However, the same does not hold true for the Maxwell equations, which govern how electromagnetic fields are generated from charge- and current densities[40, Chapter 7][41, Chapter 6]

$$\begin{aligned} \boldsymbol{\nabla} \cdot \boldsymbol{E} &= \frac{1}{\epsilon_0}\rho \\ \boldsymbol{\nabla} \times \boldsymbol{E} &= -\frac{\partial \boldsymbol{B}}{\partial t} \\ \boldsymbol{\nabla} \cdot \boldsymbol{B} &= 0 \\ \boldsymbol{\nabla} \times \boldsymbol{B} &= \mu_0 \boldsymbol{J} + \mu_0\epsilon_0\frac{\partial \boldsymbol{E}}{\partial t}, \end{aligned} \tag{2.2}$$

where ρ and $\boldsymbol{J}$ are the charge- and current densities, ϵ_0 the electric constant and μ_0 the magnetic constant. To demonstrate the behaviour under Galilean transformations, the partial derivatives appearing in these equations should be expressed in the coordinates of S' using the chain rule. Furthermore, it should be noted that in a moving frame, we may have additional currents that are not present in the stationary frame. For example, a charge distribution, $\rho_0(\boldsymbol{r})$ at rest in S, gains velocity in the moving frame S', thus creating a current according to

$$\boldsymbol{j}'(\boldsymbol{r}', t) = -\boldsymbol{v}\rho_0(\boldsymbol{r}, t). \tag{2.3}$$

At this point, invariance of the Maxwell equations can be demonstrated if and only if a substitution can be made

$$\begin{aligned} &\boldsymbol{E} \to \boldsymbol{E}'; \quad \boldsymbol{B} \to \boldsymbol{B}' \\ &\rho \to \rho'; \quad \boldsymbol{j} \to \boldsymbol{j}' \end{aligned} \tag{2.4}$$

that reduce the equations to their untransformed form. However, for Galilean transformations, such a substitution does *not* exist, implying that either something is wrong with the Maxwell equations or the Galilean transformations. Here, I will assume the latter to be the case, so in the following, I will lay out a transformation rule that respects the structure of the Maxwell equations.

However, using aforementioned procedure to find a correct transformation is a rather lengthy one and does not reveal much of the physics. To obtain a more intuitive picture of the correct transformation, I will simplify our problem by considering a specific instance of the Maxwell equations: the homogeneous case

$$\begin{aligned} \boldsymbol{\nabla} \cdot \boldsymbol{E} &= 0 \\ \boldsymbol{\nabla} \times \boldsymbol{E} &= -\frac{\partial \boldsymbol{B}}{\partial t} \\ \boldsymbol{\nabla} \cdot \boldsymbol{B} &= 0 \\ \boldsymbol{\nabla} \times \boldsymbol{B} &= \mu_0 \epsilon_0 \frac{\partial \boldsymbol{E}}{\partial t}, \end{aligned} \tag{2.5}$$

which is valid in the absence of charge- and current densities. Although these equations are less complicated than the inhomogeneous counterparts, it is desirable to further simplify them by decoupling the electric and magnetic field. This can be achieved by first applying the cross-product to the second- and fourth equation

$$\begin{aligned} \boldsymbol{\nabla} \times (\boldsymbol{\nabla} \times \boldsymbol{E}) &= -\frac{\partial \boldsymbol{\nabla} \times \boldsymbol{B}}{\partial t} \\ \boldsymbol{\nabla} \times (\boldsymbol{\nabla} \times \boldsymbol{B}) &= \mu_0 \epsilon_0 \frac{\partial \boldsymbol{\nabla} \times \boldsymbol{E}}{\partial t}, \end{aligned} \tag{2.6}$$

followed by insertion of the identity $\boldsymbol{\nabla} \times (\boldsymbol{\nabla} \times \boldsymbol{F}) = \boldsymbol{\nabla}(\boldsymbol{\nabla} \cdot \boldsymbol{F}) - \nabla^2 \boldsymbol{F}$, yielding the result

$$\begin{aligned} \nabla^2 \boldsymbol{E} &= -\mu_0 \epsilon_0 \frac{\partial^2 \boldsymbol{E}}{\partial t^2} \\ \nabla^2 \boldsymbol{B} &= -\mu_0 \epsilon_0 \frac{\partial^2 \boldsymbol{B}}{\partial t^2}. \end{aligned} \tag{2.7}$$

These equations can be identified as three-dimensional wave equations with a propagation speed of $c = \frac{1}{\sqrt{\mu_0 \epsilon_0}}$. Possible solutions to these equations are given by the linearly polarized plane waves from previous chapter (Eqn. (E.1)). The first postulate thus creates a paradox:

the speed of light is expressed in fundamental constants, so it should be the same regardless of the inertial frame, whereas from the Galilean transformations one would expect the speed to be $c + v$ if the emitter of light is moving. If we insist that the Galilean transformations are not entirely correct, we need to introduce the second postulate, stating that the speed of light is the same regardless of the inertial frame.[88]

2.2.2 Lorentz Transformations

Based on the two relativistic postulates, I will derive new transformation laws that respect the structure of the Maxwell equations. For simplicity, I will derive these transformation rules for the previously introduced frames S and S'. The universality of the speed of light can only be explained if the notion of time and space is different depending on the inertial frame. Therefore, to avoid any prior assumptions, I will ascribe the space-time coordinates $\{x, y, z, t\}$ to S and $\{x', y', z', t'\}$ to S'.

Suppose that we have a trolley carrying a point-like light source that is following the origin of S'. At $t = t' = 0$, the light source will start emitting spherical waves which, according to the second postulate, travel at the speed c regardless of the inertial frame. Accordingly, to each spatial interval traversed by the light, $|\boldsymbol{r}_2 - \boldsymbol{r}_1|$ in S and $|\boldsymbol{r}'_2 - \boldsymbol{r}'_1|$ in S', we can associate a time interval, $t_2 - t_1$ and $t'_2 - t'_1$, required for the light to propagate said regions in space. Therefore, the following relation should hold in both frames

$$\frac{|\boldsymbol{r}_2 - \boldsymbol{r}_1|}{|t_2 - t_1|} = \frac{|\boldsymbol{r}'_2 - \boldsymbol{r}'_1|}{|t'_2 - t'_1|} = c. \tag{2.8}$$

From simple manipulations, we arrive at[88, 89]

$$(x_2-x_1)^2+(y_2-y_1)^2+(z_2-z_1)^2-c^2(t_2-t_1)^2 = (x'_2-x'_1)^2+(y'_2-y'_1)^2+(z'_2-z'_1)^2-c^2(t'_2-t'_1)^2 = 0, \tag{2.9}$$

which can be further simplified by introducing the compactified notation

$$\Delta x^\mu \Delta x_\mu = \Delta x'^\mu \Delta x'_\mu = 0. \tag{2.10}$$

In this expression, the position four-vector is defined as

$$x^\mu = \begin{cases} ct & \mu = 0 \\ x & \mu = 1 \\ y & \mu = 2 \\ z & \mu = 3 \end{cases}; \quad x_\mu = \begin{cases} -ct & \mu = 0 \\ x & \mu = 1 \\ y & \mu = 2 \\ z & \mu = 3 \end{cases}, \tag{2.11}$$

where the zeroth component represents time and the remaining three space. Hereafter, I will assume that Greek indices represent the index of a four vector, whereas Latin indices represent its spatial component. Furthermore, according to this convention, raising and lowering the index switches the sign of the zeroth component. This operation can be represented tensorially by the Minkowski metric[40]

$$x^{\mu} = \eta^{\mu\nu} x_{\nu}; \quad \eta = \mathrm{diag}(-1, 1, 1, 1). \tag{2.12}$$

The space-time interval in expression (2.10) is particularly useful to find the class of transformations that preserve the speed of light. Given a transformation between the two frames

$$x^{\mu} = \Lambda^{\mu}_{\nu} x'^{\nu}, \tag{2.13}$$

the speed of light is preserved if the following relation holds

$$\Lambda^{\rho}_{\mu} \eta^{\mu\nu} \Lambda^{\sigma}_{\nu} = \eta^{\rho\sigma}, \tag{2.14}$$

because in this case, we have

$$\Delta x^{\mu} \Delta x_{\mu} = \Delta x_{\nu} \eta^{\nu\mu} \Delta x_{\mu} = \Delta x'_{\rho} \Lambda^{\rho}_{\nu} \eta^{\nu\mu} \Lambda^{\sigma}_{\mu} \Delta x'_{\sigma} = \Delta x'_{\rho} \eta^{\rho\sigma} \Delta x'_{\sigma} = \Delta x'^{\sigma} \Delta x'_{\sigma}. \tag{2.15}$$

Transformations of this type form a group and are referred to as Lorentz transformations.

The action of these transformations mixes the space-time coordinates of the two frames. Lorentz transformations that only mix spatial components ($\exists i, j$ s.t. $\Lambda^{j}_{i} \neq 0$) can be thought of as ordinary rotations, whereas translations, or boosts ($\exists \mu$ s.t. $\Lambda^{\mu}_{0} \neq 0$ and $\Lambda^{0}_{\mu} \neq 0$), are associated with the admixture of spatial and temporal coordinates and *vice versa*. In line with the group properties of Lorentz transformations, two consecutive Lorentz transformation can generally be decomposed into a rotation and a boost. The admixture of space with time resulting from boosts does not seem all that unfamiliar, since this also occurs in the Galilean transformations (Eqn. (2.1)) to describe relative motion between frames. However, the admixture of time with space seems extremely counter-intuitive and it highlights an essential feature of special relativity: time is not absolute.

In our specific example we have $\Lambda^{j}_{i} = 0$, thus implying that our Lorentz transformation is a boost, described by the following non-trivial relations[90, chapter 2]

$$\begin{aligned} ct &= \Lambda^{0}_{1} x' + \Lambda^{0}_{0} ct'; \quad & ct' &= -\Lambda^{1}_{0} x + \Lambda^{0}_{0} ct \\ x &= \Lambda^{1}_{1} x' + \Lambda^{1}_{0} ct'; \quad & x' &= \Lambda^{1}_{1} x - \Lambda^{0}_{1} ct. \end{aligned} \tag{2.16}$$

Using the second postulate of relativity, the coefficients of this linear transformation can be obtained. In both frames, the spherical wave travels the following distance along the x/x'-axis

$$x = ct; \quad x' = ct'. \tag{2.17}$$

Substituting these relations into the transformation rule gives

$$\frac{t}{t'} = \Lambda^1_1 + \Lambda^1_0; \quad \frac{t'}{t} = \Lambda^1_1 - \Lambda^0_1, \tag{2.18}$$

which can be combined to yield the following equation

$$(\Lambda^1_1)^2 - (\Lambda^1_0)^2 = 1. \tag{2.19}$$

To solve for these elements, we need an additional relation, which can be found by evaluating the coordinates of S' at the origin

$$0 = \Lambda^1_1 x - \Lambda^0_1 ct \rightarrow \frac{x}{t} = v = \frac{c\Lambda^0_1}{\Lambda^1_1}. \tag{2.20}$$

Therefore, the elements read

$$\begin{aligned} \Lambda^1_1 &= \frac{1}{\sqrt{1-\frac{v^2}{c^2}}} = \gamma \\ \Lambda^0_1 &= \frac{v}{c\sqrt{1-\frac{v^2}{c^2}}} = \beta\gamma. \end{aligned} \tag{2.21}$$

From similar manipulations, it can be shown that $\Lambda^0_0 = \gamma$, which is hereafter referred to as the Lorentz factor. From these coefficients we arrive at the final form of the Lorentz transformations[88]

$$\begin{aligned} t &= \gamma(t' + \frac{v}{c^2}x') \\ x &= \gamma\big(x' + vt'\big) \\ y &= y' \\ z &= z'. \end{aligned} \tag{2.22}$$

In this example, we chose to consider a transformation to a frame that is moving along the x-axis, although these relations can be readily generalized to arbitrary directions.

As alluded to before, the admixture of space and time provided by Lorentz transformations drastically changes the properties of space-time. For instance, in a relativistic framework, the concept of simultaneity needs re-evaluation. To illustrate this, I have created a schematic representation of our Lorentz transformation in the form of a space-time diagram (Fig. 2.2). In such a diagram, time is represented by a coordinate axis that may mix with the other axes upon transformation, contrary to classical mechanics where time is a universal parameter.

An important feature of Fig. 2.2 is that the ct'- and x'-axis are tilted towards the speed of light. In the unprimed frame, all simultaneous events occur in the xy-plane perpendicular to the ct-axis, whereas all simultaneous events in the primed frame lie in the $x'y$-plane.

Figure 2.2: ***Left****: ordinary rotation of axes, from unprimed (dashed) to primed (full) axes. Transformations of this type are a subgroup of all Lorentz transformations, where only the spatial coordinates are mixed, i.e.* $\exists i, j \quad s.t. \ \Lambda^j_i \neq 0$ *. Here, the ct-axis is left out intentionally.* ***Right****: boost i.e.* $\exists \mu \quad s.t. \ \Lambda^\mu_0 \neq 0$ *and* $\Lambda^0_\mu \neq 0$*, from unprimed (dashed) to primed (full) axes. Here, the z-axis is left out and the diagonal black line represents a light ray. Note that in the primed frame, the* ct'*- and* x'*- axis have tilted symmetrically towards the light line, thus leaving the speed of light unchanged in the transformed frame.*

Therefore, two events that are simultaneous in frame S, are not necessarily simultaneous in frame S'.

Furthermore, when observed from different intertial frames, length intervals are not equivalent. For example, some interval along the x-axis in frame S

$$\ell = x_2 - x_1, \tag{2.23}$$

is not the same when evaluated in the moving frame S'

$$\ell' = x'_2 - x'_1 = \gamma\big(x_2 - vt\big) - \gamma\big(x_1 - vt\big) = \gamma(x_2 - x_1), \tag{2.24}$$

which is referred to as length contraction.[91, 92] An analogous phenomenon occurs for time intervals

$$\Delta t = \frac{1}{\gamma}\Delta t', \tag{2.25}$$

referred to as time-dilation.[93, 94] Furthermore, to every moving object, we can associate the following quantity

$$\begin{aligned} d\tau &= \frac{1}{c}\sqrt{\eta_{\mu\nu}dx^\mu dx^\nu} = \sqrt{dt^2 - \frac{dx^2}{c^2} - \frac{dy^2}{c^2} - \frac{dz^2}{c^2}} \\ &= \sqrt{1 - \frac{1}{c^2}\left(\frac{dx^2}{dt^2} - \frac{dy^2}{dt^2} - \frac{dz^2}{dt^2}\right)}dt = \frac{1}{\gamma}dt. \end{aligned} \tag{2.26}$$

In the rest frame of this object, it evaluates to

$$d\tau = dt', \tag{2.27}$$

thus describing the passage of time as perceived from this frame. Accordingly, this quantity is called the proper time.[95] The major advantage of the proper time is its invariance under Lorentz transformation, thus being independent of the frame from which it is observed.

2.2.3 Potentials and Fields: a Relativistic Formulation

I recall that our initial goal was to find a transformation that leaves the Maxwell equations invariant. Before proceeding, I will evaluate whether our transformation obeys this constraint, thereby also deriving transformation rules for the electromagnetic fields in the process. Following a similar procedure as before, invariance can be demonstrated by first transforming the partial derivatives using the chain rule and making the following substitution for the electromagnetic fields[96]

$$\begin{aligned} E'_x &= E_x & B'_x &= B_x \\ E'_y &= \gamma(E_y - vB_z) & B'_y &= \gamma(B_y + \frac{v}{c^2}E_z) \\ E'_z &= \gamma(E_z + vB_y) & B'_z &= \gamma(B_z - \frac{v}{c^2}E_y), \end{aligned} \tag{2.28}$$

where the (un)primed quantities are evaluated in the (un)primed coordinates. To avoid clutter of notation, I left out explicit coordinate dependence, although this feature should not be taken lightly, as it has profound consequences on the nature of the electromagnetic interactions. However, I will postpone the discussion on the coordinates until we have found proper transformation rules for the charge- and current densities as well.

Since these distributions are extended objects, they occupy a certain interval in three-dimensional space, thus implying that their shape will be deformed according to Eqn. (2.24). The Lorentz contraction, however, will only manifest itself in one direction, thus implying the following relation between a moving charge, $\rho'(\boldsymbol{r}', t')$, and its value at rest, $\rho_0(\boldsymbol{r}, t)$[40, Section 12.3.4]

$$\rho'(\boldsymbol{r}', t') = \gamma\rho_0(\boldsymbol{r}, t). \tag{2.29}$$

Inserting this deformed charge density into Eqn. (2.3), allows us to find an expression for the transformed current density

$$\boldsymbol{j}'(\boldsymbol{r}', t') = \gamma\boldsymbol{v}\rho_0(\boldsymbol{r}, t) = \boldsymbol{u}\rho_0(\boldsymbol{r}, t); \quad \boldsymbol{u} = \frac{d\boldsymbol{r}}{d\tau}, \tag{2.30}$$

where in the second equality, I have expressed the velocity in terms of the proper time. Comparing these two equations, it follows that we can gather the charge- and current density in a four vector

$$\rho^\mu = \rho_0 u^\mu \begin{cases} c\rho' & \mu = 0 \\ j'^i & \mu = 1,2,3 \end{cases}, \tag{2.31}$$

which, in turn, is defined in terms of the four-velocity

$$u^\mu = \frac{dx^\mu}{d\tau} = \begin{cases} \gamma c & \mu = 0 \\ u^i = \gamma v^i & \mu = 1,2,3 \end{cases}. \tag{2.32}$$

However, in above example, I have assumed that the charge is at rest in S, whereas more general relations can be inferred from the transformation properties of four vectors

$$\begin{aligned} \rho' &= \gamma(\rho + \frac{v}{c^2} j_x) \\ j'_x &= \gamma\big(j_x + v\rho) \\ j'_y &= j_y \\ j'_z &= j_z. \end{aligned} \tag{2.33}$$

By making the substitutions in Eqn. (2.28) and (2.33), we can thus preserve the structure of the Maxwell equations. Furthermore, from the four-current, it can be clearly demonstrated that the continuity equation is Lorentz invariant

$$\partial_\mu j^\mu = 0; \quad \partial_\mu = (-\frac{1}{c}\partial_t, \boldsymbol{\nabla}). \tag{2.34}$$

What remains to discuss are the coordinate substitutions in the transformed fields and densities. For example, if we take the second line in Eqn. (2.28) and explicitly write the coordinate dependence

$$E'_y(\boldsymbol{r}', t') = \gamma(E_y(\boldsymbol{r}, t) - vB_z(\boldsymbol{r}, t)), \tag{2.35}$$

the right-hand-side can be written in terms of the primed coordinates by inserting the Lorentz transformation

$$E'_y(\boldsymbol{r}', t') = \gamma\Bigg(E_y\big(\gamma(x'+vt'), y', z', \gamma(t'+\frac{v}{c^2}x')\big) - vB_z\big(\gamma(x'+vt'), y', z', \gamma(t'+\frac{v}{c^2}x')\big)\Bigg). \tag{2.36}$$

The consequences of this can be better understood by the following example. Suppose that we are observing a charge distribution from a certain point. Any change in the charge distribution can be observed from the emitted electromagnetic fields. However, due to the finite speed of light, it will take some time before this field will reach the observation point, suggesting that the observed fields in fact display a delayed image of the charge distribution, also referred to as retardation. Because Lorentz transformations inherently take the finiteness of the speed of light into account, the effects of retardation are included by making this coordinate substitution. Another interesting feature of these transformation rules is that apparently the electric- and magnetic field mix. Similar to the fact that two observers do not always agree on the notion of space and time, neither will they agree on the definition of the electric and magnetic fields.

Although the transformation rules in Eqn. (2.28) are completely valid, they are rather unwieldy. More elegant relations can be derived by considering the potential formulation of electrodynamics. The central idea to this formulation is the Helmholtz decomposition, which states that any vector field can be decomposed into a curl free (irrotational) and divergence free (solenoidal) component, provided that the curl and divergence of this field approach zero faster than $\frac{1}{r^2}$ as $r \to \infty$.[97, 98][40, Appendix B] For a vector field, $\boldsymbol{F}$, to which this condition applies, the Helmholtz decomposition assumes the form

$$\boldsymbol{F} = -\boldsymbol{\nabla} U + \boldsymbol{\nabla} \times \boldsymbol{W}, \tag{2.37}$$

where the scalar function and vector function, U and $\boldsymbol{W}$, are given by

$$U(\boldsymbol{r}) = \frac{1}{4\pi} \int d^3\boldsymbol{r}' \frac{D(\boldsymbol{r}')}{|\boldsymbol{r} - \boldsymbol{r}'|}; \quad \boldsymbol{W} = \frac{1}{4\pi} \int d^3\boldsymbol{r}' \frac{\boldsymbol{C}(\boldsymbol{r}')}{|\boldsymbol{r} - \boldsymbol{r}'|} \tag{2.38}$$

with the integrands defined as

$$D(\boldsymbol{r}) = \boldsymbol{\nabla} \cdot \boldsymbol{F}; \quad \boldsymbol{C}(\boldsymbol{r}) = \boldsymbol{\nabla} \times \boldsymbol{F}. \tag{2.39}$$

Because the curl of every gradient and the divergence of every curl vanishes, it is straightforward to demonstrate that the first- and second terms in the decomposition are indeed irrotational and solenoidal.

According to the third Maxwell equation (Eqn. (2.2)), the magnetic field is always divergence free, suggesting that this field is purely solenoidal.[40, Chapter 10][41, Chapter 6] Its Helmholtz decomposition thus reads

$$\boldsymbol{B} = \boldsymbol{\nabla} \times \boldsymbol{A}, \tag{2.40}$$

where $\boldsymbol{A}$ is referred to as the vector potential. The electric field, on the other hand, is only divergence-free in the absence of charge density. In addition, the second Maxwell equation implies that the electric field is generally not curl-free. However, by substituting Eqn. (2.40) in the second Maxwell equation, it is possible to obtain an auxiliary vector field that is irrotational

$$\boldsymbol{\nabla} \times \left(\boldsymbol{E} + \frac{\partial \boldsymbol{A}}{\partial t} \right) = 0, \tag{2.41}$$

suggesting that it can be expressed as the gradient of a scalar potential

$$-\boldsymbol{\nabla}\phi = \boldsymbol{E} + \frac{\partial \boldsymbol{A}}{\partial t} \to \boldsymbol{E} = -\boldsymbol{\nabla}\phi - \frac{\partial \boldsymbol{A}}{\partial t}. \tag{2.42}$$

By inserting Eqs. (2.40) and (2.42) into the Maxwell equations, it is possible to reformulate them in terms of potentials

$$
\begin{gathered}
\nabla^2\phi + \frac{\partial}{\partial t}(\boldsymbol{\nabla}\cdot\boldsymbol{A}) = -\frac{1}{\epsilon_0}\rho \\
\left(\nabla^2\boldsymbol{A} - \mu_0\epsilon_0\frac{\partial^2\boldsymbol{A}}{\partial t^2}\right) - \boldsymbol{\nabla}\left(\boldsymbol{\nabla}\cdot\boldsymbol{A} + \mu_0\epsilon_0\frac{\partial\phi}{\partial t}\right) = -\mu_0\boldsymbol{j}.
\end{gathered}
\tag{2.43}
$$

Therefore, the potential formulation comes with the benefit of reducing the amount of required vector components (from six to four), albeit at the cost of more complicated differential equations.

The additional complexity of these equations can be somewhat reduced by exploiting the redundancies of the potential formulation. It can be shown that this formulation is not unique: we can add the gradient of any real function to the vector potential without changing the magnetic field

$$
\boldsymbol{\nabla}\times(\boldsymbol{A} + \boldsymbol{\nabla}\chi) = \boldsymbol{\nabla}\times\boldsymbol{A},
\tag{2.44}
$$

because the curl of a gradient always vanishes. The magnetic field is thus invariant under transformations of the form $\boldsymbol{A}\rightarrow\boldsymbol{A}+\boldsymbol{\nabla}\chi$. However, this does not hold for the electric field

$$
\boldsymbol{E} = -\boldsymbol{\nabla}\phi - \frac{\partial\boldsymbol{A}}{\partial t} - \frac{\partial\boldsymbol{\nabla}\chi}{\partial t}.
\tag{2.45}
$$

By extending our definition of our transformation

$$
\begin{gathered}
\boldsymbol{A}\rightarrow\boldsymbol{A}+\boldsymbol{\nabla}\chi \\
\phi\rightarrow\phi - \frac{\partial\chi}{\partial t},
\end{gathered}
\tag{2.46}
$$

it can be shown that the electric field is invariant

$$
\boldsymbol{E} = -\boldsymbol{\nabla}\phi + \boldsymbol{\nabla}\frac{\partial\chi}{\partial t} - \frac{\partial\boldsymbol{\nabla}\chi}{\partial t} - \frac{\partial\boldsymbol{A}}{\partial t} = -\boldsymbol{\nabla}\phi - \frac{\partial\boldsymbol{A}}{\partial t}.
\tag{2.47}
$$

Transformations of this type are called gauge transformations and their form should be kept in mind, because they are applied extensively throughout this thesis.[99] To fix the additional degrees of freedom provided by gauge transformations, a gauge condition ought to be imposed. In most quantum chemical applications the condition $\boldsymbol{\nabla}\cdot\boldsymbol{A} = 0$ is imposed, thus implying that it does not have a longitudinal component. From this condition, we obtain the following equations

$$
\begin{gathered}
\nabla^2\phi = -\frac{1}{\epsilon_0}\rho \\
\left(\nabla^2\boldsymbol{A} - \mu_0\epsilon_0\frac{\partial^2\boldsymbol{A}}{\partial t^2}\right) - \mu_0\epsilon_0\boldsymbol{\nabla}\left(\frac{\partial\phi}{\partial t}\right) = -\mu_0\boldsymbol{j},
\end{gathered}
\tag{2.48}
$$

where the solutions of the first equation gives the well-known Coulomb potential. Accordingly, this gauge condition is called Coulomb gauge. However, imposing Coulomb gauge does not fix all additional degrees of freedom, as this gauge condition indicates a family of transformations, having the following constraint on the gauge function $\nabla^2\chi = 0$.

At first sight, it seems that the instantaneous nature of the scalar potential contradicts the second postulate of relativity. Furthermore, the gauge condition manifestly breaks Lorentz invariance, as it does not treat space and time on equal footing. However, from careful analysis, it follows that all effects related to retardation are captured by the vector potential, thus respecting relativistic laws.[100] In a relativistic context, the analysis is simplified if the gauge condition itself is also Lorentz invariant. Therefore, a more suitable condition is given by the Lorentz gauge

$$\boldsymbol{\nabla}\cdot\boldsymbol{A} + \frac{1}{c^2}\frac{\partial\phi}{\partial t} = 0, \tag{2.49}$$

providing us with more symmetric equations for the potentials

$$\begin{aligned} \nabla^2\phi - \frac{1}{c^2}\frac{\partial^2\phi}{\partial t^2} &= -\frac{1}{\epsilon_0}\rho \\ \nabla^2\boldsymbol{A} - \mu_0\epsilon_0\frac{\partial^2\boldsymbol{A}}{\partial t^2} &= -\mu_0\boldsymbol{j}. \end{aligned} \tag{2.50}$$

Note that this expression depends on the d'Alembertian

$$\Box = \partial^\mu\partial_\mu = \nabla^2 - \frac{1}{c^2}\frac{\partial^2}{\partial t^2}, \tag{2.51}$$

which is a Lorentz invariant quantity by construction. Using the definition of the current four vector, these two equations can be combined in one

$$\Box A^\mu = -\mu_0 J^\mu. \tag{2.52}$$

From the structure of this equation, it can be argued that the four-potential is a valid four-vector, since the d'Alembertian is Lorentz invariant, whereas the right-hand-side is given by the four-current. The right- and left-hand-side can only be made consistent if the four-potential $A^\mu = (\phi/c, \boldsymbol{A})$, is indeed a four-vector. Finding transformation rules for the fields is thus much more efficient by first transforming the potentials and then compute the fields from these potentials.

For example, let us consider a point charge at rest in S. Being at rest, the vector potential is zero, while the scalar potential is given by the Coulomb potential. In the moving frame, S', the charge is in motion, thus implying the following potentials

$$\begin{aligned} \phi'(\boldsymbol{r}', t') &= \gamma\phi(\boldsymbol{r}, t) \\ \boldsymbol{A}'(\boldsymbol{r}', t') &= \gamma\boldsymbol{v}\phi(\boldsymbol{r}, t) \end{aligned} \tag{2.53}$$

Therefore, the field is purely electric in the rest frame, whereas it gains a magnetic component in the moving frame. This effect can be identified with magnetic induction, whose discovery long predates the development of relativistic theory. In Section B.1 of the appendix, it will be shown that this effect is fundamental to spin-orbit coupling.

2.2.4 Relativistic Kinematics

Having thus established a coordinate transformation that preserves the Maxwell equations, one may wonder why the invariance of the Maxwell equations should be favoured over the invariance of Newton's second law as prescribed by the Galilean transformations. After all, Galilean transformations intuitively make sense from everyday experiences. Every train enthusiast can testify that from the outside of a train, a walking passenger indeed seems to move at the sum of his/her own speed and the speed of the train. These seemingly different transformations can be connected by recognizing that the velocity of everyday objects does not even reach a fraction of the speed of light, thus hinting at the fact that Galilean transformations are a limiting case of Lorentz transformations. At these velocity scales, it is safe to assume that the following limit applies $c \to \infty$, hereafter referred to as the non-relativistic limit. Within this limit, it can be shown that $\gamma \to 1$ and $\beta \to 0$, which gives rise to the Galilean transformation upon substitution in Eqn. (2.15), implying that these transformations effectively hold true at low speeds. Provided that the speeds appearing in our system are small enough compared to the speed of light, it is justified to utilize the familiar concepts of classical kinematics. At elevated speeds, however, we are forced to generalize these concepts to a relativistic framework.

Using the previously introduced definition of the four-velocity (Eqn. (2.32)), it is possible to generalize the well-known concept of momentum to the relativistic domain

$$p^\mu = m_0 u^\mu = \begin{cases} \gamma m_0 c = mc & \mu = 0 \\ \gamma m_0 v^i = m v^i & \mu = 1,2,3 \end{cases}. \tag{2.54}$$

Here, I have defined the rest mass, m_0, and the instantaneous mass $m = \gamma m_0$. Using these relations, it can be argued that massive objects become even heavier when put in motion. From the structure of the Lorentz factor, γ, it thus follows that at the light-speed, massive objects gain an infinite mass, thus prohibiting anything except light or any other massless object to travel at this speed. Although the spatial components of the four-momentum can be recognized straightforwardly as the relativistic generalizations of classical momentum, the zeroth component has a less clear meaning. To reveal the physical interpretation of this component, I will exploit that the square of the four momentum

$$p^\mu p_\mu = m^2(v^2 - c^2) = -m_0^2 c^2 \tag{2.55}$$

is conserved in time

$$\frac{d(p^\mu p_\mu)}{d\tau} = 2p^\mu \frac{dp_\mu}{d\tau} = 0. \tag{2.56}$$

In this expression we can further identify the four-force

$$F^\mu = \frac{dp^\mu}{d\tau} = \begin{cases} \frac{dmc}{d\tau} & \mu = 0 \\ \frac{dp^i}{d\tau} & \mu = 1, 2, 3. \end{cases} \tag{2.57}$$

By expanding the dot product from Eqn. (2.56) into its individual components, we arrive at the following expression

$$2m\boldsymbol{u} \cdot \boldsymbol{F} - 2mc\frac{dmc}{d\tau} = 0. \tag{2.58}$$

Further eliminating the common factors yields the result

$$\frac{dmc^2}{d\tau} = \boldsymbol{F} \cdot \boldsymbol{v} = \frac{\boldsymbol{F} \cdot d\boldsymbol{r}}{d\tau} = \frac{dE}{d\tau}, \tag{2.59}$$

where in the last line, I have used the relation between work and energy. Therefore, we can make the identification

$$E = mc^2 \rightarrow p^0 = mc = \frac{E}{c}, \tag{2.60}$$

which implies that the zeroth component is energy and even more surprisingly that energy is equivalent to mass.[101] This relation is particularly useful to describe nuclear decay, where the total mass of the decay products is slightly smaller than the mass of the original nucleus, thus implying that the mass difference has been converted into energy. Even though this difference is often tiny, the factor of c^2 implies that possibly a vast amount of energy can be released in such processes.

From the square of the four-momentum, we can derive an alternative expression for the relativistic energy that separates the rest energy from the kinetic energy

$$E = \pm\sqrt{c^2p^2 + m_0^2c^4}. \tag{2.61}$$

A cumbersome feature of this equation is that it allows for negative energies. However, in the current context, the negative energies do not form a problem. After all, the positive and negative energies are separated by a barrier of $2mc^2$ and for classical point-particles, energies can only vary continuously. Therefore, the negative energy solutions can be discarded in a classical context. The non-relativistic kinetic energy can be obtained by subtracting the energy at rest and expanding the (positive) square root

$$E - m_0c^2 = m_0c^2\sqrt{\frac{p^2}{m_0^2c^2} + 1} - m_0c^2 = \frac{p^2}{2m_0} - \frac{p^4}{8m_0^3c^2} + \cdots, \tag{2.62}$$

where the zeroth order term can be recognized as the non-relativistic kinetic energy.

In its current form, however, this expression has limited use, as it does not include any influences of external electromagnetic fields. By minimizing an interaction Lagrangian, as proposed by Schwarzschild in 1903[102], it follows that the influences of these fields on a charged particle can be introduced by substituting the four-momentum with the mechanical four-momentum

$$p_\mu \rightarrow \pi_\mu = p_\mu - qA_\mu, \tag{2.63}$$

which is referred to as minimal substitution.[103] Therefore, the relativistic energy of a point particle in an electromagnetic field can be expressed as

$$E = \pm\sqrt{m_0^2c^4 + c^2\pi^2} + q\phi; \quad \boldsymbol{\pi} = \boldsymbol{p} - q\boldsymbol{A}. \tag{2.64}$$

Based on this classical energy, I will proceed to derive a relativistic wave equation.

2.3 Relativistic Wave Equation

2.3.1 The Dirac Equation and Its Predecessors

The classical description of a point particle is deterministic in the sense that everything there is to know can be calculated with certainty from the position and momentum of the particle. In a quantum mechanical framework, however, observable properties are associated with Hermitian operators that give the probabilities of measurement outcomes when acted on the wave function. Assuming the position representation, the following substitution has to be made to promote classical observables to Hermitian operators

$$E \rightarrow i\hbar\partial_t; \quad \boldsymbol{p} \rightarrow \frac{\hbar}{i}\boldsymbol{\nabla}. \tag{2.65}$$

However, applying this procedure to the relativistic energy of a point particle (Eqn. (2.61)) is cumbersome, because defining a square-root operator requires special consideration. A straightforward solution is to expand the square root (Eqn. (2.62)), truncate it at finite order and making the aforementioned operator substitutions.[90] To first order, this gives the Schrödinger Hamiltonian

$$\hat{H}_s = i\hbar\frac{\partial}{\partial t} = \frac{\hat{p}^2}{2m_e} = \frac{(\boldsymbol{\sigma}\cdot\hat{\boldsymbol{p}})^2}{2m_e}, \tag{2.66}$$

where in the last equality I have applied the Dirac identity, $(\boldsymbol{\sigma}\cdot\boldsymbol{A})(\boldsymbol{\sigma}\cdot\boldsymbol{B}) = \boldsymbol{A}\cdot\boldsymbol{B} + i\boldsymbol{\sigma}\cdot(\boldsymbol{A}\times\boldsymbol{B})$.

The validity of the last equality suggests that in the free-particle case, spin is a hidden degree of freedom, which is revealed by the influence of an external magnetic field. To introduce these fields into our Hamiltonian, the momentum ought to be substituted with the mechanical momentum (Eqn. (2.63)), which should then be promoted to an operator. It should be noted that minimal substitution provides a relativistic coupling between particle and fields, whereas we apply this to a non-relativistic Hamiltonian. However, strictly speaking all magnetic interactions vanish in the non-relativistic limit, as can be inferred from the Maxwell equations, leaving us with electrostatic interactions.[104] From a pragmatic point of view, it is completely valid to use this relativistic coupling in this setting. Starting from the Schrödinger Hamiltonian, minimal substitution gives the following result

$$\hat{H}_p = \frac{\left(\boldsymbol{\sigma} \cdot (\hat{\boldsymbol{p}} + e\boldsymbol{A})\right)^2}{2m_e} - e\phi, \tag{2.67}$$

which gives the Pauli Hamiltonian in its more familiar form after applying the Dirac identity

$$\hat{H}_p = \frac{\hat{p}^2}{2m_e} + \frac{e}{2m_e}(\hat{\boldsymbol{p}} \cdot \boldsymbol{A} + \boldsymbol{A} \cdot \hat{\boldsymbol{p}}) + \frac{e^2 A^2}{2m_e} + \frac{e\hbar}{2m_e}(\boldsymbol{\sigma} \cdot \boldsymbol{B}) - e\phi. \tag{2.68}$$

Here, the field-matter interaction is mediated through five terms. The first two terms are responsible for the coupling of the electronic motion with the external fields, which can be combined into a single term ($\frac{e}{m_e}\boldsymbol{A} \cdot \hat{\boldsymbol{p}}$) if Coulomb gauge is imposed. The third term corresponds to diamagnetic interactions, whereas the fourth term is responsible for the Zeeman splitting of spin-levels as induced by the external magnetic field. The last term gives an electric interaction between the scalar potential and the electron charge, which is the Coulombic attraction if our external fields stem from the nuclei. It is important to note that spin is introduced *ad hoc*, because it was an arbitrary decision to use $(\boldsymbol{\sigma} \cdot \boldsymbol{\pi})$ in our Hamiltonian instead of $\boldsymbol{\pi}$.

In its current form, our Hamiltonian does not include relativistic corrections, which can be taken into consideration by including higher-order terms from Eqn. (2.62) in our Hamiltonian. The next order to include depends on a fourth power of the momentum, which corrects for the increase of electron mass for higher velocities. However, unlike the kinetic energy, which is positive-definite $\langle \hat{T} \rangle = \langle \psi | \frac{\hbar^2}{2m_e} \hat{p}^2 | \psi \rangle = \frac{\hbar^2}{2m_e} \langle \hat{p}\psi | \hat{p}\psi \rangle > 0$, the fourth-power term is negative-definite for similar reasons. Any variational procedure that is based on this Hamiltonian is doomed to fail, because the fourth-power term will draw the energy towards negative infinity. Nevertheless, it is possible to include the effects of this operator as a perturbation of the Pauli Hamiltonian. To describe strong relativistic effects, this approach does not seem to be ideal.

Instead of quantizing the square-root expansion, it might be a better idea to apply this procedure to the square of the energy,

$$\left[\Box + \left(\frac{m_e c}{\hbar}\right)^2\right] \psi_{KG}(\boldsymbol{r}, t) = 0, \tag{2.69}$$

leading to the Klein-Gordon equation.[105, 106] Being constructed from the Lorentz invariant d'Alembertian operator, this equation seems like a perfectly valid relativistic wave equation, although it is met with two problematic features: it allows for negative energies and negative probability densities. The problem of negative energy solutions was to be expected, since it already manifest itself in the classical case (Eqn. (2.61)). In a quantum mechanical framework, however, the presence of such solutions cannot be ignored anymore, because discontinuous jumps in energy are allowed. Upon decaying to lower and lower energy states, an infinite amount of energy is released. States of negative energy exhibit the additional paradoxical feature of requiring energy absorption to decelerate their motion, which has never been observed experimentally.[81] Furthermore, the existence of negative densities completely breaks down the probabilistic interpretation of the wave function.

Paul Dirac was especially frustrated with the second problem and thus set out to find an alternative to the Klein-Gordon equation. In his work, he proposed to factorize the Klein-Gordon equation

$$\Bigg(\hat{p}_0+\alpha_1\hat{p}_1+\alpha_2\hat{p}_2+\alpha_3\hat{p}_3+m_ec\beta\Bigg)\Bigg(-\hat{p}_0+\alpha_1\hat{p}_1+\alpha_2\hat{p}_2+\alpha_3\hat{p}_3+m_ec\beta\Bigg)\psi(\boldsymbol{r},t)=0, \tag{2.70}$$

in terms of the quantities $\{\alpha_i\}$ and β.[107] By expanding the two factors

$$\begin{aligned}\Bigg(&-\hat{p}_0^2+\alpha_1\alpha_1\hat{p}_1^2+\alpha_2\alpha_2\hat{p}_2^2+\alpha_3\alpha_3\hat{p}_3\hat{p}_3+m_e^2c^2\beta\beta \\ &+(\alpha_1\alpha_2+\alpha_2\alpha_1)\hat{p}_2\hat{p}_1+(\alpha_1\alpha_3+\alpha_3\alpha_1)\hat{p}_3\hat{p}_1 \\ &+(\alpha_2\alpha_3+\alpha_3\alpha_2)\hat{p}_3\hat{p}_2+m_ec(\alpha_1\beta+\beta\alpha_1)\hat{p}_1 \\ &+m_ec(\alpha_2\beta+\beta\alpha_2)\hat{p}_2+m_ec(\alpha_3\beta+\beta\alpha_3)\hat{p}_3\Bigg)\psi(\boldsymbol{r},t)=0,\end{aligned} \tag{2.71}$$

it can be shown that these quantities need to obey the following algebra in order for the above expression to reduce to the Klein-Gordon equation

$$\begin{aligned}\{\alpha_i,\alpha_j\}&=2\delta_{ij}\\ \{\alpha_i,\beta\}&=0.\end{aligned} \tag{2.72}$$

Therefore, $\{\alpha_i\}$ and β are non-commutative, implying that they can be represented by matrices. One possible set of matrices is given by

$$\alpha_i=\begin{pmatrix}0_2 & \sigma_i\\ \sigma_i & 0_2\end{pmatrix};\quad \beta=\begin{pmatrix}I_2 & 0_2\\ 0_2 & -I_2\end{pmatrix}, \tag{2.73}$$

also referred to as the Dirac matrices. We arrive at the following expression for the time-dependent Dirac equation

$$\big(c\boldsymbol{\alpha}\cdot\hat{\boldsymbol{p}}+m_ec^2\beta\big)\psi(\boldsymbol{r},t)=\hat{h}_D\psi(\boldsymbol{r},t)=i\hbar\frac{\partial\psi(\boldsymbol{r},t)}{\partial t}. \tag{2.74}$$

The relativistic character of the Dirac equation can be further highlighted by multiplying from the left by β

$$\big(i\hbar\gamma^\mu\partial_\mu+m_ec\big)\psi(\boldsymbol{r},t)=0;\quad \gamma^\mu=(\beta,-\beta\boldsymbol{\alpha}), \tag{2.75}$$

where appears the gamma matrices, obeying the algebra

$$\{\gamma^\mu, \gamma^\nu\} = -2\eta^{\mu\nu} I_4. \tag{2.76}$$

This notation suggests that the gamma matrices form a four-vector

$$\big(i\hbar\gamma'^{\mu}\partial'_{\mu} + m_e c\big)\psi(\boldsymbol{r}, t) = \big(\gamma_\rho \Lambda^\rho_\nu \eta^{\nu\mu} \Lambda^\sigma_\mu \hat{p}_\sigma + m_e c\big)\psi(\boldsymbol{r}, t) = 0, \tag{2.77}$$

although this can only hold true if their algebra is conserved upon Lorentz transformations. Using the algebra of the gamma matrices, this can be confirmed[107]

$$\{\gamma'^{\mu}, \gamma'^{\nu}\} = \Lambda^\mu_\rho \Lambda^\nu_\sigma \{\gamma^\rho, \gamma^\sigma\} = -2\Lambda^\mu_\rho \eta^{\rho\sigma} \Lambda^\nu_\sigma I_4 = -2\eta^{\rho\sigma} I_4. \tag{2.78}$$

Although the aforementioned covariant form of the Dirac equation is useful to demonstrate its transformation properties, it is typically not used in electronic structure theory, where the point of depart is given by the time-independent Dirac equation. This equation can be derived by expressing the time-dependent wave function as $\psi(\boldsymbol{r}, t) = T(t)\psi(\boldsymbol{r})$ and inserting it into Eqn. (2.74)

$$\frac{\hat{h}_D \psi(\boldsymbol{r})}{\psi(\boldsymbol{r})} = \frac{i\hbar}{T(t)} \frac{\partial T(t)}{\partial t}. \tag{2.79}$$

However, it should be noted that this separation does not hold for all inertial frames. Within the special frame where our separation is valid, above equation holds for all values of $\boldsymbol{r}$ and t, suggesting that it can only be true if both sides equal a constant that can be identified with the energy. Therefore, the time-independent Dirac equation reads

$$\big(c\boldsymbol{\alpha} \cdot \hat{\boldsymbol{p}} + m_e c^2 \beta\big)\psi(\boldsymbol{r}) = E\psi(\boldsymbol{r}). \tag{2.80}$$

By applying the minimal substitution procedure and aligning the energy scale with the non-relativistic energy (such as in Eqn. (2.64)), the latter achieved by the substitution $\beta \to \beta' = \beta - I_4$, we arrive at the following result

$$\big(c\boldsymbol{\alpha} \cdot \hat{\boldsymbol{p}} + m_e c^2 \beta' - e\phi + ec\boldsymbol{\alpha} \cdot \boldsymbol{A}\big)\psi(\boldsymbol{r}) = E\psi(\boldsymbol{r}). \tag{2.81}$$

Note that all light–matter interactions are mediated by two linear terms, unlike the interaction terms in the Pauli Hamiltonian in Eqn. (2.68) which may also include the spin-Zeeman term and the quadratic diamagnetic term.

2.3.2 Physical Properties of the Dirac Equation

In our derivation, we have introduced the Dirac matrices from the necessity to have consistent equations. The physical content of these matrices can be revealed in the Heisenberg picture, where states are time-independent, whereas observables evolve according to $\hat{\Omega}(t) = e^{i\hat{H}t/\hbar}\hat{\Omega}(0)e^{-i\hat{H}t/\hbar}$. Using the Heisenberg equation of motion

$$\frac{d\hat{\boldsymbol{r}}}{dt} = -i[\hat{\boldsymbol{r}}, \hat{h}_D] = c\boldsymbol{\alpha}, \tag{2.82}$$

it can thus be concluded that the Dirac matrices can be identified as velocity operators. However, the algebraic properties of the Dirac matrices create a paradox, from which we have
$c^2|\boldsymbol{\alpha}|^2 = 3c^2 I_4$, thus contradicting the second postulate of relativity. Fortunately, the same algebraic properties imply that the three components cannot be known simultaneously, similar to angular momenta. If one of these three components is completely known, for example $c\alpha_x$, its eigenvalues $\pm c$ imply that the velocity is still much higher than expected from a massive particle like the electron. It can be demonstrated that the Dirac electron undergoes highly oscillatory motion (referred to as *zitterbewegung* in ref. [108]) superimposed on its average motion. It is the latter type of motion that is more in line with the expected behaviour of massive particles (see ref. [109, Section 7.3] for a more detailed derivation).

From the structure of the Dirac matrices, it can be further concluded that the Dirac wave function is a four-component function

$$\psi(\boldsymbol{r}) = \begin{pmatrix} \psi^1(\boldsymbol{r}) \\ \psi^2(\boldsymbol{r}) \\ \psi^3(\boldsymbol{r}) \\ \psi^4(\boldsymbol{r}) \end{pmatrix}. \tag{2.83}$$

Based on the results from previous sections, it almost comes as a reflex to conclude that everything with four components *is* a four vector. For the Dirac wave function this is definitely not the case. Two of the four degrees of freedom are related to spin symmetry, since the Dirac wave function can be expressed in terms of two Pauli spinors[90, Section 4.5]

$$\psi(\boldsymbol{r}) = \begin{pmatrix} \psi^L(\boldsymbol{r}) \\ \psi^S(\boldsymbol{r}) \end{pmatrix}, \tag{2.84}$$

where ψ^L and ψ^S are conventionally referred to as the large- and small component. In Section B.1 of the appendix, the validity of this identification is further demonstrated. It thus remains to explain the origin of the remaining two degrees of freedom, or put in other words, why we need two Pauli-spinors in our wave function. A straightforward mathematics-oriented answer to this question is that the matrices should be at least four-dimensional to obey the algebraic rules from Eqn. (2.72). However, a more satisfying answer can be found from the operation of charge conjugation.

The action of this operation allows us to relate the solutions of the minimally coupled time-dependent Dirac equation, to the same equation but with opposite external charges[89, Section 1.6][90, Chapter 5][110, Section 2.8.1]

$$\big(c\boldsymbol{\alpha}\cdot\hat{\boldsymbol{p}} + m_e c^2\beta + e\phi - ec\boldsymbol{\alpha}\cdot\boldsymbol{A}\big)\hat{C}\psi(\boldsymbol{r},t) = i\hbar\partial_t\hat{C}\psi(\boldsymbol{r},t). \tag{2.85}$$

In Section B.2 of the appendix it is demonstrated that the explicit action of charge conjugation is given by

$$\hat{C}\psi(\boldsymbol{r},t) = \begin{pmatrix} \psi^{S\beta*}(\boldsymbol{r},t) \\ -\psi^{S\alpha*}(\boldsymbol{r},t) \\ -\psi^{L\beta*}(\boldsymbol{r},t) \\ \psi^{L\alpha*}(\boldsymbol{r},t) \end{pmatrix}, \tag{2.86}$$

which suggests that this operator consists of a matrix operator that permutes the components, and the complex conjugation operator

$$\hat{C} = \hat{\mathcal{K}}_0 \hat{U}_c. \tag{2.87}$$

Since charge conjugation swaps the role of the large- and small component, it follows that these two components are needed to accommodate for this symmetry. Furthermore, in the time-independent case, charge conjugation can be used to relate the solutions of positive- and negative energies

$$\big(c\boldsymbol{\alpha}\cdot\hat{\boldsymbol{p}} + m_e c^2\beta + e\phi - ec\boldsymbol{\alpha}\cdot\boldsymbol{A}\big)\hat{C}\psi(\boldsymbol{r}) = -E\hat{C}\psi(\boldsymbol{r}), \tag{2.88}$$

where the negative energy sign appears from complex conjugation of the time-dependent wave function $\hat{\mathcal{K}}_0(e^{-iEt/\hbar}\psi(\boldsymbol{r})) = e^{iEt/\hbar}\hat{\mathcal{K}}_0(\psi(\boldsymbol{r}))$. Charge conjugation hence reveals the intricate relation between positrons and negative-energy electronic solutions.

However, before jumping to conclusions, I recall that in a quantum mechanical framework negative energy solutions are a problematic feature. The relativistic hydrogen atom, for instance, is predicted to decay within nanoseconds if we allow our system to decay to negative energy solutions. To solve this problem, Dirac proposed that all negative energy solutions are occupied, which prohibits decay by virtue of the exclusion principle.[81] In its time, this proposition was highly controversial, since it implies that all space is permeated by an infinitely dense collection of negative energy particles, more commonly referred to as the Dirac sea. However, Dirac argued that the negative energy sea will not have a significant effect on its surroundings, provided that the density of these states is homogeneous enough. For a completely filled negative energy continuum, this assumption seems to be reasonable. However, the Dirac sea should induce measurable effects in regions where homogeneity is broken. When a negative-energy electron is excited from the Dirac sea, such that it now occupies a positive energy state, a hole is left in the Dirac sea. This hole has the same physical characteristics as the electron, except that its charge is opposite. Therefore, the Dirac equation predicts the existence of anti-matter, which was experimentally confirmed by Anderson through the discovery of the positron.[111] In the presence of charge, inhomogeneities are induced in the Dirac sea, also referred to as vacuum polarization, the effects of which are only measurable at extremely high charges.[110] A more rigorous description of these effects can be obtained from the theory of quantum electrodynamics. The negative energy solutions are not present anymore in this theory, but are rather replaced by positive energy positronic solutions, thus solving the problems associated with the Dirac sea. However, quantum electrodynamics is far beyond the scope of this thesis and I will rather apply Dirac's approach to negative energy solutions.

2.3.3 The Radial Dirac Equation

Having established the main features of the Dirac equation, I now proceed to study this equation under the influence of a central potential ($V(r)$), a class of systems that encompasses atoms, thus being essential for quantum chemistry. Spherical symmetry provides one-dimensional radial equations that in some cases are even solvable analytically. This section is mainly inspired from the seventh chapter in *Introduction to Relativistic Quantum Chemistry*.[90]

In the non-relativistic case, the Hamiltonian commutes with the angular momentum operator, $[\hat{H}_s, \hat{\boldsymbol{\ell}}]$, thus implying that in this case the wave function is an angular momentum eigenstate

$$\psi_{\ell m}(\boldsymbol{r}) = \frac{1}{r} R(r) Y_{\ell m_\ell}(\theta, \phi), \tag{2.89}$$

where ℓ and m are the azimuthal and magnetic quantum number. Because spin is not explicitly present in the non-relativistic Schrödinger Hamiltonian, it follows that $\left[\hat{H}_s, \hat{\boldsymbol{s}}\right] = 0$.

However, in a relativistic formulation, these two relations do not hold anymore

$$\left[\hat{h}_D, \hat{\boldsymbol{\ell}}\right] = i\hbar\big(c\boldsymbol{\alpha} \times \hat{\boldsymbol{p}}\big); \quad \left[\hat{h}_D, \frac{\hbar}{2}\hat{\boldsymbol{\Sigma}}\right] = -i\hbar\big(c\boldsymbol{\alpha} \times \hat{\boldsymbol{p}}\big), \tag{2.90}$$

where appears the four component spin operator $\hat{\boldsymbol{\Sigma}} = \begin{pmatrix} \boldsymbol{\sigma} & 0 \\ 0 & \boldsymbol{\sigma} \end{pmatrix}$. Interestingly, these two equations exactly cancel, suggesting that the total angular momentum

$$\hat{\boldsymbol{j}} = \hat{\boldsymbol{\ell}} + \frac{\hbar}{2}\hat{\boldsymbol{\Sigma}} \tag{2.91}$$

commutes with the Hamiltonian

$$\left[\hat{h}_D, \hat{\boldsymbol{j}}\right] = 0. \tag{2.92}$$

Therefore, for central potentials, the corresponding wave functions are rather eigenfunctions of the total angular momentum. This function is given by a four component spinor, which in turn can be expressed in terms of two Pauli spinors. To learn more about the structure of the four component eigenfunctions, it turns out to be useful to start from the two component case. The two component functions are also total angular momentum eigenfunctions, although the associated total angular momentum operator is defined in terms of the more conventional spin operator in terms of the Pauli matrices. The structure of these functions can be found by applying a Clebsch-Gordan series

$$|\ell s; j m_j\rangle = \sum_{m_\ell=-\ell}^{\ell} \sum_{m_s=-\frac{1}{2}}^{\frac{1}{2}} |\ell m_\ell s m_s\rangle\langle \ell m_\ell s m_s | \ell s; j m_j\rangle, \tag{2.93}$$

in terms of the uncoupled basis, $|\ell m_\ell s m_s\rangle = |\ell m_\ell\rangle \otimes |s m_s\rangle$. This basis implies that the resulting function is also an eigenfunction of $\hat{s}^2$ and $\hat{\ell}^2$, which generally holds for two-component states, but not for four component spinors. In the current context, it is preferred to express these states in the position representation

$$\xi_{jm_j}(\theta,\phi) = \sum_{m_\ell=-\ell}^{\ell}\sum_{m_s=-\frac{1}{2}}^{\frac{1}{2}} \langle \hat{\boldsymbol{r}}|\ell m_\ell s m_s\rangle\langle \ell m_\ell s m_s|\ell s; jm_j\rangle = \sum_{m_\ell=-\ell}^{\ell}\sum_{m_s=-\frac{1}{2}}^{\frac{1}{2}} \langle \ell m_\ell s m_s|\ell s; jm_j\rangle Y_{\ell m_\ell}|sm_s\rangle, \tag{2.94}$$

which defines the spherical spinors. From the rules of the Clebsch-Gordon decompositions, it follows that the total angular momentum assumes the values $\ell \pm \frac{1}{2}$. However, from this result, it can be concluded that j is not a unique label, because at least two combinations of ℓ and s can give the same value of j. For example, $j = \frac{3}{2}$, can be obtained from parallel coupling of $\ell = 1; s = \frac{1}{2}$ or anti-parallel coupling of $\ell = 2; s = \frac{1}{2}$. A more useful quantum number can be found from the action of the operator

$$\hat{\kappa} = -\big(\boldsymbol{\sigma}\cdot\hat{\boldsymbol{\ell}}\big) - \hbar = \frac{1}{\hbar}\Big(\hat{\ell}^2 + \hat{s}^2 - \hat{j}^2\Big) - \hbar \tag{2.95}$$

onto the spherical spinors

$$\hat{\kappa}\xi_{j,m_j}(\theta,\phi) = \left[\frac{1}{\hbar}\Big(\hat{\ell}^2 + \hat{s}^2 - \hat{j}^2\Big) - \hbar\right]\xi_{j,m_j}(\theta,\phi) \tag{2.96}$$

$$= \hbar\big(\ell(\ell+1) - j(j+1) - \frac{1}{4}\big)\xi_{j,m_j}(\theta,\phi) = \hbar\kappa\xi_{j,m_j}(\theta,\phi). \tag{2.97}$$

The κ quantum number can assume positive and negative integer values

$$\kappa = \begin{cases} \ell & \text{for } j = \ell - \frac{1}{2} \\ -\ell - 1 & \text{for } j = \ell + \frac{1}{2} \end{cases}. \tag{2.98}$$

To each of the two combinations of ℓ and s that yields the same value of j, we can assign an equal but opposite value of κ, thus resolving the ambiguity associated with j. Therefore, we arrive at a uniquely labelled expression for the spherical spinors

$$\xi_{\kappa,m_j}(\theta,\phi) = \begin{pmatrix} sgn(-\kappa)\sqrt{\frac{\kappa+\frac{1}{2}-m_j}{2\kappa+1}}Y_{\ell,m_j-\frac{1}{2}} \\ \sqrt{\frac{\kappa+\frac{1}{2}+m_j}{2\kappa+1}}Y_{\ell,m_j+\frac{1}{2}} \end{pmatrix}. \tag{2.99}$$

In analogy with the non-relativistic hydrogen atom, it can be argued from symmetry considerations that the four-component hydrogenic wave function assumes the form

$$\begin{pmatrix}\psi^L(\boldsymbol{r}) \\ \psi^S(\boldsymbol{r})\end{pmatrix} = \frac{1}{r}\begin{pmatrix} P(r)\xi_{\kappa^L m_j}(\theta,\phi) \\ iQ(r)\xi_{\kappa^S m_j}(\theta,\phi)\end{pmatrix} \tag{2.100}$$

where the values of κ are intentionally labelled differently for the large- and small component. Because the wave function is an eigenfunction of total angular momentum, they are either equal or opposite: $\kappa^L = \pm\kappa^S$. To find the correct relation between these two quantum numbers, I will insert this ansatz into the Dirac equation,

$$\frac{1}{r}\begin{pmatrix} V & c\boldsymbol{\sigma}\cdot\hat{\boldsymbol{p}} \\ c\boldsymbol{\sigma}\cdot\hat{\boldsymbol{p}} & V-2mc^2 \end{pmatrix}\begin{pmatrix} P\xi_{\kappa^L m_j} \\ iQ\xi_{\kappa^S m_j} \end{pmatrix} = \frac{E}{r}\begin{pmatrix} P\xi_{\kappa^L m_j} \\ iQ\xi_{\kappa^S m_j} \end{pmatrix}. \tag{2.101}$$

and apply the separation of variables procedure. In this equation and the ones that follow, the radial- and angular dependence have been suppressed.

To facilitate this procedure, I will split the kinetic energy term $(\boldsymbol{\sigma}\cdot\hat{\boldsymbol{p}})$ into a radial and angular part. From the relation $(\boldsymbol{\sigma}\cdot\boldsymbol{e}_r)(\boldsymbol{\sigma}\cdot\boldsymbol{e}_r) = I_2$, we obtain the following result

$$\boldsymbol{\sigma}\cdot\hat{\boldsymbol{p}} = \frac{1}{r}\sigma_r(\boldsymbol{\sigma}\cdot\boldsymbol{r})(\boldsymbol{\sigma}\cdot\hat{\boldsymbol{p}}), \tag{2.102}$$

where appears the radial Pauli matrix

$$\sigma_r = \boldsymbol{e}_r\cdot\boldsymbol{\sigma} = \begin{pmatrix} \cos\theta & e^{-i\phi}\sin\theta \\ e^{i\phi}\sin\theta & -\cos\theta \end{pmatrix}. \tag{2.103}$$

Subsequently, we can obtain the desired separation by inserting the Dirac identity

$$\begin{aligned} \boldsymbol{\sigma}\cdot\hat{\boldsymbol{p}} &= \frac{1}{r}\sigma_r(\boldsymbol{r}\cdot\hat{\boldsymbol{p}}) + \frac{1}{r}\sigma_r i\boldsymbol{\sigma}\cdot(\boldsymbol{r}\times\hat{\boldsymbol{p}}) = \sigma_r(\hat{p}_r + \frac{1}{r}i\boldsymbol{\sigma}\cdot\hat{\boldsymbol{\ell}}) \\ &= -i\sigma_r(\hbar\frac{\partial}{\partial r} - \frac{1}{r}\boldsymbol{\sigma}\cdot\hat{\boldsymbol{\ell}}) = -i\sigma_r\big(\hbar\frac{\partial}{\partial r} - \frac{1}{r}(\hat{\kappa}+\hbar)\big), \end{aligned} \tag{2.104}$$

where appears the radial momentum $\hat{p}_r = \boldsymbol{e}_r\cdot\hat{\boldsymbol{p}}$ and the $\hat{\kappa}$ operator. Inserting this result into the Dirac equation yields the following system of equations

$$\begin{aligned} -c\left[\frac{1}{r}(\kappa^S+\hbar) - \hbar\frac{\partial}{\partial r}\right]\frac{1}{r}Q\sigma_r\xi_{\kappa^S m_j} &= \Big[E - V\Big]\frac{1}{r}P\xi_{\kappa^L m_j} \\ c\left[\frac{1}{r}(\kappa^L+\hbar) - \hbar\frac{\partial}{\partial r}\right]\frac{1}{r}P\sigma_r\xi_{\kappa^L m_j} &= \Big[E - V + 2mc^2\Big]\frac{1}{r}Q\xi_{\kappa^S m_j}. \end{aligned} \tag{2.105}$$

In these equations all angular dependence is contained in the spherical spinors and radial Pauli matrix, which implies the relations

$$\begin{aligned} \sigma_r\xi_{\kappa^S m_j} &= -\xi_{\kappa^L m_j} \\ \sigma_r\xi_{\kappa^L m_j} &= -\xi_{\kappa^S m_j}. \end{aligned} \tag{2.106}$$

From the identity $\sigma_r\xi_{\kappa m_j} = -\xi_{-\kappa m_j}$,[112] it can thus be concluded that $\kappa^S = -\kappa^L$, implying that the small component is opposite in parity compared to the large component. By projecting out the spherical spinors, we can isolate differential equations for the radial wave function

$$-c\left[\frac{1}{r}(\kappa^S+\hbar)-\hbar\frac{\partial}{\partial r}\right]\frac{1}{r}Q=\left[E-V\right]\frac{1}{r}P \tag{2.107}$$
$$c\left[\frac{1}{r}(\kappa^L+\hbar)-\hbar\frac{\partial}{\partial r}\right]\frac{1}{r}P=\left[E-V+2mc^2\right]\frac{1}{r}Q.$$

In case of hydrogenic systems, where the potential is given by $V(r)=-\frac{Ze^2}{4\pi\epsilon_0 r}$, this equation is analytically solvable. The solution of these equations is beyond the scope of this thesis and the reader is referred to refs. [113, Section 3.3] and [114, Chapter 6] for further detail. A problematic feature of these solutions is their singular behaviour at the origin for $|\kappa|=1$. However, this singularity can be classified as a weak singularity, because the wave function can still be normalized. In the calculation of many-electron system, this singularity is avoided by applying other nuclear distributions than the conventional point-charge distribution, for example a Gaussian distribution[115] or the Fermi nuclear model.[116]

2.4 Four-Component Relativistic SCF Methods

2.4.1 Similarities and Differences with Non-Relativistic Theory

Here, the findings from previous sections will be extended to many-electron systems. In a four-component relativistic framework, the Hamiltonian can still be written as the general form in Eqn. (1.45), although the integrals are expressed in terms of four-component orbitals.[117] The one-electron integrals follow straightforwardly from Eqn. (2.81)

$$h_{pq}=\int d^3\boldsymbol{r}\psi_p^\dagger\left[c\boldsymbol{\alpha}\cdot\hat{\boldsymbol{p}}+mc^2\beta'+V\right]\psi_q. \tag{2.108}$$

To derive a two-electron interaction operator, one possible route is to establish the relativistic interaction between two moving classical point charges and quantize this expression. However, already at the classical level, formulating this expression is complicated. I recall that from the finiteness of the speed of light, it follows that the electromagnetic interaction is retarded. The presence of retardation implies that the full history of the point particles needs to be known to find the interaction between them. For this reason, it is not possible express this interaction in closed form, thus requiring us to expand it in orders of the $1/c$. At lowest order, this expansion yields the familiar Coulomb repulsion between electrons (see. Eqn. (1.47)), whereas the next order corresponds to the Breit operator

$$\hat{g}^B(r_{ij})=-\frac{e^2}{8\pi\epsilon_0 c^2 r_{ij}}\left(c\boldsymbol{\alpha}_i\cdot c\boldsymbol{\alpha}_j+\frac{(c\boldsymbol{\alpha}_i\cdot\boldsymbol{r}_{ij})(c\boldsymbol{\alpha}_j\cdot\boldsymbol{r}_{ij})}{r_{ij}^2}\right) \tag{2.109}$$

which captures effects related to magnetic interactions and retardation.[118] The first- and second term in this operator are also referred to as the Gaunt and gauge term, the latter of which depends on the choice of gauge.[119, 120] Here, Coulomb gauge is imposed, whereas the Lorentz gauge, for instance, removes the gauge term. Throughout this thesis, I will neglect such interactions and only consider the Coulomb repulsion between the electrons.

Due to the structural similarities between the relativistic and non-relativistic many-electron Hamiltonian, most electronic structure theories can be carried over the the relativistic domain, albeit with the proper assumptions. Indeed, the Hartree-Fock determinant can be readily generalized to the relativistic domain by defining a Slater determinant consisting of four-component orbitals. A relativistic extension to DFT, however, requires more elaborate theory. To generalize the fundamental theorems of DFT, it is required to invoke the theory of quantum electrodynamics, where the negative energy electrons are converted into positive energy positrons. However, even within this framework, it is difficult to formulate the Hohenberg-Kohn theorems, since a variational procedure of QED is not as well-established as in the non-relativistic regime. However, the variational properties of QED can be postulated by the observation that everyday matter (consisting of electrons, protons, atoms etc.) is stable.[121] Using these results, it can be shown that relativistic DFT is very similar to its non-relativistic counterpart. In principle, relativistic DFT requires functionals that are optimized for relativistic calculations, although in practice, functionals from non-relativistic theory are used, which is justified from a pragmatic point of view.

With the similarities between relativistic and non-relativistic DFT further established, I can now proceed to define the generator of orbital rotations. In the relativistic case, rotations involving negative-energy orbitals require consideration as well. The rotations between negative-energy orbitals do not change the energy, as this quantity is defined in terms of occupied positive-energy solutions. The negative-energy orbitals can thus be thought of as an additional type of virtual orbitals. Therefore, in line with Section 1.3, the relativistic extension of the generator of orbital rotations can be defined as

$$\hat{\kappa} = \sum_{ai} \left[\kappa_{a^+i^+} a^\dagger_{a^+} a_{i^+} - \kappa^*_{a^+i^+} a^\dagger_{i^+} a_{a^+} + \kappa_{i^+a^-} a^\dagger_{i^+} a_{a^-} - \kappa^*_{i^+a^-} a^\dagger_{a^-} a_{i^+} \right]. \tag{2.110}$$

Likewise, when extending this machinery to response theory, it follows that the positive-negative/negative-positive rotations need to be included to fully relax the perturbed state. Moreover, in the context of magnetic interactions, it can even be argued that these rotations correspond to diamagnetic interactions.[122] However, these additional rotations should be treated with care, to avoid variational collapse towards the negative-energy continuum. In fact, it has been shown that the energy should be minimized with respect to the positive-positive rotations and maximized with respect to the positive-negative rotations, thus corresponding to a *minmax* principle.[123]

Alternatively, the relativistic SCF procedure can be understood as an excited state search, which aims to find the lowest positive energy solution on top of the negative-energy solutions. Formally, this method can be solved by projecting out the lower states in each iteration, creating a reduced matrix which is subsequently diagonalized. Although the reduced problem is bounded from below, this bound can fall below the exact eigenvalue, because in the full problem the eigenvalue increases due to the interlace theorem. This feature of the Dirac equation is conventionally referred to as *prolapse*.[124] In practice, however, explicit projectors are seldom used, because the same effect can be achieved by discarding the negative-energy solutions and only use positive-energy solutions to construct the Fock matrix in accordance with the *aufbau* principle. This procedure is facilitated by the large energy gap of $2mc^2$ between the positive- and negative-energy solutions, which makes it easy to distinguish either type of solutions at every step of the SCF cycle.

In the special case of atomic symmetry, the relativistic analogue of Eqn. (1.66) can be solved using grid-based methods. Here, the orbitals assume the general structure of Eqn. (2.100), where the angular part is fully known from symmetry, whereas the radial functions are to be determined on the grid. Furthermore, the pseudo-eigenvalue equation assumes the general form of Eqn. (2.107), with the averaged two-electron interaction from HF theory, or the exchange-correlation potential from DFT included in the potential.[113] This procedure will be used in Section 4.3 to generate reference data effectively corresponding to the complete basis set limit.

2.4.2 Kinetic Balance

We proceed to expand the large- and small component in a set of functions $\{\chi_i(\boldsymbol{r})\}$

$$\psi^X(\boldsymbol{r}) = \sum_i c_i^X \chi_i(\boldsymbol{r}); \quad X = L, S, \tag{2.111}$$

and find the coefficients of by following the *minmax* procedure. However, the first basis set calculations based on the Dirac equation were met with problems associated to the lower bounds of the energy.[125] For instance, basis set calculations of the relativistic hydrogen atom fell much below its corresponding value from a non-relativistic framework.[126] These problems are rooted in the basis set choice, which was essentially the same for the large- and small component functions. To better understand the shortcomings of our basis set expansion, I will write the expansion in a more general form

$$\psi(\boldsymbol{r}) = \begin{pmatrix} \chi^L & 0 \\ 0 & \chi^S \end{pmatrix} \begin{pmatrix} \boldsymbol{c}^L \\ \boldsymbol{c}^S \end{pmatrix}; \quad \chi_i^L = \begin{pmatrix} \chi_i^{L\alpha} \\ \chi_i^{L\beta} \end{pmatrix}; \quad \chi_i^S = \begin{pmatrix} \chi_i^{S\alpha} \\ \chi_i^{S\beta} \end{pmatrix}, \tag{2.112}$$

where the basis functions of the large- and small component are allowed to be expanded in terms of different functions. Expressed in this basis, the Dirac Hamiltonian assumes the form

$$H = \begin{pmatrix} V^{LL} & c\pi^{LS} \\ c\pi^{SL} & V^{SS} - 2mc^2 S^{SS} \end{pmatrix}, \tag{2.113}$$

which is constructed from the matrices

$$\begin{aligned} V_{ij}^{XX} &= \int d^3\boldsymbol{r}\chi_i^{X\dagger} V \chi_j^X; \quad X = L, S \\ \pi_{ij}^{LS} &= \int d^3\boldsymbol{r}\chi_i^{L\dagger}\boldsymbol{\sigma}\cdot\hat{\boldsymbol{p}}\chi_j^S \\ S_{ij}^{XX} &= \int d^3\boldsymbol{r}\chi_i^{X\dagger}\chi_j^X. \end{aligned} \tag{2.114}$$

In matrix form, the eigenvalue problem thus reads

$$H\begin{pmatrix} \boldsymbol{c}^L \\ \boldsymbol{c}^S \end{pmatrix} = E\begin{pmatrix} S^{LL} & 0 \\ 0 & S^{SS} \end{pmatrix}\begin{pmatrix} \boldsymbol{c}^L \\ \boldsymbol{c}^S \end{pmatrix}, \tag{2.115}$$

which can be decoupled to yield a similar relation as Eqn. (B.3)

$$T^{LL} = \frac{1}{2m_e}\pi^{LS}\left[S^{SS} + \frac{ES^{SS} - V^{SS}}{2mc^2}\right]^{-1}\pi^{SL} \approx \frac{1}{2m_e}\pi^{LS}\pi^{SL}; \quad c \ll 1. \tag{2.116}$$

Note that in the non-relativistic limit, above expression should reduce to the non-relativistic kinetic energy. Let us closer inspect the expression on the right-hand-side of (2.116). In the complete basis set limit, this term can indeed be related to the non-relativistic kinetic energy

$$\begin{aligned} \frac{1}{2m_e}\left[\pi^{LS}\pi^{SL}\right]_{ik} &= \frac{1}{2m_e}\sum_j \int d^3\boldsymbol{r}\int d^3\boldsymbol{r}'\chi_i^{L\dagger}(\boldsymbol{r})\boldsymbol{\sigma}\cdot\hat{\boldsymbol{p}}\chi_j^S(\boldsymbol{r})\chi_j^{S\dagger}(\boldsymbol{r}')\boldsymbol{\sigma}\cdot\hat{\boldsymbol{p}}'\chi_k^L(\boldsymbol{r}') \\ &= \frac{1}{2m_e}\int d^3\boldsymbol{r}\int d^3\boldsymbol{r}'\chi_i^{L\dagger}(\boldsymbol{r})\boldsymbol{\sigma}\cdot\hat{\boldsymbol{p}}\delta(\boldsymbol{r}-\boldsymbol{r}')\boldsymbol{\sigma}\cdot\hat{\boldsymbol{p}}'\chi_k^L(\boldsymbol{r}') \\ &= \frac{1}{2m_e}\int d^3\boldsymbol{r}\chi_i^{L\dagger}(\boldsymbol{r})(\boldsymbol{\sigma}\cdot\hat{\boldsymbol{p}})(\boldsymbol{\sigma}\cdot\hat{\boldsymbol{p}})\chi_k^L(\boldsymbol{r}) \\ &= \frac{1}{2m_e}\int d^3\boldsymbol{r}\chi_i^{L\dagger}(\boldsymbol{r})\hat{p}^2\chi_k^L(\boldsymbol{r}), \end{aligned} \tag{2.117}$$

implying that the non-relativistic limit can only yield the correct result if a complete basis set is used. In practice, however, a complete basis set amounts to an infinite set of functions, which is not feasible in any computational scheme. Let us now suppose that our basis set is not complete anymore, yielding the expression below

$$\begin{aligned} \frac{1}{2m_e}\left[\pi^{LS}\pi^{SL}\right]_{ik} &= \frac{1}{2m_e}\int d^3\boldsymbol{r}\chi_i^{L\dagger}(\boldsymbol{r})\hat{p}^2\chi_k^L(\boldsymbol{r}) \\ &\quad - \frac{1}{2m_e}\sum_j \int d^3\boldsymbol{r}\int d^3\boldsymbol{r}'\chi_i^{L\dagger}(\boldsymbol{r})\boldsymbol{\sigma}\cdot\hat{\boldsymbol{p}}\chi_j^C(\boldsymbol{r})\chi_j^{C\dagger}(\boldsymbol{r}')\boldsymbol{\sigma}\cdot\hat{\boldsymbol{p}}'\chi_k^L(\boldsymbol{r}'). \end{aligned} \tag{2.118}$$

Here the functions $\{\chi_i^C\}$ form the orthogonal complement of $\{\chi_i^S\}$ whose union $\{\chi_i^C\}\cup\{\chi_i^S\}$ is complete. If we express the small component functions in the basis[127, 128, 129, 130]

$$\chi_i^S = \boldsymbol{\sigma}\cdot\hat{\boldsymbol{p}}\chi_i^L, \tag{2.119}$$

the second term in Eqn. (2.118) reduces to zero by orthogonality

$$\begin{aligned}&\frac{1}{2m_e}\sum_j\int d^3\boldsymbol{r}\int d^3\boldsymbol{r}'\chi_i^{L\dagger}(\boldsymbol{r})\boldsymbol{\sigma}\cdot\hat{\boldsymbol{p}}\chi_j^C(\boldsymbol{r})\chi_j^{C\dagger}(\boldsymbol{r}')\boldsymbol{\sigma}\cdot\hat{\boldsymbol{p}}'\chi_k^L(\boldsymbol{r}') \qquad (2.120)\\ &\qquad = \frac{1}{2m_e}\sum_j\int d^3\boldsymbol{r}\int d^3\boldsymbol{r}'\chi_i^{S\dagger}(\boldsymbol{r})\chi_j^C(\boldsymbol{r})\chi_j^{C\dagger}(\boldsymbol{r}')\chi_k^S(\boldsymbol{r}') = 0.\end{aligned}$$

The choice of small component space in Eqn. (2.119), referred to as restricted kinetic balance, thus restores the deficit in the kinetic energy.[131] As implied by Eqn. (2.119), the condition of restricted kinetic balance requires a two-component basis. Expressed in a scalar basis, Eqn. (2.119) translates to the weaker condition of unrestricted kinetic balance $\phi_i^{Sx} = \partial_j\phi_i^{Lx};\quad x = \alpha,\beta$, which has the undesirable feature of introducing spurious solutions. It is possible, however, to combine restricted kinetic balance with a scalar basis, but this requires an alternative scheme based on the so-called modified Dirac equation, which is the preferred method in this thesis. However, I will not delve into further details, because the aim of this section is to outline the main idea of kinetic balance. The interested reader is referred to refs. 37, 132. Regardless of the specifics, the kinetic balance procedure allows basis set calculations to be performed at the four-component relativistic level of theory, especially providing a drastic improvement for heavy-element compounds.

2.4.3 Symmetry Reductions from Time-Reversal Symmetry

However, these improvements in accuracy are met with elevated computational costs, since the wave function consists of four components, contrary to the one or two components appearing in non-relativistic calculations. Several approximations to the Dirac Hamiltonian are known that aim to reduce the amount of components, such as the exact two-component relativistic Hamiltonian (X2C),[133, 134, 135, 136] the zeroth-order regular approximation (ZORA)[137, 138, 139] and the Douglas-Kroll-Hess (DKH)[140, 141, 142] Hamiltonians. However, the discussion of these Hamiltonians is beyond the scope of this thesis and the reader is referred to ref.117 for more details. Instead of approximating the Dirac equation, I will discuss how the computational costs can be reduced using the time-reversal symmetry of the Dirac equation.

Let us first consider some general features of this symmetry. I will define $\hat{\mathcal{K}}$ as the time-reversal operator, which is anti-linear and anti-unitary

$$\begin{aligned}\hat{\mathcal{K}}(a\psi_1 + b\psi_2) &= a^*\hat{\mathcal{K}}\psi_1 + b^*\hat{\mathcal{K}}\psi_2 \qquad (2.121)\\ \langle\hat{\mathcal{K}}\psi_1|\hat{\mathcal{K}}\psi_2\rangle &= \langle\psi_1|\psi_2\rangle^* = \hat{\mathcal{K}}\langle\psi_1|\psi_2\rangle.\end{aligned}$$

In general, any anti-unitary operator can be expressed as

$$\hat{\mathcal{K}} = \hat{U}_T \hat{\mathcal{K}}_0, \tag{2.122}$$

where $\hat{\mathcal{K}}_0$ is the complex conjugation operator introduced in Eqn. (2.87), and $\hat{U}_T$ a unitary operator, whose representation depends on the form of the wave function, i.e. two- or four-component (see Section B.3 for an explicit representation in the four component case). Systems are time-reversal symmetric, if the Hamiltonian commutes with the time-reversal operator $\left[\hat{\mathcal{K}}, \hat{H}\right] = 0$, which is generally the case for systems with an even amount of electrons in the absence of an external magnetic field. For such systems, Kramers theorem states that the action of the time-reversal operator defines pairs of functions (Kramers partners)[143]

$$\hat{\mathcal{K}}\psi = \bar{\psi}; \quad \hat{\mathcal{K}}\bar{\psi} = -\psi, \tag{2.123}$$

that are degenerate

$$E_\psi = \langle\psi|\hat{H}|\psi\rangle = \langle\psi|\hat{\mathcal{K}}^{-1}\hat{\mathcal{K}}\hat{H}\hat{\mathcal{K}}^{-1}\hat{\mathcal{K}}|\psi\rangle = \langle\bar{\psi}|\hat{H}|\bar{\psi}\rangle = E_{\bar{\psi}}. \tag{2.124}$$

Kramers partners are not exclusive to relativistic formulations, since the two possible spin functions are related by time-reversal

$$\hat{\mathcal{K}}|\alpha\rangle = |\beta\rangle; \quad \hat{\mathcal{K}}|\alpha\rangle = -|\beta\rangle, \tag{2.125}$$

thus forming a pair of Kramers partners. However, it should be kept in mind that spin symmetry is much more restrictive, because for any spin-free operator, $\hat{O}$, the matrix elements between functions of opposite spin are necessarily zero

$$\begin{gathered}\langle\phi_p^\alpha|\hat{O}|\phi_q^\beta\rangle = 0; \quad \forall p, q \\ |\phi_p^\alpha\rangle = \chi_p(\boldsymbol{r})|\alpha\rangle; \quad |\phi_q^\beta\rangle = \chi_q(\boldsymbol{r})|\beta\rangle\end{gathered} \tag{2.126}$$

implying a block-diagonal structure of the matrix representation

$$\Omega = \begin{pmatrix} \Omega^{\alpha\alpha} & 0 \\ 0 & \Omega^{\beta\beta} \end{pmatrix} \begin{cases} \Omega_{pq}^{\alpha\alpha} = \langle\phi_p^\alpha|\hat{\Omega}|\phi_q^\alpha\rangle \\ \Omega_{pq}^{\beta\beta} = \langle\phi_p^\beta|\hat{\Omega}|\phi_q^\beta\rangle. \end{cases} . \tag{2.127}$$

Furthermore, from the structure of the spin-orbitals, it can be shown that these two blocks are identical

$$\Omega_{pq}^{\alpha\alpha} = \int d^3\boldsymbol{r}\chi_p^*\hat{\Omega}\chi_q = \Omega_{pq}^{\beta\beta}. \tag{2.128}$$

Therefore, only one sub-matrix is needed in this simple example, thus reducing the computational cost roughly by a factor of four.

For general Kramers partners, however, these reductions are not as impressive. Let us construct the matrix representation of a general time-reversal symmetric operator, i.e. $\hat{\Omega} = \hat{\mathcal{K}}^{-1}\hat{\Omega}\hat{\mathcal{K}}$, in a basis of Kramers parters

$$\Omega = \begin{pmatrix} \langle\psi_p|\hat{\Omega}|\psi_q\rangle & \langle\psi_p|\hat{\Omega}|\bar{\psi}_q\rangle \\ \langle\bar{\psi}_p|\hat{\Omega}|\psi_q\rangle & \langle\bar{\psi}_p|\hat{\Omega}|\bar{\psi}_q\rangle \end{pmatrix} \tag{2.129}$$

Here, the off-diagonal blocks only vanish if the two functions in the matrix element are Kramers partners

$$\langle\bar{\psi}_p|\hat{\Omega}|\psi_p\rangle = \langle\psi_p|\hat{\Omega}|\bar{\psi}_p\rangle = 0. \tag{2.130}$$

However, some symmetry gains can be achieved by relating the off-diagonal and on-diagonal blocks through time-reversal

$$\begin{aligned}\hat{\mathcal{K}}\langle\psi_p|\hat{\Omega}|\psi_q\rangle &= \langle\hat{\mathcal{K}}\psi_p|\hat{\mathcal{K}}\hat{\Omega}\hat{\mathcal{K}}^{-1}|\hat{\mathcal{K}}\psi_q\rangle = \langle\bar{\psi}_p|\hat{\Omega}|\bar{\psi}_q\rangle = \langle\psi_p|\hat{\Omega}|\psi_q\rangle^* \\ \hat{\mathcal{K}}\langle\bar{\psi}_p|\hat{\Omega}|\psi_q\rangle &= \langle\hat{\mathcal{K}}\bar{\psi}_p|\hat{\mathcal{K}}\hat{\Omega}\hat{\mathcal{K}}^{-1}|\hat{\mathcal{K}}\psi_q\rangle = -\langle\psi_p|\hat{\Omega}|\bar{\psi}_q\rangle = \langle\bar{\psi}_p|\hat{\Omega}|\psi_q\rangle^*,\end{aligned} \tag{2.131}$$

yielding the expression

$$\Omega = \begin{pmatrix} A & B \\ -B^* & A^* \end{pmatrix} \begin{cases} A_{pq} = \langle\psi_p|\hat{\Omega}|\psi_q\rangle \\ B_{pq} = \langle\psi_p|\hat{\Omega}|\bar{\psi}_q\rangle. \end{cases} \tag{2.132}$$

In this expression, the blocks A and B are unique, suggesting that only these two blocks need to be stored for calculations. Throughout each SCF cycle, it is thus desirable to preserve the structure in Eqn. (2.132). Maintaining this structure can either be achieved by expressing the generator of orbital rotations in terms of Kramers replacement operators,[144] or by employing the quaternion scheme.[145] In this work, the quaternion scheme is preferred, because it simultaneously allows for the efficient treatment of point-group symmetry. In Appendix B.3 the quaternion scheme is discussed more thoroughly.

Moreover, the treatment of transition moments benefits heavily from the structure provided by time-reversal symmetry. If our interaction operator is time-reversal symmetric, it follows that the property gradient assumes the same form as Eqn.(2.132). Operators that are anti-symmetric with respect to time-reversal, $\hat{T}_A$, can be made time-reversal symmetric by extracting an imaginary phase, i.e. $\hat{T}_A = -i(i\hat{T}_A) = -i\hat{T}_S$, although the hermiticity of the operator is now inverted. By exploiting both the structure provided by time-reversal and hermiticity, it can be shown that the property gradient assumes the structure[146]

$$\boldsymbol{E}_\Omega = \begin{pmatrix} \boldsymbol{C} \\ \boldsymbol{D} \\ -\boldsymbol{D}^* \\ \boldsymbol{C}^* \\ h\boldsymbol{C}^* \\ h\boldsymbol{D}^* \\ -h\boldsymbol{D} \\ h\boldsymbol{C} \end{pmatrix} \begin{cases} C_{ia} = \langle\psi_i|\hat{\Omega}|\psi_a\rangle \\ D_{ia} = \langle\psi_i|\hat{\Omega}|\bar{\psi}_a\rangle. \end{cases} . \tag{2.133}$$

where h is $(-1), 1$ for (anti-)Hermitian operators. From the structure of the response equations, which generally preserve time-reversal symmetry, it follows that the solution vectors can be expressed in a similar form[146]

$$\boldsymbol{X}_n = \begin{pmatrix} \boldsymbol{V}_n \\ \boldsymbol{W}_n \\ -\boldsymbol{W}_n^* \\ \boldsymbol{V}_n^* \\ h\boldsymbol{V}_n^* \\ h\boldsymbol{W}_n^* \\ -h\boldsymbol{W}_n \\ h\boldsymbol{V}_n \end{pmatrix} \tag{2.134}$$

$$V_{n;ai} = Z_{n;ai} + hY_{n;ai}; \quad W_{n;ai} = Z_{n;a\bar{i}} + hY_{n;a\bar{i}} \tag{2.135}$$

Transition moments calculated from such vectors thus read

$$\boldsymbol{X}_n^\dagger \boldsymbol{E}_\Omega = \begin{cases} = 4Re[\boldsymbol{C}^\dagger \boldsymbol{V}_n] + 4Re[\boldsymbol{D}^\dagger \boldsymbol{W}_n] & \text{if } h_E h_X = 1 \\ = 0 & \text{if } h_E h_X = -1 \end{cases}, \tag{2.136}$$

which vanishes for opposite hermiticity of both vectors and gives rise to real transition moments for the same hermiticity.

Using the tools described in this chapter, we are in a position to generalize all findings from Chapter 1 to the relativistic domain, thus enabling us to properly describe relativistic effects in our simulations of X-ray spectroscopy. However, there is still much room left for improvements in our model. In particular, based on the large discrepancy between the wave length and the extent of the system, I have applied the dipole approximation. However, in the X-ray domain, this approximation might not hold anymore. Therefore, in the following chapter, these assumptions will be challenged.

Chapter 3

Light–Matter Interactions Beyond the Dipole Approximation

3.1 Introduction

We have come a long way since we started our discussion about the basic principles of SCF linear-response theory, followed by relativistic quantum chemistry. With the theoretical tools of the preceding chapters in place, we are almost ready to discuss some practical examples. However, before proceeding I need to address one key assumption made in Chapter 1. I recall that in the UV-Vis regime, the spatial extent of the target molecule is typically much smaller than the wave length of light. For that reason, it is justified to apply the dipole approximation, according to which the electromagnetic fields can be approximated by a uniform field. However, in the X-ray regime, this approximation comes into question because the wave length is of comparable size relative to the molecule. Figure 3.1 depicts a similar situation as in Figure 1.1, although in this case, the benzene molecule is interacting with X-rays, having a much shorter wavelength ($\lambda = 2.6$ nm).

Considering that the dipole approximation essentially boils down to the first order multipole expansion of the electromagnetic fields, there are generally two methods to correct for the shortcomings of this approximation. The first and most straightforward method avoids a multipole expansion altogether and bases its interaction on the exact electromagnetic fields, thus retaining their sinusoidal character in the interaction operator. Using the full interaction operator, all non-dipolar effects are exactly included, although the formalism is somewhat more complicated due to the frequency dependence of this operator.

Alternatively, the multipole expansion can be truncated beyond first order, thus taking higher-order multipole moments into account. Multipole moments can be understood as idealizations of charge- and current distributions. For example, the electric-dipole moment is a vectorial quantity that gives the overall direction in which the charge distribution is polarized. The electric-quadrupole moment, on the other hand, describes the overall broadness of a charge distribution, akin to the variance of statistical distributions. Further inhomogeneities of the distributions are described by higher-order multipole moments, which, in Cartesian form, are defined as

$$Q^{[n]}_{j_1\cdots j_n} = \int d^3\boldsymbol{r}\, r_{j_1} r_{j_2}\cdots r_{j_n}\,\rho(\boldsymbol{r},t); \quad m^{[n]}_{j_1\cdots j_{n-1};i} = \frac{n}{n+1}\int d^3\boldsymbol{r}\, r_{j_1} r_{j_2}\cdots r_{j_{n-1}}\big(\boldsymbol{r}\times\boldsymbol{j}(\boldsymbol{r},t)\big)_i. \tag{3.1}$$

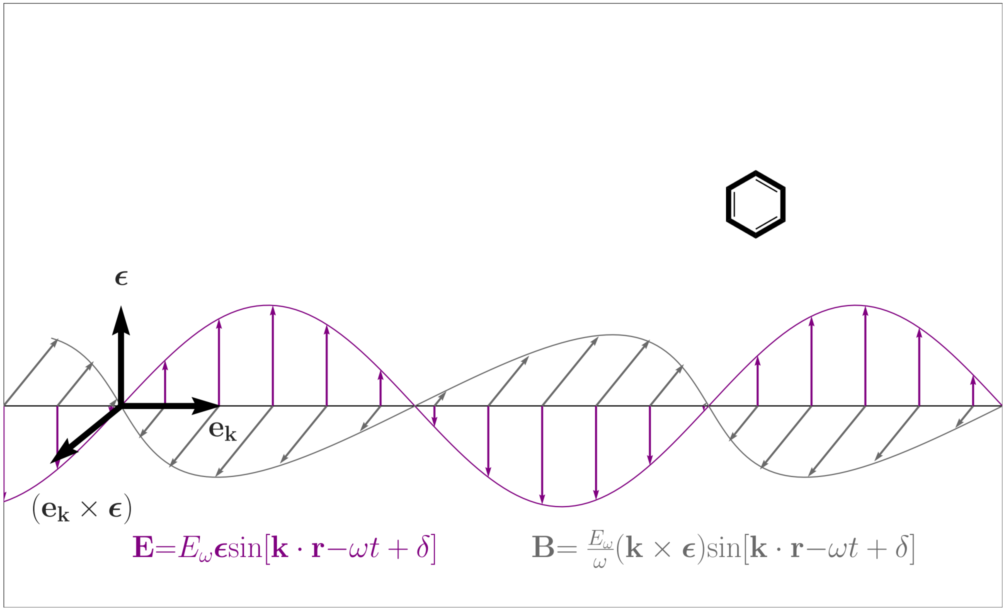

Figure 3.1: Schematic representation of benzene molecule interacting with X-rays ($\lambda = 2.6$ nm), consisting of an electric (violet) and magnetic (grey) component. Note that in this figure, the wave length is comparable in size to the benzene molecule, suggesting that it is affected by the curvature of the light. The mathematical expressions describing the electromagnetic fields are given at the bottom of the box. The propagation- and polarization direction are described by the unit vectors $\boldsymbol{e}_k$ and $\boldsymbol{\epsilon}$, respectively, with the latter being defined by the relation $\boldsymbol{e}_k = \frac{c}{\omega}\boldsymbol{k}$.

By including the contributions of all multipole moments, the charge- or current distributions can be recovered exactly. However, in practice, this is often not necessary, because typically the most dominant contributions stem from the lowest-order multipole moments. Complicated charge- or current distributions can thus be simplified by only considering these dominant contributions. This approach turns out to be particularly useful when describing intermolecular interactions.[147] In the current context, however, I will use this machinery to approximate light–matter interactions.

Using either the full- or truncated light–matter interaction, I will describe two types of spectroscopy: near-edge X-ray absorption fine structure (NEXAFS) and X-ray natural circular dichroism (XNCD). NEXAFS can straightforwardly be calculated from the absorption cross-section derived from linearly polarized light. The calculation of XNCD, however, is slightly more complicated, as it involves the difference between the absorption cross-section of left- and right-handed circularly polarized light

$$\Delta\sigma(\omega) = \sigma_L(\omega) - \sigma_R(\omega). \tag{3.2}$$

From considerations of parity inversion, it can be argued that the circular dichroism of isotropic samples, e.g. gases and solutions, is non-zero only for chiral molecules (see Section C.1).[148] In fact, for enantiomers, the circular dichroism is equal but opposite, thus making circular dichroism one of the few spectroscopic techniques to distinguish enantiomers. Similar effects can be achieved for non-chiral systems by either imposing anisotropic conditions,[149] such as in crystals, or by applying an additional external magnetic field. However, the latter suggestion creates a different type of interaction, also referred to as X-ray magnetic circular dichroism.[34]

Leaning on the results from the previous chapter, all derivations will be performed in a four-component relativistic framework. These derivations are mainly based on articles with my co-authorship (see. refs. 1, 2, 3 for more detail). Alternatively, it is also possible to derive a similar formalism in a non-relativistic framework, although it is more complicated, due to the many terms required to describe the light–matter interaction. Therefore, the non-relativistic formalism will not be further pursued here. For more details see refs. 31, 32, 150. Furthermore, unless stated otherwise, I will use notation from exact-state theory throughout my derivations, since the generalization to SCF theory follows straightforwardly from the procedure outlined in Section 1.3.3.

3.2 General Expressions for Monochromatic Light

To derive interaction operators that correct for the shortcomings of the dipole approximation, we have to start from the solutions of the homogeneous Maxwell equations. I would like to emphasize the versatility of these equations. On one hand they are indispensable in the formulation of relativistic theory, whereas in current context, they serve as a starting point to derive more accurate light–matter interaction operators. The most general expression for monochromatic light is given below

$$\begin{aligned} \boldsymbol{E}(\boldsymbol{r},t) &= \mathcal{E}_1\boldsymbol{\epsilon}_1\sin(\boldsymbol{k}\cdot\boldsymbol{r}-\omega t+\delta_1)+\mathcal{E}_2\boldsymbol{\epsilon}_2\sin(\boldsymbol{k}\cdot\boldsymbol{r}-\omega t+\delta_2); \quad \mathcal{E}_1=\mathcal{E}\cos\theta; \quad \mathcal{E}_2=\mathcal{E}\sin\theta \\ \boldsymbol{B}(\boldsymbol{r},t) &= \frac{\mathcal{E}_1}{c}\boldsymbol{\epsilon}_2\sin(\boldsymbol{k}\cdot\boldsymbol{r}-\omega t+\delta_1)-\frac{\mathcal{E}_2}{c}\boldsymbol{\epsilon}_1\sin(\boldsymbol{k}\cdot\boldsymbol{r}-\omega t+\delta_2); \quad \mathcal{E}=\sqrt{\mathcal{E}_1^2+\mathcal{E}_2^2}, \end{aligned} \tag{3.3}$$

where the fields now have two sinusoidal components, each of which having a distinct phase shift, δ_1 and δ_2, amplitude, $\mathcal{E}_1$ and $\mathcal{E}_2$ and polarization direction, $\boldsymbol{\epsilon}_1$ and $\boldsymbol{\epsilon}_2$. The relative size of the amplitudes can be parametrized by the angle θ. Furthermore, the polarization vectors span a right-handed coordinate system together with the wave vector, i.e. $\boldsymbol{\epsilon}_1\times\boldsymbol{\epsilon}_2=\frac{c}{\omega}\boldsymbol{k}=\boldsymbol{e}_k$. In passing, I note that due to the linear nature of the homogeneous Maxwell equations, any linear combination of two or more solutions is itself also a solution, allowing the possibility of complicated fields. The interaction of non-standard fields with molecules has been explored in ref. 151. Here, I will restrict myself to the more simple monochromatic case.

By imposing that the phases differ by an integer multiple of π, i.e. $\delta_2=\delta_1+m\pi; \quad m\in\mathbb{Z}$, we obtain expressions for linearly polarized light

$$\boldsymbol{E}(\boldsymbol{r},t)=\mathcal{E}\boldsymbol{\epsilon}\sin(\boldsymbol{k}\cdot\boldsymbol{r}-\omega t+\delta); \quad \boldsymbol{B}(\boldsymbol{r},t)=\frac{\mathcal{E}}{\omega}\boldsymbol{k}\times\boldsymbol{\epsilon}\sin(\boldsymbol{k}\cdot\boldsymbol{r}-\omega t+\delta), \tag{3.4}$$

in which appears the polarization vector

$$\boldsymbol{\epsilon}=\cos\theta\boldsymbol{\epsilon}_1+(-1)^m\sin\theta\boldsymbol{\epsilon}_2. \tag{3.5}$$

Therefore, the parameter θ defines the polarization direction. Figure 3.2 shows a graphical representation of linearly polarized light.

Circularly polarized light can be obtained by setting $\theta=\frac{1}{4}\pi$ (which implies that $|\varepsilon_1|=|\varepsilon_2|=\frac{1}{\sqrt{2}}\varepsilon$), while simultaneously imposing that the difference between the phases is a half-integer multiple of π, i.e. $\delta_2=\delta_1+\frac{1}{2}\pi+m\pi; \quad m\in\mathbb{Z}$

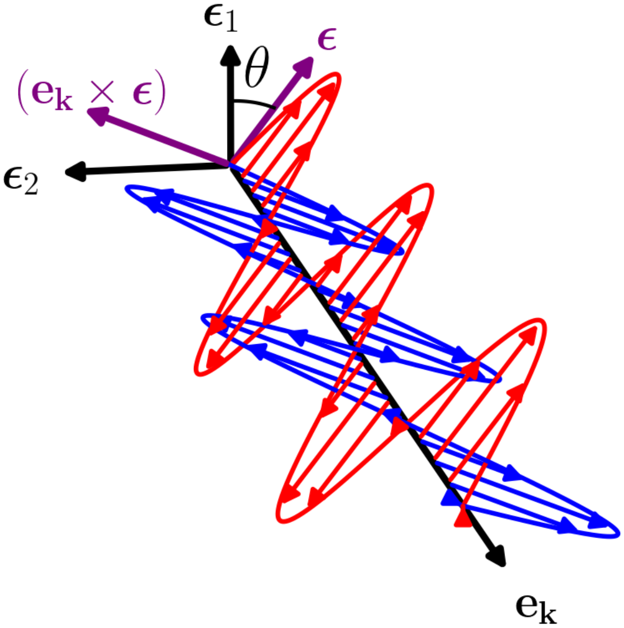

Figure 3.2: Snapshot of linearly polarized light traced out over space, in terms of its electric (red) and magnetic (blue) component, at an angle θ.

$$\begin{aligned}\boldsymbol{E}(\boldsymbol{r},t) &= \frac{1}{\sqrt{2}}\mathcal{E}\boldsymbol{\epsilon}_1 \sin(\boldsymbol{k}\cdot\boldsymbol{r} - \omega t + \delta) + (-1)^m \frac{1}{\sqrt{2}}\mathcal{E}\boldsymbol{\epsilon}_2 \cos(\boldsymbol{k}\cdot\boldsymbol{r} - \omega t + \delta) \\ \boldsymbol{B}(\boldsymbol{r},t) &= \frac{\mathcal{E}}{c\sqrt{2}}\boldsymbol{\epsilon}_2 \sin(\boldsymbol{k}\cdot\boldsymbol{r} - \omega t + \delta) - (-1)^m \frac{\mathcal{E}}{c\sqrt{2}}\boldsymbol{\epsilon}_1 \cos(\boldsymbol{k}\cdot\boldsymbol{r} - \omega t + \delta).\end{aligned} \tag{3.6}$$

When observed against its propagation direction, the polarization vector traces a circle, hence its name. Because of this, circularly polarized light is generally shaped as a helix (see Figure 3.2). Therefore, this type of light is chiral, which implies that it cannot be superimposed onto its mirror image. Consequently, a distinction has to be made between right- and left-handed circularly polarized light. According to the IUPAC convention, the handedness is defined by the direction of rotation of the electric field vector at $-\omega t + \delta = 0$ against the propagation direction.[152] Accordingly, circularly polarized light is right-handed if the vector rotates anti-clockwise and *vice versa*. It turns out that the integer m determines the handedness: even for left-handedness and odd for right-handedness.

Besides its polarization, another important feature of electromagnetic radiation is its intensity, which can be calculated by time-averaging the magnitude of the Poynting vector over a full oscillation

$$I = \langle S \rangle_T; \quad \boldsymbol{S} = \frac{1}{\mu_0}\boldsymbol{E} \times \boldsymbol{B}. \tag{3.7}$$

The Poynting vector expresses the energy transfer that is carried by the fields. By inserting the general definition of monochromatic light into this vector, we obtain

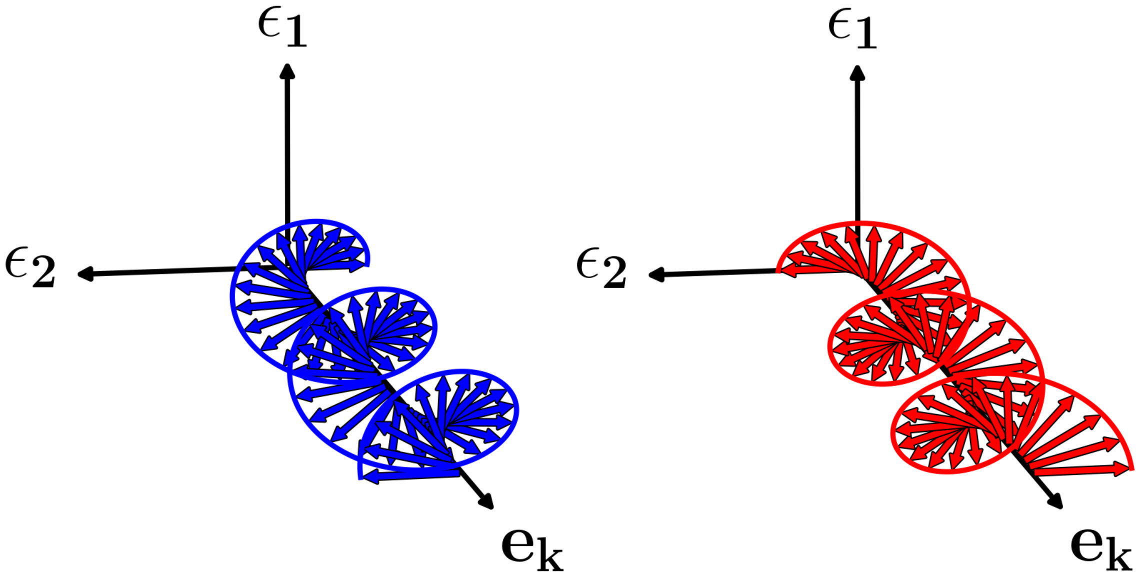

(a) Right handed circularly polarized light *(b) Left handed circularly polarized light*

Figure 3.3: Electric component of right- (m odd) and left handed (m even) circularly polarized light, traced out over space at a fixed position and phase ($t = 0$ and $\delta = 0$).

$$\boldsymbol{S} = \frac{\mathcal{E}_1^2}{c\mu_0}\boldsymbol{e}_k \sin^2(\boldsymbol{k}\cdot\boldsymbol{r} - \omega t + \delta_1) + \frac{\mathcal{E}_2^2}{c\mu_0}\boldsymbol{e}_k \sin^2(\boldsymbol{k}\cdot\boldsymbol{r} - \omega t + \delta_2), \tag{3.8}$$

which, upon time-averaging, yields the following expression for the intensity

$$I = \frac{1}{T}\int_0^T dtS = \frac{1}{2}c\epsilon_0\mathcal{E}^2, \tag{3.9}$$

thus reflecting that the intensity is independent of the polarization type.

3.3 Full Semi-Classical Light–Matter Interaction

To derive an interaction operator based on these fields, we first have to convert them to potentials and then couple these potentials to the Hamiltonian using minimal substitution. As explained in Section 2.2.3, a Helmholtz decomposition should be applied to convert the fields from Eqn. (3.3) into potentials. I recall that the Helmholtz theorem holds for fields that go to zero faster than $\frac{1}{r^2}$, which is clearly not the case for the sinusoidal fields in Eqn. (3.3). However, in this case, a weaker condition applies, stating that any *differentiable* vector field can be decomposed in terms of a solenoidal and irrotational part, although these two components are not described in terms of $D(\boldsymbol{r})$ and $\boldsymbol{C}(\boldsymbol{r})$ (Eqn. (2.38)).[40, Appendix B] As outlined in Section 2.2.3, potentials are defined up to a gauge transformation, suggesting that we have to impose a gauge condition to construct our potentials. Here, I will impose Coulomb gauge, which implies that the vector potential is purely solenoidal. Furthermore, by virtue of the first and third homogeneous Maxwell equation, i.e. $\boldsymbol{\nabla}\cdot\boldsymbol{E} = 0$ and $\boldsymbol{\nabla}\cdot\boldsymbol{B} = 0$, the fields are purely solenoidal as well. It thus follows that they can be expressed as

$$\boldsymbol{E} = -\frac{\partial \boldsymbol{A}}{\partial t}; \quad \boldsymbol{B} = \boldsymbol{\nabla} \times \boldsymbol{A}, \tag{3.10}$$

where the scalar potential term, $\boldsymbol{\nabla}\phi$, necessarily vanishes, because it is purely irrotational by construction. Therefore, the scalar potential can assume any constant value, thus implying that we can set it to zero.

From comparison of Eqn.(3.10) and Eqn.(3.3) it follows that the potentials in the Coulomb gauge assume the form

$$\boldsymbol{A}(\boldsymbol{r},t) = -\frac{\mathcal{E}_1}{\omega}\boldsymbol{\epsilon}_1 \cos(\boldsymbol{k}\cdot\boldsymbol{r} - \omega t + \delta_1) - \frac{\mathcal{E}_2}{\omega}\boldsymbol{\epsilon}_2 \cos(\boldsymbol{k}\cdot\boldsymbol{r} - \omega t + \delta_2); \quad \phi(\boldsymbol{r},t) = 0. \tag{3.11}$$

By inserting these potentials into the Dirac Hamiltonian, the following interaction operator can be derived

$$\hat{V}(t) = -\frac{e}{\omega}\mathcal{E}_1(c\boldsymbol{\alpha}\cdot\boldsymbol{\epsilon}_1)\cos(\boldsymbol{k}\cdot\boldsymbol{r} - \omega t + \delta_1) - \frac{e}{\omega}\mathcal{E}_2(c\boldsymbol{\alpha}\cdot\boldsymbol{\epsilon}_2)\cos(\boldsymbol{k}\cdot\boldsymbol{r} - \omega t + \delta_2). \tag{3.12}$$

As demonstrated in Section 1.2, the frequency components of this operator

$$\hat{V}(\omega) = -\frac{e\mathcal{E}}{2\omega}(c\boldsymbol{\alpha}\cdot\tilde{\boldsymbol{\epsilon}})e^{i\boldsymbol{k}\cdot\boldsymbol{r}}; \quad \tilde{\boldsymbol{\epsilon}} = \boldsymbol{\epsilon}_1\cos\theta e^{i\delta_1} + \boldsymbol{\epsilon}_2\sin\theta e^{i\delta_2}. \tag{3.13}$$

can be used to find the absorption-cross section

$$\sigma^{full}(\omega) = \frac{2\pi\omega}{\hbar I}|\langle f|\frac{e\mathcal{E}}{2\omega}(c\boldsymbol{\alpha}\cdot\tilde{\boldsymbol{\epsilon}})e^{i\boldsymbol{k}\cdot\boldsymbol{r}}|i\rangle|^2 f(\omega;\omega_{fi},\gamma_{fi}) = \frac{\pi\omega}{\epsilon_0\hbar c}|\langle f|\frac{e}{\omega}(c\boldsymbol{\alpha}\cdot\tilde{\boldsymbol{\epsilon}})e^{i\boldsymbol{k}\cdot\boldsymbol{r}}|i\rangle|^2 f(\omega;\omega_{fi},\gamma_{fi}), \tag{3.14}$$

where in the second equality the field-strength dependency was eliminated by inserting Eqn. (3.9). In practice, however, the dimensionless oscillator strength is preferred over the absorption cross-section. The former can be obtained from the latter by removing the linewidth function and applying the prefactor substitution $\frac{\pi\omega}{\epsilon_0\hbar c} \rightarrow \frac{2m_e\omega}{\hbar e^2}$. The oscillator strength thus reads

$$f^{full}(\omega) = \frac{2m_e\omega}{\hbar e^2}|\langle f|\frac{e}{\omega}(c\boldsymbol{\alpha}\cdot\tilde{\boldsymbol{\epsilon}})e^{i\boldsymbol{k}\cdot\boldsymbol{r}}|i\rangle|^2. \tag{3.15}$$

Therefore, we need to calculate transition moments from the following effective interaction operator

$$\boldsymbol{T}(\omega) = \langle f|\hat{\boldsymbol{T}}(\omega)|i\rangle; \quad \hat{\boldsymbol{T}}(\omega) = \frac{e}{\omega}c\boldsymbol{\alpha}e^{i\boldsymbol{k}\cdot\boldsymbol{r}}. \tag{3.16}$$

However, this operator has neither a well-defined hermiticity, nor is it time-reversal symmetric ($\boldsymbol{\alpha}$ is time-reversal anti-symmetric), thus suggesting that the simplifications described in Section 2.4.3 do not apply. Nonetheless, it is possible to decompose this operator in a Hermitian and anti-Hermitian component through the relation

$$\hat{\boldsymbol{T}}(\omega) = \frac{1}{2}\big(\hat{\boldsymbol{T}} + \hat{\boldsymbol{T}}^\dagger\big) + \frac{1}{2}\big(\hat{\boldsymbol{T}} - \hat{\boldsymbol{T}}^\dagger\big) = \hat{\boldsymbol{T}}_H + \hat{\boldsymbol{T}}_A, \tag{3.17}$$

yielding the following result

$$\begin{aligned}\hat{\boldsymbol{T}}_H &= \frac{e}{\omega}c\boldsymbol{\alpha}\cos(\boldsymbol{k}\cdot\boldsymbol{r}) \\ \hat{\boldsymbol{T}}_A &= \frac{e}{\omega}ic\boldsymbol{\alpha}\sin(\boldsymbol{k}\cdot\boldsymbol{r}).\end{aligned} \tag{3.18}$$

Even though $\hat{\boldsymbol{T}}_A$ has the desirable properties of being time-reversal symmetric and anti-Hermitian, $\hat{\boldsymbol{T}}_H$ is anti-symmetric upon time-reversal. The Hermitian component can be made time-reversal symmetric by extracting an imaginary phase

$$\langle f|\hat{\boldsymbol{T}}_H|i\rangle = -i\langle f|i\hat{\boldsymbol{T}}_H|i\rangle \tag{3.19}$$

and inserting it back at the end of the calculation.

Due to the generality of the polarization vector, Eqn. (3.15) applies both to the absorption of linearly polarized light

$$f^{full}(\omega) = \frac{2m_e\omega}{\hbar e^2}|\boldsymbol{\epsilon}\cdot\boldsymbol{T}(\omega)|^2 = \frac{2m_e\omega}{\hbar e^2}|\boldsymbol{\epsilon}\cdot i\boldsymbol{T}_H(\omega)|^2 + \frac{2m_e\omega}{\hbar e^2}|\boldsymbol{\epsilon}\cdot\boldsymbol{T}_A(\omega)|^2 \tag{3.20}$$

and circularly polarized light

$$f^{full}_{L/R}(\omega) = \frac{2m_e\omega}{\hbar e^2}|\boldsymbol{\epsilon}_{L/R}\cdot\boldsymbol{T}(\omega)|^2; \quad \boldsymbol{\epsilon}_{L/R} = \frac{1}{\sqrt{2}}(\boldsymbol{\epsilon}_1 \pm i\boldsymbol{\epsilon}_2) = \boldsymbol{\epsilon}^*_{R/L}, \tag{3.21}$$

where the polarization vector, $\boldsymbol{\epsilon}$, is defined in Eqn. (3.5). Using the definition of circular dichroism (Eqn. (E.13)), we arrive at the compact expression below

$$\begin{aligned}\Delta f^{full}(\omega) &= \frac{2m_e\omega}{\hbar e^2}\Big\{(\boldsymbol{\epsilon}_L\cdot\boldsymbol{T})(\boldsymbol{\epsilon}_R\cdot\boldsymbol{T}^*) - (\boldsymbol{\epsilon}_L\cdot\boldsymbol{T}^*)(\boldsymbol{\epsilon}_R\cdot\boldsymbol{T})\Big\} \\ &= \frac{2m_e\omega}{\hbar e^2}(\boldsymbol{\epsilon}_L\times\boldsymbol{\epsilon}_R)\cdot(\boldsymbol{T}\times\boldsymbol{T}^*) = -i\frac{2m_e\omega}{\hbar e^2}\boldsymbol{e}_k\cdot(\boldsymbol{T}\times\boldsymbol{T}^*) = \frac{4m_e\omega}{\hbar e^2}\boldsymbol{e}_k\cdot(i\boldsymbol{T}_H\times\boldsymbol{T}_A),\end{aligned} \tag{3.22}$$

which is a relativistic extension of the previously reported result by Hansen and Avery.[153] In the second equality, the identity $(\boldsymbol{a}\times\boldsymbol{b})\cdot(\boldsymbol{c}\times\boldsymbol{d}) = (\boldsymbol{a}\cdot\boldsymbol{c})(\boldsymbol{b}\cdot\boldsymbol{d}) - (\boldsymbol{a}\cdot\boldsymbol{d})(\boldsymbol{b}\cdot\boldsymbol{c})$ has been applied.

I stress again that this operator contains *all* non-dipolar corrections, from order zero to infinity. It can be connected to the electric-dipole approximation by applying the limit $kr \ll 1$

$$\boldsymbol{T}(\omega) = \langle f|\frac{e}{\omega}c\boldsymbol{\alpha}e^{i\boldsymbol{k}\cdot\boldsymbol{r}}|i\rangle \xrightarrow{kr\ll 1} \boldsymbol{\mathcal{Q}}^{[1]} = \langle f|\frac{e}{\omega}c\boldsymbol{\alpha}|i\rangle, \tag{3.23}$$

where $\hat{\boldsymbol{\mathcal{Q}}}^{[1]}$ is the electric-dipole moment operator in the velocity representation. This representation deserves its name due to the velocity interpretation of the Dirac matrices, as prescribed by the Heisenberg equation of motion (Eqn. (2.82)). In addition, this relation can be used to make a connection with the electric-dipole operator in its more conventional form introduced in Eqn. (E.10)

$$\langle f|\frac{e}{\omega}c\alpha_p|i\rangle = -\frac{i}{\hbar}\langle f|\frac{e}{\omega}\big[r_p, \hat{h}_D\big]|i\rangle = -i\langle f|\hat{Q}^{[1]}_p|i\rangle, \tag{3.24}$$

where I have assumed exact-state conditions, i.e. $\hat{H}|n\rangle = E_n|n\rangle$. It is common convention to refer to $\hat{\boldsymbol{\mathcal{Q}}}^{[1]}$ and $\hat{\boldsymbol{Q}}^{[1]}$ as the velocity- and length gauge. However, this nomenclature is rather misleading because it suggests the existence of some special gauge condition, whereas the Coulomb gauge is imposed for the velocity representation and multipolar gauge (see section 3.5) for the length representation. Therefore, I will insist to refer to them as representations. The velocity representation has its non-relativistic analogue, since we have

$$\langle f|\frac{e}{\omega}c\alpha_q|i\rangle \xrightarrow{\lim_{c\to\infty}} \langle f_{nr}|\frac{e}{\omega m_e}\hat{p}_q|i_{nr}\rangle, \tag{3.25}$$

which can be converted to the length representation using an equivalent commutator relation

$$\frac{\hat{p}_q}{m_e} = -\frac{i}{\hbar}\big[r_q, \hat{H}_s\big]. \tag{3.26}$$

Here, the left-hand-side can be identified with the non-relativistic velocity operator, thus further establishing the analogies between relativistic and non-relativistic theory. As a final note, it should be stressed that in its current form, the above conversion only works under exact-state conditions. Its generalization to approximate state-theory requires special considerations, which will be discussed in section 3.6.2.

The electric-dipole moment operator introduces selection rules, because transition moments are only non-vanishing if the integrand contains at least one totally symmetric component. It can thus be concluded that this operator only allows transitions that transform as one of the Cartesian coordinates

$$\begin{aligned} \boldsymbol{Q}^{[1]} &= Q_x^{[1]}\boldsymbol{e}_x \quad (\Gamma_x) \\ &+ Q_y^{[1]}\boldsymbol{e}_y \quad (\Gamma_y) \\ &+ Q_z^{[1]}\boldsymbol{e}_z \quad (\Gamma_z). \end{aligned} \tag{3.27}$$

These limitations, however, do not apply to the full interactions operator. The symmetry content of this operator can be revealed by applying the plane wave expansion

$$e^{i\boldsymbol{k}\cdot\boldsymbol{r}} = 4\pi\sum_{\ell=0}^{\infty}\sum_{m=-\ell}^{\ell} i^{\ell} j_{\ell}(kr) Y_{\ell}^{m}(\boldsymbol{e}_k) Y_{\ell}^{m*}(\boldsymbol{e}_r). \tag{3.28}$$

This expansion contains contributions from all possible symmetries of the full rotation group, since the spherical harmonics can be thought of as position space irreps (irreducible representations) of this group. However, the overall symmetry of the full interaction operator is also influenced by the Dirac matrices, which transform as Cartesian coordinates. Therefore, the symmetries generated from the plane wave expansion need to be combined with the Cartesian symmetry stemming from the Dirac matrices. From this procedure, which is discussed in more detail in Section C.2, it follows that the full interaction contains contributions from all symmetries, except the totally symmetric irrep of the full rotation group. The lack of this symmetry can be understood from the directionality imposed by the Dirac matrices. In lower point groups, which are subgroups of the full rotation group, different irreps may coalesce. In the context of molecular calculations, it proves to be particularly useful to express this operator in terms of the irreps of the D_{2h} group

$$\begin{aligned} e^{\pm i\boldsymbol{k}\cdot\boldsymbol{r}} &= \cos(k_x x)\cos(k_y y)\cos(k_z z) \quad (\Gamma_0) \\ &- \sin(k_x x)\sin(k_y y)\cos(k_z z) \quad (\Gamma_{R_z}) \\ &- \sin(k_x x)\cos(k_y y)\sin(k_z z) \quad (\Gamma_{R_y}) \\ &- \cos(k_x x)\sin(k_y y)\sin(k_z z) \quad (\Gamma_{R_x}) \\ &\mp i\sin(k_x x)\sin(k_y y)\sin(k_z z) \quad (\Gamma_{xyz}) \\ &\pm i\cos(k_x x)\cos(k_y y)\sin(k_z z) \quad (\Gamma_z) \\ &\pm i\cos(k_x x)\sin(k_y y)\cos(k_z z) \quad (\Gamma_y) \\ &\pm i\sin(k_x x)\cos(k_y y)\cos(k_z z) \quad (\Gamma_x), \end{aligned} \tag{3.29}$$

which again demonstrates how the full interaction operator allows for more symmetries than the electric-dipole moment operator.

Exactly which of the symmetry components contributes to the oscillator strength depends on the orientation of the molecular system with respect to the light. In these examples, however, it is assumed that the molecular orientation is fixed in space, whereas in more realistic samples, such as gases and liquids, molecules can tumble freely, hence inducing isotropic conditions. These effects will be discussed in detail in Section 3.7, but for now it suffices to assume that all components of either Eqn. (3.27) or Eqn. (3.28) contribute under isotropic conditions.

From this analysis it thus follows that within the electric-dipole approximation, isotropic oscillator strengths are non-vanishing if the transition transforms as one of the Cartesian coordinates. The full interaction operator, however, is much less restrictive, as it only forbids transitions of spherical symmetry, i.e. $j = 0 \rightarrow j = 0$. Furthermore, in a relativistic framework, spin-selection rules do not apply anymore, implying that most of the conventional selection rules derived in the non-relativistic electric-dipole approximation are abolished. However, these selection rules are still useful to make global predictions about the relative intensities of transitions. A dipole-forbidden transition, for instance, is expected to be less intense than a dipole-allowed transition.

We thus have the machinery at our disposal to either calculate transitions within the electric-dipole approximation, or include all non-dipolar effects exactly. However, we may also want to describe these interactions at an intermediate level.

3.4 Truncated Light–Matter Interactions: Generalized Velocity Representation

3.4.1 Origin Independence

The general strategy to derive such a formalism is to expand the full interaction with respect to the wave-vector and truncate it at some finite order

$$\hat{\boldsymbol{T}}(\omega) \approx \sum_{n=0}^{N} \hat{\boldsymbol{T}}^{[n]}(\omega); \quad \hat{\boldsymbol{T}}^{[n]}(\omega) = \frac{1}{n!}\frac{e}{\omega}c\boldsymbol{\alpha}(i\boldsymbol{k}\cdot\boldsymbol{r})^n. \tag{3.30}$$

However, truncated expansions of this kind inherently introduce origin dependence in the interaction operator. By shifting the origin according to $\boldsymbol{O} \rightarrow \boldsymbol{O} + \boldsymbol{a}$, we have

$$\hat{\boldsymbol{T}}^{[n]}(\omega;\boldsymbol{O}) \to \hat{\boldsymbol{T}}^{[n]}(\omega;\boldsymbol{O}+\boldsymbol{a}) = \sum_{m=0}^{n} \frac{1}{m!}(i\boldsymbol{k}\cdot\boldsymbol{a})^m \hat{\boldsymbol{T}}^{[n-m]}(\omega;\boldsymbol{O}). \tag{3.31}$$

This origin-dependency is problematic because spectroscopic quantities, such as the absorption cross-section, should not depend on the choice of origin, which is a mathematical artifact. It should be noted, however, that this origin is not necessarily the same as the origin of the coordinate system. For example, the authors from Refs. 154 and 155 cleverly make use of this distinction to derive origin-independent magnetic properties. To avoid confusion, I will hereafter designate the former as gauge-origin and the latter as coordinate-origin.

For the full interaction operator, this dependence on gauge-origin does not pose a problem

$$\hat{\boldsymbol{T}}(\omega;\boldsymbol{O}) \to \hat{\boldsymbol{T}}(\omega;\boldsymbol{O}+\boldsymbol{a}) = \frac{e}{\omega}c\boldsymbol{\alpha}e^{i\boldsymbol{k}\cdot\boldsymbol{r}}e^{i\boldsymbol{k}\cdot\boldsymbol{a}}, \tag{3.32}$$

because the gauge-origin dependence of this operator manifests itself as a phase factor, which does not contribute to the oscillator strength. Therefore, we should proceed cautiously when deriving observable quantities from truncated expansions.

Inserting the operator from Eqn. (3.30) into the oscillator strength yields the result

$$f^{full}(\omega) = \frac{2m_e\omega}{\hbar e^2}\sum_{n=0}^{\infty}\sum_{m=0}^{\infty} T^{[n]}(\omega)T^{[m]*}(\omega); \quad T^{[n]}(\omega) = \langle f|\tilde{\boldsymbol{\epsilon}}\cdot\hat{\boldsymbol{T}}^{[n]}(\omega)|i\rangle. \tag{3.33}$$

Having two indices, the elements in this summation can be thought of as the elements of a matrix. It turns out to be beneficial to use the fact that we can sum these terms in any order that we want. In the following, I will extensively use techniques that exploit the freedom in choice of summation index. These techniques are explained in full detail in Section C.3.

In its current form, the elements are summed column-wise, whereas it would be completely valid to sum these terms along the anti-diagonals of this matrix. A summation of this type is particularly useful because along the anti-diagonal, all terms are of the same order in the wave vector. Eqn. (3.33) can hence be rewritten as such a sum by using $n+m$ as an index for the anti-diagonals, as it assumes a distinct positive integer value along each anti-diagonal

$$f^{full}(\omega) = \sum_{n=0}^{\infty} f^{[n]}(\omega); \quad f^{[n]}(\omega) = \frac{2m_e\omega}{\hbar e^2}\sum_{m=0}^{n} T^{[n-m]}(\omega)T^{[m]*}(\omega). \tag{3.34}$$

It has been shown by Bernadotte *et al.*[27] that for each order, the oscillator strength is independent on the gauge-origin. To explicitly demonstrate this, I will follow an alternative approach that is being proposed in ref. 1.

As a starting point, I will insert definition of the shifted operators (Eqn. (3.31)) into the n-th order oscillator strength

$$\begin{aligned} f^{[n]}(\omega;\boldsymbol{O}+\boldsymbol{a}) &= \frac{2m_e\omega}{\hbar e^2}\sum_{m=0}^{n} T^{[n-m]}(\omega;\boldsymbol{O}+\boldsymbol{a})T^{[m]*}(\omega;\boldsymbol{O}+\boldsymbol{a}) \\ &= \frac{2m_e\omega}{\hbar e^2}\sum_{m=0}^{n}\sum_{p=0}^{n-m}\sum_{q=0}^{m}\frac{(-1)^q}{p!q!}(i\boldsymbol{k}\cdot\boldsymbol{a})^{p+q}T^{[n-m-p]}(\omega;\boldsymbol{O})T^{[m-q]*}(\omega;\boldsymbol{O}). \end{aligned} \tag{3.35}$$

If we think of the first two summation indices as matrix indices, it can be argued that the corresponding summations fill the upper left diagonal of a matrix. Using similar machinery as in Eqn. (3.34), the summation can be carried out over the anti-diagonal, thus requiring us to redefine the summation according to the index $y = m + p$

$$f^{[n]}(\omega; \boldsymbol{O} + \boldsymbol{a}) = \frac{2m_e\omega}{\hbar e^2} \sum_{y=0}^{n} \sum_{m=0}^{y} \sum_{q=0}^{m} \frac{(-1)^q}{(y-m)!q!} (\boldsymbol{k} \cdot \boldsymbol{a})^{y-m+q} T^{[n-y]}(\omega; \boldsymbol{O}) T^{[m-q]*}(\omega; \boldsymbol{O}). \tag{3.36}$$

Subsequently, I will make the substitution $y \to u = n - y$, yielding the result below

$$f^{[n]}(\omega; \boldsymbol{O} + \boldsymbol{a}) = \frac{2m_e\omega}{\hbar e^2} \sum_{u=0}^{n} \sum_{m=0}^{n-u} \sum_{q=0}^{m} \frac{(-1)^q}{(n-u-m)!q!} (i\boldsymbol{k} \cdot \boldsymbol{a})^{n-u-m+q} T^{[u]}(\omega; \boldsymbol{O}) T^{[m-q]*}(\omega; \boldsymbol{O}). \tag{3.37}$$

Here, the second and third summation fill the lower triangle and the diagonal of a matrix. Along the diagonal and each sub-diagonal, the index $v = m - q$ is constant and assumes a distinct value. By using v as a summation index, we can thus write the n-th order oscillator strength as

$$f^{[n]}(\omega; \boldsymbol{O} + \boldsymbol{a}) = \frac{2m_e\omega}{\hbar e^2} \sum_{u=0}^{n} \sum_{v=0}^{n-u} T^{[u]}(\omega; \boldsymbol{O}) T^{[v]*}(\omega; \boldsymbol{O}) \frac{(i\boldsymbol{k} \cdot \boldsymbol{a})^{n-u-v}}{(n-(u+v))!} \mathcal{M}. \tag{3.38}$$

Here, the factor

$$\mathcal{M} = \sum_{q=0}^{n-(u+v)} \binom{n-(u+v)}{q} (-1)^q = (1-1)^{n-(u+v)} \tag{3.39}$$

is only non-zero if $n - (u + v) = 0$, yielding the end result

$$f^{[n]}(\omega; \boldsymbol{O} + \boldsymbol{a}) = \frac{2m_e\omega}{\hbar e^2} \sum_{u=0}^{n} T^{[u]}(\omega; \boldsymbol{O}) T^{[n-u]*}(\omega; \boldsymbol{O}), \tag{3.40}$$

which is clearly equivalent to Eqn. (3.34) upon relabelling of the summation indices. Therefore, order-by-order the oscillator strength is gauge-origin independent because the origin-dependent terms cancel exactly. It thus follows that the n-th order oscillator strength is a meaningful physical quantity, unlike, for example, the individual transition moments that are used to construct this quantity.

3.4.2 Simplifications from Time-Reversal Symmetry

Although Eqn. (3.30) makes sense physically, there is still much room for improvement. By exploiting time-reversal symmetry of the interaction operators, it can be shown that some orders in Eqn. (3.30) vanish. For these purposes, I will re-express the transition moments

$$\mathcal{T}^{[n]} = (-i)^{n-1} T^{[n]}(\omega) = \langle f | \frac{1}{n!} \frac{e}{\omega} \tilde{\boldsymbol{\epsilon}} \cdot ic\boldsymbol{\alpha} (\boldsymbol{k} \cdot \boldsymbol{r})^n | i \rangle, \tag{3.41}$$

such that the operator inside the integral is time-reversal symmetric. From the results of Section 2.4.3, it thus follows that the corresponding transition moments are real. The simplifications that follow from this property, are generally different for absorption of linearly polarized light and circular dichroism. Therefore, I will start to analyze the former case. Expressed in these redefined transition moments, the n-th order oscillator strength reads

$$f^{[n]}(\omega) = i^n \frac{2m_e\omega}{\hbar e^2} \sum_{m=0}^{n} (-1)^m \mathcal{T}^{[n-m]}(\omega)\mathcal{T}^{[m]*}(\omega). \tag{3.42}$$

It should be noted that the terms in this summation come in pairs. To further pursue this idea, it proves to be useful to separate the even- from the odd-order terms

$$\begin{aligned} f^{[2n]}(\omega) &= (-1)^n \frac{2m_e\omega}{\hbar e^2} \sum_{m=0}^{2n} (-1)^m \mathcal{T}^{[2n-m]}(\omega)\mathcal{T}^{[m]*}(\omega) \\ f^{[2n+1]}(\omega) &= (-1)^n i \frac{2m_e\omega}{\hbar e^2} \sum_{m=0}^{2n+1} (-1)^m \mathcal{T}^{[2n+1-m]}(\omega)\mathcal{T}^{[m]*}(\omega) \end{aligned} \tag{3.43}$$

Let us start by closer inspecting the terms of even order, which can be expressed as

$$\begin{aligned} f^{[2n]}(\omega) = {} & \frac{2m_e\omega}{\hbar e^2} \mathcal{T}^{[n]}(\omega)\mathcal{T}^{[n]*}(\omega) \\ & + (-1)^n \frac{2m_e\omega}{\hbar e^2} \sum_{m=0}^{n-1} (-1)^m \mathcal{T}^{[2n-m]}(\omega)\mathcal{T}^{[m]*}(\omega) \\ & + (-1)^n \frac{2m_e\omega}{\hbar e^2} \sum_{m=n+1}^{2n} (-1)^m \mathcal{T}^{[2n-m]}(\omega)\mathcal{T}^{[m]*}(\omega). \end{aligned} \tag{3.44}$$

The two summations have common terms, although their summation indices do not agree. Both of these two summations can be grouped together by redefining these indices. The first summation will be redefined such that the summation order is reversed, whereas the latter summation will be shifted such that the index starts at zero. These change can be achieved by redefining the first- and second summation according to $m \to n - m$ and $m \to m - n$, which yields the following result

$$f^{[2n]}(\omega) = \frac{2m_e\omega}{\hbar e^2} \sum_{m=0}^{n} (-1)^m (2 - \delta_{m0}) Re[\mathcal{T}^{[n+m]}(\omega)\mathcal{T}^{[n-m]*}(\omega)]. \tag{3.45}$$

For odd orders, the oscillator strength can be expressed as

$$\begin{aligned} f^{[2n+1]}(\omega) = {} & (-1)^n i \frac{2m_e\omega}{\hbar e^2} \sum_{m=0}^{n} (-1)^m \mathcal{T}^{[2n+1-m]}(\omega)\mathcal{T}^{[m]*}(\omega) \\ & + (-1)^n i \frac{2m_e\omega}{\hbar e^2} \sum_{m=n+1}^{2n+1} (-1)^m \mathcal{T}^{[2n+1-m]}(\omega)\mathcal{T}^{[m]*}(\omega). \end{aligned} \tag{3.46}$$

Similar to the results for even-order terms, the above expression can be simplified by redefining the first- and second summation according to $m \rightarrow n-m$ and $m \rightarrow m-n-1$,

$$f^{[2n+1]}(\omega) = (-1)^n \frac{2m_e\omega}{\hbar e^2} \sum_{m=0}^{n} (-1)^{n-m} 2Im\big[\mathcal{T}^{[n+1-m]}(\omega)\mathcal{T}^{[n-m]*}(\omega)\big] = 0, \tag{3.47}$$

which always vanishes, because the transition moments are real.

However, these results do not generally hold for circular dichroism, which at n-th order assumes the form

$$\Delta f^{[n]}(\omega) = f_L^{[n]}(\omega) - f_R^{[n]}(\omega) = -i^{n+1} \frac{2m_e\omega}{\hbar e^2} \sum_{m=0}^{n} (-1)^m \boldsymbol{e}_k \cdot (\boldsymbol{\mathcal{T}}^{[n-m]}(\omega) \times \boldsymbol{\mathcal{T}}^{[m]*}(\omega)) \tag{3.48}$$
$$\boldsymbol{\mathcal{T}}^{[n]}(\omega) = \langle f | \frac{1}{n!} \frac{e}{\omega} ic\boldsymbol{\alpha}(\boldsymbol{k}\cdot\boldsymbol{r})^n | i \rangle$$

It again turns out to be useful to separate even from odd contributions

$$\Delta f^{[2n]}(\omega) = (-1)^{n+1} i \frac{2m_e\omega}{\hbar e^2} \sum_{m=0}^{2n} (-1)^m \boldsymbol{e}_k \cdot (\boldsymbol{\mathcal{T}}^{[2n-m]}(\omega) \times \boldsymbol{\mathcal{T}}^{[m]*}(\omega)) \tag{3.49}$$
$$\Delta f^{[2n+1]}(\omega) = (-1)^{n} \frac{2m_e\omega}{\hbar e^2} \sum_{m=0}^{2n+1} (-1)^m \boldsymbol{e}_k \cdot (\boldsymbol{\mathcal{T}}^{[2n-m+1]}(\omega) \times \boldsymbol{\mathcal{T}}^{[m]*}(\omega)).$$

Following a similar strategy as previous case, the even-order contributions can be expressed as

$$\begin{aligned}\Delta f^{[2n]}(\omega) = & -i \frac{2m_e\omega}{\hbar e^2} \boldsymbol{e}_k \cdot (\boldsymbol{\mathcal{T}}^{[n]}(\omega) \times \boldsymbol{\mathcal{T}}^{[n]*}(\omega)) \\ & + (-1)^{n+1} i \frac{2m_e\omega}{\hbar e^2} \sum_{m=0}^{n-1} (-1)^m \boldsymbol{e}_k \cdot (\boldsymbol{\mathcal{T}}^{[2n-m]}(\omega) \times \boldsymbol{\mathcal{T}}^{[m]*}(\omega)) \\ & + (-1)^{n+1} i \frac{2m_e\omega}{\hbar e^2} \sum_{m=n+1}^{2n} (-1)^m \boldsymbol{e}_k \cdot (\boldsymbol{\mathcal{T}}^{[2n-m]}(\omega) \times \boldsymbol{\mathcal{T}}^{[m]*}(\omega)),\end{aligned} \tag{3.50}$$

which can be simplified by applying the substitutions $m \rightarrow n-m$ and $m \rightarrow m-n$ to the first- and second summation

$$\begin{aligned}\Delta f^{[2n]}(\omega) = & -i \frac{2m_e\omega}{\hbar e^2} \boldsymbol{e}_k \cdot (\boldsymbol{\mathcal{T}}^{[n]}(\omega) \times \boldsymbol{\mathcal{T}}^{[n]*}(\omega)) - \frac{2m_e\omega}{\hbar e^2} \sum_{m=1}^{n} (-1)^m \boldsymbol{e}_k \cdot i(\boldsymbol{\mathcal{T}}^{[n+m]}(\omega) \times \boldsymbol{\mathcal{T}}^{[n-m]*}(\omega)) \\ & + \frac{2m_e\omega}{\hbar e^2} \sum_{m=1}^{n} (-1)^m \boldsymbol{e}_k \cdot i(\boldsymbol{\mathcal{T}}^{[n+m]*}(\omega) \times \boldsymbol{\mathcal{T}}^{[n-m]}(\omega)) = 0.\end{aligned} \tag{3.51}$$

This expression again vanishes by virtue of the realness of the transition moments. Likewise, the odd-order contributions can be rewritten as

$$\begin{aligned}\Delta f^{[2n+1]}(\omega) = (-1)^n \frac{2m_e\omega}{\hbar e^2} &\sum_{m=0}^{n} (-1)^m \boldsymbol{e}_k \cdot (\boldsymbol{\mathcal{T}}^{[2n-m+1]}(\omega) \times \boldsymbol{\mathcal{T}}^{[m]*}(\omega)) \\ + (-1)^n \frac{2m_e\omega}{\hbar e^2} &\sum_{m=n+1}^{2n+1} (-1)^m \boldsymbol{e}_k \cdot (\boldsymbol{\mathcal{T}}^{[2n-m+1]}(\omega) \times \boldsymbol{\mathcal{T}}^{[m]*}(\omega)),\end{aligned} \tag{3.52}$$

which yields the end results upon the index substitutions $m \to n - m$ and $m \to m - n - 1$ in the first- and second summation

$$\Delta f^{[2n+1]}(\omega) = \frac{2m_e\omega}{\hbar e^2} \boldsymbol{e}_k \cdot \sum_{m=0}^{n} (-1)^m 2Re\big\{\boldsymbol{\mathcal{T}}^{[n+m+1]}(\omega) \times \boldsymbol{\mathcal{T}}^{[n-m]*}(\omega)\big\}. \tag{3.53}$$

Therefore, for circular dichroism, only odd contributions are relevant, whereas the even terms only contribute to the absorption of linearly polarized light.

3.4.3 Electric and Magnetic Contributions

We have thus derived the working equations to describe a truncated light–matter interaction at arbitrary order. However, at first sight, there does not seem to be a relation with the truncated interaction operators appearing in Eqn. (3.34) and the multipole moments introduced at the beginning of this chapter. To be more precise, in its current form, the oscillator strength does not distinguish between electric and magnetic components. In the following, I will demonstrate how such a decomposition can be achieved.

As a starting point, I will rewrite the n-th order interaction operator in the following manner

$$\hat{\mathcal{T}}^{[n]}(\omega) = \frac{1}{(n+1)!}\frac{e}{\omega} i(\tilde{\boldsymbol{\epsilon}} \cdot c\boldsymbol{\alpha})(\boldsymbol{k} \cdot \boldsymbol{r})^n + \frac{n}{(n+1)!}\frac{e}{\omega} i(\tilde{\boldsymbol{\epsilon}} \cdot c\boldsymbol{\alpha})(\boldsymbol{k} \cdot \boldsymbol{r})^n. \tag{3.54}$$

The reason for this decomposition becomes more clear in the subsequent step, where I will insert the identity

$$(\boldsymbol{k} \times \tilde{\boldsymbol{\epsilon}}) \cdot (\boldsymbol{r} \times c\boldsymbol{\alpha}) = (c\boldsymbol{\alpha} \cdot \tilde{\boldsymbol{\epsilon}})(\boldsymbol{k} \cdot \boldsymbol{r}) - (\boldsymbol{r} \cdot \tilde{\boldsymbol{\epsilon}})(\boldsymbol{k} \cdot c\boldsymbol{\alpha}) \tag{3.55}$$

which yields the result

$$\begin{aligned}\hat{\mathcal{T}}^{[n]}(\omega) = &\frac{1}{(n+1)!}\frac{e}{\omega}\Big((\tilde{\boldsymbol{\epsilon}} \cdot ic\boldsymbol{\alpha})(\boldsymbol{k} \cdot \boldsymbol{r}) + n(\boldsymbol{r} \cdot \tilde{\boldsymbol{\epsilon}})(\boldsymbol{k} \cdot ic\boldsymbol{\alpha})\Big)(\boldsymbol{k} \cdot \boldsymbol{r})^{n-1} \\ &+ \frac{n}{(n+1)!}\frac{e}{\omega}(\boldsymbol{k} \times \tilde{\boldsymbol{\epsilon}}) \cdot (\boldsymbol{r} \times ic\boldsymbol{\alpha})(\boldsymbol{k} \cdot \boldsymbol{r})^{n-1} = k_{j_1}k_{j_2}\cdots k_{j_n}\tilde{\epsilon}_p \hat{\mathcal{X}}^{[n]}_{j_1\cdots j_n;p}(\omega).\end{aligned} \tag{3.56}$$

In the last line, I have introduced the multipole moment operator in component form

$$\hat{\mathcal{X}}^{[n]}_{j_1\cdots j_n;p}(\omega) = \frac{1}{(n+1)!}\hat{\mathcal{Q}}^{[n+1]}_{j_1\cdots j_n;p} - \frac{i}{\omega}\frac{1}{n!}\hat{m}^{[n]}_{j_1\cdots j_{n-1};r}\varepsilon_{rj_np} \tag{3.57}$$

which is expressed in terms of the two operators

$$\hat{\mathcal{Q}}^{[n+1]}_{j_1\cdots j_n;p} = \frac{ie}{\omega} r_{j_1}\cdots r_{j_{n-1}}(c\alpha_p r_{j_n} + nc\alpha_{j_n} r_p) \tag{3.58}$$

and

$$\hat{m}^{[n]}_{j_1\cdots j_{n-1};r} = \frac{n}{n+1} r_{j_1}\cdots r_{j_{n-1}}(\boldsymbol{r}\times\hat{\boldsymbol{j}})_r; \quad \hat{\boldsymbol{j}} = -ec\boldsymbol{\alpha}. \tag{3.59}$$

Because this operator yields the velocity representation electric-dipole moment (Eqn. (3.23)) at zeroth order, Eqn. (3.57) is referred to as the generalized velocity representation. In this representation, the second operator can straightforwardly be recognized as a magnetic operator, due to its similarities with the magnetic multipole moments introduced in Eqn. (E.12). It should be noted that the compact form of the current density operator is a special feature of relativistic theory, since the non-relativistic current density may also contain explicit contributions depending on the external field and the electron spin. Having established that the second operator in Eqn. (3.57) is magnetic in nature, it seems only logical to conclude that the first operator, $\hat{\mathcal{Q}}^{[n+1]}_{j_1\cdots j_n;p}$, is an electric multipole moment operator. However, before jumping to conclusions, it should be confirmed that this operator is indeed purely electric in character.

For this proof, it is more suitable to start from $\hat{V}^{[n]}(\omega)$ rather than $\hat{\boldsymbol{\mathcal{T}}}^{[n]}$

$$\begin{aligned}\hat{V}^{[n]}(\omega) &= -\frac{\mathcal{E}}{2} i^{n-1} k_{j_1}k_{j_2}\cdots k_{j_n}\tilde{\epsilon}_p \hat{\mathcal{X}}^{[n]}_{j_1\cdots j_n;p}(\omega) \\ &= -\frac{\mathcal{E}}{2} i^{n-1} k_{j_1}k_{j_2}\cdots k_{j_n}\tilde{\epsilon}_p \frac{1}{(n+1)!}\hat{\mathcal{Q}}^{[n+1]}_{j_1\cdots j_n;p} + \frac{\mathcal{E}}{2} i^{n-1} k_{j_1}k_{j_2}\cdots k_{j_n}\tilde{\epsilon}_p \frac{i}{\omega}\frac{1}{n!}\hat{m}^{[n]}_{j_1\cdots j_{n-1};r}\varepsilon_{rj_np}.\end{aligned} \tag{3.60}$$

Furthermore, it is useful to express the electromagnetic fields in terms of their frequency components

$$\boldsymbol{E}(\boldsymbol{r},t) = \boldsymbol{E}(\boldsymbol{r},\omega)e^{-i\omega t} + \boldsymbol{E}(\boldsymbol{r},-\omega)e^{i\omega t}; \quad \boldsymbol{B}(\boldsymbol{r},t) = \boldsymbol{B}(\boldsymbol{r},\omega)e^{-i\omega t} + \boldsymbol{B}(\boldsymbol{r},-\omega)e^{i\omega t} \tag{3.61}$$

and evaluate their n-th order derivatives at $\boldsymbol{r}' = 0$

$$\left.\frac{\partial^n \boldsymbol{E}(\boldsymbol{r}',\omega)}{\partial r'_{j_1}\cdots\partial r'_{j_n}}\right|_{\boldsymbol{r}'=0} = i^n\frac{\mathcal{E}}{2i}\tilde{\boldsymbol{\epsilon}}k_{j_1}k_{j_2}\cdots k_{j_n}; \quad \left.\frac{\partial^n \boldsymbol{B}(\boldsymbol{r}',\omega)}{\partial r'_{j_1}\cdots\partial r'_{j_n}}\right|_{\boldsymbol{r}'=0} = i^n\frac{\mathcal{E}}{2i}\frac{1}{\omega}(\boldsymbol{k}\times\tilde{\boldsymbol{\epsilon}})k_{j_1}k_{j_2}\cdots k_{j_n}. \tag{3.62}$$

By comparing Eqn. (3.62) with Eqn. (3.60), it follows that

$$\hat{V}^{[n]}(\omega) = \left(-\frac{i}{(n+1)!}\left.\frac{\partial^n E_p(\boldsymbol{r}',\omega)}{\partial r'_{j_1}\cdots\partial r'_{j_n}}\right|_{\boldsymbol{r}'=0}\mathcal{Q}^{[n+1]}_{j_1\cdots j_n;p} + \frac{1}{n!}\left.\frac{\partial^{n-1} B_r(\boldsymbol{r}',\omega)}{\partial r'_{j_1}\cdots\partial r'_{j_{n-1}}}\right|_{\boldsymbol{r}'=0} m^{[n]}_{j_1\cdots j_{n-1};r}\right), \tag{3.63}$$

in which $\mathcal{Q}^{[n+1]}_{j_1\cdots j_n;p}$ couples with the n-th order derivative of the electric field, whereas $m^{[n]}_{j_1\cdots j_{n-1};r}$ couples with the $(n-1)$-th order derivative of the magnetic field. Therefore, the two operators in Eqn. (3.57) are indeed electric and magnetic in nature.

By expressing the n-th order oscillator strength in terms of Eqn. (3.57)

$$f^{[n]}(\omega) = i^n \frac{2m_e\omega}{\hbar e^2}\left(\frac{\omega}{c}\right)^n \sum_{m=0}^{n} (-1)^m \tilde{\epsilon}_p \tilde{\epsilon}_q e_{k;j_1} e_{k;j_2} \cdots e_{k;j_n} \langle f|\hat{\mathcal{X}}^{[n-m]}_{j_1\cdots j_{n-m};p}(\omega)|i\rangle \langle f|\hat{\mathcal{X}}^{[m]}_{j_{n-m+1}\cdots j_n;q}(\omega)|i\rangle^* \tag{3.64}$$

it is possible to isolate a purely electric contribution

$$\begin{aligned} f^{[n]}_{QQ}(\omega) = i^n \frac{2m_e\omega}{\hbar e^2}\left(\frac{\omega}{c}\right)^n &\sum_{m=0}^{n} (-1)^m \tilde{\epsilon}_p \tilde{\epsilon}_q e_{k;j_1} e_{k;j_2} \cdots e_{k;j_n} \\ &\times \langle f|\frac{1}{(n-m+1)!}\hat{\mathcal{Q}}^{[n-m+1]}_{j_1\cdots j_{n-m};p}|i\rangle \langle f|\frac{1}{(m+1)!}\hat{\mathcal{Q}}^{[m+1]}_{j_{n-m+1}\cdots j_n;p}|i\rangle^*, \end{aligned} \tag{3.65}$$

a mixed electric-magnetic contribution

$$\begin{aligned} f^{[n]}_{QM}(\omega) = i^n \frac{2m_e\omega}{\hbar e^2}\left(\frac{\omega}{c}\right)^n \sum_{m=0}^{n} \Bigg[\\ (-1)^m \tilde{\epsilon}_p \tilde{\epsilon}_q e_{k;j_1} e_{k;j_2} \cdots e_{k;j_n} \langle f|\frac{1}{(n-m+1)!}\hat{\mathcal{Q}}^{[n-m+1]}_{j_1\cdots j_{n-m};p}|i\rangle \langle f|-\frac{i}{\omega}\frac{1}{m!}\hat{m}^{[m]}_{j_{n-m+1}\cdots j_{n-1};r}\varepsilon_{rj_np}|i\rangle^* \\ + (-1)^m \tilde{\epsilon}_p \tilde{\epsilon}_q e_{k;j_1} e_{k;j_2} \cdots e_{k;j_n} \langle f|-\frac{i}{\omega}\frac{1}{(n-m)!}\hat{m}^{[n-m]}_{j_1\cdots j_{n-m-1};r}\varepsilon_{rj_{n-m}p}|i\rangle \langle f|\frac{1}{(m+1)!}\hat{\mathcal{Q}}^{[m]}_{j_{n-m+1}\cdots j_n;p}|i\rangle^* \Bigg], \end{aligned} \tag{3.66}$$

and a purely magnetic contribution

$$\begin{aligned} f^{[n]}_{MM}(\omega) = i^n \frac{2m_e\omega}{\hbar e^2}\left(\frac{\omega}{c}\right)^n &\sum_{m=0}^{n} (-1)^m \tilde{\epsilon}_p \tilde{\epsilon}_q e_{k;j_1} e_{k;j_2} \cdots e_{k;j_n} \\ &\langle f|-\frac{i}{\omega}\frac{1}{(n-m)!}\hat{m}^{[n-m]}_{j_1\cdots j_{n-m-1};r}\varepsilon_{rj_{n-m}p}|i\rangle \langle f|-\frac{i}{\omega}\frac{1}{m!}\hat{m}^{[m]}_{j_{n-m+1}\cdots j_{n-1};s}\varepsilon_{sj_np}|i\rangle^* \end{aligned} \tag{3.67}$$

I stress that each of these contributions is dependent on the choice of gauge-origin, unlike the accumulated value of these three components. By changing from one origin to the other, we are effectively shifting the weight of the contribution, while keeping their sum constant. However, this should not be confused with the mixing of electric and magnetic fields upon Lorentz transformation (Eqn. (2.28)).[150] Here, the electric and magnetic fields rather mix because a truncated expansion can only describe the interaction locally. It can thus be argued that this decomposition does make little sense physically, since it inherently depends on the choice of gauge-origin.[33] For centrosymmetric systems, such as atoms or metal complexes, it is possible to define a unique origin at the center. For general systems, however, such a symmetry may not exist, implying that this decomposition should be used with caution or avoided altogether.

3.5 Truncated Light–Matter Interactions: Generalized Length Representation

In the previous section, I have shown how in the generalized velocity representation, multipole moments appear in a rather unusual form. A formalism can be derived that is based on multipole moments in their more conventional form by imposing multipolar gauge. To derive an appropriate gauge condition, I will follow the procedure described by Bloch,[156] although there is a variety of alternative methods to reach this goal.[157, 158, 159] The approach that is treated here starts from the Taylor expansion of the potentials centered around the expansion point $\boldsymbol{a}$

$$\begin{aligned}\tilde{\phi}(\boldsymbol{r},t) &= \sum_{n=0}^{\infty}\frac{1}{n!}\left[(\boldsymbol{\delta}_a\cdot\boldsymbol{\nabla}')^n\tilde{\phi}(\boldsymbol{r}',t)\right]\Big|_{\boldsymbol{r}'=\boldsymbol{a}}; \quad \boldsymbol{\delta}_a=\boldsymbol{r}-\boldsymbol{a} \\ \tilde{\boldsymbol{A}}(\boldsymbol{r},t) &= \sum_{n=0}^{\infty}\frac{1}{n!}\left[(\boldsymbol{\delta}_a\cdot\boldsymbol{\nabla}')^n\tilde{\boldsymbol{A}}(\boldsymbol{r}',t)\right]\Big|_{\boldsymbol{r}'=\boldsymbol{a}},\end{aligned} \tag{3.68}$$

where I applied a compactified notation that avoids the excessive use of indices. Note that the relation $\boldsymbol{\nabla}\tilde{\phi}=-\boldsymbol{E}-\frac{\partial}{\partial t}\tilde{\boldsymbol{A}}$ can be inserted in the expansion of the scalar potential

$$\tilde{\phi}(\boldsymbol{r},t)=\tilde{\phi}(\boldsymbol{a},t)-\sum_{n=1}^{\infty}\frac{1}{n!}\left[(\boldsymbol{\delta}_a\cdot\boldsymbol{\nabla}')^{n-1}\boldsymbol{\delta}_a\cdot\boldsymbol{E}(\boldsymbol{r}',t)\right]\Big|_{\boldsymbol{r}'=\boldsymbol{a}}-\frac{\partial}{\partial t}\sum_{n=1}^{\infty}\frac{1}{n!}\left[(\boldsymbol{\delta}_a\cdot\boldsymbol{\nabla}')^{n-1}\boldsymbol{\delta}_a\cdot\tilde{\boldsymbol{A}}(\boldsymbol{r}',t)\right]\Big|_{\boldsymbol{r}'=\boldsymbol{a}}. \tag{3.69}$$

Interestingly, this expression resembles a gauge transformation

$$\tilde{\phi}(\boldsymbol{r},t)=\phi_a(\boldsymbol{r},t)-\partial_t\chi_a(\boldsymbol{r},t), \tag{3.70}$$

with the time-derivative term corresponding to the gauge function. Isolating ϕ_a, thus enables us to express the scalar potential completely in terms of the electric field

$$\phi_a(\boldsymbol{r},t)=\tilde{\phi}(\boldsymbol{a},t)-\sum_{n=1}^{\infty}\frac{1}{n!}\left[(\boldsymbol{\delta}_a\cdot\boldsymbol{\nabla}')^{n-1}\boldsymbol{\delta}_a\cdot\boldsymbol{E}(\boldsymbol{r}',t)\right]\Big|_{\boldsymbol{r}'=\boldsymbol{a}}. \tag{3.71}$$

Accordingly, the gauge function is defined as

$$\chi_a(\boldsymbol{r},t)=\sum_{n=1}^{\infty}\frac{1}{n!}\left[(\boldsymbol{\delta}_a\cdot\boldsymbol{\nabla}')^{n-1}\big(\boldsymbol{\delta}_a\cdot\tilde{\boldsymbol{A}}(\boldsymbol{r}',t)\big)\right]\Big|_{\boldsymbol{r}'=\boldsymbol{a}}. \tag{3.72}$$

To derive an expression for the vector potential, we use the partner relation

$$\tilde{\boldsymbol{A}}(\boldsymbol{r},t)=\boldsymbol{A}_a(\boldsymbol{r},t)+\boldsymbol{\nabla}\chi_a(\boldsymbol{r},t). \tag{3.73}$$

thus requiring us to evaluate the gradient of the gauge function

$$\boldsymbol{\nabla}\chi=\sum_{n=0}^{\infty}\frac{1}{(n+1)!}\left[(\boldsymbol{\delta}_a\cdot\boldsymbol{\nabla}')^n\tilde{\boldsymbol{A}}(\boldsymbol{r}',t)\right]\Big|_{\boldsymbol{r}'=\boldsymbol{a}}+\sum_{n=1}^{\infty}\frac{n}{(n+1)!}\left[(\boldsymbol{\delta}_a\cdot\boldsymbol{\nabla}')^{n-1}\boldsymbol{\nabla}'\big(\boldsymbol{\delta}_a\cdot\tilde{\boldsymbol{A}}(\boldsymbol{r}',t)\big)\right]\Big|_{\boldsymbol{r}'=\boldsymbol{a}}. \tag{3.74}$$

The transformed vector potential reads

$$\begin{aligned}\boldsymbol{A}_a(\boldsymbol{r},t) =&\sum_{n=0}^{\infty}\frac{1}{n!}\Big[(\boldsymbol{\delta}_a\cdot\boldsymbol{\nabla}')^n\tilde{\boldsymbol{A}}(\boldsymbol{r}',t)\Big]\Big|_{\boldsymbol{r}'=\boldsymbol{a}} \\ &-\sum_{n=0}^{\infty}\frac{1}{(n+1)!}\Big[(\boldsymbol{\delta}_a\cdot\boldsymbol{\nabla}')^n\tilde{\boldsymbol{A}}(\boldsymbol{r}',t)\Big]\Big|_{\boldsymbol{r}'=\boldsymbol{a}}-\sum_{n=1}^{\infty}\frac{n}{(n+1)!}\Big[(\boldsymbol{\delta}_a\cdot\boldsymbol{\nabla}')^{n-1}\boldsymbol{\nabla}'\big(\boldsymbol{\delta}_a\cdot\tilde{\boldsymbol{A}}(\boldsymbol{r}',t)\big)\Big]\Big|_{\boldsymbol{r}'=\boldsymbol{a}} \\ =&\sum_{n=1}^{\infty}\frac{n}{(n+1)!}\Big[(\boldsymbol{\delta}_a\cdot\boldsymbol{\nabla}')^{n-1}\Big\{(\boldsymbol{\delta}_a\cdot\boldsymbol{\nabla}')\tilde{\boldsymbol{A}}(\boldsymbol{r}',t)-\boldsymbol{\nabla}'\big(\boldsymbol{\delta}_a\cdot\tilde{\boldsymbol{A}}(\boldsymbol{r}',t)\big)\Big\}\Big]\Big|_{\boldsymbol{r}'=\boldsymbol{a}}.\end{aligned} \tag{3.75}$$

As a finishing touch, I will apply the identity

$$\boldsymbol{\delta}_a\times\boldsymbol{B}(\boldsymbol{r}',t)=\boldsymbol{\delta}_a\times(\boldsymbol{\nabla}'\times\tilde{\boldsymbol{A}}(\boldsymbol{r}',t))=\boldsymbol{\nabla}'\big(\boldsymbol{\delta}_a\cdot\tilde{\boldsymbol{A}}(\boldsymbol{r}',t)\big)-\boldsymbol{\delta}_a\cdot\boldsymbol{\nabla}'\tilde{\boldsymbol{A}}(\boldsymbol{r}',t), \tag{3.76}$$

allowing us to express the vector potentials in terms of the magnetic field

$$\boldsymbol{A}_a(\boldsymbol{r},t)=-\sum_{n=1}^{\infty}\frac{n}{(n+1)!}\Big[(\boldsymbol{\delta}_a\cdot\boldsymbol{\nabla}')^{n-1}\big(\boldsymbol{\delta}_a\times\boldsymbol{B}(\boldsymbol{r}',t)\big)\Big]\Big|_{\boldsymbol{r}'=\boldsymbol{a}}. \tag{3.77}$$

Therefore, multipolar gauge provides a unique separation of electric and magnetic interactions.

An intriguing feature of multipolar gauge is that it appears to eliminate gauge freedom, since we can apply any gauge transformation to $(\tilde{\phi},\tilde{\boldsymbol{A}})$ without altering the structure of $(\phi_a,\boldsymbol{A}_a)$. However, the additional degrees of freedom associated to gauge transformations now reside inside the choice of expansion point, suggesting that potentials corresponding to different expansion points are related by gauge transformations. To further validate this idea, I will introduce the potentials $(\phi_b,\boldsymbol{A}_b)$ which are expressed in multipolar gauge with the expansion point centred at $\boldsymbol{b}$. Starting from the potentials, $(\phi_a,\boldsymbol{A}_a)$, the potentials $(\tilde{\phi},\tilde{\boldsymbol{A}})$ can be obtained through the relations Eqs. (3.70) and (3.73). Provided that we do not truncate our expansion, we are allowed to freely choose the expansion point in Eqs. (3.68), thus suggesting that we can make the following connection

$$\begin{aligned}\tilde{\phi}(\boldsymbol{r},t)&=\phi_b(\boldsymbol{r},t)-\frac{\partial}{\partial t}\chi_b(\boldsymbol{r},t)\\ \tilde{\boldsymbol{A}}(\boldsymbol{r},t)&=\boldsymbol{A}_b(\boldsymbol{r},t)+\boldsymbol{\nabla}\chi_b(\boldsymbol{r},t).\end{aligned} \tag{3.78}$$

By combining both gauge transformations, we can relate $(\phi_a,\boldsymbol{A}_a)$ to $(\phi_b,\boldsymbol{A}_b)$

$$\begin{aligned}\phi_a(\boldsymbol{r},t)&=\phi_b(\boldsymbol{r},t)-\partial_t\chi_{a\to b}\\ \boldsymbol{A}_a(\boldsymbol{r},t)&=\boldsymbol{A}_b(\boldsymbol{r},t)+\boldsymbol{\nabla}\chi_{a\to b},\end{aligned} \tag{3.79}$$

with the gauge function defined as

$$\chi_{a\to b}=\chi_b-\chi_a=\sum_{n=1}^{\infty}\frac{1}{n!}\bigg(\Big[(\boldsymbol{\delta}_b\cdot\boldsymbol{\nabla}')^{n-1}\big(\boldsymbol{\delta}_b\cdot\tilde{\boldsymbol{A}}(\boldsymbol{r}',t)\big)\Big]\Big|_{\boldsymbol{r}'=\boldsymbol{b}}-\Big[(\boldsymbol{\delta}_a\cdot\boldsymbol{\nabla}')^{n-1}\big(\boldsymbol{\delta}_a\cdot\tilde{\boldsymbol{A}}(\boldsymbol{r}',t)\big)\Big]\Big|_{\boldsymbol{r}'=\boldsymbol{a}}\bigg). \tag{3.80}$$

$$\begin{tikzcd}
& (\tilde{\phi}, \tilde{\mathbf{A}}) \arrow[dr, "\chi_b"] & \\
(\phi_a, \mathbf{A}_a) \arrow[ur, "-\chi_a"] \arrow[rr, "\chi_{a\to b}"] & & (\phi_b, \mathbf{A}_b)
\end{tikzcd}$$

Figure 3.4: graph that represents the two consecutive gauge transformations that are required to transform $(\phi_a, \boldsymbol{A}_a)$ *to* $(\phi_b, \boldsymbol{A}_b)$.

In Figure 3.5, the procedure outlined above is represented schematically.
However, I stress that the relations from Eqs. (3.78), which form an essential step in the transformation, are only valid if we do not truncate our expansion. Upon truncation, our gauge transformation breaks down, since we have

$$\begin{aligned}
\sum_{n=0}^{N}\frac{1}{n!}\Big[(\boldsymbol{\delta}_a\cdot\boldsymbol{\nabla}')^n\tilde{\phi}(\boldsymbol{r}',t)\Big]\Big|_{\boldsymbol{r}'=\boldsymbol{a}} &\neq \sum_{n=0}^{N}\frac{1}{n!}\Big[(\boldsymbol{\delta}_b\cdot\boldsymbol{\nabla}')^n\tilde{\phi}(\boldsymbol{r}',t)\Big]\Big|_{\boldsymbol{r}'=\boldsymbol{b}} \\
\sum_{n=0}^{N}\frac{1}{n!}\Big[(\boldsymbol{\delta}_a\cdot\boldsymbol{\nabla}')^n\tilde{\boldsymbol{A}}(\boldsymbol{r}',t)\Big]\Big|_{\boldsymbol{r}'=\boldsymbol{a}} &\neq \sum_{n=0}^{N}\frac{1}{n!}\Big[(\boldsymbol{\delta}_b\cdot\boldsymbol{\nabla}')^n\tilde{\boldsymbol{A}}(\boldsymbol{r}',t)\Big]\Big|_{\boldsymbol{r}'=\boldsymbol{b}},
\end{aligned} \tag{3.81}$$

for some finite order N. Therefore, different expansion points are only connected by a gauge transformation if the expansion is not truncated. The inequivalence of two expansion points effectively implies that we have a gauge-origin dependence, similar to Eqn. (3.31). This inherent origin dependence will haunt us throughout the rest of this chapter.

Using the potentials from Eqs. (3.71) and (3.77), the following interaction operator can be derived

$$\hat{V}_a(t) = e\sum_{n=0}^{\infty}\frac{1}{(n+1)!}\Big[(\boldsymbol{\delta}_a\cdot\boldsymbol{\nabla}')^n\big(\boldsymbol{\delta}_a\cdot\boldsymbol{E}(\boldsymbol{r}',t)\big)\Big]\Big|_{\boldsymbol{r}'=\boldsymbol{a}} - ec\sum_{n=1}^{\infty}\frac{n}{(n+1)!}\Big[(\boldsymbol{\delta}_a\cdot\boldsymbol{\nabla}')^{n-1}\big(\boldsymbol{\delta}_a\times\boldsymbol{B}(\boldsymbol{r}',t)\big)\cdot c\boldsymbol{\alpha}\Big]\Big|_{\boldsymbol{r}'=\boldsymbol{a}}, \tag{3.82}$$

where I left out the constant term in the scalar potential, as it does not contribute to transition moments due to the orthogonality of states. However, for certain approximative schemes, such as STEX (see Section 5), this assumption might not hold. By inserting the definition of the electromagnetic fields (Eqn. (3.3)) and isolating the resulting frequency components, we obtain the following operator

$$\hat{V}_a(\omega) = e^{i\boldsymbol{k}\cdot\boldsymbol{a}}e\frac{\mathcal{E}}{2i}(\boldsymbol{\delta}_a\cdot\tilde{\boldsymbol{\epsilon}})\sum_{n=0}^{\infty}\frac{1}{(n+1)!}(i\boldsymbol{\delta}_a\cdot\boldsymbol{k})^n - e^{i\boldsymbol{k}\cdot\boldsymbol{a}}ec\frac{\mathcal{E}}{2i}\Big(\boldsymbol{\delta}_a\times\big(\frac{1}{\omega}\boldsymbol{k}\times\tilde{\boldsymbol{\epsilon}}\big)\Big)\cdot c\boldsymbol{\alpha}\sum_{n=1}^{\infty}\frac{n}{(n+1)!}(i\boldsymbol{\delta}_a\cdot\boldsymbol{k})^{n-1}. \tag{3.83}$$

If we then write the dot-products in component form, we can isolate a multipole moment operator

$$\hat{V}_a(\omega) = -\frac{\mathcal{E}}{2i}\left(\hat{Q}_p^{[1]}\tilde{\epsilon}_p + \sum_{n=1}^{\infty}i^n\tilde{\epsilon}_p k_{j_1}k_{j_2}\cdots k_{j_n}\hat{X}^{[n]}_{j_1\cdots j_n;p}\right), \tag{3.84}$$

which is expressed as

$$\hat{X}^{[n]}_{j_1\cdots j_n;p} = \frac{1}{(n+1)!}\hat{Q}^{[n+1]}_{j_1\cdots j_n;p} - \frac{i}{\omega}\frac{1}{n!}\hat{m}^{[n]}_{j_1\cdots j_{n-1};r}\varepsilon_{rj_np}, \tag{3.85}$$

in terms of the electric multipole moment operator

$$\hat{Q}^{[n+1]}_{j_1\cdots j_n;p} = -er_{j_1}\cdots r_{j_n}r_p \tag{3.86}$$

and the magnetic multipole moment operator (Eqn. (3.59)). At first order, Eqn. (3.85) yields the length representation (Eqn. (3.24)) and is thus referred to as the generalized length representation.

Before proceeding with the derivation of oscillator strengths, let us first appreciate the similarities between the generalized length- and velocity representation. Similar to the previous section, we arrive at some multipole moment operator that is decomposed into an electric and magnetic component. Indeed when inserting the frequency component derivatives of the fields (Eqn. (3.62)) into the interaction operator expressed in multipolar gauge (Eqn. (3.82)), the same result as in Eqn. (3.63) can be obtained. However, in multipolar gauge, these manipulations are not entirely necessary, because the separation of electric- and magnetic components could also have been inferred from the structure of the potentials (Eqs. (3.71) and (3.77)), thus reflecting how this separation is inherent to multipolar gauge.

Due to the similarities between both representations, the n-th order oscillator strength in the generalized length representation is almost identical to Eqn. (3.64)

$$f^{[n]}(\omega) = i^n\frac{2m_e\omega}{\hbar e^2}\left(\frac{\omega}{c}\right)^n\sum_{m=0}^{n}(-1)^m\tilde{\epsilon}_p\tilde{\epsilon}_q e_{k;j_1}e_{k;j_2}\cdots e_{k;j_n}\langle f|\hat{X}^{[n-m]}_{j_1\cdots j_{n-m};p}(\omega)|i\rangle\langle f|\hat{X}^{[m]}_{j_1\cdots j_m;q}(\omega)|i\rangle^*, \tag{3.87}$$

with the only difference being the definition of the multipole moment operator. Furthermore, from considerations of time-reversal symmetry it follows that the absorption of linearly polarized light only contains even-order contributions, whereas circular dichroism only depends on the odd-order ones, in accordance with the results from Section 3.4.2. However, an important distinction between the two representation is that at face-value, the n-th order oscillator strength in the generalized length representation is not origin independent. The arguments proposed in Section 3.4.1, do not necessarily apply to Eqn. (3.87), due to the structure of the generalized length representation. At order n, the electric multipole moment is constructed from $n+1$ position operators, whereas the magnetic multipole moment contains n position operators. This in contrast to the generalized velocity representation where both operators contain the same amount of position operators, resulting in the simple origin dependence provided by Eqn. (3.31). The more complicated origin dependence of the generalized length representation prohibits the exact cancellation between origin dependent terms, as described in Section 3.4.1. It has been shown by Lindh *et al.* that gauge-origin independence can be achieve by using Eqn. (3.24) (or Eqn. (3.26) in a non-relativistic framework) to convert the current density operator in the magnetic multipole moment into a position operator, which is referred to as the 'correct length gauge' by the authors.[30, 150] However, they also note that although the result is indeed origin independent, the integrals required for these calculations are rather cumbersome, which renders this approach impractical.

3.6 Connecting the Generalized Length- and Velocity Representation

At this point it seems that the generalized velocity representation is preferred over the generalized length representation, due to the gauge-origin independence of the former. However, in this section, I will show that the two representations are two sides of the same coin, although their equivalence only holds in an exact-state formalism. Indeed when applying approximate methods, such as SCF theory, both representations may give different results. Therefore, this section will be devoted to the connection between both representations. In other words, I will find the conditions that dictate when both representations produce the same oscillator strengths. In previous sections, the distinction between exact- and approximate-state theory is less relevant, as the results are equally valid in both cases. However, in the current section, this distinction becomes essential. I will thus divide this section into two parts: the first one being devoted to exact-state theory and the second to approximate-state theory.

3.6.1 Exact-State-Formalism: a Gauge Theoretical Approach

As a starting point, I recall that the potentials corresponding to the generalized length representation are expressed in multipolar gauge, whereas the potentials are expressed in Coulomb gauge for the generalized velocity representation. On a classical level, we know that both sets of potentials yield the same fields, since they are related by a gauge transformation. In a quantum mechanical framework, a similar effect can be achieved by the action of local unitary operators[99, 160, 161]

$$U(\boldsymbol{r},t) = e^{\frac{i}{\hbar}e\chi(\boldsymbol{r},t)}; \quad U^{\dagger}(\boldsymbol{r},t)U(\boldsymbol{r},t) = \hat{I} \tag{3.88}$$

where χ is the same gauge function as the one from classical theory. This operator is local in the sense that for every point in space, a different unitary transformation is defined that is connected continuously to its local neighbourhood.

Inserting the identity operator into the time-dependent Dirac equation

$$\left(\hat{h}_D - i\hbar\partial_t\right)U^{\dagger}(\boldsymbol{r},t)U(\boldsymbol{r},t)\psi(\boldsymbol{r},t) = 0, \tag{3.89}$$

and multiply on the left with $\hat{U}(\boldsymbol{r},t)$ thus allows us to transform this equation according to our local unitary operator

$$\left(\hat{h}_D - i\hbar\partial_t\right)\psi(\boldsymbol{r},t) = 0 \rightarrow \left(\hat{h}'_D - i\hbar\partial_t\right)\psi'(\boldsymbol{r},t) = 0, \tag{3.90}$$

where appears the transformed wave function

$$\psi'(\boldsymbol{r},t) = U(\boldsymbol{r},t)\psi(\boldsymbol{r},t) \tag{3.91}$$

and the transformed Hamiltonian

$$\hat{h}'_D = U\hat{h}_D U^{\dagger} - i\hbar U\partial_t(U^{\dagger}) = U\hat{h}_D U^{\dagger} - e\partial_t\chi(\boldsymbol{r},t). \tag{3.92}$$

Using the Baker-Campbell-Hausdorf expansion, introduced in Eqn. (1.57), the transformed Hamiltonian can be expressed as

$$\hat{h}'_D = \hat{h}_D - e\partial_t \chi(\boldsymbol{r},t) + e\frac{i}{\hbar}\big[\chi(\boldsymbol{r},t),\hat{h}_D\big] + \frac{e^2}{2\hbar^2}\big[\chi(\boldsymbol{r},t),[\chi(\boldsymbol{r},t),\hat{h}_D]\big] + \cdots . \tag{3.93}$$

Using the commutator identity $[\hat{\boldsymbol{p}}, f(\boldsymbol{r})] = -i\hbar\boldsymbol{\nabla} f(\boldsymbol{r})$, it can be shown that the first commutator term in this expansion evaluates to

$$e\frac{i}{\hbar}\big[\chi(\boldsymbol{r},t),\hat{h}_D\big] = -ec\boldsymbol{\alpha}\cdot\boldsymbol{\nabla}\chi(\boldsymbol{r},t). \tag{3.94}$$

This relation also implies that any higher-order commutator vanishes, as this expression commutes with any multiplicative operator. Therefore, the transformed Hamiltonian reads

$$\hat{h}'_D = \beta m_e c^2 + c\boldsymbol{\alpha}\cdot\big(\hat{\boldsymbol{p}} + e(\boldsymbol{A} - \boldsymbol{\nabla}\chi(\boldsymbol{r},t))\big) - e(\phi + \partial_t\chi(\boldsymbol{r},t)), \tag{3.95}$$

which is equivalent to substituting with gauge-transformed potentials. As a main advantage, this procedure allows us the track the changes of the wave function induced by the transformation of the potentials. This derivation could also have been carried out in a non-relativistic framework, which yields the same end result, although the commutators vanish at third order and higher.

Because these transformations only affect the interaction operator, we can re-express Eqn. (3.93) as

$$\hat{V}'(t) = \hat{V}(t) - e\partial_t\chi(\boldsymbol{r},t) + e\frac{i}{\hbar}\big[\chi(\boldsymbol{r},t),\hat{h}_D\big], \tag{3.96}$$

which can be decomposed in terms of frequency components

$$\hat{V}'(\omega) = \hat{V}(\omega) + ei\omega\chi(\boldsymbol{r},\omega) + e\frac{i}{\hbar}\big[\chi(\boldsymbol{r},\omega),\hat{h}_D\big]. \tag{3.97}$$

What thus remains is to assess how transition moments change upon this gauge transformation. The two states involved in transition moments are stationary states of the zeroth order Hamiltonian, which does not depend on the light–matter interaction and is hence unaffected by this gauge transformation. From these considerations it can thus be concluded that gauge transformations leave transition moments unchanged, since we have

$$\begin{aligned}\langle f|ei\omega\chi(\boldsymbol{r},\omega)|i\rangle + \langle f|e\frac{i}{\hbar}\big[\chi(\boldsymbol{r},\omega),\hat{h}_D\big]|i\rangle &= \langle f|ei\omega\chi(\boldsymbol{r},\omega)|i\rangle + e\frac{iE_i}{\hbar}\langle f|\chi(\boldsymbol{r},\omega)|i\rangle \\ &\quad - e\frac{iE_f}{\hbar}\langle f|\chi(\boldsymbol{r},\omega)|i\rangle = 0,\end{aligned} \tag{3.98}$$

where I have assumed exact-state- and resonance ($\omega = \omega_{fi}$) conditions.

When transforming the interaction operator from the Coulomb gauge to multipolar gauge, we have to use the gauge function provided by Eqn. (3.72). In this derivation, I will set $\boldsymbol{a} = 0$, implying the following frequency component of the gauge function

$$\chi(\boldsymbol{r},\omega) = -\frac{\mathcal{E}}{2\omega}\sum_{n=0}^{\infty}\frac{1}{(n+1)!}(i\boldsymbol{r}\cdot\boldsymbol{k})^n(\boldsymbol{r}\cdot\tilde{\boldsymbol{\epsilon}}) = \frac{\mathcal{E}}{2e\omega}\sum_{n=0}^{\infty}\frac{i^n}{(n+1)!}\tilde{\epsilon}_p k_{j_1}k_{j_2}\cdots k_{j_n}\hat{Q}^{[n+1]}_{j_1\cdots j_n;p}, \tag{3.99}$$

where in the last equality, I have inserted the definition of the generalized length representation electric-multipole moments. Using this gauge function, Eqn. (3.97) assumes the form

$$\hat{V}_a(\omega) = -\frac{\mathcal{E}}{2}\sum_{n=0}^{\infty} i^{n-1} k_{j_1} k_{j_2} \cdots k_{j_n} \tilde{\epsilon}_p \left[\hat{\mathcal{X}}^{[n]}_{j_1 \cdots j_n;p}(\omega) + \frac{1}{(n+1)!} \hat{Q}^{[n+1]}_{j_1 \cdots j_n;p} + \frac{1}{\hbar\omega}\frac{1}{(n+1)!} \left[\hat{Q}^{[n+1]}_{j_1 \cdots j_n;p}, \hat{h}_D \right] \right], \tag{3.100}$$

where the commutator evaluates to

$$\frac{1}{\hbar\omega}\left[\tilde{\epsilon}_p k_{j_1} \cdots k_{j_n} \hat{Q}^{[n+1]}_{j_1 \cdots j_n p}, \hat{h}_D \right] = -\tilde{\epsilon}_p k_{j_1} \cdots k_{j_n} \hat{\mathcal{Q}}^{[n+1]}_{j_1 \cdots j_n p}. \tag{3.101}$$

Upon insertion of this operator into the transformed operator, we obtain

$$\hat{V}_a(\omega) = -\frac{\mathcal{E}}{2}\sum_{n=0}^{\infty} i^{n-1} k_{j_1} k_{j_2} \cdots k_{j_n} \tilde{\epsilon}_p \hat{X}^{[n]}_{j_1 \cdots j_n;p}(\omega), \tag{3.102}$$

which is equivalent to Eqn. (3.82) up to a phase factor.

It should be noted that this transformation only affects the electric multipole moment, whereas the magnetic multipole moment remains unchanged. As a shortcut to these lengthy manipulations, we can combine Eqs. (3.98) and Eqn. (3.101), which directly relates the electric-multipole moments in the two representations

$$\langle f | \tilde{\epsilon}_p k_{j_1} \cdots k_{j_n} \hat{Q}^{[n+1]}_{j_1 \cdots j_n p} | i \rangle = \frac{1}{\hbar\omega_{fi}} \langle f | \left[\hat{h}_D, \tilde{\epsilon}_p k_{j_1} \cdots k_{j_n} \hat{Q}^{[n+1]}_{j_1 \cdots j_n p} \right] | i \rangle = \langle f | \tilde{\epsilon}_p k_{j_1} \cdots k_{j_n} \hat{\mathcal{Q}}^{[n+1]}_{j_1 \cdots j_n p} | i \rangle. \tag{3.103}$$

The gauge transformation and the commutator identity shown above can be used interchangeably to convert transition moments, since they are derived from the same principles. Even though the above results demonstrate that we can replace gauge transformations with commutator relations, such as Eqn. (3.103), the converse is not always the case. For example, the 'correct length gauge', as discussed by Lindh *et al.*, transforms operators through commutator identities, although it is not directly related to a gauge transformation.[30, 150]

Starting from the n-th order oscillator strength in the generalized length representation (Eqn. (3.87)), Eqn. (3.103) can be used to convert it into the generalized velocity representation using the above relation. From the fact that the latter is origin-independent, it thus follows that the former shares this feature. However, similar to Eqn. (3.85), these relations are only valid for exact states, whereas special considerations are needed for approximate state theories. In the following section, I will connect the generalized length- and velocity representations for SCF theory. Instead of using the gauge transformation outlined above, I will directly use Eqn. (3.103), thus significantly simplifying the derivation. For a conversion based on explicit gauge transformations, the reader should consult ref. 162.

3.6.2 Conversion at the SCF Level

In this section, I will demonstrate that the *generalized* length and velocity representation can be interconverted at the SCF linear-response level of theory. Besides the necessity of a complete basis set, the conversion generally depends on the level of theory, requiring special considerations for each electronic structure method. For truncated cluster expansions, for example, the two representations are not equivalent, as demonstrated by Pedersen and Koch.[163] This conversion has been carried out successfully at the TD-HF,[46] non-hybrid TDDFT[162] and MCSCF[164] level of theory. However, all these derivations assume the electric-dipole approximation, whereas here, I will extend it for electric-multipole moments to arbitrary order and for that matter, any multiplicative operator. To keep the derivation as general as possible, I will make the following substitutions: $\hat{\Omega} = \tilde{\epsilon}_p k_{j_1} \cdots k_{j_n} \hat{Q}^{[n+1]}_{j_1 \cdots j_n p}$ and $\hat{\Gamma} = \tilde{\epsilon}_p k_{j_1} \cdots k_{j_n} \hat{\mathcal{Q}}^{[n+1]}_{j_1 \cdots j_n p}$. Furthermore, I will treat the TD-HF and TDDFT case separately, as it turns out that slightly different conditions apply to these two cases.

For approximate methods, the second equality in Eqn. (3.103) does not always hold. In the basis set approximation, operators are represented as matrices and commutators of such matrices are only equal to the exact commutator in the complete basis set limit (more precise conditions are given in Ref.165). Furthermore, approximate states are not eigenstates of the exact Hamiltonian, hence implying that the first equality in Eqn. (3.103) does not apply either. This falsely suggests that in the complete basis set limit, transition moments in the length and velocity representation should not be equal at the SCF level of theory. In practice, however, it has been observed that electric dipole transition moments in the two representations become nearly equal for large basis sets.[29, 30, 33, 1] Assuming that the complete basis-set limit applies, I will demonstrate under which conditions these representations are strictly equivalent at the SCF level of theory. I will start with TD-HF theory, since the discussion of this theory is less complicated than TDDFT.

Let us first multiply Eqn. (1.121) with the eigenvalue of the solution vector of the generalized eigenvalue problem (Eqn. (1.114)) and insert the square of the generalized metric

$$\hbar\omega_{fi}\mathbf{X}^{\dagger}\mathbf{E}_{\Omega} = \hbar\omega_{fi}\mathbf{X}^{\dagger}S^{[2]}S^{[2]}\mathbf{E}_{\Omega}. \tag{3.104}$$

We can now substitute the generalized eigenvalue equation in this expression

$$\hbar\omega_{fi}\mathbf{X}^{\dagger}\mathbf{E}_{\Omega} = \begin{pmatrix} \boldsymbol{Z}^{\dagger} & \boldsymbol{Y}^{T} \end{pmatrix} \begin{pmatrix} A & B \\ B^{*} & A^{*} \end{pmatrix} \begin{pmatrix} \boldsymbol{g}_{\Omega} \\ -\boldsymbol{g}_{\Omega}^{*} \end{pmatrix}. \tag{3.105}$$

After working out the matrix multiplications and grouping together the various commutators we obtain

$$\hbar\omega_{fi}\mathbf{X}^{\dagger}\mathbf{E}_{\Omega} = \sum_{ai} \left(Z_{ai}^{*} \langle \Phi_i^a | \left[\hat{H}, \hat{\Omega}^{\text{ov}} \right] | \Phi_0 \rangle + Y_{ai} \langle \Phi_0 | \left[\hat{H}, \hat{\Omega}^{\text{ov}} \right] | \Phi_i^a \rangle \right), \tag{3.106}$$

where appears the reduced operator

$$\hat{\Omega}^{\text{ov}} = \Omega_{ai}\hat{a}_a^{\dagger}\hat{a}_i + \Omega_{ai}^{*}\hat{a}_i^{\dagger}\hat{a}_a \tag{3.107}$$

in which occupied-occupied (oo) and virtual-virtual (vv) blocks of Ω_{pq} are zero. In the following, it will be shown that in Eqn. (3.106) the reduced operator can be replaced with the full operator $\hat{\Omega}$. For these purposes, let us first consider the commutator of the Hamiltonian and the full operator and recognize that it assumes the structure

$$[\hat{H}, \hat{\Omega}] = h_{pq}^{\Omega} a_p^{\dagger} a_q + \frac{1}{4}\mathcal{L}_{pq,rs}^{\Omega} a_p^{\dagger} a_r^{\dagger} a_s a_q, \tag{3.108}$$

where the one-index transformed integrals are defined as

$$\begin{array}{rcl} h^{\Omega}_{pq} & = & \Omega_{pt}h_{tq} - h_{pt}\Omega_{tq} \\ \mathcal{L}^{\Omega}_{pq,rs} & = & \Omega_{pt}\mathcal{L}_{tq,rs} - \mathcal{L}_{pt,rs}\Omega_{tq} + \Omega_{rt}\mathcal{L}_{pq,ts} - \mathcal{L}_{pq,rt}\Omega_{ts} \end{array} \tag{3.109}$$

in terms of the anti-symmetrized two-electron integrals

$$\mathcal{L}_{pq,rs} = (pq|rs) - (pr|qs). \tag{3.110}$$

To assess whether the full and reduced operator give the same result, I will proceed to compute the matrix elements from Eqn. (3.108) which is constructed from the full operator. These matrix elements can be conveniently expressed in terms of the Fock matrix and the anti-symmetrized two-electron integrals

$$\langle\Phi_i^a|\left[\hat{H},\hat{\Omega}\right]|\Phi_0\rangle = \sum_t \left[\Omega_{at}F_{ti} - F_{at}\Omega_{ti} + \Omega_{jt}\mathcal{L}_{ai,tj} - \mathcal{L}_{ai,jt}\Omega_{tj}\right]. \tag{3.111}$$

Here one should note that in the complete basis set limit resolution of the identity, $\sum_t |t\rangle\langle t| = 1$, gives equivalence with the commutator $\left[\hat{H},\hat{\Omega}\right]$ in first quantization. Next, due to the variational condition, i.e. $F_{ia} = 0$, the terms depending on the oo and vv block of $\hat{\Omega}$ vanish

$$\langle\Phi_i^a|\left[\hat{H},\hat{\Omega}\right]|\Phi_0\rangle = \sum_j \Omega_{aj}F_{ji} - \sum_b F_{ab}\Omega_{bi} + \sum_{jb}\left[\Omega_{jb}\mathcal{L}_{ai,bj} - \mathcal{L}_{ai,jb}\Omega_{bj}\right]. \tag{3.112}$$

The remaining terms thus depend only on the occupied-virtual/virtual-occupied blocks of $\hat{\Omega}$. I have thereby demonstrated the equivalence of matrix elements $\langle\Phi_i^a|\left[\hat{H},\hat{\Omega}\right]|\Phi_0\rangle$ and $\langle\Phi_i^a|\left[\hat{H},\hat{\Omega}^{\mathrm{ov}}\right]|\Phi_0\rangle$. However, this is only valid if the summation in Eqn. (3.107) is complete over these blocks, which is not always the case when certain approximation schemes are employed. In Section C.4, I will describe the restricted excitation window approach, which is an important example that violates this condition.

In conclusion, I have made the following identification

$$\hbar\omega_{fi}\mathbf{X}^{\dagger}\mathbf{E}_{\Omega} = \mathbf{X}^{\dagger}\mathbf{E}_{[H,\Omega]} = \mathbf{X}^{\dagger}\mathbf{E}_{\Gamma}, \tag{3.113}$$

where $\mathbf{E}^{[1]}_{[H,\Omega]}$ and $\mathbf{E}^{[1]}_{\Gamma}$ are the property gradients derived from the operators $[\hat{H},\hat{\Omega}]$ and $\hat{\Gamma}$, respectively. Note that the second equality only holds in the complete basis set limit.

When extending this derivation to the TDDFT domain, there seems to be one major obstacle: DFT is not expressed in terms of the exact Hamiltonian (see Section 1.3). A first guess to circumvent this problem, would be to replace the Hamiltonian operator in Eqn. (3.103) with the Kohn-Sham Fock operator. In the canonical case, that is, $\hat{F}^{KS}|\phi_p\rangle = \varepsilon_p|\phi_p\rangle$, we do find that

$$\langle\varphi_a|\left[\hat{F}^{KS},\hat{\Omega}\right]|\varphi_i\rangle = (\varepsilon_a - \varepsilon_i)\langle\varphi_a|\hat{\Omega}|\varphi_i\rangle. \tag{3.114}$$

However, if we select $-i\hbar\hat{\Omega} = \mathbf{r}$, the commutator $\left[\hat{F}^{KS},\hat{\Omega}\right]$ not only gives the velocity operator, $\hat{\mathbf{p}}/m$ in the non-relativistic case, but for hybrid functionals also an exchange contribution, as observed already by Fock in the context of HF theory.[166] Notwithstanding, observing that the above difference of eigenvalues of the Kohn-Sham Fock operator appear in the diagonal blocks of the electronic Hessian in the canonical case together with the exchange contribution

$$A_{ai,bj} = \delta_{ij}\delta_{ab}(\varepsilon_a - \varepsilon_i) + (ai|jb) - \gamma(ab|ji) + W_{xc;ai,jb}, \tag{3.115}$$

hints at a fortuitous cancellation of terms, as realized by Starace[167] and Harris[168] in the context of TDHF. The following section is largely based on their derivations.

As a first step, I will rewrite the electronic Hessian (Eqn. (1.109)) as

$$\begin{aligned} A_{ai,bj} &= \langle 0| \Big[-a_i^\dagger a_a, \Big[a_b^\dagger a_j, \hat{F}^{KS} \Big]\Big] |0\rangle + W_{xc;ai,jb} + (ai|jb) - \gamma(ab|ji) \\ B_{ai,bj} &= \langle 0| \Big[a_i^\dagger a_a, \Big[a_j^\dagger a_b, \hat{F}^{KS} \Big]\Big] |0\rangle + W_{xc;ai,bj} + (ai|bj) - \gamma(aj|bi). \end{aligned} \tag{3.116}$$

Following a similar procedure as in the previous paragraph, the eigenvalue equation of this Hessian (Eqn. (3.104)) can be inserted into the TDDFT transition moments, yielding the following expression

$$\begin{aligned} \hbar\omega_{n0}\boldsymbol{X}^\dagger \boldsymbol{E}_\Omega = {} & Z_{ai}^* \langle \Phi_i^a | \Big[\hat{F}^{KS}, \hat{\Omega}^{\text{ov}} \Big] |\Phi_0\rangle + Y_{ai} \langle \Phi_0 | \Big[\hat{F}^{KS}, \hat{\Omega}^{\text{ov}} \Big] |\Phi_i^a\rangle \\ & + Z_{ai}^* W_{xc;ai,jb}\Omega_{bj} + Z_{ai}^*(ai|jb)\Omega_{bj} - \gamma Z_{ai}^*(ab|ji)\Omega_{bj} \\ & - Z_{ai}^* W_{xc;ai,bj}\Omega_{bj}^* - Z_{ai}^*(ai|bj)\Omega_{bj}^* + \gamma Z_{ai}^*(aj|bi)\Omega_{bj}^* \\ & + Y_{ai} W_{xc;jb,ia}\Omega_{bj} + Y_{ai}(jb|ia)\Omega_{bj} - \gamma Y_{ai}(ib|ja)\Omega_{bj} \\ & - Y_{ai} W_{xc;bj,ia}\Omega_{bj}^* - Y_{ai}(bj|ia)\Omega_{bj}^* + \gamma Y_{ai}(ij|ba)\Omega_{bj}^*. \end{aligned} \tag{3.117}$$

Furthermore, it can be demonstrated straightforwardly that the reduced operator can be replaced with the full operator if the variational condition applies, i.e. $F_{ai}^{KS} = 0$

$$\langle \Phi_i^a | \Big[\hat{F}^{KS}, \hat{\Omega} \Big] |0\rangle = F_{at}^{KS}\Omega_{ti} - \Omega_{at}F_{ti}^{KS} = F_{ab}^{KS}\Omega_{bi} - \Omega_{aj}F_{ji}^{KS}. \tag{3.118}$$

However, it is less clear what we should do about all these additional terms involving the exchange-correlation kernel and the two-electron integrals. As alluded to before, some of these terms may cancel with the additional contributions stemming from the commutator involving the Kohn-Sham Fock operator. To verify this, I will closer inspect this commutator in the limit of a complete basis set. By virtue of this assumption, the operators expressed in second quantization become equivalent to the corresponding first-quantized operator. Furthermore, the commutator of these two operators evaluates to a one-electron operator, reducing the many-body integral to an orbital integral according to the Slater-Condon rules

$$\langle \Phi_i^a | \Big[\hat{F}^{KS}, \hat{\Omega} \Big] |0\rangle = \int d^3\boldsymbol{r} \phi_a^\dagger(\boldsymbol{r}) \Big[\hat{F}^{KS}, \hat{\Omega} \Big] \phi_i(\boldsymbol{r}). \tag{3.119}$$

This commutator can be further simplified by recognizing that the local terms inside $\hat{F}^{KS}$ commute with $\hat{\Omega}$, thus leaving us with the following two non-vanishing terms

$$\int d^3\boldsymbol{r} \phi_a^\dagger(\boldsymbol{r}) [\hat{F}^{KS}, \hat{\Omega}] \phi_i(\boldsymbol{r}) = \int d^3\boldsymbol{r} \phi_a^\dagger(\boldsymbol{r}) \Big[\hat{T}_s, \hat{\Omega} \Big] \phi_i(\boldsymbol{r}) - \gamma \int d^3\boldsymbol{r} \phi_a^\dagger(\boldsymbol{r}) \Big[\hat{K}, \hat{\Omega} \Big] \phi_i(\boldsymbol{r}), \tag{3.120}$$

where appears the exchange operator, $\hat{K}$, which is a non-local operator defined as

$$\hat{K}\phi_p(\boldsymbol{r}) = \sum_j \phi_j(\boldsymbol{r}) \int d^3\boldsymbol{r}' \frac{\phi_j^*(\boldsymbol{r}')\phi_p(\boldsymbol{r}')}{|\boldsymbol{r}-\boldsymbol{r}'|}. \tag{3.121}$$

The first of these commutators gives the same result as Eqn. (3.103), whereas the latter term contains the exchange contributions discussed earlier. Expanding the latter commutator yields the following result

$$-\gamma \int d^3\boldsymbol{r}\phi_a^\dagger(\boldsymbol{r})\left[\hat{K},\hat{\Omega}\right]\phi_i(\boldsymbol{r}) = \gamma \int d^3\boldsymbol{r} \int d^3\boldsymbol{r}'\phi_a^\dagger(\boldsymbol{r})\phi_j(\boldsymbol{r})\frac{\hat{\Omega}-\hat{\Omega}'}{|\boldsymbol{r}-\boldsymbol{r}'|}\phi_j^\dagger(\boldsymbol{r}')\phi_i(\boldsymbol{r}'). \tag{3.122}$$

Using an approach inspired by the work of Harris[168], it can be shown that this expression cancels with exchange terms in Eqn. (3.117). For these purposes, consider the third violating term in this equation

$$(ab|ji)\Omega_{bj} = (ji|ab)\Omega_{bj} = \int d^3\boldsymbol{r} \int d^3\boldsymbol{r}' \int d^3\boldsymbol{r}''\phi_j^\dagger(\boldsymbol{r})\phi_i(\boldsymbol{r})\frac{1}{|\boldsymbol{r}-\boldsymbol{r}'|}\phi_a^\dagger(\boldsymbol{r}')\phi_b(\boldsymbol{r}')\phi_b^*(\boldsymbol{r}'')\hat{\Omega}''\phi_j(\boldsymbol{r}''). \tag{3.123}$$

The resolution of the identity can be inserted in the summation over the virtual orbitals,

$$\sum_i \phi_i(\boldsymbol{r}')\phi_i^\dagger(\boldsymbol{r}'') + \sum_a \phi_a(\boldsymbol{r}')\phi_a^\dagger(\boldsymbol{r}'') = \delta(\boldsymbol{r}'-\boldsymbol{r}''), \tag{3.124}$$

yielding the result

$$(ab|ji)\Omega_{bj} = \int d^3\boldsymbol{r} \int d^3\boldsymbol{r}'\phi_j^\dagger(\boldsymbol{r}')\phi_i(\boldsymbol{r}')\frac{\hat{\Omega}}{|\boldsymbol{r}-\boldsymbol{r}'|}\phi_a^\dagger(\boldsymbol{r})\phi_j(\boldsymbol{r}) - (ji|ak)\Omega_{kj}. \tag{3.125}$$

Likewise, the sixth violating term in Eqn. (3.117) can be rewritten as

$$(aj|bi)\Omega_{bj}^* = \int d^3\boldsymbol{r} \int d^3\boldsymbol{r}'\phi_j^\dagger(\boldsymbol{r}')\phi_i(\boldsymbol{r}')\frac{\hat{\Omega}'}{|\boldsymbol{r}-\boldsymbol{r}'|}\phi_a^\dagger(\boldsymbol{r})\phi_j(\boldsymbol{r}) - (ki|aj)\Omega_{jk}. \tag{3.126}$$

Subtracting these two terms and relabelling some summation indices, gives

$$(aj|bi)\Omega_{bj}^* - (ab|ji)\Omega_{bj} = \int d^3\boldsymbol{r} \int d^3\boldsymbol{r}'\phi_j^\dagger(\boldsymbol{r}')\phi_i(\boldsymbol{r}')\frac{\hat{\Omega}'-\hat{\Omega}}{|\boldsymbol{r}-\boldsymbol{r}'|}\phi_a^\dagger(\boldsymbol{r})\phi_j(\boldsymbol{r}), \tag{3.127}$$

which exactly cancels the additional exchange terms appearing from the commutator with the Kohn-Sham Fock operator. Therefore, all violating terms in Eqn. (3.117) containing γ cancel. The remaining terms cancel amongst each other, provided that the orbitals are real. Therefore, at the TDDFT level of theory, the generalized length- and velocity representation are equivalent if simultaneously the basis set is complete *and* the orbitals are real, which is not generally the case in relativistic calculations due to the presence of spin-orbit coupling.

The findings of this section suggest that with a sufficiently large basis set, the generalized length representation should be origin-independent, because in that case the transition moments are equivalent to the generalized velocity representation. However, in its current formulation, origin dependence of the former has *never* been observed. Typically, for gauge-origins close to the coordinate origin, the two representations become equivalent with increasing basis set size, whereas equivalence is lost when the gauge-origin is displaced from the coordinate origin. At the displaced origin, the transition moments are equivalent if the following relation holds

$$\frac{1}{\hbar\omega_{fi}}\langle f|\big[\hat{h}_D, \tilde{\epsilon}_p k_{j_1}\cdots k_{j_n}\hat{Q}^{[n+1]}_{j_1\cdots j_n p}(\boldsymbol{O}+\boldsymbol{a})\big]|i\rangle = \langle f|\tilde{\epsilon}_p k_{j_1}\cdots k_{j_n}\hat{\mathcal{Q}}^{[n+1]}_{j_1\cdots j_n p}(\boldsymbol{O}+\boldsymbol{a})|i\rangle, \tag{3.128}$$

where the length representation electric multipole moment transforms as

$$\tilde{\epsilon}_p k_{j_1}\cdots k_{j_n}\hat{Q}^{[n+1]}_{j_1\cdots j_n p}(\boldsymbol{O}) \rightarrow \tilde{\epsilon}_p k_{j_1}\cdots k_{j_n}\hat{Q}^{[n+1]}_{j_1\cdots j_n p}(\boldsymbol{O}+\boldsymbol{a}) = \sum_{m=0}^{n}\frac{1}{m!}(\boldsymbol{k}\cdot\boldsymbol{a})^m\tilde{\epsilon}_p k_{j_1}\cdots k_{j_{n-m}}\hat{Q}^{[n-m+1]}_{j_1\cdots j_{n-m}p}(\boldsymbol{O}), \tag{3.129}$$

thus implying that lower-order commutation relations should also hold to connect both representations. It is very demanding for a given basis set to obey all these commutators simultaneously, inducing small differences between the transition moments in both representations, which prohibit cancellation between the origin-dependent terms in the oscillator strength. It appears that origin independence in the length representation is only possible if alternative schemes are employed, based on either London orbitals[169] or a singular value decomposition of the rotational strength tensor[170, 171] (see Eqn. (3.152) for a definition of this tensor).

3.7 Rotational Averaging

Until now it has been tacitly assumed that the relative orientation between our molecule and the electromagnetic field is fixed in space. Such a model can be related experimentally to an ensemble of non-interacting molecules that are not moving and all pointing in the same direction. However, this situation is rather artificial, as molecules are allowed to rotate and tumble freely in more realistic samples such as gases and liquids (see Fig. 3.7). Therefore, due to this motion, the absorption measured from experiment is an average of all possible orientations. From a mathematical point of view, this is completely equivalent to fixing a molecule in space and averaging over every possible polarization and propagation direction of light.

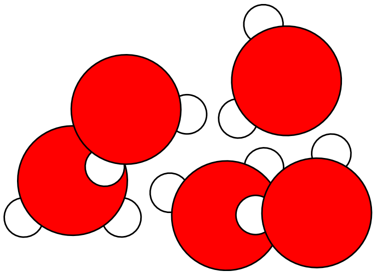

Figure 3.5: Schematic representation of an ensemble of freely moving water molecules.

The fixed molecular frame is spanned by the unit vectors $(\boldsymbol{e}_x, \boldsymbol{e}_y, \boldsymbol{e}_z)$. For convenience the wave vector is aligned with the radial unit vector

$$\boldsymbol{e}_k = \boldsymbol{e}_r = \boldsymbol{e}_x \sin\theta\cos\phi + \boldsymbol{e}_y \sin\theta\sin\phi + \boldsymbol{e}_z \cos\theta, \tag{3.130}$$

which is defined in terms of the angles θ and ϕ (see Fig. 3.7).

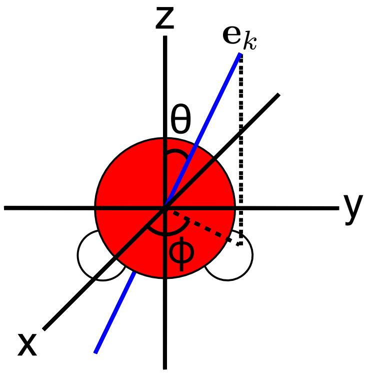

Figure 3.6: fixed molecule with variable propagation direction of light, represented by the blue line and parametrized by the angles θ and ϕ.

Furthermore, the polarization vectors $\boldsymbol{\epsilon}_1$ and $\boldsymbol{\epsilon}_2$ lie in the orthogonal plane to this vector and can thus be expressed as a linear combination of the unit vectors

$$\begin{aligned}\boldsymbol{e}_\theta &= \boldsymbol{e}_x \cos\theta\cos\phi + \boldsymbol{e}_y \cos\theta\sin\phi - \boldsymbol{e}_z \sin\theta \\ \boldsymbol{e}_\phi &= -\boldsymbol{e}_x \sin\phi + \boldsymbol{e}_y \cos\phi.\end{aligned} \tag{3.131}$$

Within this basis, the polarization vectors can be conveniently parametrized using a third angle, χ

$$\boldsymbol{\epsilon}_1 = \cos\chi \boldsymbol{e}_\theta + \sin\chi \boldsymbol{e}_\phi; \quad \boldsymbol{\epsilon}_2 = \cos\chi \boldsymbol{e}_\phi - \sin\chi \boldsymbol{e}_\theta. \tag{3.132}$$

Using the definition of these unit vectors, the oscillator strength can be expressed as a function of these three angles. In general, the rotational average of any function depending on these three angles can be calculated according to the formula

$$\langle f(\theta,\phi,\chi)\rangle_{\theta,\phi,\chi} = \frac{1}{8\pi^2}\int_0^\pi d\theta \int_0^{2\pi} d\phi \int_0^{2\pi} d\chi \sin\theta f(\theta,\phi,\chi). \tag{3.133}$$

In the following I will discuss separately how these concepts apply to the full- and truncated oscillator strength. Furthermore, I will separately treat the absorption of linearly polarized light and circular dichroism.

3.7.1 Full Oscillator Strength

I will start off with deriving an expression for the isotropically averaged absorption of linearly polarized light using the full interaction operator. Using the parametrization from the previous section, the isotropic oscillator strength reads

$$f_{iso}^{full}(\omega) = \frac{2m_e\omega}{\hbar e^2}\left\langle \langle\epsilon_p\epsilon_q\rangle_\chi \langle f|\frac{e}{\omega}c\alpha_p e^{i\boldsymbol{k}(\theta,\phi)\cdot\boldsymbol{r}}|i\rangle\langle f|\frac{e}{\omega}c\alpha_q e^{i\boldsymbol{k}(\theta,\phi)\cdot\boldsymbol{r}}|i\rangle^*\right\rangle_{\theta,\phi}, \tag{3.134}$$

where the averaging over χ can be factorized outside of the transition moment and hence evaluated analytically

$$\langle\epsilon_p\epsilon_q\rangle_\chi = \frac{1}{2}(\delta_{pq} - e_{r;p}e_{r;q}). \tag{3.135}$$

The averaging over the two other angles is more cumbersome, because the exponential form of the full interaction operator prohibits the angular dependence to be factorized outside of the transition moment. In practice, the averaging over θ and ϕ is carried out using Lebedev quadrature, which is a scheme to handle 2D angular integrals numerically.[172, 173, 174, 175, 176, 177] For this type of quadrature an angular grid is defined that preserves octahedral symmetry. Accordingly, the integral is approximated by a weighted sum of the function evaluated on the grid points

$$\langle f\rangle_{\theta,\phi} \approx \sum_{ij} w_{ij} f(\theta_i, \phi_j), \tag{3.136}$$

where the weights are found by enforcing that this scheme exactly integrates all spherical harmonics up to a given order. These weights are then tabulated, implying that we only need to know the function at a certain amount of grid points to approximate the integral.

The rotational averaging of circular dichroism follows a very similar approach, although there is one major difference: Eqn. (3.22) does not depend on χ

$$\Delta f(\omega) = -i\frac{2m_e\omega}{\hbar e^2}\left\langle e_{k;i}(\theta,\phi)\cdot\varepsilon_{ijk}\langle f|\frac{e}{\omega}c\alpha_j e^{i\boldsymbol{k}(\theta,\phi)\cdot\boldsymbol{r}}|i\rangle\langle f|\frac{e}{\omega}c\alpha_k e^{i\boldsymbol{k}(\theta,\phi)\cdot\boldsymbol{r}}|i\rangle^*\right\rangle_{\theta,\phi}. \tag{3.137}$$

The independence of this expression on the angle χ reflects the helical symmetry of circularly polarized light (Fig. 3.2). As was the case for the absorption of linearly polarized light, the rotation over θ and ϕ is performed using Lebedev quadrature.

3.7.2 Truncated Oscillator Strength

The true strength of the truncated approach becomes apparent when evaluating the rotational average, which can be carried out analytically. This procedure assumes the same form for the generalized length- and velocity representation. Therefore, I will limit myself to the latter case, although it should be kept in mind that these techniques apply to both representations. For the absorption of linearly polarized light, the isotropic average assumes the form

$$\begin{aligned} f_{iso}^{[2n]}(\omega) = \frac{2m_e\omega}{\hbar c^2}\left(\frac{\omega}{c}\right)^{2n}\sum_{m=0}^{n}(-1)^m(2-\delta_{m0})\Big\langle \langle\epsilon_p\epsilon_q\rangle_\chi e_{k;j_1}e_{k;j_2}\cdots e_{k;j_{2n}}\Big\rangle_{\theta,\phi} \\ \times Re\left[\langle f|\hat{\mathcal{X}}^{[n+m]}_{j_1\cdots j_{n-m};p}(\omega)|i\rangle\langle f|\hat{\mathcal{X}}^{[n-m]}_{j_{n-m+1}\cdots j_{2n};q}(\omega)|i\rangle^*\right], \end{aligned} \tag{3.138}$$

where the angular terms completely factorize outside of the transition moment. Therefore, the rotational averaging hinges on the calculation of the tensor $\left\langle \langle\epsilon_p\epsilon_q\rangle_\chi e_{k;j_1}e_{k;j_2}\cdots e_{k;j_{2n}}\right\rangle_{\theta,\phi}$, where the χ-dependent part assumes the same form as Eqn. (3.135)

$$\left\langle \langle\epsilon_p\epsilon_q\rangle_\chi e_{k;j_1}e_{k;j_2}\cdots e_{k;j_{2n}}\right\rangle_{\theta,\phi} = \frac{1}{2}\delta_{pq}\left\langle e_{k;j_1}e_{k;j_2}\cdots e_{k;j_{2n}}\right\rangle_{\theta,\phi} - \frac{1}{2}\left\langle e_{r;p}e_{r;q}e_{k;j_1}e_{k;j_2}\cdots e_{k;j_{2n}}\right\rangle_{\theta,\phi} \tag{3.139}$$

$$= \frac{1}{8\pi}\delta_{pq}\int_0^{2\pi} d\phi\int_0^{\pi} d\theta \sin\theta e_{k;j_1}e_{k;j_2}\cdots e_{k;j_{2n}} - \frac{1}{8\pi}\int_0^{2\pi} d\phi\int_0^{\pi} d\theta\sin\theta e_{r;p}e_{r;q}e_{k;j_1}e_{k;j_2}\cdots e_{k;j_{2n}}.$$

Therefore, we need to find expressions for integrals of the form

$$E_{uvw} = \frac{1}{8\pi}\int_0^{2\pi} d\phi\int_0^{\pi} d\theta\sin\theta e_{k;x}^{u}e_{k;y}^{v}e_{k;z}^{w}; \quad u+v+w=2n, \tag{3.140}$$

where the indices u, v and w accumulate the powers of $e_{k;i}$. In passing, it should be noted that a similar tensor is required to rotationally average the truncated circular dichroism

$$\Delta f^{[2n+1]} = \frac{2m_e\omega}{\hbar c^2}\left(\frac{\omega}{c}\right)^{2n+1}\sum_{m=0}^{n}(-1)^m\left\langle e_{k;j_1}e_{k;j_2}\cdots e_{k;j_{2n+1}}e_{k;i}\right\rangle_{\theta,\phi} \tag{3.141}$$
$$\times\, \varepsilon_{ipq}2Re\big\{\langle f|\hat{\mathcal{X}}^{[n+m+1]}_{j_1\cdots j_{n+m};p}(\omega)|i\rangle\langle f|\hat{\mathcal{X}}^{[n-m]}_{j_{n+m+1}\cdots j_{2n+1};q}(\omega)|i\rangle^*\big\}.$$

The integral in Eqn. (3.140) can be made more manageable by first rewriting it as

$$E_{uvw} = \frac{1}{8\pi}\int_0^{2\pi} d\phi\cos^u\phi\sin^v\phi\int_0^{\pi} d\theta\sin\theta\sin^{u+v}\theta\cos^w\theta \tag{3.142}$$

and then applying the relations

$$\int_0^{\pi} d\theta\cos^p\theta\sin^q\theta = \big(1+(-1)^p\big)\int_0^{\pi/2} d\theta\cos^p\theta\sin^q\theta \tag{3.143}$$
$$\int_0^{2\pi} d\phi\cos^p\phi\sin^q\phi = \big(1+(-1)^p\big)\big(1+(-1)^q\big)\int_0^{\pi/2} d\phi\cos^p\phi\sin^q\phi,$$

such that the integral only needs to be evaluated in the $(+,+,+)$ octant of Euclidian space

$$E_{uvw} = \frac{1}{8\pi}\big(1+(-1)^u\big)\big(1+(-1)^v\big)\big(1+(-1)^w\big)\int_0^{\pi/2} d\phi\cos^u\phi\sin^v\phi\int_0^{\pi/2} d\theta\cos^{u+v}\theta\sin^w\theta. \tag{3.144}$$

Therefore, this integral vanishes if any of the indices is odd. Further manipulations show that this integration factor can be expressed in terms of the trivariate beta function

$$E_{uvw} = \frac{1}{32\pi}\big(1+(-1)^u\big)\big(1+(-1)^v\big)\big(1+(-1)^w\big)B\Big(\frac{u+1}{2},\frac{v+1}{2},\frac{w+1}{2}\Big), \tag{3.145}$$

which in turn can be expressed in terms of the gamma functions

$$B(a,b,c) = \frac{\Gamma(a)\Gamma(b)\Gamma(c)}{\Gamma(a+b+c)}; \quad \Gamma(a) = 2\int_0^\infty dx e^{-x^2} x^{2a-1}. \tag{3.146}$$

The gamma function is readily available in math libraries, thus allowing straightforward implementation. As a final remark, it should be stressed that the method outlined above is much more practical than the traditional procedure based on linear combinations of fundamental Cartesian isotropic tensors.[178, 179, 180, 181, 182, 183]

It is illuminating to consider the rotationally averaged oscillator strengths to lowest orders. At $n = 0$, the absorption of linearly polarized light reads

$$f_{iso}^{[0]}(\omega) = \frac{2m_e\omega}{\hbar c^2}\left\langle \langle \epsilon_p \epsilon_q \rangle_\chi \right\rangle_{\theta,\phi} Re\left[\langle f|\hat{\mathcal{Q}}_p^{[0]}|i\rangle\langle f|\hat{\mathcal{Q}}_q^{[0]}|i\rangle^*\right], \tag{3.147}$$

where the rotational factor assumes a particularly simple form

$$\left\langle \langle \epsilon_p \epsilon_q \rangle_\chi \right\rangle_{\theta,\phi} = \frac{1}{3}\delta_{pq}, \tag{3.148}$$

thus yielding the result

$$f_{iso}^{[0]}(\omega) = \frac{2m_e\omega}{3\hbar c^2}\boldsymbol{\mathcal{Q}}^{[0]} \cdot \boldsymbol{\mathcal{Q}}^{[0]}. \tag{3.149}$$

Likewise, to first order, the circular dichroism reads

$$\Delta f_{iso}^{[1]} = \frac{4m_e\omega}{3\hbar c^2}\left(\frac{\omega}{c}\right)\varepsilon_{ipq}\langle f|\hat{\mathcal{X}}_{i;p}^{[1]}(\omega)|i\rangle\langle f|\hat{\mathcal{Q}}_q^{[0]}|i\rangle^* = \frac{8m_e\omega}{3\hbar c^2}\left(\frac{\omega}{c}\right)\frac{-i}{\omega}\boldsymbol{m}^{[1]} \cdot \boldsymbol{\mathcal{Q}}^{[1]} = R_{iso}^{[1]}, \tag{3.150}$$

which is more commonly referred to as the rotational strength. In a non-relativistic framework, it is customary to assess the effectiveness of a certain method by applying the so-called sum rules. For example, it can be argued that the sum of the dipole oscillator strengths over all possible excitations should equal the amount of electrons in the system, which is referred to as the Thomas-Reiche-Kuhn sum-rule.[184, 185, 186] Likewise, the sum of all rotational strengths should vanish.[187, 188] However, the derivation of these rules hinges on two key steps: the insertion of the resolution of the identity and the canonical commutation relation. The first step is problematic in a relativistic framework, as the resolution of the identity also includes negative-energy states. The second step can be made because one of the two dipole moments in Eqn. (3.147) is converted into the velocity representation, which is the momentum operator in the non-relativistic limit. However, in the relativistic case, the velocity representation is given by the Dirac matrices, which do not have the same commutation properties as the momentum operator. For these reasons, it is until this day unknown whether these sum rules even apply in a relativistic framework. Hence, they will not be further pursued in this thesis.

3.7.3 Angular Dependence of Truncated the Differential Oscillator Strength

In the previous section, it was shown how the anisotropic oscillator strength can be expressed as a function of the propagation- and polarization direction, which allowed us to evaluate the isotropic average. However, explicit knowledge about the angular dependence can also be used to identify directions in which the signal is unusually large, or small. Depending on the symmetry of the angular distribution, the different multipolar contribution may be isolated and identified. This information is especially relevant for ECD, where the presence of isotropic condition determine whether the signal vanishes for achiral systems, as demonstrated in Section C.1. Furthermore, due to its independence of χ, the ECD signal for all possible directions can be mapped out on the surface of a sphere. In particular, the angular dependence of the first-order truncated differential oscillator strength can be expressed in a straightforward manner

$$\begin{aligned}\Delta f^{[1]}(\theta,\phi) &= e_{k;i}R^{[1]}_{ij}e_{k;j} \qquad (3.151)\\ &= R^{[1]}_{\text{iso}} + \frac{1}{2}(R^{[1]}_{zz} - R^{[1]}_{\text{iso}})(3\cos^2\theta - 1)\\ &+ \frac{1}{2}(R^{[1]}_{xz} + R^{[1]}_{zx})\sin 2\theta\cos\phi + \frac{1}{2}(R^{[1]}_{yz} + R^{[1]}_{zy})\sin 2\theta\sin\phi\\ &+ \frac{1}{2}(R^{[1]}_{xx} - R^{[1]}_{yy})\sin^2\theta\cos 2\phi + \frac{1}{2}(R^{[1]}_{xy} + R^{[1]}_{yx})\sin^2\theta\sin 2\phi\end{aligned}$$

where I have introduced the rotational strength tensor $R^{[1]}_{ij}$ (cf. Ref. 189)

$$R^{[1]}_{ij} = \frac{4m_e\omega^2}{\hbar c e^2}\left(\mathbf{X}^{[1]}_j \times \mathbf{X}^{[0]}\right)_i; \quad R^{[1]}_{\text{iso}} = \frac{1}{3}(R^{[1]}_{xx} + R^{[1]}_{yy} + R^{[1]}_{zz}). \qquad (3.152)$$

From Eqn. (3.151) it can be seen that the anisotropic part of $\Delta f^{[1]}(\theta,\phi)$ is a linear combination of d-orbitals weighted by the relevant elements of the rotatory strength tensor. This can be made more explicit by rewriting the first-order differential oscillator strength as

$$\begin{aligned}\Delta f^{[1]}(\theta,\phi) = \sqrt{15}R^{[1]}_{\text{iso}}s &+ \sqrt{3}\left(R^{[1]}_{zz} - R^{[1]}_{\text{iso}}\right)d_{z^2} + \left(R^{[1]}_{xx} - R^{[1]}_{yy}\right)d_{x^2-y^2}\\ &+ \left(R^{[1]}_{xz} + R^{[1]}_{zx}\right)d_{xz} + \left(R^{[1]}_{yz} + R^{[1]}_{zy}\right)d_{yz} + \left(R^{[1]}_{xy} + R^{[1]}_{yx}\right)d_{xy}, \qquad (3.153)\end{aligned}$$

where I have used a common normalization for all solid harmonics.

From Eqn. (3.141) it is observed that rotational strength tensors can be generalized to arbitrary odd orders. It will also be seen that the differential oscillator strength $\Delta f^{[2n+1]}$ contains products of $2(n+1)$ components of the unit wave vector and is therefore spanned by spherical harmonics of *even* $\ell = 0, 2, \ldots, 2(n+1)$. The explicit equations of these distributions in terms of these spherical harmonics is rather complicated and thus will not be shown explicitly.

Having gathered all the theoretical tools to describe X-ray spectroscopies beyond the dipole approximation, we have thus reached the end of this chapter. In the following, I will proceed to demonstrate how these techniques can be applied in practice and what are the possible pitfalls associated with them.

Chapter 4

Applications

4.1 Implementation

In contemporary quantum chemistry, the formulation of theory is only half the work, since an efficient implementation is crucial to make quantum chemical calculations feasible, which often involve many tedious mathematical operations. For that reason, this section will be devoted to the implementation of both the full- and truncated light–matter interaction operator. Both of these developments have been carried out in Dirac, which is a quantum chemical code adapted to four-component relativistic calculations.[190, 37] The implementation of these interactions is still a work in progress, so below follows a statement of all the available functionalities. It is possible to carry out intensity calculations using the full- and truncated interaction operators, both under isotropic and anisotropic conditions. However, in the current implementation, ECD calculations can only be carried out using the full interaction operator, whereas the truncated ECD is still under development. The truncated ECD reported in Section 4.5, was calculated using an external script with the transition moments from Dirac as input. In the following, I will give a brief overview of the implementation of the full- and truncated interaction, highlighting their unique features. In the upcoming section and the ones that follow, this part of the code will be referred to as the BED implementation, where the abbreviation stands for beyond the electric-dipole approximation. Although this abbreviation does not necessarily apply to ECD, which at first order is already beyond this approximation, it will be used regardless for brevity's sake.

4.1.1 Full Interaction

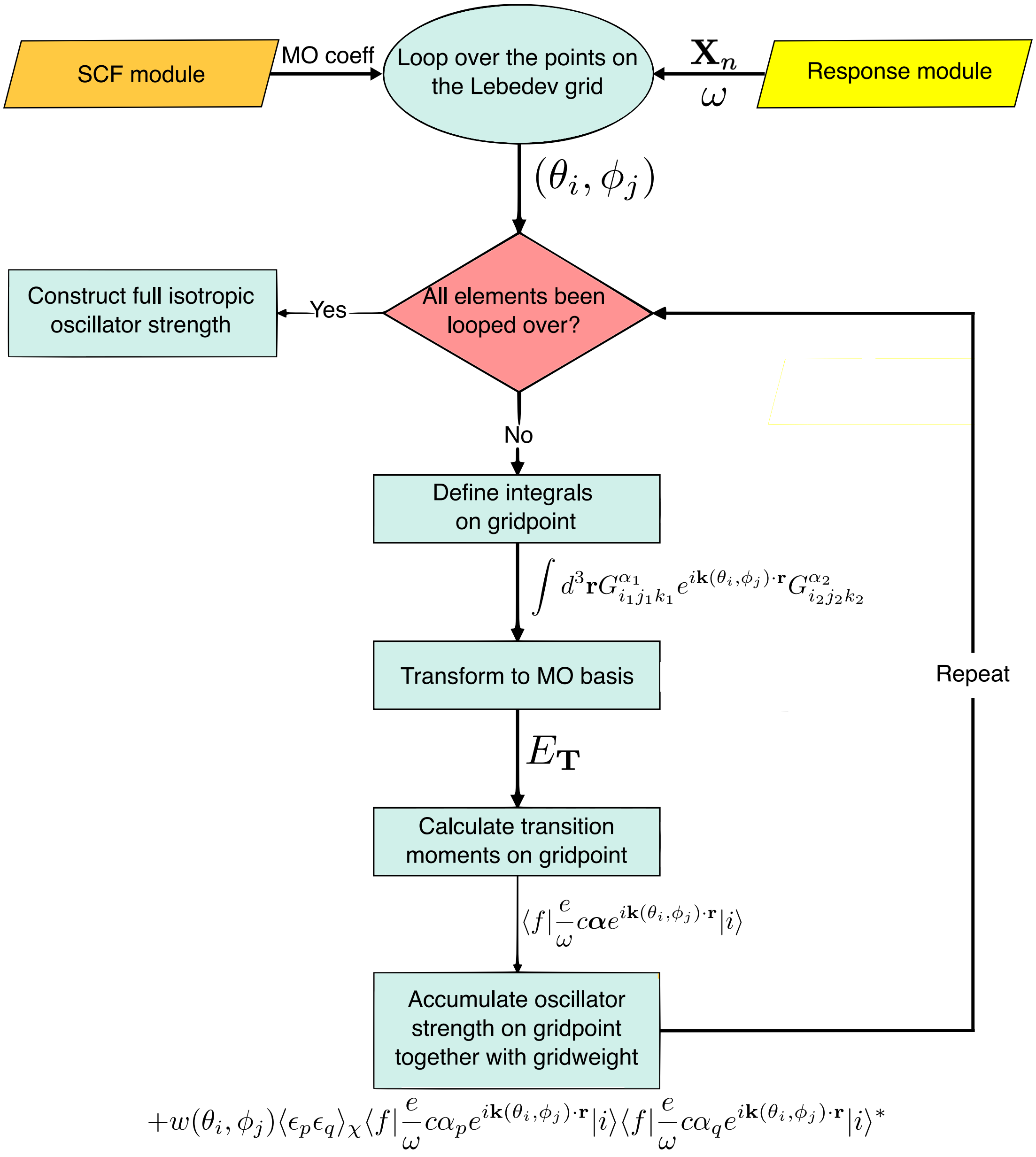

Figure 4.1: flow chart the full light–matter interaction part of the BED implementation. Rectangular boxes indicate an operation or modules, whereas the arrows and the symbols besides them indicate the output or input. $\boldsymbol{X}_n$ *and* ω *are the solution vector and frequency obtained from Eqn. (1.114). The property gradient,* $\boldsymbol{E}_T$*, is defined according to Eqn. (1.103) and (3.16).*

Figure 4.1 depicts a flow chart of the BED implementation responsible for the calculation of the full oscillator strength. In the isotropic case, the code starts with a loop over the points on the

Lebedev grid, thus sampling the various propagation directions of the incoming light. The same code applies to the anisotropic case, although in that case the loop contains only one grid point in a user-defined direction. The property integrals need to be defined on each grid point, due to the angular dependence of the full interaction operator Eqn. (3.134). These integrals are provided by the HERMIT integral package,[191] which is based on a scalar Cartesian Gaussian basis

$$G^{\alpha}_{ijk} = N^{\alpha}_{ijk} x^i y^j z^k e^{-\alpha r^2}; \quad l = i + j + k \tag{4.1}$$

where N^{α}_{ijk} is a normalization constant. Using this basis, the integrals of the full interaction assume the form

$$\begin{aligned}\int d^3\boldsymbol{r} G^{\alpha_1}_{i_1 j_1 k_1} e^{i\boldsymbol{k}\cdot\boldsymbol{r}} G^{\alpha_2}_{i_2 j_2 k_2} &= N^{\alpha_1}_{i_1 j_1 k_1} N^{\alpha_2}_{i_2 j_2 k_2} \\ \times \int_{-\infty}^{\infty} dx x^{i_1+i_2} e^{-(\alpha_1+\alpha_2)x^2} e^{ik_x x} &\int_{-\infty}^{\infty} dy y^{j_1+j_2} e^{-(\alpha_1+\alpha_2)y^2} e^{ik_y y} \int_{-\infty}^{\infty} dz z^{k_1+k_2} e^{-(\alpha_1+\alpha_2)z^2} e^{ik_z z},\end{aligned} \tag{4.2}$$

which can be identified with the Fourier transform of a Gaussian function. This identification has been realized independently in several works, e.g. ref. 31 and 192, the latter of which in the context of dynamic structure factors. This expression can be simplified by relabelling the exponents and discarding the normalization constants:

$$\begin{gathered}\int d^3\boldsymbol{r} e^{i\boldsymbol{k}\cdot\boldsymbol{r}} x^i y^j z^k e^{-ar^2} = \int_{-\infty}^{\infty} dx e^{ik_x x} x^i e^{-ax^2} \int_{-\infty}^{\infty} dy e^{ik_y y} y^j e^{-ay^2} \int_{-\infty}^{\infty} dz e^{ik_z z} z^k e^{-az^2} \\ a = \alpha_1 + \alpha_2; \quad i = i_1 + i_2; \quad j = j_1 + j_2; \quad k = k_1 + k_2\end{gathered} \tag{4.3}$$

Because this integral is equivalent for each Cartesian component, it suffices to only treat the x-component. For these purposes, it proves to be useful to start with the special case $i = 0$, which readily evaluates to

$$\int_{-\infty}^{\infty} dx e^{-ax^2} e^{ik_x x} = e^{-\frac{k_x^2}{4a}} \sqrt{\frac{\pi}{a}}. \tag{4.4}$$

Starting from above equation, the general case, i.e. $i \neq 0$, can be obtained by differentiation under the integral sign

$$\int_{-\infty}^{\infty} dx e^{ik_x x} x^n e^{-ax^2} = (-i)^n \frac{d^n}{dk_x^n}[e^{-\frac{k_x^2}{4a}} \sqrt{\frac{\pi}{a}}] = (-i)^n \frac{2\sqrt{\pi}}{(4a)^{\frac{n+1}{2}}} \frac{d^n}{dQ^n}[e^{-Q^2}] = (-i)^n \frac{2\sqrt{\pi}}{(4a)^{\frac{n+1}{2}}} e^{-Q^2} \mathcal{H}_n(Q), \tag{4.5}$$

where I have introduced the physicist's definition of the Hermite polynomials

$$\mathcal{H}_n(Q) = (-1)^n e^{-Q^2} \frac{d^n}{dQ^n}[e^{Q^2}]. \tag{4.6}$$

in terms of the dimensionless variable

$$Q = \frac{k_x}{2\sqrt{a}}. \tag{4.7}$$

Therefore, the full property integral evaluates to

$$\int d^3\boldsymbol{r} e^{i\boldsymbol{k}\cdot\boldsymbol{r}} x^i y^j z^k e^{-ar^2} = \frac{(-i)^{i+j+k} 8\pi^{\frac{3}{2}}}{(4a)^{\frac{i+j+k+3}{2}}} e^{-\frac{\omega^2}{4c^2a}} \mathcal{H}_i\left(\frac{k_x}{2\sqrt{a}}\right) \mathcal{H}_j\left(\frac{k_y}{2\sqrt{a}}\right) \mathcal{H}_k\left(\frac{k_z}{2\sqrt{a}}\right). \tag{4.8}$$

Expressed in this form, these integrals can be readily evaluated using existing analytic schemes such as McMurchie-Davidson.[31] Lindh *et al.* demonstrated an alternative scheme bases on Gauss-Hermite quadrature.[33]

One main obstacle in the implementation of these integrals is their frequency dependency. Due to the exponential shape of the interaction operator, this dependency cannot be factorized outside of the integral, thus requiring the output of a response calculation to define these integrals (see Fig. 4.1). Lindh *et al.* avoided the necessity to calculate all the frequencies by employing an interpolation scheme.[35]

In the next step of the algorithm, the property gradient

$$g_{T_p;ai} = \langle \phi_a^L | c\sigma_p e^{i\boldsymbol{k}\cdot\boldsymbol{r}} | \phi_i^S \rangle + \langle \phi_a^S | c\sigma_p e^{i\boldsymbol{k}\cdot\boldsymbol{r}} | \phi_i^L \rangle, \tag{4.9}$$

is obtained by transforming the property integrals to MO basis

$$g_{T_p;ai} = c_{\mu a}^{L*} \langle \chi_\mu^L | c\sigma_p e^{i\boldsymbol{k}\cdot\boldsymbol{r}} | \chi_\nu^S \rangle c_{\nu i}^S + c_{\mu a}^{S*} \langle \chi_\mu^S | c\sigma_p e^{i\boldsymbol{k}\cdot\boldsymbol{r}} | \chi_\nu^L \rangle c_{\nu i}^L, \tag{4.10}$$

where the implicit summation convention has been applied and the small component basis is generated according to kinetic balance (see Section 2.4.2). From the property gradient, transition moments can be computed according to Eqn. (1.121). Depending on the user input, these transition moments are then inserted in Eqn. (3.20), Eqn. (3.22) or both, yielding the anisotropic (differential) oscillator strength corresponding to the specific grid point. This result is accumulated with the grid weight, such that we end up with the isotropic (differential) oscillator strength once the loop terminates.

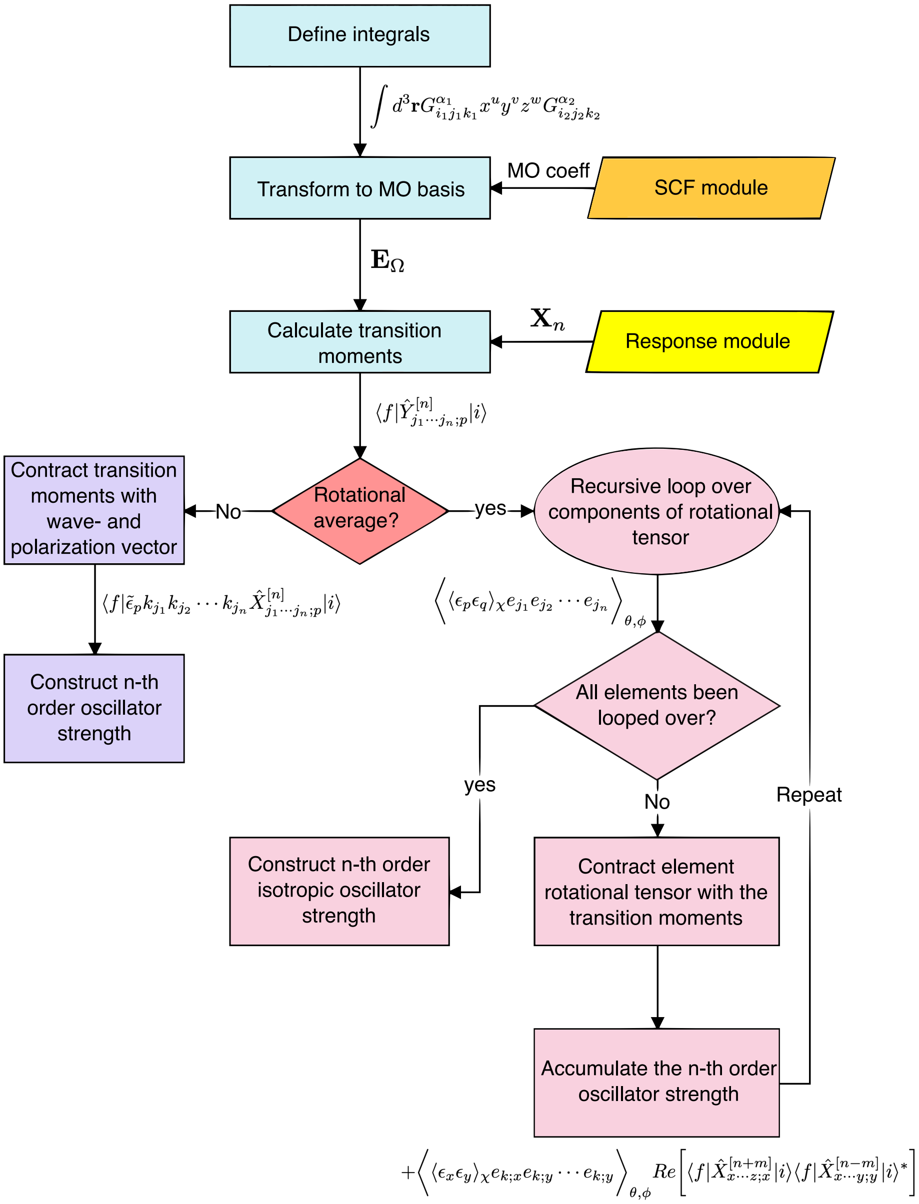

Figure 4.2: code flow chart of the implementation of the truncated light–matter interaction. The boxes indicate an operation or module, whereas the arrows and the symbols besides them indicate the output or input. Here, the operator $\hat{Y}^{[n]}$ denotes the multipole operators in either representation (Eqn. (3.57) and (3.85)) stripped of its frequency prefactors. $\boldsymbol{X}_n$ and ω are the solution vector and frequency obtained from Eqn. (1.114). The property gradient, $\boldsymbol{E}_\Omega$, is defined according to Eqn. (1.103) with $\hat{Y}^{[n]}$ as the operator.

4.1.2 Truncated Interaction

In Figure 4.2, the flowchart of the truncated BED implementation is depicted. Similar to previous case, the starting point of this chart is the generation of the property integrals. Regardless of its type, the multipole moments generally require the following integrals

$$\int d^3\boldsymbol{r} G^{\alpha_1}_{i_1j_1k_1} x^u y^v z^w G^{\alpha_2}_{i_2j_2k_2} = N^{\alpha_1}_{i_1j_1k_1} N^{\alpha_2}_{i_2j_2k_2} \times \int dx x^{i_1+i_2+u} e^{-(\alpha_1+\alpha_2)x^2} \int dy y^{j_1+j_2+v} e^{-(\alpha_1+\alpha_2)y^2} \int dz z^{k_1+k_2+w} e^{-(\alpha_1+\alpha_2)z^2}, \tag{4.11}$$

which essentially boils down to solving integrals of the form

$$\int_{-\infty}^{\infty} dx x^i e^{-ar^2} = \left(1+(-1)^i\right) \int_0^{\infty} dx x^i e^{-ar^2}, \tag{4.12}$$

where the right-hand-side can be related to the gamma function, introduced in previous section (Eqn. (3.146)). Therefore, the multipole integrals can be expressed as

$$\int d^3\boldsymbol{r} x^i y^j z^k e^{-ar^2} = \frac{1}{8}(1+(-1)^i)(1+(-1)^j)(1+(-1)^k) a^{-\frac{3+i+j+k}{2}} \Gamma\left(\frac{1+i}{2}\right) \Gamma\left(\frac{1+j}{2}\right) \Gamma\left(\frac{1+k}{2}\right), \tag{4.13}$$

where I have left out the normalization constants and relabelled the powers and the exponents. In practice, however, this relation is seldom used, as these integrals can be obtained recursively using, for example, the McMurchie-Davidson scheme. Using a similar approach as in Eqn. (4.10), the property gradient can be obtained from the associated integrals, although the exact transformation depends on whether the operator in question is diagonal or off-diagonal with respect to the large- and small component. Contrary to the full interaction, these property integrals are independent of the frequency, although the response module is still needed to compute transition moments and provide the frequency-dependent prefactor of the oscillator strength.

These transition moments are all stored in the same one-dimensional array. A hierarchical ordering is applied to this array, which principally sorts the multipole moments based on their type, then their order and then the combinations of Cartesian powers. In the following, I will consider the simplest example of the generalized length representation electric multipole moments, although this storage scheme can straightforwardly be generalized to other types of multipole moments. For these purposes, I will index this multipole moment in an alternative manner

$$Q^{[L]}_{ab} = \langle f| -e x^{L-a} y^{a-b} z^b |i\rangle, \tag{4.14}$$

which can be used to generate only the unique multipole moments of a given order. Furthermore, a and b can be understood as matrix indices that fill the lower triangle (see Fig. 4.3). Instead of explicitly storing a two-dimensional matrix, the multipole moments can be stored in a one-dimensional array, where the element (a, b) in the matrix corresponds to element $i = b + (a-1)(a-2)/2$ in the array.

$$\begin{pmatrix} x^2 & & \\ xy & xz & \\ y^2 & yz & z^2 \end{pmatrix} \qquad \begin{pmatrix} x^2 & xy & xz & y^2 & yz & z^2 \end{pmatrix}$$

Figure 4.3: Storage of the 3*-th order electric-length multipole moments. This scheme can be readily generalized for other types of multipole moments. For a given order, the unique multipole moments can be stored in a lower-triangular matrix (left), which can be represented as a one-dimensional array (right).*

As can be inferred from Figure 4.2, the code proceeds differently if either isotropic or anisotropic conditions are imposed. Under anisotropic conditions, the transition moments are contracted with the wave- and polarization vectors, thus yielding Eqn. (3.64) or (3.87). The contracted transition moments are then used to construct the anisotropic oscillator strength. It should be noted that the subroutines written for these purposes hold for arbitrary order, thus implying that the anisotropic absorption cross-section can be calculated to arbitrary order.

To calculate the isotropic oscillator strength, however, a slightly more complicated scheme is required, because it involves the contraction between transition moments and the tensor, $\langle\langle\epsilon_p\epsilon_q\rangle_\chi e_{k;j_1}e_{k;j_2}\cdots e_{k;j_{2n}}\rangle_{\theta,\phi}$ (Eqn. (3.138)). A brute-force approach would involve a distinct subroutine for each order of $\sigma^{[n]}$, whereas current approach uses a *single* subroutine for all orders. This feature is achieved by applying recursive subroutines, which can be defined in a self-referential manner. In Figure 4.4, a code snippet is given containing an example of a recursive loop.

At first sight, this subroutine does not seem to be all that special, since its main function is to fill up an array for a specific index value. However, upon closer inspection, it can be observed that this routine calls itself for negative outcomes of the if-statement. When the routine calls itself, the index of the array is shifted by one unit and the process is repeated until the final index is reached. What effectively happens, is that an array of a certain dimension is filled with all possible combinations of one, two and three. These values represent all possible index values of $\langle\langle\epsilon_p\epsilon_q\rangle_\chi e_{k;j_1}e_{k;j_2}\cdots e_{k;j_{2n}}\rangle_{\theta,\phi}$. When the final index is reached, a specific element of this tensor is calculated, contracted with the transition moments and accumulated. At the end of the line, we are left with the isotropic truncated oscillator strength. As alluded to before, the generality of this subroutine allows the truncated isotropic oscillator strength to be accumulated to arbitrary order.

4.2 Convergence of the Multipole Expansion

Having a fully functional implementation at our disposal that can compute oscillator strengths beyond the electric-dipole approximation, we can proceed with our first calculations. For any newly developed functionality it is always good practice to proceed cautiously and start with calculations on simple test systems, which facilitates the identification of bugs and unanticipated results. Therefore, this section will mainly focus on the UV-Vis and X-ray absorption spectra of the radium atom, whose spherical symmetry will significantly simplify the problem at hand.

```
recursive subroutine bedloop(m,k2,indices,iterm,jterm,FOSC,ATMPPF,OMEGA)
#include "dgroup.h"
#include "dcbxpp.h"
real*8 :: FOSC(MAXEXC,NBSYM), ATMPPF(MAXEXC,NPPAPT,NBSYM),OMEGA(MAXEXC,NBSYM)
integer :: indices(k2),ind(3),k2

if(m==k2) then
        do i=1,3
        indices(m) = i
        call rotfac_bed(indices,k2,iterm,jterm,FOSC,ATMPPF,OMEGA)
    enddo
    return
else
    do i=1,3
        indices(m) = i
        call bedloop(m+1,k2,indices,iterm,jterm,FOSC,ATMPPF,OMEGA)
    enddo
endif
END SUBROUTINE BEDLOOP
```

Figure 4.4: code snippet from the file src/prp/bed_osc.F90 in DIRAC. *The array FOSC contains the nth order oscillator strength for a given excitation and symmetry, ATMPFF contains the transition moments for a given excitation, operator and symmetry, while OMEGA denotes the frequencies. When the if statement is not met, a loop over 1,2 and 3 is initiated that fills the array INDICES at location m. In this loop the subroutine calls itself, while the index m is shifted by one, thus repeating the process for the next entry of INDICES. As a result, this subroutine will fill INDICES with all possible combinations of 1,2 and 3, until it has reached the final index of INDICES. At this point, the subroutine will call ROTFAC_BED, which creates the rotational tensor for that specific index combination and contracts it with the relevant transition moments. The recursive loop repeats this for all possible combinations in INDICES, thus accumulating the isotropic truncated oscillator strength iteratively.*

Furthermore, this symmetry induces selection rules for multipole transitions. Presumably, the main characteristics of the spectra will be described by the electric-dipole oscillator strength (Eqn. (3.149)), whereas finer details are given by contributions depending on the magnetic-dipole and electric-quadrupole. In Section C.2, the relevant selection rules will be derived in detail. Here I will rather briefly summarize them:

- electric-dipole: $\Delta j = 0, \pm 1; \quad \Delta m = 0, \pm 1; \quad (j = 0 \nrightarrow j = 0)$
- magnetic-dipole: $\Delta j = 0, \pm 1; \quad \Delta m = 0, \pm 1; \quad (j = 0 \nrightarrow j = 0)$
- electric-quadrupole: $\Delta j = 0, \pm 1, \pm 2; \quad \Delta m = 0, \pm 1, \pm 2; \quad (j = 0 \nrightarrow j = 0)$
- full interaction: $(j = 0 \nrightarrow j = 0)$.

In the following, I will put these rules to practice and calculate absorption intensities of the radium atom in both the core- and valence regions. The results from this section are taken from ref. 1.

4.2.1 Computational Details

Unless otherwise stated the data reported in this section have been obtained with a development version of the Dirac electronic structure code[190] (Figure 4.5: revision `52c65be`; Table 4.1; Figure 4.6: revision `5a7d81c`).

Using the full interaction, the valence- and core spectrum of the radium atom were calculated at the TDDFT[79] level of theory using the PBE0[193, 194] exchange-correlation functional, based on the Dirac–Coulomb Hamiltonian and within the restricted excitation window (REW) approach (see Section C.4). In these calculations the (SS|SS) integrals are replaced by an interatomic SS energy correction.[195] For technical reasons that become clearer later, the calculations involving truncated interactions were restricted to the $ns_{1/2} \rightarrow 7p_{1/2}; \quad n = 1, 2, \cdots, 7$ excitations of the radium atom and carried out at the TD-HF level of theory. Furthermore, in these calculations integral screening was turned off and the (SS|SS) integrals included. For both series of calculations, the dyall.ae3z basis set is used.[196, 197]

4.2.2 Full Light-Matter Interaction

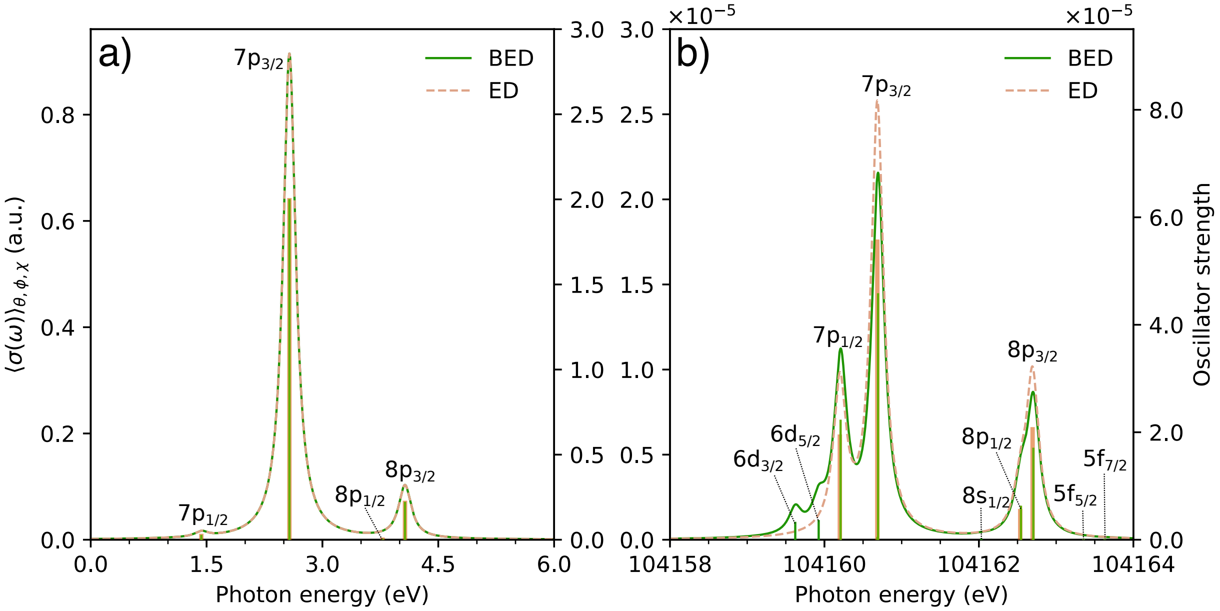

Figure 4.5: Non-dipolar effects on electronic absorption of radium: (a) the valence and (b) K-edge spectra for Ra within and beyond the ED approximation (ED and BED, respectively) at the 4c-TD-PBE0/dyall.ae3z level of theory, using Coulomb gauge (velocity representation) for the former and the full interaction operator in Eqn. (3.134) and an 86-point ($L_{max} = 12$) Lebedev grid for the latter. The labels indicate the character of the receiving orbital. Note the differences in scales on the axes in the valence and X-ray region. Oscillator strengths are summed over contributions from transitions within each degenerate (same ΔJ components) and near-degenerate (different ΔJ components) set, and the sticks have been convoluted with a Lorentzian lifetime broadening of 1000 cm^{-1}. The experimental $1s$ *ionization energy is* 103922 ± 7.2 *eV.[198]*

Figure 4.5 shows the valence and K-edge spectra of Ra within and beyond the ED approximation, the latter computed with the full light-matter interaction operator. The energy range of the K-edge spectrum well exceeds the $1s_{1/2}$ ionization energy (see caption Fig. 4.5), which presumably can be attributed to the lack of core-hole relaxation effects in these calculations. Expectedly, all ED forbidden transitions, except for excitations associated with $\Delta J = 0$ change in total angular momentum quantum number, gain intensity upon going beyond the ED approximation. In the valence region, however, they remain several orders of magnitude smaller than the ED counterparts, such that ED and BED spectra are essentially identical. In the X-ray region, the main contributions from the $1s_{1/2} \rightarrow 6d$ manifold corresponds to $\Delta J = 2$ transitions, while the ED allowed $\Delta J = 1$ transitions dominate for the $1s_{1/2} \rightarrow 7/8p$ manifold. Note that the small energy differences between different ΔJ components in a given set makes them indiscernible in the spectrum, and their oscillator strengths were thus combined in Figure 4.5. Upon inclusion of non-dipolar effects, intensity is primarily redistributed from the $1s_{1/2} \rightarrow 7/8p_{3/2}$ sets (a ∼20% reduction compared to ∼13% for the $1s_{1/2} \rightarrow 7/8p_{1/2}$ excitations) to the $6d$ transitions.

However, even if the spectral broadness is sufficiently small to fully distinguish the peaks, the corrections to the dipole-allowed transitions are rather modest. Non-dipolar effects are expected to gain importance if either the wave length of light is small, or the spatial extent of the system is large. For the radium atom, these effects are suppressed due to the compactness of the $1s_{1/2}$ orbital. In the Section 4.4, I will discuss an example of a system with symmetry equivalent centers, where the core transition is delocalized over the centers, thus enhancing non-dipolar effects.

4.2.3 Truncated Light-Matter Interaction

When carrying out equivalent calculations using the truncated light-matter interaction formulations, both in the velocity and the length representation, nonsensical results were obtained for core excitations. Rather than reporting these numbers, I will illustrate and analyze this behavior using a simpler computational setup. Table 4.1 reports anisotropic oscillator strengths for radium $ns_{1/2} \rightarrow 7p_{1/2}$ $(n = 1, .., 7)$ excitations at various orders in the generalized velocity representation as well as obtained using the full light-matter interaction. The orbital rotation operator, Eqn. (1.85), is restricted to the $ns_{1/2}$ and the $7p_{1/2}$ orbitals of the selected excitation, and I only report results for the B_{1u} irreducible representation of the D_{2h} point group. To avoid issues of numerical integration I have performed TD-HF rather than TDDFT calculations. Furthermore, to avoid possible numerical noise due to rotational averaging, I have chosen an oriented experiment, with the wave and polarization vectors oriented along the y- and z-axes, respectively.

It is observed that for the $7s_{1/2} \rightarrow 7p_{1/2}$ excitation, the electric-dipole approximation holds since the zeroth-order oscillator strength $f^{[0]}$ reproduces the oscillator strength f_{full}, using the full interaction, to within the reported digits. For other excitations, the second-order oscillator strength $f^{[2]}$ has to be included in order to get reasonable agreement with the full interaction. For the $1s_{1/2} \rightarrow 7p_{1/2}$ transition, however, higher-order contributions to the oscillator strength blow up. A similar behavior, but to a lesser degree, is observed for the $2s_{1/2} \rightarrow 7p_{1/2}$ transition. Also, it should be noted that the oscillator strength for the $3s_{1/2} \rightarrow 7p_{1/2}$ transition, accumulated to 12th order, is negative. Very similar behavior is observed for multipolar gauge (data not shown). In Table 4.1 the corresponding norm $k = \omega/c$ of the wave vector is listed for each excitation. Interestingly, the apparent divergence in the expansion of the full light-matter interaction occurs when $k \approx 1\ a_0^{-1}$. Indeed, if it is not assumed that $\omega = \omega_{fi}$, where $\hbar\omega_{fi}$ is the excitation energy, and instead ω is treated as a variable, so as to artificially vary k appearing in the interaction operator, it is found that the oscillator strengths for all excitations blow up around $k = 1\ a_0^{-1}$ (Figure 4.6). It seems reasonable that the convergence behaviour of an expansion of oscillator strengths in orders of the norm of the wave vector should change when $k \approx 1\ a_0^{-1}$. However, this conclusion requires some caution, since k is not a dimensionless quantity. The proper expansion parameter is rather the dimensionless quantity kr and the above observations suggest that the effective radius $r \approx 1\ a_0$. For the valence $7s_{1/2} \rightarrow 7p_{1/2}$ excitation the effective radius r is more diffuse, which explains why the apparent divergence sets in for $k < 1\ a_0^{-1}$, as seen in Figure 4.6.

The oscillator strengths of given (even) order are calculated according to Eqn. (3.64) or (3.87). I have also investigated to what extent transition moments over effective interaction operators $\hat{T}_{\text{full}}^{[n]}$ of order n in the wave vector, Eqn. (3.30), sum up to transition moments over the full interaction operator and again find apparent divergences for core excitations. Again, when treating ω as a variable and not setting it equal to ω_{fi}, we find that these apparent divergences occur for all $ns_{1/2} \rightarrow 7p_{1/2}$ excitations when $k > 1\ a_0^{-1}$. Going deeper in our analysis, I note that transition

Table 4.1: Anisotropic oscillator strengths for radium $ns_{1/2} \rightarrow 7p_{1/2}$ excitations at various orders in Coulomb gauge (velocity representation) as well as with the full semi-classical light-matter interaction operator at the 4c-TD-HF/dyall.ae3z level of theory. Numbers in parentheses are exponents of 10. For each excitation, the second line contains the accumulated oscillator strength (ac) to given order. The wave $\mathbf{k}$ *and polarization* $\boldsymbol{\epsilon}$ *vectors were oriented along the* y*- and* z*-axes, respectively.*

n	ΔE (eV)	ω/c (a.u.)		0	2	4	6	8	10	12	f_{full}
7	1.82142	4.88(-04)		6.664(-01)	9.370(-07)	-2.335(-12)	6.710(-19)	2.819(-24)	-5.422(-30)	5.928(-36)	
			ac	6.664(-01)	6.664(-01)	6.664(-01)	6.664(-01)	6.664(-01)	6.664(-01)	6.664(-01)	6.664(-01)
6	41.04937	1.10(-02)		9.850(-05)	8.799(-08)	1.253(-11)	4.800(-15)	-9.481(-19)	1.982(-22)	-4.937(-26)	
			ac	9.850(-01)	9.859(-05)	9.859(-05)	9.859(-05)	9.859(-05)	9.859(-05)	9.859(-05)	9.841(-05)
5	269.05081	7.22(-02)		3.947(-04)	-3.662(-07)	-1.568(-10)	6.514(-14)	4.330(-15)	-7.432(-17)	9.082(-19)	
			ac	3.947(-04)	3.943(-04)	3.943(-04)	3.943(-04)	3.943(-04)	3.943(-04)	3.943(-04)	3.943(-04)
4	1240.4258	3.33(-01)		1.754(-04)	-3.161(-07)	-1.242(-08)	1.028(-08)	-5.164(-09)	1.683(-09)	3.974(-10)	
			ac	1.754(-04)	1.751(-04)	1.751(-04)	1.751(-04)	1.751(-04)	1.751(-04)	1.751(-04)	1.751(-04)
3	4888.5865	1.31(+00)		6.018(-05)	2.170(-08)	-3.342(-06)	4.760(-05)	-3.680(-04)	1.849(-03)	-6.737(-03)	
			ac	6.018(-05)	6.020(-05)	5.686(-05)	1.045(-04)	-2.635(-04)	1.585(-03)	-5.152(-03)	6.011(-05)
2	19398.588	5.20(+00)		1.784(-05)	5.379(-07)	-1.750(-04)	3.918(-02)	-4.758(+00)	3.758(+02)	-2.155(+00)	
			ac	1.784(-05)	1.838(-05)	-1.567(-04)	3.903(-02)	-4.719(+00)	3.711(+02)	3.689(+02)	1.807(-05)
1	104647.71	2.81(+01)		3.143(-06)	5.310(-08)	6.767(-03)	-4.469(+01)	1.594(+05)	-3.688(+08)	6.190(+11)	
			ac	3.143(-06)	3.196(-06)	6.770(-03)	-4.468(+01)	1.593(+05)	-3.686(+08)	6.186(+11)	3.579(-06)

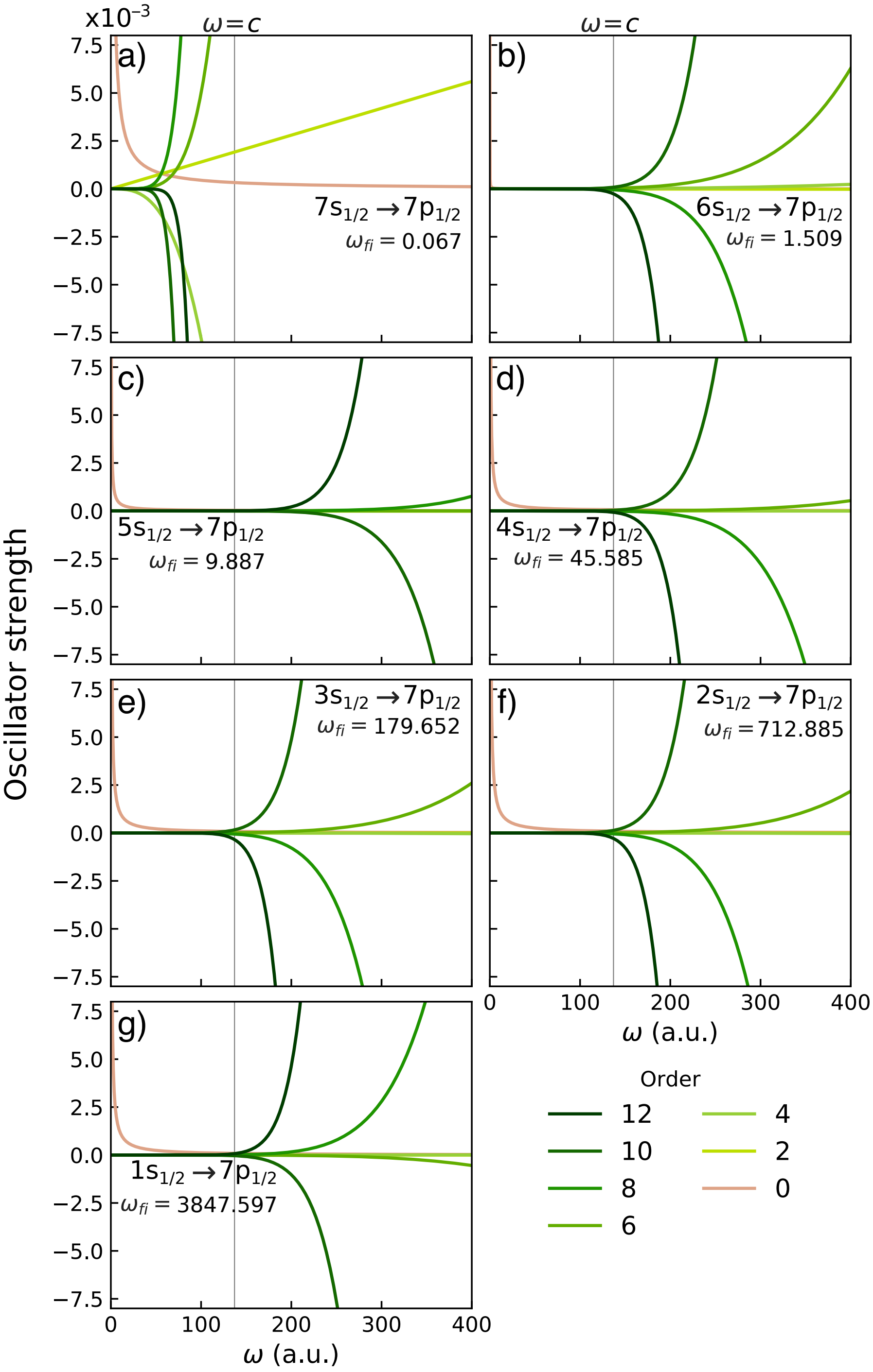

Figure 4.6: Convergence behavior of the oscillator strengths for $ns_{1/2} \rightarrow 7p_{1/2}$ transitions of radium at various orders (colored lines) in the wave vector within the Coulomb gauge (velocity representation) : (a)–(g) correspond to $n = 7, 6, \ldots, 1$. Except for the valence transitions, the oscillator strengths seem to diverge after $\omega = c$, which is indicated by a vertical dashed line. Excitation energies (ω_{fi}) are in a.u.

moments are obtained by contracting the property gradient of the selected operator with the solution vector for the selected excitation, Eqn. (1.121). Due to the restrictions on the orbital rotation operator in our particular case, the scalar product is reduced to the multiplication of two numbers. It can be found that an expansion of the property gradient of the full interaction in orders of the wave vector displays the same apparent divergence for core excitations as was observed for both oscillator strengths and transition moments. Again, by artificially varying k, we find that these apparent divergences occur when $k > 1\ a_0^{-1}$ for *all* excitations.

With our particular orientation of the experiment, the full and truncated effective interaction operators at order n are given by

$$\hat{T}^{\text{full}}(\omega) = \frac{e}{\omega} c\alpha_z e^{+iky}; \quad \hat{T}^{[n]}(\omega) = \frac{e}{\omega}\frac{i^n}{n!} c\alpha_z (ky)^n . \tag{4.15}$$

Elements of the property gradient of the truncated effective interaction operator are accordingly given by

$$g_{T^{[n]};ai} = -\frac{e}{\omega}(ik)^n \left\{ \langle \varphi_a^L | c\sigma_z \frac{y^n}{n!} | \varphi_i^S \rangle + \langle \varphi_a^S | c\sigma_z \frac{y^n}{n!} | \varphi_i^L \rangle \right\} \tag{4.16}$$

where superscripts L and S refer to the large and small components of molecular orbital φ_p, respectively. As discussed in Section 4.1.1, the property gradient is compounded from products of Cartesian Gaussian-type orbitals (see Eqn. (4.1)) with two expansion coefficients on the form

$$c_{\mu a}^* \langle \chi_\mu | c \frac{y^n}{n!} | \chi_\nu \rangle c_{\nu i}, \tag{4.17}$$

with the factor outside the curly brackets in Eqn. (4.16) multiplied on at the end. In the present case, the coefficients are real due to symmetry.[145] For $n = 12$ it is found that the largest contribution, in terms of magnitude, to the property gradient comes from a small component p_y function with exponent $\alpha_1 = 1.56556662(-02)\ a_0^{-2}$ combined with a large component p_y function with exponent $\alpha_2 = 1.24964369(-02)\ a_0^{-2}$. These are the most diffuse s and p functions, respectively, of the large component dyall.ae3z basis set. The resulting AO-integral has a value $-1.19437467(+6)$ a.u. and is multiplied with a coefficient $c_1 = -4.55940113(-8)$ from $1s_{1/2}$ and a coefficient $c_2 = -0.844080786$ from $7p_{1/2}$. By calculating AO-integrals with high precision using Mathematica,[199] the above AO-integrals, provided by the HERMIT integral package, are found to be very stable. On the other hand, the very small c_1 coefficient is at the limits of the precision one can expect from the diagonalization of the Fock matrix, in particular given its ill-conditioning due to the presence of negative-energy solutions. I have, however, investigated the sensitivity of our results with respect to the HF convergence (in terms of the gradient) and find that they are quite stable at tight thresholds.

In the test case analyzed in Section 4.2.3, the wave $\mathbf{k}$ and polarization $\boldsymbol{\epsilon}$ vectors are oriented along the y- and z-axes, respectively, such that the full and truncated effective interaction operator at order n are given by Eqn. (4.15). In the following, the convergence will be studied of the underlying AO-integrals over the truncated interaction towards the corresponding AO-integral over the full interaction. These involve only the scalar parts of the operators, so in practice I will work with the expression

$$\langle \chi_\mu | e^{+iky} | \chi_\nu \rangle = \sum_{n=0}^{\infty} \frac{(ik)^n}{n!} \langle \chi_\mu | y^n | \chi_\nu \rangle, \tag{4.18}$$

where χ_μ and χ_ν are scalar basis functions. I shall limit attention to p_y functions (G_{010}^{α}) since the largest integrals in this study involved such basis functions with diffuse exponents.

The final step of our analysis is to study the convergence of the AO-integrals over the truncated interaction towards the corresponding integral over the full interaction operator. Restricting attention to our particular case in Eqn. (4.15) and Gaussian p_y functions we have

$$\langle G_{010}^{\alpha_1}|\hat{T}^{\mathrm{full}}(\omega)|G_{010}^{\alpha_2}\rangle = \sum_{m=0}^{\infty}\langle G_{010}^{\alpha_1}|\hat{T}^{[2m]}(\omega)|G_{010}^{\alpha_2}\rangle. \tag{4.19}$$

After eliminating the factors on both sides related to the x- and z-integration, it can be shown that

$$\langle G_1^{\alpha_1}|e^{+iky}|G_1^{\alpha_2}\rangle_y = \sum_{n=0}^{\infty}\frac{(ik)^n}{n!}\langle G_1^{\alpha_1}|y^n|G_1^{\alpha_2}\rangle_y; \quad G_j^{\alpha} = N_j^{\alpha}y^j e^{-\alpha y^2}, \tag{4.20}$$

where the left-hand-side can be evaluated using the results from previous section (Eqn. (4.5))

$$\langle G_1^{\alpha_1}|e^{+iky}|G_1^{\alpha_2}\rangle_y = N_1^{\alpha_1}N_1^{\alpha_2}\sqrt{\frac{\pi}{\alpha_1+\alpha_2}}\left(\frac{i}{2\sqrt{\alpha_1+\alpha_2}}\right)^2 e^{-Q^2}H_2\left(Q\right). \tag{4.21}$$

Using Eqn. (4.13), we obtain for the right-hand-side integral

$$\langle G_1^{\alpha_1}|y^n|G_1^{\alpha_2}\rangle_y = N_1^{\alpha_1}N_1^{\alpha_2}\frac{1}{2}\left[1+(-1)^{(2+n)}\right](\alpha_1+\alpha_2)^{-(n+3)/2}\,\Gamma\left(\frac{n+3}{2}\right). \tag{4.22}$$

It thus follows that this integral vanishes unless it is even-valued, i.e. $n = 2m$. Again, eliminating common factors yields the following expression

$$-(4Q^2-2)e^{-Q^2} = \sum_{m=0}^{\infty}(-1)^m a_m; \quad a_m = Q^{2m}\frac{(2m+2)\,(2m+1)}{(m+1)!} \tag{4.23}$$

in terms of the dimensionless parameter Q (Eqn. (4.7)) The right-hand expression has the form of an alternating series, which converges according to the Leibniz criterion provided that $\lim\limits_{m\to\infty} a_m = 0$ and the absolute value of the coefficients, $|a_m|$, decreases monotonically. The first condition follows readily from Eqn. (4.23), whereas the second condition holds, if we have $\frac{a_{m+1}}{a_m} < 1; \quad \forall m$. This fraction evaluates to

$$\frac{a_{m+1}}{a_m} = Q^2\frac{(2m+3)}{(m+1)(2m+1)}, \tag{4.24}$$

which, depending on the specific order and the value of Q, is not always smaller than one. Eventually at elevated orders, this fraction necessarily becomes smaller than one, implying monotonic decrease after that order. For that reason, I will split this series in two parts

$$\sum_{m=0}^{m_c}(-1)^m a_m + \sum_{n=m_c}^{\infty}(-1)^n a_n, \tag{4.25}$$

such that the second summation is monotonically decreasing. The first of these summation converges because it consists of a finite amount of terms, whereas the second summation obeys the Leibniz criterion. Therefore, the total summation should converge as well. For the $1s_{1/2} \to 7p_{1/2}$ excitation and the above choice of exponents we find that $m_c \approx Q^2 = 6998.7$. For this value of Q, the left-hand-side of Eqn. (4.23) is essentially zero, whereas the right-hand side converges extremely slowly towards this value. In fact, using Mathematica,[199] no convergence was observed even after summing 10000 terms. Considering instead the $2s_{1/2} \rightarrow 7p_{1/2}$ excitation, for which $m_c \approx 240$, reasonable convergence is found after summing 282 terms. The sheer amounts appearing in this expansion thus renders the schemes based on truncated interactions impractical at high excitation energy.

4.2.4 Conclusion

In summary it was found that for increasing excitation energies, the use of truncated light-matter interaction becomes increasingly problematic because of the slow convergence of such expansions. This is not a basis set problem which can be alleviated by increasing the basis set, since this slow convergence was observed at the level of the individual underlying AO-integrals. In particular, for core excitations, extremely slow convergence was observed for integrals involving Cartesian Gaussian-type orbitals with diffuse exponents. This can be understood, since such diffuse functions will be less efficient than tight ones in damping the increasing Cartesian powers appearing in an expansion of the full light-matter interaction in orders of the norm of the wave vector (Eqn. (4.18)). This in turn suggests that the use of Slater-type orbitals, which have slower decay than Gaussian-type orbitals, will be even more problematic. This is indeed the case, as shown in the appendix of ref. 1.

4.3 Basis Set Convergence

A proper choice of basis set is key to reach quantitative accuracy in quantum chemical calculations. Especially in the current context, where unconventional interaction operators are being used, it is important to give special considerations to the choice of basis set. Therefore, in this section, it will be assessed whether conventional basis sets are flexible enough to satisfy the demands of these interaction operators.

Conventional basis sets are constructed by choosing a set of functions that minimize the energy. Typically, more energy is gained by adding tight functions than diffuse functions.[62] Because of this, energy-optimized basis sets saturate the core region faster than the tail-region. The full and truncated light–matter interaction may require addition of further basis functions. A problem in this respect is the lack of a variational principle for transition moments. Alternatively, basis sets for use beyond energies can be constructed using the equivalent core approximation,[200, 201] Slater's rule[202, 203] or the completeness-optimization scheme.[204, 205] Another strategy is to systematically increase the basis set size, until the property of interest has become stable.

Sørensen *et al.* performed such a series in a non-relativistic framework using the full and truncated interaction operator, the latter limited to second order, expressed with the ANO-RCC basis sets.[29, 33] Even though the series did not fully converge for the larger basis sets, their results indicated that the full interaction operator is more stable with respect to basis set choice. In addition, Sørensen *et al.* argued that each multipole moment requires different basis sets, making it exceedingly difficult to construct basis sets that can describe the truncated interaction at higher orders. They concluded that the full interaction operator should be the standard for calculations involving non-dipolar effects. For zeroth- and first-order interactions, the length representation seems to be the preferred choice in the literature, although there is not a concise answer as to which representation has a superior basis set convergence.[206, 207, 150, 208]

Another strategy to gauge the quality of a basis set is to compare with a reference value. In this section, the basis set requirements for non-dipolar effects are assessed by comparing calculations using Gaussian basis sets and the molecular code DIRAC[37] to equivalent finite-difference calculations using the atomic code GRASP.[209] If the grid size of the latter is chosen sufficiently large, the results effectively correspond to the complete basis set limit, thus forming a suitable reference to the basis set calculations. For these purposes, I will study the $1s_{1/2} \rightarrow 7p_{1/2}$ and the $7s_{1/2} \rightarrow 7p_{1/2}$ transitions in the radium atom, representative of core and valence excitations, respectively. This section is based on ref. 3, so the reader is referred to this article for more details.

4.3.1 Radial Transition Moment Distributions

Due to the spherical symmetry of the radium atom, its orbitals assume the general structure given in Eqn. (2.100), where the functions $P(r)$ and $Q(r)$ can either be calculated on a numerical grid, or from basis set calculations. Inserting these orbitals into the transition moments thus enables us to compare basis set calculations with a numerical reference. However, the alert reader may note that the transition moments from Eqn. (1.121) contain contributions from many orbitals, whereas the numerical approach gives single orbitals (see Section 2.4.1). For that reason, the restricted excitation window approach is applied to reduce Eqn. (1.121) to an orbital-orbital transition, i.e. $1s_{1/2} \rightarrow 7p_{1/2}$ and $7s_{1/2} \rightarrow 7p_{1/2}$.

Since the $s_{1/2}$ and $p_{1/2}$ orbitals in the finite basis approximation are constructed exclusively from s- and p-exponents, the basis set considerations boil down to finding what additional diffuse or tight s/p-functions are required to converge intensities. In general, diffuse and tight functions improve the description of the outer and inner regions of the wave function. To examine which regions need improvement, we visualize the transition moment densities as radial distributions

$$R_{\Omega}(r) = \int_0^{2\pi} d\phi \int_0^{\pi} d\theta \; r^2 \sin\theta \; \Omega_{fi}(\mathbf{r}); \qquad \Omega_{fi}(\mathbf{r}) = \phi^{\dagger}_{n_i,\kappa_i,m_i}(\mathbf{r})\hat{\Omega}\phi_{n_f,\kappa_f,m_f}(\mathbf{r}) \tag{4.26}$$

where $\Omega_{fi}(\mathbf{r})$ is the density that integrates to the transition moment, T_{Ω}.

For the specific transition studied in this chapter, the quantum numbers of the two orbitals read: $n_i = 1, 7, \kappa_i = -1$, $m_i = m_f = \frac{1}{2}$, $n_f = 7$ and $\kappa_f = 1$, whereas the relevant operators are $\Omega = T, Q, m, \mathcal{Q}$ (see Eqs. (3.16) (3.57) (3.85)). From parity it follows that only odd electric and even magnetic multipoles contribute. We have chosen a frame in which the wave vector $\mathbf{k}$ is aligned with the z-axis and the polarization vector $\boldsymbol{\epsilon}$ with the y-axis. The radial distribution for the electric-length multipoles then becomes

$$R_{Q}^{[2n+1]}(r) = \frac{er^{2n+1}}{(2n+1)(2n+3)}(P_{7,1}P_{n_i,-1} + Q_{7,1}Q_{n_i,-1}), \tag{4.27}$$

the electric-velocity

$$R_{\mathcal{Q}}^{[2n+1]}(r) = \frac{-ecr^{2n}}{\omega(2n+1)(2n+3)}\left((2n-1)P_{7,1}Q_{n_i,-1} - (2n+3)Q_{7,1}P_{n_i,-1}\right) \tag{4.28}$$

and the magnetic multipole distribution

$$R_{M}^{[2n]} = \frac{iec2n(2n-1)r^{2n+1}}{\sqrt{2}(2n+1)^2(2n+3)}\left(P_{7,1}Q_{n_i,-1} + Q_{7,1}P_{n_i,-1}\right), \tag{4.29}$$

where the r-dependence of the radial functions P and Q have been suppressed. The radial distribution associated with the full interaction reads

$$R_T(r) = \frac{iec}{3\omega}\Big(\big(j_0(kr) - j_2(kr)\big)P_{7,1}Q_{n_i,-1} + 3j_0(kr)Q_{7,1}P_{n_i,-1}\Big), \tag{4.30}$$

where $j_0(kr)$ and $j_2(kr)$ are the zeroth and second order spherical Bessel functions, given by

$$j_0(kr) = \frac{\sin kr}{kr}; \quad j_2(kr) = \left(\frac{3}{(kr)^2} - \frac{1}{kr}\right)\sin kr - \frac{3}{(kr)^2}\cos kr. \tag{4.31}$$

The spherical Bessel functions appear in these expression as a consequence of the plane wave expansion (Eqn. (3.28)). For small values of kr, the limiting forms of the spherical Bessel functions are[210]

$$\lim_{kr\to 0} j_\ell(kr) \sim \frac{(kr)^\ell}{(2\ell+1)!!}. \tag{4.32}$$

This relation implies that all Bessel functions except j_0 are zero at the origin. We can use this result to obtain

$$\lim_{kr\to 0} R_T(r) = \frac{iec}{3\omega}\Big(P_{7,1}Q_{n_i,-1} + 3Q_{7,1}P_{n_i,-1}\Big) = iR_Q^{[1]}(r). \tag{4.33}$$

Therefore, the electric-dipole approximation is correctly retrieved in the long wavelength limit of Eqn. (4.30).

Without performing any calculation, the shape of Eqs. (4.27)–(4.30) already tells us useful information about the basis set requirements of the interaction operators. For example, the radial distributions corresponding to the multipole moments (Eqs. (4.27)–(4.29)) all contain a prefactor depending on a power of the radial distance. This prefactor is in competition with the terms associated with the atomic radial functions: the former tends towards infinity for large distances, whereas the latter decays to zero. Because the atomic functions decay exponentially, the transition moments are finite. From these considerations it follows that the multipole moments with increasing order sample regions farther and farther away from the nucleus and thus we expect that they may require additional diffuse functions for their proper description. This is in sharp contrast with the full interaction, Eqn. (4.30). Instead of the radial powers, this distribution depends on the spherical Bessel functions, which assume the following asymptotic form[210]

$$\lim_{kr\to\infty} j_\ell(kr) \sim (kr)^{-1}\sin\left(kr - \frac{1}{2}\ell\pi\right). \tag{4.34}$$

Therefore, the spherical Bessel functions decay to zero for $kr \to \infty$, which implies that the radial distribution of the full interaction will decay much faster than the multipole distributions. Consequently, the full interaction is expected to require fewer diffuse basis functions than the multipole moment operators.

4.3.2 Computational Details

To compare basis set effects in both the valence and core regions, the $7s_{1/2} \rightarrow 7p_{1/2}$ and the $1s_{1/2} \rightarrow 7p_{1/2}$ transition of the radium atom were studied. The transitions were constrained to occur between single orbitals to facilitate the comparison between the Gaussian-type-orbital calculations in DIRAC[190, 37] and the numerical reference calculations in GRASP.[209] Since GRASP only computes *occupied* orbitals, the orbitals were optimized, using average-of-configurations (AOC) Hartree–Fock,[211] with respect to *excited-state* determinants, i.e., [Rn]$7s^1_{1/2}7p^1_{1/2}$ for the valence transition and [Ra]$1s^{-1}_{1/2}7p^1_{1/2}$ for the core transition. Even though the $7p_{1/2}$ orbital is formally occupied in these configurations, I treat it as a virtual orbital to construct transition moments. In the case of GRASP these were obtained by inserting the $P_{n\kappa}$ and $Q_{n\kappa}$ radial functions into Eqs. (4.27)–(4.30). Since transition moments are only determined up to a complex phase, I defined them such that all radial distributions are real and have a positive maximum value. Since the radial functions from GRASP are calculated on a numerical grid and thus effectively correspond to the complete basis set limit, the GRASP transition moments were used as reference. In the case of DIRAC, I applied overlap selection to prevent the core-excited state to collapse during the SCF cycles.[212, 213, 214] I then used the orbitals of the excited state calculations in a ground state four-component time-dependent Hartree–Fock (4c-TD-HF) calculation within the linear response regime.[79] The restricted excitation window method[215, 216] was invoked to only consider one amplitude in Eqn. (1.85). The radial distributions were then divided by this remaining amplitude to compare the results of the basis set calculations with the numerical reference values. In DIRAC the radial distributions were calculated on a radial grid with the visualization module, which performs the angular integration on a Lebedev grid ($L_{\text{max}} = 64$). Due to the quaternion symmetry scheme[145] in DIRAC, all transition moments are real by default (see Section 2.4.3).

The basis set calculations were carried out at the Hartree–Fock level of theory using the Dirac–Coulomb Hamiltonian and the dyall.aeXz (X=2,3,4) basis sets.[196, 217] These basis sets are constructed from uncontracted Cartesian Gaussian basis functions which are designed for correlated calculations and hence contain basis functions of high orbital angular momentum. I trimmed off the g, h and i functions because for atomic systems they will only contribute to the space of virtual orbitals. The small component basis sets were generated according to the condition of restricted kinetic balance[128, 127, 131, 218] and the $(SS|SS)$ integrals were treated exactly, for consistency with the numerical calculations. Furthermore, I found that with the default linear dependence threshold (10^{-6} and 10^{-8} for the large and small component space, respectively), several basis functions were deleted. Especially the small component of the $1s_{1/2}$ was susceptible to the deletion of functions. This deteriorates the quality of the results, so for all calculations, the linear dependence threshold was set to 10^{-9} and 10^{-10} for the large and small component space, respectively. In Section D.1, the problems associated with linear dependence are further discussed.

4.3.3 Results and Discussion

We start by comparing the radial distributions of the core and valence excitations within the electric-dipole approximation (velocity representation; Figure 4.7). To illustrate their radial extent, the expectation value of the radial distance for different s orbitals are indicated. A striking observation is that the radial distribution for the core transition is much more localized around the nucleus than that of the valence transition. This follows from the locality of the core orbital. Furthermore, the valence distribution oscillates considerably more than the core distribution, and one can see that the oscillations follow the shell structure of the atom. The electric transition dipole distribution is stable with respect to the choice of basis set, since all basis set calculations overlap with the numerical reference. The relative deviations (depicted in the right corner of Figure 4.7) further confirm this.

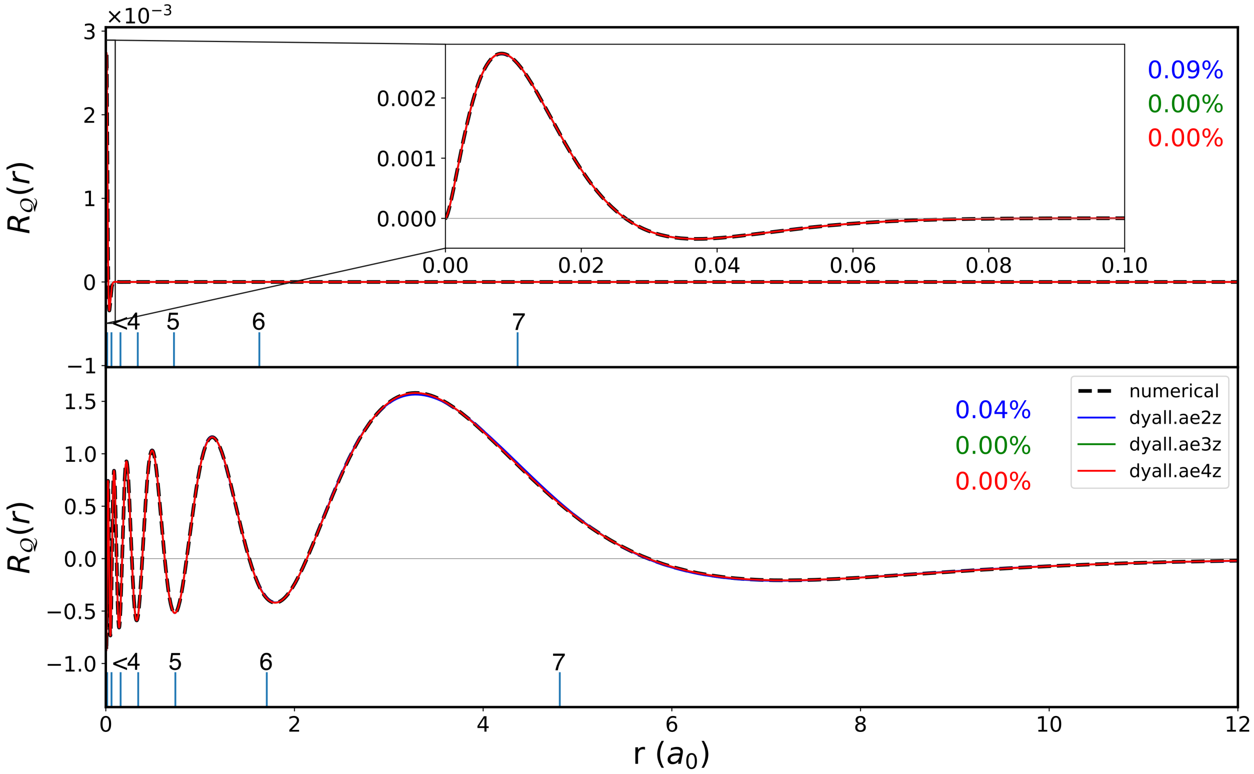

Figure 4.7: Radial distribution of the electric-velocity dipole moment ($R_Q^{[1]}$) *for the* $1s_{1/2}$ *(top panel) and* $7s_{1/2} \rightarrow 7p_{1/2}$ *(bottom panel) transitions. Expectation values of the radial position for the relevant s orbitals are indicated as vertical sticks where the labels represent the index of the s orbital, i.e.* $n_i s_{1/2}$ $(n_i = 1, \ldots, 7)$*. The percentages in the upper right corner of each box are the relative errors of the transition moments, i.e.* $|\frac{T_{bas} - T_{num}}{T_{num}}| \times 100\%$.

Therefore, for both transitions, the dyall.ae2z basis set is sufficient to properly describe electric transition dipole moments.

To gauge the importance of non-dipolar effects, the electric-velocity dipole distributions are compared to those of the full interaction in Figure 4.8. The basis set convergence of the full interaction appears to be similar as the electric-dipole moment, since the full interaction is unaffected by the choice of basis set. For the valence transition, the electric-dipole distributions basically coincide with the full interaction, which confirms the validity of the electric-dipole approximation in this energy regime. Even, for the core transition, the difference between the distributions of the electric-dipole and full interaction is modest. The electric-dipole approximation breaks down if the wavelength of the electromagnetic field is small compared to the spatial extent of the transition. Though the wavelength for the core transition falls in the hard X-ray regime, the compactness of the radium $1s_{1/2}$ orbital reduces the importance of non-dipolar effects. In the next two sections, I will discuss systems with symmetry equivalent centers, for which the core transitions are delocalized, thus increasing the importance of non-dipolar effects.

The oscillatory behavior in Figures 4.7 and 4.8, or the lack thereof, can be understood by considering the radial part of the atomic orbitals involved in the core and valence transition (Figures

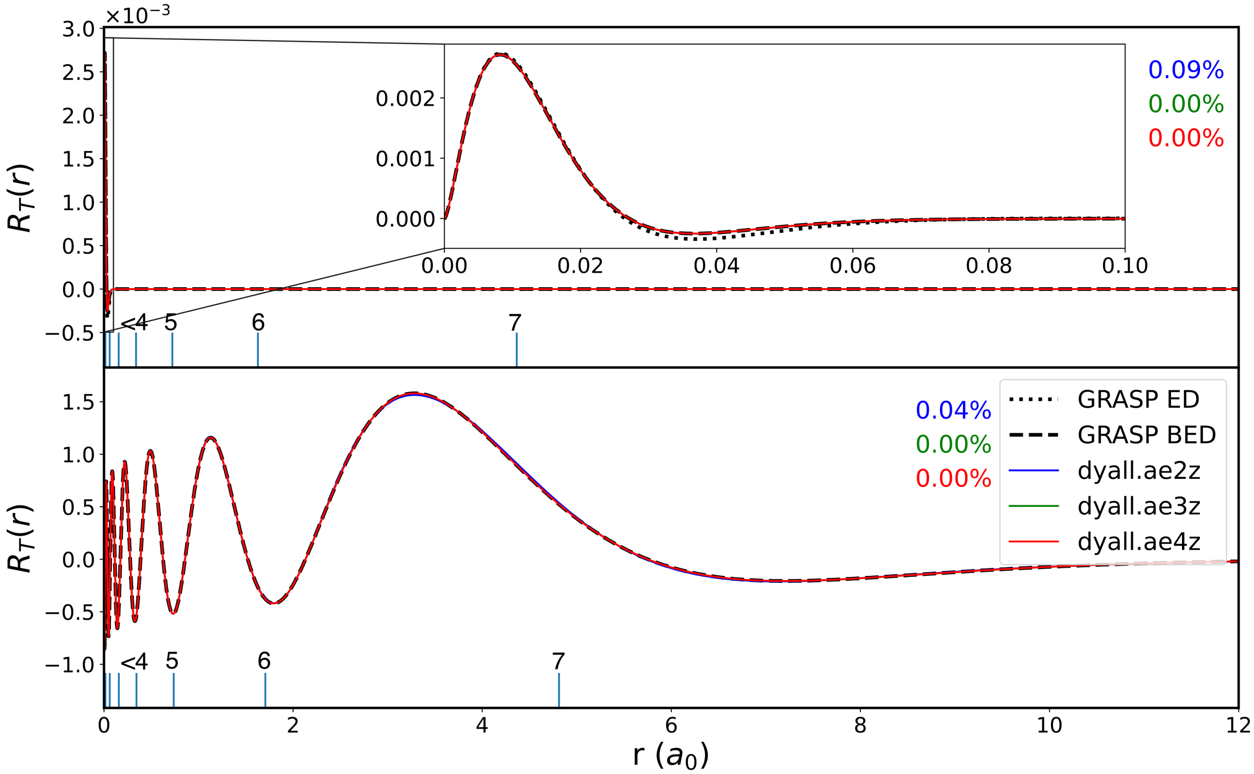

Figure 4.8: Radial distribution of the full interaction (R_T) for the $1s_{1/2}$ (top panel) and $7s_{1/2} \to 7p_{1/2}$ (bottom panel) transitions. To assess the validity of the electric-dipole approximation, the numerical reference curve from the full interaction (GRASP BED) is compared with the reference curve from the electric-velocity dipole (GRASP ED). Expectation values of the radial position are shown for the relevant s orbitals. The labels represent the index of the s orbital, i.e. $n_i s_{1/2}$ ($n_i = 1, \ldots, 7$). The percentages in the upper right corner of each box are the relative errors of the transition moments, i.e. $|\frac{T_{bas}-T_{num}}{T_{num}}|\times 100\%$.

4.9 and 4.10, respectively). Note that the $7p_{1/2}$ orbitals are, as expected, not identical for the two transitions, since the orbitals have been optimized in different excited configurations. For all orbitals, the basis set calculations nearly coincide with the numerical reference, which makes it difficult to assess the performance of each basis set. Therefore, the error curves in Figures 4.9 and 4.10 need to be analyzed to properly assess the basis set convergence. From the analytical formulas in Eqs. (4.27)-(4.29), it is expected that the basis set error is most relevant at large radial distances. For that reason, I will investigate the error at much larger distances than the range of the radial functions (bottom row subfigures).

To some extent, all error curves in these plots are oscillatory, reflecting the incompleteness of the basis set. In general, the amplitude of the oscillations diminish with larger basis sets, although the frequency increases. This trend can clearly be observed in Figures 4.9 and 4.10: the small error associated with the dyall.ae2z basis is even further reduced by using the dyall.ae3z basis set, at the expense of a higher frequency of the oscillations, while the dyall.ae4z set flattens most of the error curves. However, the additional improvement introduced by the dyall.ae4z basis set is marginal for

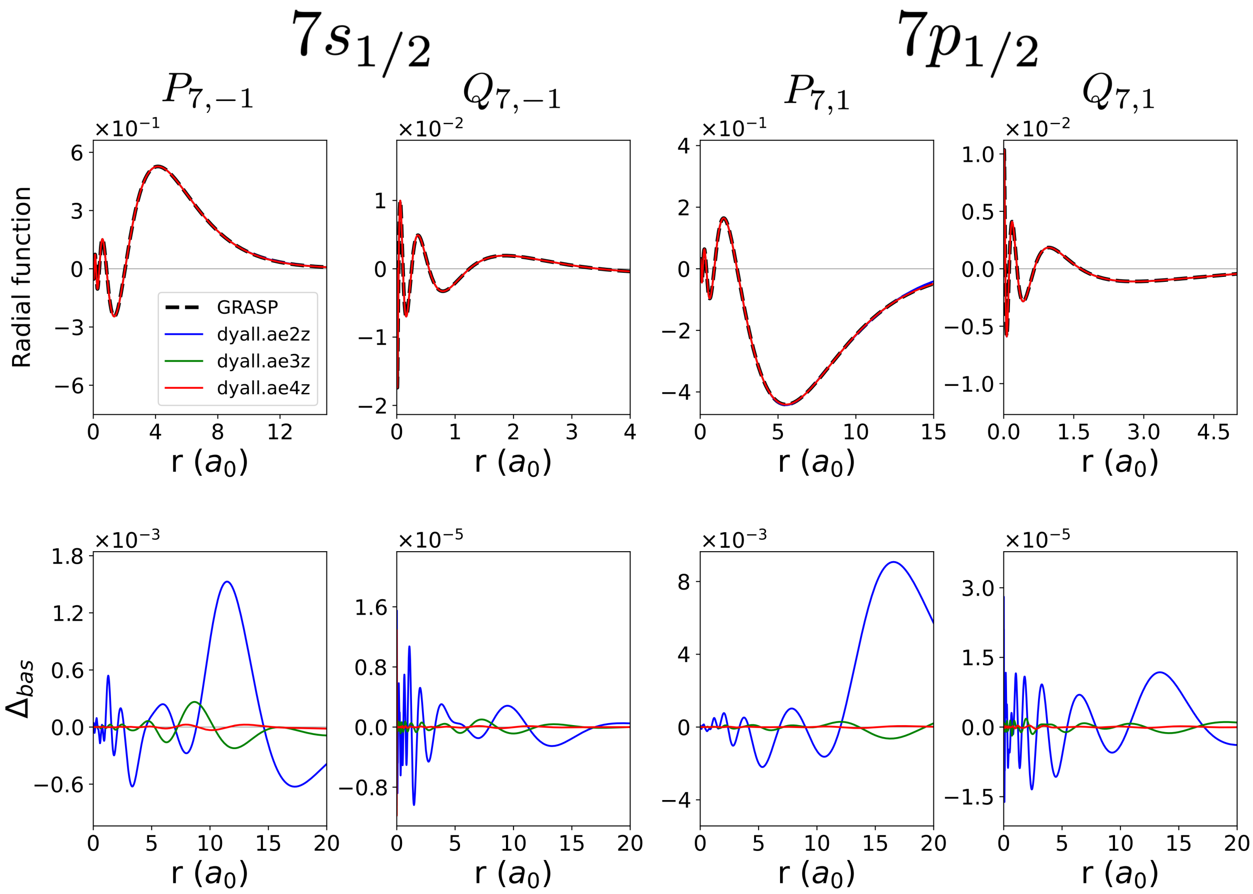

Figure 4.9: Radial functions of the large and small component of the $7s_{1/2}$ *(*$\langle r\rangle = 4.365a_0$*) and* $7p_{1/2}$ *orbital (top row) and their deviations from the numerical reference (bottom row). These orbitals were taken from the radium atom with* $[Rn]7s^1_{1/2}7p^1_{1/2}$ *configuration. The basis set orbitals were calculated at the 4c-HF level using* DIRAC*, while the numerical reference was calculated with GRASP. Note that the scaling is different for each individual box and that the error curves are plotted in a different range than the radial functions.*

the $Q_{1,-1}$ function, and the dyall.ae4z curve seems to oscillate more compared to the dyall.ae3z curve.

It has proven to be challenging to completely eliminate the error of the $Q_{1,-1}$ function, as it is highly susceptible to problems associated with linear dependence. As explained in Section D.1 of the appendix, the first attempts to calculate the radial distributions of the magnetic multipole moments were met with difficulties. In these calculations, the default linear dependence threshold was in place, further accentuating the oscillations of the $Q_{1,-1}$ function, which in turn caused severe oscillations in the radial distributions of the magnetic multipole moments. Although it may seem straightforward in hindsight, finding the reason for these oscillations has been a problem that significantly halted the progress of this project. Only after extensive experimentation, I found almost accidentally that changing the linear dependence threshold ameliorated the problem. By increasing the linear dependence threshold, I could significantly reduce the deviations from the

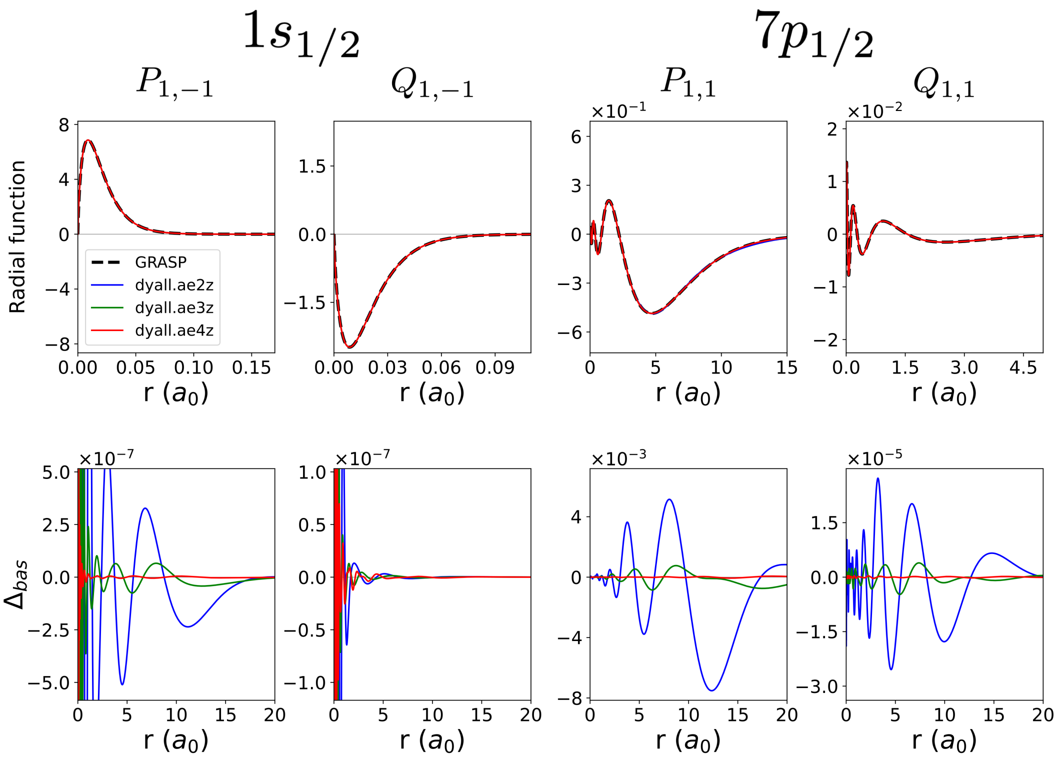

Figure 4.10: Radial functions of the large and small component of the $1s_{1/2}$ $(\langle r \rangle = 0.01454\ a_0)$ *and* $7p_{1/2}$ *orbital (top row) and their deviations from the numerical reference (bottom row). These orbitals were taken from the radium atom with [Ra]*$1s^{-1}_{1/2}7p^{1}_{1/2}$ *configuration. The basis set orbitals were calculated at the 4c-HF level using* DIRAC, *while the numerical reference was calculated with GRASP. Note that the scaling is different for each individual box and that the error curves are plotted in a different range than the radial functions.*

reference, although the basis set convergence of the $Q_{1,-1}$ function is still not completely smooth. The minute differences between numerical and basis set orbitals suggest the radial distributions of the multipole moments should be stable across basis sets series.

In practice, this is, however, not completely true. Figures 4.11 and 4.12 depict the radial distributions of the electric-length multipoles, $\hat{Q}^{[2n+1]}$, for the valence and core transitions, respectively. In both figures, the peak of the reference curve appears close to the origin and moves farther away at higher orders. Additionally, the peak height and the integrated value of these curves seems to rise upon increase of the order. The same trend can be observed in the error curves, which are most pronounced in the regions far from the nucleus. In the following, I will define an error below 1% as acceptable convergence. Therefore, the dyall.ae2z basis set is an acceptable choice for multipole moments below order 2. For $2 < n < 5$, the dyall.ae3z is needed to reduce the error below 1%. Even with the largest basis set, the accuracy goal is not reached for the highest two orders. These trends are even more pronounced in the case of the core transition (Figure 4.12). For this transition, the largest dyall.ae4z basis set is already needed at $n > 3$. In general, the overall error increases with the order of the multipole moments. These findings can be understood by considering the form of the radial distribution in Eqn. (4.27). The multiplication by the power of the radial distance of increasing orders blows up the moderate deviations in radial densities (Figures 4.9 and 4.10).

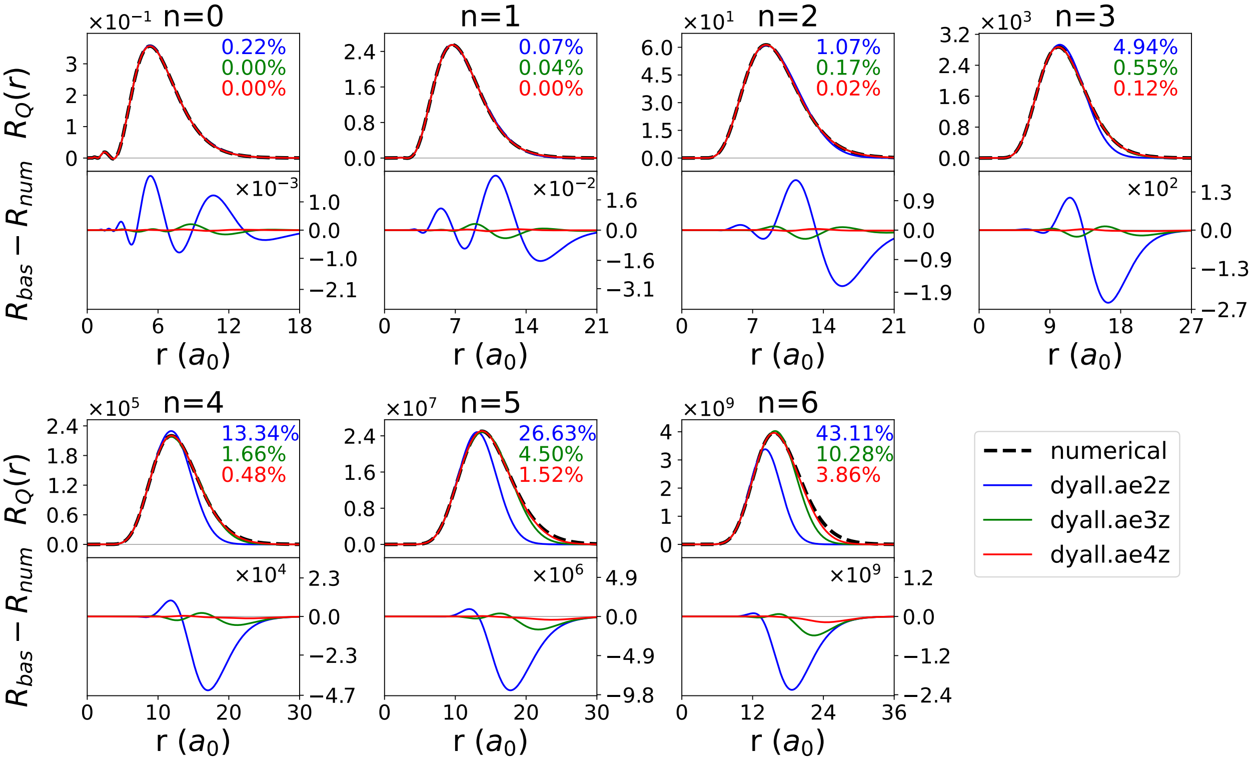

Figure 4.11: Valence transition ($7s_{1/2} \rightarrow 7p_{1/2}$): radial distributions of electric multipole moments in the generalized length representation, $\hat{Q}^{[2n+1]}, n \in [0, 6]$. In each box, the upper panel contains the radial distribution, while the lower panel contains the deviation with the numerical reference. Note that each subfigure has different scales. The percentages in the upper right corner of each box are the relative errors of the transition moments, i.e. $|\frac{T_{bas}-T_{num}}{T_{num}}|\times 100\%$.

Figure 4.13 contains the radial distributions of the magnetic multipole moments $\hat{m}^{[2n]}$ for the valence transition. For the lowest two orders, these distributions have distinct shapes, whereas their shapes start to be reminiscent of the electric multipole distributions in Figures 4.11 and 4.12 for higher orders. Likewise, the peaks of the radial distributions move away from the origin and become higher upon increasing the order. The overall errors indicate that the dyall.ae3z basis set is preferable for $2 < n < 5$, whereas the dyall.ae4z basis set should be used at higher orders. However, for $n = 6$ and $n = 7$, the dyall.ae4z basis does not reduce the overall error below 1%. The magnetic multipole moments for the core transition (Figure 4.14) follow the same trend, although the higher order multipole moments tend to converge with more difficulties towards the numerical reference. Already at $n = 4$, the dyall.ae4z basis set is not enough to reduce the error below 1%. In general, the basis set convergence of the magnetic multipole moments seem to follow the same trends as the electric-length multipole moments, although the convergence of the former is much more demanding. Furthermore, note that the dyall.ae4z curve has two peaks for $n = 5$, whereas the reference curve

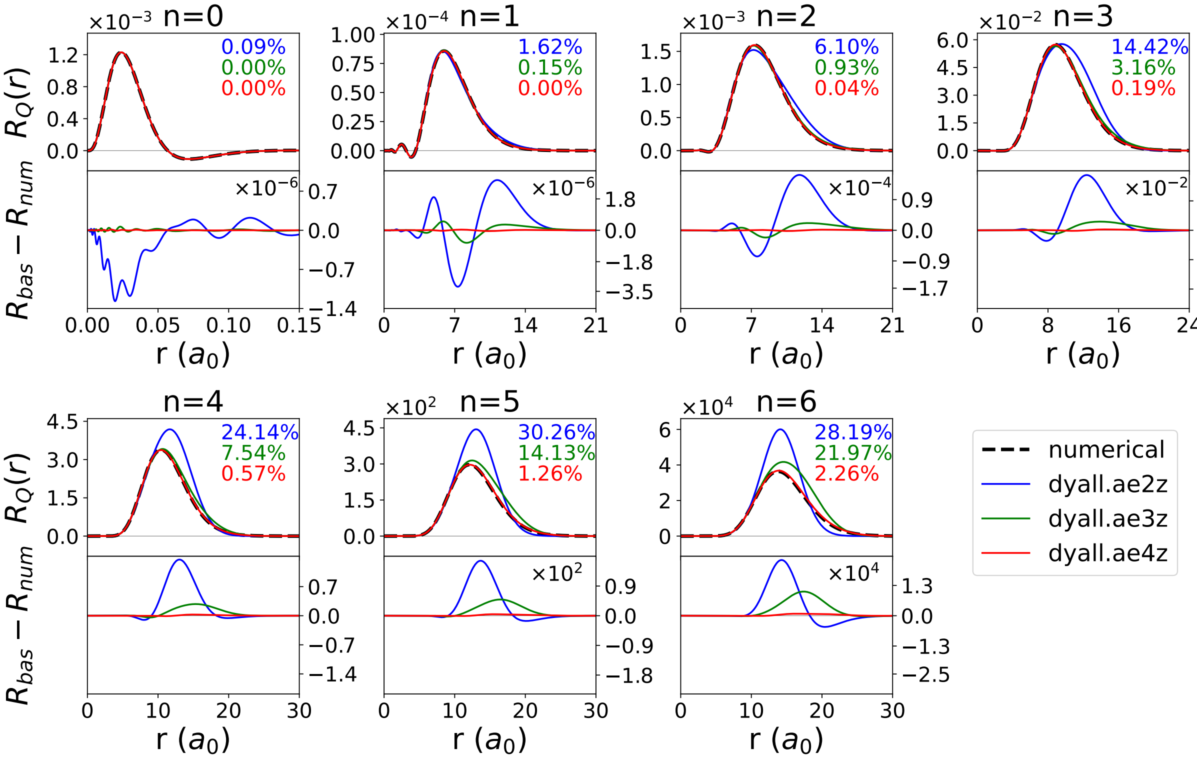

Figure 4.12: Core transition ($1s_{1/2} \rightarrow 7p_{1/2}$): radial distributions of electric multipole moments in the generalized length representation, $\hat{Q}^{[2n+1]}, n \in [0, 6]$. In each box, the upper panel contains the radial distribution, while the lower panel contains the deviation with the numerical reference. Note that each box has a different scale. The percentages in the upper right corner of each box are the relative errors of the transition moments, i.e.$\left|\frac{T_{bas}-T_{num}}{T_{num}}\right|\times 100\%$.

only contains one peak.

Similar artifacts arise in the radial distributions of the electric-velocity multipole moments $\hat{\mathcal{Q}}^{[2n+1]}$ (Figures 4.15 and 4.16 for valence and core transitions, respectively). In both cases, the reference curve follows the same pattern as the other multipole moment. For the valence transition, the dyall.ae2z basis set is sufficient to converge the lowest three orders, whereas the dyall.ae3z basis set should be used at higher orders. For the core transition, the radial distributions are extremely problematic to converge. At $n > 3$ the dyall.ae4z is still not enough to converge towards the reference. Furthermore, at these orders, the dyall.ae4z curves contain additional peaks that are not present in the reference curves. Due to these artifacts, the overall error for $n > 4$ follows a counter-intuitive trend: the dyall.ae2z basis set performs better then the larger bases.

Interestingly, the artificial peaks only appear for the magnetic and electric-velocity distributions, whereas the electric-length distributions converge smoothly towards the numerical reference. This observation can be understood from the problematic basis set convergence of the $Q_{1,-1}$ function (Figure 4.10). After all, the magnetic and electric-velocity distributions depend on the $\boldsymbol{\alpha}$-matrices, which couple the small and large components, whereas the electric-length distribution is diagonal in these two components (see for example Eqs. (4.27)–(4.30)). In Figure 4.10, it was observed that the larger basis sets introduce small oscillations in the error curve of the $Q_{1,-1}$ function.

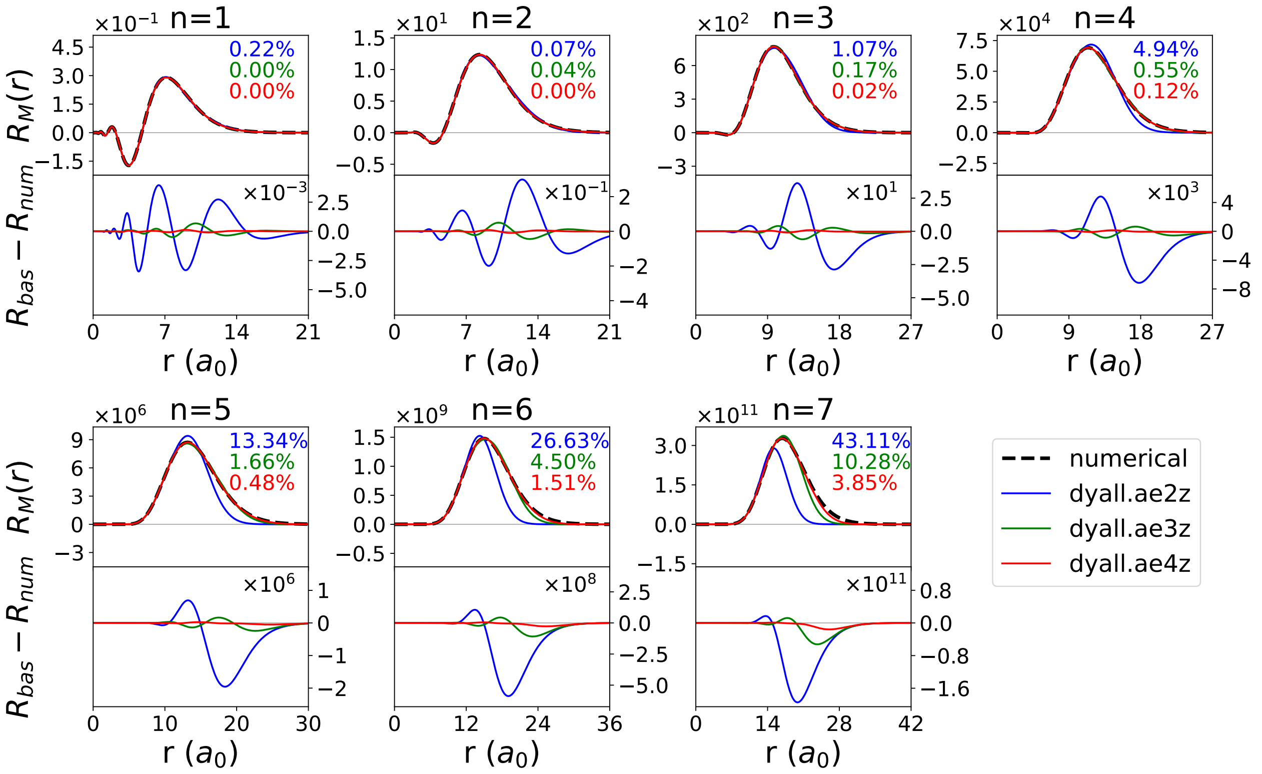

Figure 4.13: Valence transition ($7s_{1/2} \to 7p_{1/2}$)*: radial distributions of magnetic multipole moments* $\hat{m}^{[2n]}, n \in [1,7]$*. In each box, the upper panel contains the radial distribution, while the lower panel contains the deviation with the numerical reference. Note that each box has a different scale. The percentages in the upper right corner of each box are the relative errors of the transition moments, i.e.* $|\frac{T_{bas}-T_{num}}{T_{num}}|\times 100\%$.

These oscillations in the electric-length multipoles are contained in the small–small contribution to the transition density and are thus comparatively small. For the two other types of multipole moments, the oscillations reside in the large–small contribution and are amplified at large distances by the power of the radial distance, thus creating the artificial peaks in Figures 4.14 and 4.16. Similar artifacts are avoided when applying the full interaction operator. As can be inferred from Eqn. (4.30), the error associated with the tail region of the orbitals is not blown out of proportion when applying the full interaction operator. Consequently, this renders the full interaction stable with respect to basis set choice, essentially being converged already with dyall.ae2z.

Conversely, for the core transition, the low-order multipole moments require the dyall.ae3z basis set to obtain reasonable accuracy, whereas even the dyall.ae4z basis set is not enough for the highest orders. However, it might be possible that similar accuracy can be achieved with smaller basis sets. Compared to the dyall.ae2z, the dyall.ae4z basis set contains additional tight functions and high-angular momentum functions that might be irrelevant for the construction of multipole moments. I attempted to augment the dyall.ae2z basis set in an even-tempered fashion with diffuse functions to obtain a better balance between computational costs and performance, but all of these basis sets introduced unphysical oscillations, as shown in Section D.2. Alternatively, a smaller basis could

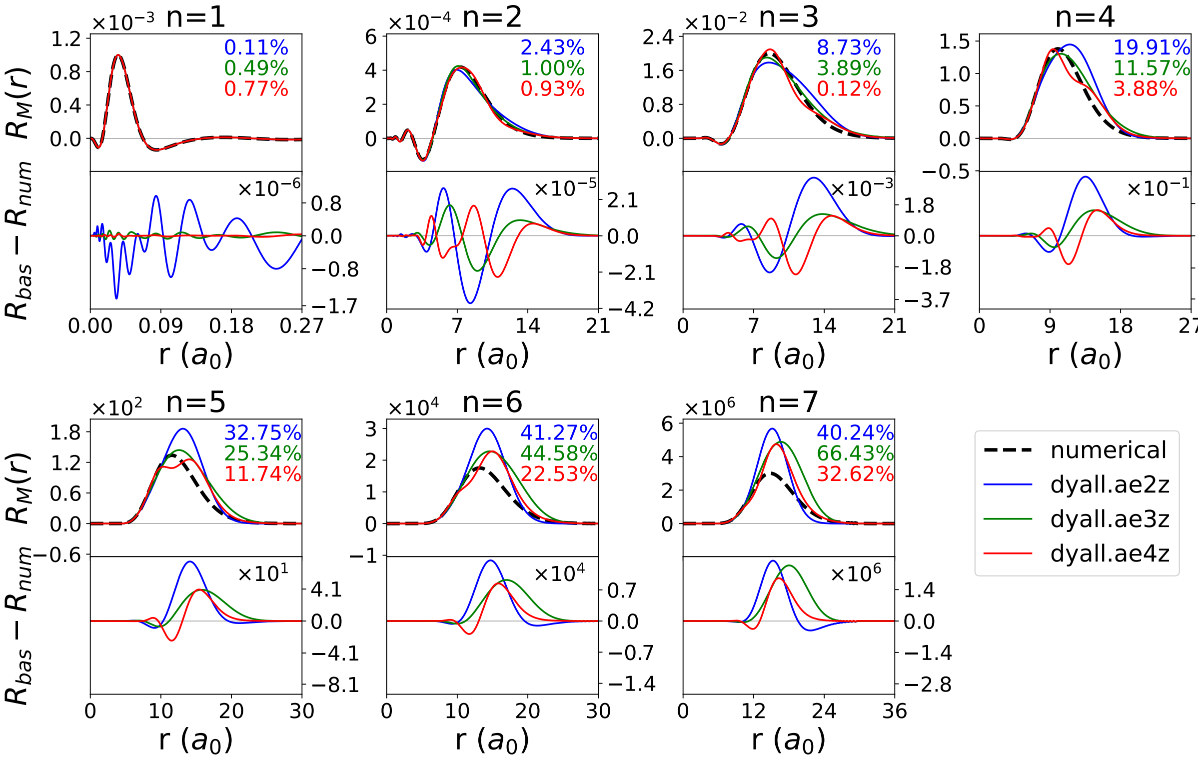

Figure 4.14: Core transition ($1s_{1/2} \rightarrow 7p_{1/2}$)*: radial distributions of magnetic multipole moments* $\hat{m}^{[2n]}, n \in [1, 7]$*. In each box, the upper panel contains the radial distribution, while the lower panel contains the deviation with the numerical reference. Note that each box has different scales. The percentages in the upper right corner of each box are the relative errors of the transition moments, i.e.* $|\frac{T_{bas}-T_{num}}{T_{num}}| \times 100\%$*.*

be constructed by applying a similar scheme as Jensen and coworkers.[219] They augmented the cc-pVnZ basis set with the core polarization functions of the cc-pCV(n+1)Z basis set. I tried a similar procedure to add diffuse functions to the dyall.ae2z basis, but this also led to unphysical oscillations. These findings suggest that the improved convergence observed with increased cardinal number X of the dyall.aeXz series is not only due to the increased range of exponents, but also their distribution within that range.

What remains is to apply the basis sets to the calculation of oscillator strengths. By inspection of Figures 4.11–4.16, it seems that the value of the transition moments become increasingly larger at higher orders, suggesting that the oscillator strengths of both the valence and core transitions have convergence problems with respect to the multipole expansion. To validate this proposition, I report the anisotropic oscillator strengths for the single orbital $1s_{1/2}$ and $7s_{1/2} \rightarrow 7p_{1/2}$ transitions for both the full and truncated interactions in Table 4.2. However, upon inspection of the values in Table 4.2, it becomes clear that the multipole expansion already converges at zeroth order for the valence transition. This appears to be in contradiction with the steady growth of transition moments seen in Figures 4.11, 4.13 and 4.15. This can be understood from the damping of the transition moments by increasing powers of the wave vector k, Eqs. (3.64) (3.87). This is not the case for the $1s_{1/2} \rightarrow 7p_{1/2}$ transition. The oscillator strength corresponding to this transition seems

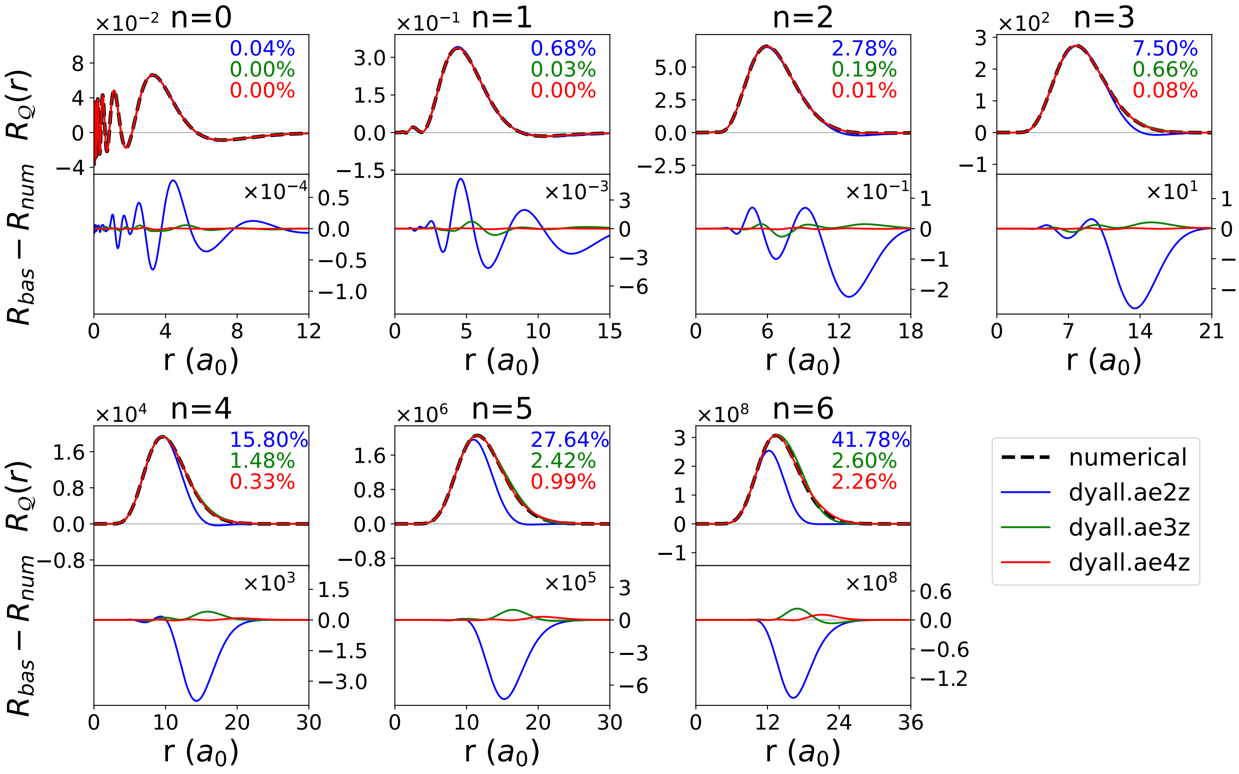

Figure 4.15: Valence transition ($7s_{1/2} \rightarrow 7p_{1/2}$): radial distributions of electric multipole moments in the generalized velocity representation $\hat{Q}^{[2n+1]}, n \in [0,6]$. In each box, the upper panel contains the radial distribution, while the lower panel contains the deviation with the numerical reference. Note that each box has a different scale. The percentages in the upper right corner of each box are the relative errors of the transition moments, i.e. $|\frac{T_{bas}-T_{num}}{T_{num}}|\times 100\%$.

to diverge at higher orders. In fact, these results are in line with Section 4.2, where it was found that the multipole expansion converges extremely slowly at higher excitation energies ($\omega = c$ ($\sim$3728 eV)).[1] The basis set series from Table 4.2 follows the same trends as the radial distributions.

A striking observation in Table 4.2 is that even with the largest basis set the oscillator strengths in the length- and velocity representation differ by orders of magnitude for both core and valence transitions. More precisely, the ratio lr:vr at zeroth order in k (electric-dipole approximation) is about 0.09 for the valence transition and 8.10 for the core transition, clearly in favor of the latter (vr) when comparing with the full interaction. However, before drawing conclusions on the relative merits of these two representations, one should keep in mind that in Section 3.6.2 it is demonstrated that one can only expect equivalence between these two representations when three conditions are met: i) complete basis set limit, ii) variational conditions satisfied and iii) no restrictions on the excitation window. None of these conditions are met for the results presented in Table 4.2. In fact, in order to compare directly with the GRASP reference I have imposed a severely restricted excitation window and I am using orbitals of a singly-excited state and not the ground state. I will now investigate what happens when we successively comply with conditions iii) and ii).

Table 4.3 contains results obtained after lifting restrictions on the virtual orbital space. I have

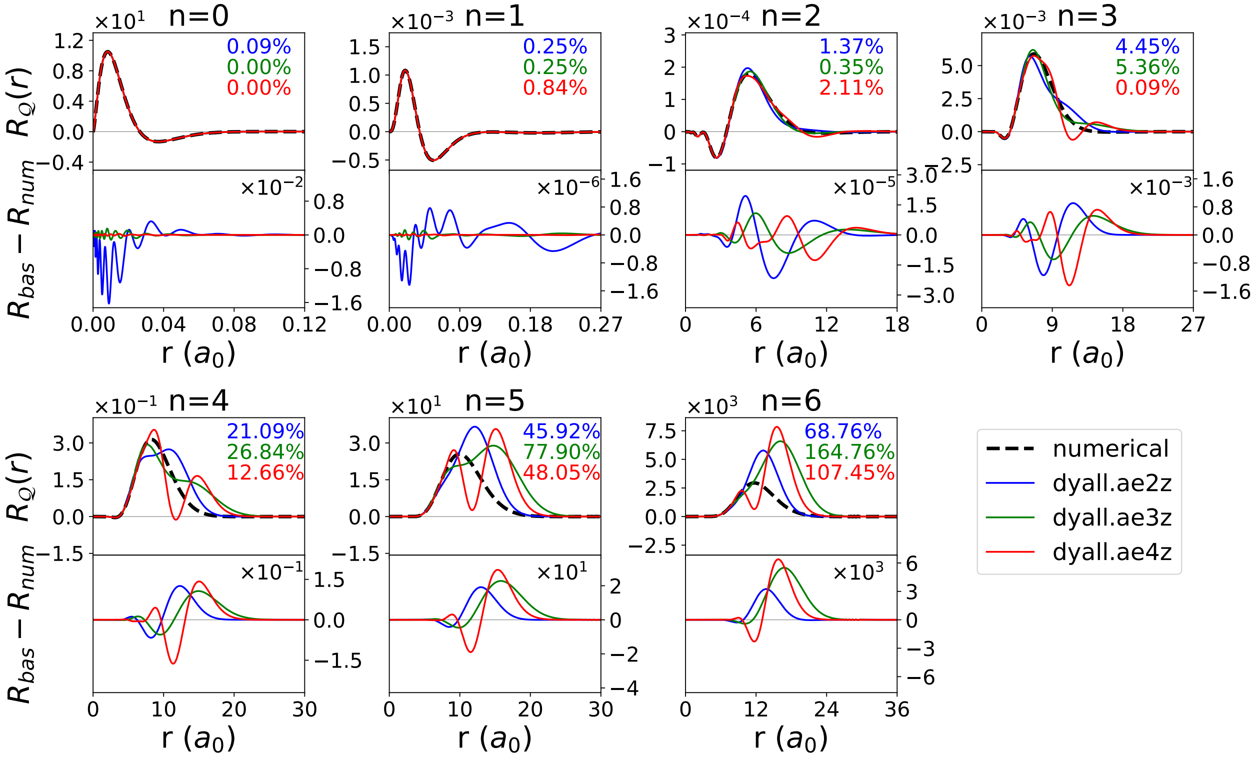

Figure 4.16: Core transition ($1s_{1/2} \rightarrow 7p_{1/2}$): radial distributions of electric multipole moments in the generalized velocity representation $\hat{Q}^{[2n+1]}, n \in [0,6]$. In each box, the upper panel contains the radial distribution, while the lower panel contains the deviation with the numerical reference. Note that each box has different scales. The percentages in the upper right corner of each box are the relative errors of the transition moments, i.e. $|\frac{T_{bas}-T_{num}}{T_{num}}| \times 100\%$.

maintained the restrictions on the occupied space. For the core excitation this is mandatory to assure convergence to the right excitation, and for the valence excitation it is found that it is in any case completely dominated by excitation of the $7s_{1/2}$ orbital. For the valence transition, comparison with Table 4.2 shows that the oscillator strength using the full interaction is significantly reduced. Its value is very well reproduced within the dipole-velocity representation, whereas the discrepancy with the dipole-length representation increases dramatically. For the core excitation there is, on the other hand, only moderate change with respect to Table 4.2. It is only when we in addition use the proper ground-state orbitals that the dipole-length and dipole-velocity oscillator strengths come into agreement (Table 4.4).

Table 4.2: Anisotropic oscillator oscillator strengths ($\frac{c}{\omega}\mathbf{k} = \mathbf{e}_z; \epsilon = \mathbf{e}_y$) *of the* $ns_{1/2} \rightarrow 7p_{1/2}$ $(n = 1, 7)$ *transitions for the full semi-classical interaction operator and accumulated to various orders in the truncated interaction, as indicated by the superscripted numbers in parenthesis, within the multipolar gauge (lr: length representation) and Coulomb gauge (vr: velocity representation), computed at the 4c-TD-HF level of theory with different basis sets. Numbers in parentheses are exponents of 10.*

Basis	ΔE (eV)	f_{full}	gauge	$f^{(\to 0)}$	$f^{(\to 2)}$	$f^{(\to 4)}$	$f^{(\to 6)}$	$f^{(\to 8)}$	$f^{(\to 10)}$	$f^{(\to 12)}$
				$7s_{1/2} \rightarrow 7p_{1/2}$						
dyall.ae2z	1.141	2.603	lr	2.356(-1)	2.356(-1)	2.356(-1)	2.356(-1)	2.356(-1)	2.356(-1)	2.356(-1)
			vr	2.603	2.603	2.603	2.603	2.603	2.603	2.603
dyall.ae3z	1.138	2.605	lr	2.341(-1)	2.341(-1)	2.341(-1)	2.341(-1)	2.341(-1)	2.341(-1)	2.341(-1)
			vr	2.605	2.605	2.605	2.605	2.605	2.605	2.605
dyall.ae4z	1.138	2.605	lr	2.342(-1)	2.342(-1)	2.342(-1)	2.342(-1)	2.342(-1)	2.342(-1)	2.342(-1)
			vr	2.605	2.605	2.605	2.605	2.605	2.605	2.605
				$1s_{1/2} \rightarrow 7p_{1/2}$						
dyall.ae2z	104444.343	1.662(-5)	lr	1.178(-4)	-1.461(-1)	1.806(2)	-1.964(5)	1.954(8)	-1.805(11)	1.556(14)
			vr	1.453(-5)	2.091(-5)	-1.210(-2)	2.072(1)	-2.582(4)	2.689(7)	-2.425(10)
dyall.ae3z	104444.304	1.665(-5)	lr	1.176(-4)	-1.439(-1)	1.726(2)	-1.799(5)	1.723(8)	-1.556(11)	1.346(14)
			vr	1.456(-5)	2.093(-5)	-1.188(-2)	1.974(1)	-2.397(4)	2.531(7)	-2.469(10)
dyall.ae4z	104444.301	1.665(-5)	lr	1.176(-4)	-1.437(-1)	1.713(2)	-1.762(5)	1.649(8)	-1.444(11)	1.203(14)
			vr	1.456(-5)	2.093(-5)	-1.180(-2)	1.926(1)	-2.262(4)	2.291(7)	-2.131(10)

Table 4.3: Anisotropic oscillator oscillator strengths ($\frac{c}{\omega}\mathbf{k} = \mathbf{e}_z; \epsilon = \mathbf{e}_y$) *of the* $ns_{1/2} \rightarrow 7p_{1/2}$ $(n = 1, 7)$ *transitions for the full semi-classical interaction operator and the dipole-length and velocity oscillator strengths, calculated with excited state orbitals and no restrictions on the space of virtual orbitals, within the multipolar gauge (lr: length representation) and Coulomb gauge (vr: velocity representation), computed at the 4c-TD-HF level of theory with different basis sets. Numbers in parentheses are exponents of 10.*

Basis	ΔE (eV)	f_{full}	$f_{\text{lr}}^{(\to 0)}$	$f_{\text{vr}}^{(\to 0)}$	ratio (lr:vr)
			$7s_{1/2} \rightarrow 7p_{1/2}$		
dyall.ae2z	0.146	5.288(-2)	1.421(-4)	5.288(-2)	2.688(-3)
dyall.ae3z	0.113	8.558(-2)	8.554(-5)	8.558(-2)	9.996(-4)
dyall.ae4z	0.111	8.778(-2)	8.218(-5)	8.778(-2)	9.362(-4)
			$1s_{1/2} \rightarrow 7p_{1/2}$		
dyall.ae2z	104444.343	1.568(-5)	1.132(-4)	1.358(-5)	8.336
dyall.ae3z	104444.303	1.571(-5)	1.130(-4)	1.361(-5)	8.306
dyall.ae4z	104444.301	1.571(-5)	1.130(-4)	1.361(-5)	8.306

Table 4.4: Anisotropic oscillator oscillator strengths ($\frac{c}{\omega}\mathbf{k} = \mathbf{e}_z; \epsilon = \mathbf{e}_y$) of the $ns_{1/2} \rightarrow 7p_{1/2}$ ($n = 1, 7$) transitions for the full semi-classical interaction operator and the dipole-length and velocity oscillator strengths, calculated with ground state orbitals and no restrictions on the space of virtual orbitals, within the multipolar gauge (lr: length representation) and Coulomb gauge (vr: velocity representation), computed at the 4c-TD-HF level of theory with different basis sets. Numbers in parentheses are exponents of 10.

Basis	ΔE (eV)	f_{full}	$f_{\text{lr}}^{(\rightarrow 0)}$	$f_{\text{vr}}^{(\rightarrow 0)}$	ratio (lr:vr)
		$7s_{1/2} \rightarrow 7p_{1/2}$			
dyall.ae2z	0.392	1.068(-3)	1.004(-3)	1.068(-3)	0.940
dyall.ae3z	0.383	1.012(-3)	9.686(-4)	1.012(-3)	0.957
dyall.ae4z	0.383	9.750(-4)	9.652(-4)	9.749(-4)	0.990
		$1s_{1/2} \rightarrow 7p_{1/2}$			
dyall.ae2z	104645.540	6.850(-5)	5.900(-5)	5.873(-5)	1.005
dyall.ae3z	104645.510	6.852(-5)	5.900(-5)	5.874(-5)	1.004
dyall.ae4z	104645.509	6.854(-5)	5.901(-5)	5.876(-5)	1.004

4.3.4 Conclusion

In this section, I have assessed the basis set requirements for 4c-TD-HF linear absorption calculations with the full semi-classical light-matter interaction operator as well as the truncated interactions in the generalized length and velocity representations. To simplify the basis set considerations, I focused my attention on the underlying transition moments for the $7s_{1/2} \rightarrow 7p_{1/2}$ and the $1s_{1/2} \rightarrow 7p_{1/2}$ transition in the radium atom. I considered the relativistic dyall.aeXz basis set with cardinal numbers X=2,3,4 and compared to a numerical reference. The comparison was facilitated by the generation and visualization of radial distributions of the corresponding transition moment densities.

To lowest orders, the dyall.ae2z basis set was sufficient to converge the length representation electric multipole moments for both transitions. At higher orders, the dyall.ae4z basis was needed. It was commonly observed that the core transition tends to be more difficult to converge than the valence transition. The basis set convergence of the magnetic multipole moments follows these trends as well, although it seems to be even more difficult to converge for the core transition. Therefore, for the generalized length representation, the dyall.ae4z basis set suffices to properly describe high-order multipoles, although the linear dependence threshold needs to be adjusted.

From all types of multipoles, the velocity representation electric multipoles appear to be most problematic to converge. Even though the valence multipoles converge towards the numerical reference, the core multipoles contain deviations from the reference in the form of oscillations and additional peaks. Due to these artifacts, the basis set convergence seems to be inverted: larger basis sets deviate further from the reference. This suggests that the generalized velocity representation should be applied with caution for $n > 3$. For the generalized velocity representation, I recommend to use the dyall.ae3z basis set, which does not seem to suffer as much from the artifacts as the dyall.ae4z basis set. In addition, I recommend to go not further than $n = 3$, because after this order, the reliability of this scheme becomes questionable.

The full interaction operator does not suffer from these problems and is already converged with the dyall.ae2z basis. Considering that the truncated interaction also suffers from slow convergence with respect to the multipole expansion, I recommend to apply the full interaction when calculating X-ray transitions.

These findings are transferable to the non-relativistic limit, because in this limit, the full interaction and the length representation electric multipole have the same characteristics. Furthermore, the magnetic multipoles and velocity representation electric multipoles converge faster towards the numerical reference than equivalent 4c calculations, because the problems associated with linear dependence disappear upon taking this limit. Therefore, I expect that in the non-relativistic limit, the basis set requirements of multipole moments are less demanding.

Conclusions are possibly less obvious for the intermediate 2-component relativistic level. The present approach would formally require the generation of radial distributions using properly picture-changed interaction operators, and these are for instance not available for the eXact 2-Component Hamiltonian (X2C), for which in general only a matrix representation, and not a real-space one, is available (see for instance discussion in Ref.117). However, again the elimination of the small components suggests that basis set convergence should improve.

4.4 Systems with Symmetry Equivalent Centers

For the calculations on the radium atom (see Section 4.2 and 4.3), it was observed that the dipole-allowed transitions only gained modest corrections when including non-dipolar effects, the explanation being that the compactness of the core-orbitals negate these effects. However, if the system under consideration contains symmetry equivalent centers, the core transitions that arise from them are delocalized, which, in principle, should enhance non-dipolar effects. For those purposes, I will consider the Cl K-edge in $TiCl_4$. In addition, this system represents a case where there is no natural choice of gauge origin, thus forming a suitable system to test origin-(in)dependence of the two representations. This system has previously been studied in the context of non-dipolar effects in linear X-ray absorption using low-order multipole expansions. In particular, it was used to demonstrate the appearance of negative oscillator strengths[28] upon truncation of the light-matter interaction in the generalized velocity representation in a non-relativistic framework.[27] Below, I will revisit this case and assess the necessity to go beyond the electric-dipole approximation. I further study numerically the gauge-origin dependence of the three schemes in the case of soft X-ray absorption. Ligand K-edge absorption spectroscopy supposedly provides direct information on the covalency of metal–ligand bonds due to the admixture of the ligand p-orbitals with the metal d-orbitals.[220, 221] The Cl K-edge absorption of $TiCl_4$ has been studied both experimentally and also theoretically within and beyond the ED approximation using truncated multipole-expanded expressions. Its experimental spectrum features a broad pre-edge peak that require a two-peak fit (in toluene: at 2821.58 and 2822.32 eV with an approximate intensity ratio of 0.84).[222] In T_d symmetry, the five 3d-orbitals of Ti belong to the e and t_2 irreducible representations, and the pre-edge bands can be assigned to excitations from the a_1 and t_2 Cl 1s-orbitals into the e and t_2 sets of 3d-orbitals on Ti, respectively. Here, I focus on the eight lowest-lying transitions $(a_1, t_2 \rightarrow e)$ which give rise to three degenerate sets (E, T_1 and T_2) of which the latter is ED allowed. The results in this section are mainly based on the findings from ref. 1.

4.4.1 Computational Details

The data reported in this section have been obtained with a development version of the DIRAC electronic structure code[190] (Tables 4.5–4.7: revision `52c65be`).

The calculated results presented in this section have been obtained by time-dependent density functional theory (TD-DFT) calculations, based on the Dirac–Coulomb Hamiltonian and within the restricted excitation window (REW) approach[215, 216] using the PBE0[193, 194] exchange-correlation functional and the dyall.ae3z basis sets.[196, 197] The small component basis sets were generated according to the condition of restricted kinetic balance, and the (SS|SS) integrals are replaced by an interatomic SS correction.[195] A Gaussian model was employed for the nuclear charge distribution.[115] A 86-point Lebedev grid ($L_{\max} = 12$) was used for the isotropic averaging of the oscillator strengths based on the full light-matter interaction operator. The gauge origin was placed in the center-of-mass and spatial symmetry was invoked in all cases except for the gauge-origin dependence calculations. The geometry of $TiCl_4$ was taken from Ref. 27 where it was obtained using the BP86 exchange-correlation functional[223, 224] and the TZP basis set.[225]

4.4.2 Full vs. Truncated Light-Matter Interaction

Table 4.5 collects the isotropically averaged oscillator strengths for the pre-edge transitions computed in 4-component relativistic framework with the full light-matter interaction operator as well as accumulated to increasing orders (up to 12th order) in the wave vector within Coulomb gauge (velocity representation) and multipolar gauge (length representation). In line with the results of Lestrange *et al.*,[28] negative oscillator strengths are found at second order for the $^1T_2$ excitations in both length and velocity representation. The same issue appears for the $^1T_1$ and ^1E sets, but at fourth order. As discussed previously,[28, 29] this behavior is expected when the cross terms involving the lower-order moments to $f^{[n]}$ dominate the diagonal contributions. As evident from the underlying contributions given in Table 4.6, the multipole expansions are alternating, and beyond fourth order, the correction is reduced at each order. Indeed, the expansions converge to the full expression at about 12th order. For the dipole-allowed $^1T_2$ set, the correction introduced by non-dipolar effects is significant, reducing the oscillator strength by a factor of $\sim$5. As seen from the comparison of the ED and full (BED) oscillator strengths summed over the three sets of transitions, included in Table 4.5, the implication of going beyond the ED approximation is a redistribution of intensity among transitions. In particular, the ED forbidden $^1T_1$ and ^1E transitions gain intensity beyond that of the T_2 set. It should be noted that this intensity redistribution cannot be observed in the spectrum due to broadening.

However, even in the hypothetical case where these transitions are well-separated, the validity of these results can be questioned. In the exact many-body wave function, the probability to find a core electron on either of the symmetry equivalent centers is strongly correlated with the motion of the other core electrons. For example, after a core electron is located on center A, the probability to find another electron on the same center decreases, whereas the probability to find it on other centers increases. This effect is poorly taken into account using SCF methods, were core electrons are described by orbitals delocalized over the centers and completely devoid of static correlation. Early accounts of this effects were made by Bagus *et al.* in their work involving core-ionized O_2^+, were a significant improvement of the ionization energy could be obtained by localizing the core orbital, albeit at the expense of losing the symmetry of the wave function. If we insist on using SCF methods to describe core excitations, we are left with a dilemma: either we localize the core orbital, which improves the energy values, but diminishes non-dipolar effects, or we use the delocalized orbitals, which induces the opposite effect.

However, this problem is a false dilemma, since there is a third option, as it was found that more complicated wave function methods (such as MCSCF[226] or CCSD[227]) can both preserve symmetry while at the same time reproducing ionization energies. To properly assess the importance of non-dipolar effects in systems with symmetry equivalent centers, it is thus necessary to go beyond standard SCF methods. Extending the DIRAC implementation to the MCSCF level of theory was one of the goals in this thesis, although it has not yet been completed. Therefore, the importance of non-dipolar effects for systems with symmetry equivalent centers remains partially unresolved. In the outlook (Sec. 5), it is further discussed what code has to be programmed to allow for MCSCF calculations beyond the electric-dipole approximation.

Table 4.5: Comparison of isotropically averaged oscillator strengths for Cl $1s \rightarrow$ *Ti* $3d$ *transitions of* $TiCl_4$ *for the full semi-classical interaction operator and accumulated to various orders, as indicated by the superscripted number in parenthesis, within multipolar gauge (lr: length representation) and Coulomb gauge (vr: velocity representation), computed at the 4c-TD-PBE0 level of theory with the dyall.ae3z basis set. Contributions from degenerate states have been summed. A 86-point* ($L_{max} = 12$) *Lebedev grid was used to obtain the isotropically averaged full BED oscillator strengths. The gauge origin is placed on the Ti atom.*

Final state	ΔE (eV)	gauge	$10^3 f^{(\rightarrow 0)}$	$10^3 f^{(\rightarrow 2)}$	$10^3 f^{(\rightarrow 4)}$	$10^3 f^{(\rightarrow 6)}$	$10^3 f^{(\rightarrow 8)}$	$10^3 f^{(\rightarrow 10)}$	$10^3 f^{(\rightarrow 12)}$	$10^3 f_{\text{full}}$
$^1T_1$	2773.351719	lr	0.000	17.976	-7.344	8.560	2.879	4.191	3.979	3.993
		vr	0.000	17.976	-7.372	8.561	2.866	4.183	3.970	
^1E	2773.351723	lr	0.000	7.199	-1.251	3.569	1.945	2.308	2.249	2.248
		vr	0.000	7.156	-1.229	3.548	1.943	2.298	2.242	
$^1T_2$	2773.351725	lr	7.825	-17.413	16.369	-4.360	2.948	1.272	1.543	1.510
		vr	7.781	-17.380	16.353	-4.358	2.942	1.271	1.540	
	Sum	lr	7.825	7.763	7.775	7.769	7.772	7.772	7.771	7.752
		vr	7.781	7.752	7.752	7.752	7.752	7.752	7.752	

Table 4.6: Comparison of isotropically averaged oscillator strengths for Cl $1s \rightarrow$ *Ti* $3d$ *transitions of* $TiCl_4$ *for the full BED operator and at various orders within multipolar gauge (lr: length representation) and Coulomb gauge (vr: velocity representation) gauges as computed at the 4c-TD-PBE0 level of theory with the dyall.ae3z basis set. Numbers in parentheses are exponents of 10. F.S. stands for final state. Contributions from degenerate states have been summed. A 86-point* ($L_{max} = 12$) *Lebedev grid was used to obtain the isotropically averaged full BED oscillator strengths. The gauge origin is placed on the Ti atom.*

F.S.	ΔE (eV)	gauge	$f^{[0]}$	$f^{[2]}$	$f^{[4]}$	$f^{[6]}$	$f^{[8]}$	$f^{[10]}$	$f^{[12]}$	f_{full}
$^1T_1$	2773.351719	lr	0.000	1.798(-02)	-2.532(-02)	1.590(-02)	-5.682(-03)	1.312(-03)	-2.125(-04)	3.993(-03)
		vr	0.000	1.798(-02)	-2.535(-02)	1.593(-02)	-5.695(-03)	1.316(-03)	-2.131(-04)	
^1E	2773.351723	lr	0.000	7.199(-03)	-8.450(-03)	4.819(-03)	-1.623(-03)	3.627(-04)	-5.937(-05)	2.248(-03)
		vr	0.000	7.156(-03)	-8.385(-03)	4.778(-03)	-1.606(-03)	3.555(-04)	-5.576(-05)	
$^1T_2$	2773.351725	lr	7.825(-03)	-2.524(-02)	3.378(-02)	-2.073(-02)	7.308(-03)	-1.675(-03)	2.706(-04)	1.510(-03)
		vr	7.781(-03)	-2.516(-02)	3.373(-02)	-2.071(-02)	7.301(-03)	-1.672(-03)	2.689(-04)	

4.4.3 Origin-Dependence

The above results were computed with the gauge-origin placed at the Ti atom. I now proceed to a numerical evaluation of their dependency on the gauge origin ($\mathbf{O}+\mathbf{a}$). The formulations based on the full semi-classical interaction operator and truncated interaction in the velocity representation are formally gauge invariant. In practical calculations, however, as discussed in Section 3.4.1, invariance in the latter case relies on the accurate cancellation of lower-order contributions multiplied with powers $(\mathbf{k} \cdot \mathbf{a})$, where $\mathbf{a}$ is the displacement. In contrast, as discussed in Section 3.6.2, in the multipolar gauge formal gauge-origin invariance appears to only be achieved in the practically unreachable limit of the complete expansion of the fields.

Table 4.7 collects the total isotropic oscillator strength for the dipole-allowed ${}^1T_2$ set for each of the three schemes for going beyond the ED approximation using different choices for the gauge origin. As expected, the results for the full light-matter interaction operator remain unchanged, providing a numerical verification of its gauge-origin invariance. The same is true for the oscillator strengths in the generalized velocity representation. However, numerical noise from the cancellation of many terms in powers of the displacement becomes apparent at large displacements. For a displacement of 100 a_0, instabilities start to appear at 10th order, and at 12th order, the oscillator strength exceeds the full result by one order of magnitude. The oscillator strengths in the multipolar gauge already at second order differ significantly upon shifting the origin from the Ti atom. In line with the discussion in Section 3.6.2, the two representations are roughly equivalent if the gauge origin coincides with the coordinate origin.

Table 4.7: Gauge-origin dependency of the isotropically averaged oscillator strengths for the ${}^1T_2$ set of Cl $1s \rightarrow$ Ti $3d$ transitions of TiCl$_4$ for the full semi-classical light-matter interaction operator and accumulated to various orders within multipolar gauge (lr: length representation) and Coulomb gauge (vr: velocity representation), computed at the 4c-TD-PBE0 level of theory and the dyall.ae3z basis set. Numbers in parentheses are exponents of 10. At this level the excitation energy is calculated as 2773.351145 eV. Contributions from the degenerate set have been summed. An 86-point ($L_{max} = 12$) Lebedev grid was used to obtain the isotropically averaged full BED oscillator strengths. The gauge origin is shifted along the x-axis (d_x) where $d_x = 0.0$ a_0 corresponds to gauge-origin in the Ti atom.

d_x (a_0)	gauge	$f^{(\rightarrow 0)}$	$f^{(\rightarrow 2)}$	$f^{(\rightarrow 4)}$	$f^{(\rightarrow 6)}$	$f^{(\rightarrow 8)}$	$f^{(\rightarrow 10)}$	$f^{(\rightarrow 12)}$	f_{full}
0	lr	7.825(-03)	-1.741(-02)	1.637(-02)	-4.360(-03)	2.948(-03)	1.272(-03)	1.543(-03)	1.510(-03)
	vr	7.781(-03)	-1.738(-02)	1.635(-02)	-4.358(-03)	2.943(-03)	1.271(-03)	1.540(-03)	
10.0	lr	7.825(-03)	-1.755(-02)	1.670(-02)	-4.738(-03)	3.238(-03)	1.097(-03)	1.670(-03)	1.510(-03)
	vr	7.781(-03)	-1.738(-02)	1.635(-02)	-4.358(-03)	2.943(-03)	1.271(-03)	1.540(-03)	
50.0	lr	7.825(-03)	-2.045(-02)	1.422(-01)	-2.951(+00)	4.429(+01)	-5.055(+02)	6.495(+03)	1.510(-03)
	vr	7.781(-03)	-1.738(-02)	1.635(-02)	-4.358(-03)	2.943(-03)	1.271(-03)	1.546(-03)	
100.0	lr	7.825(-03)	-3.148(-02)	2.398(+00)	-2.223(+02)	1.343(+04)	-6.178(+05)	3.198(+07)	1.510(-03)
	vr	7.781(-03)	-1.738(-02)	1.635(-02)	-4.358(-03)	2.943(-03)	1.021(-03)	4.785(-02)	

4.4.4 Conclusion

Two important key conclusions follow from these calculations:

- the studied transitions stemming from the Cl K-edge in TiCl$_4$ have significant non-dipolar corrections, mainly induced by the delocalization of the Cl core orbitals. However, due to the closeness of the transitions, the accumulated value of these transitions is hardly affected. Even if this were not the case, it can be questioned whether the delocalization of the core orbital is a true physical effect. To properly assess this, it is required to go beyond SCF theory.

- Formal gauge-origin invariance of oscillator strengths in multipolar gauge hinges on commutator expressions that do not necessarily hold in a finite basis. This explains the notorious lack of order-by-order gauge-origin independence in practical calculations beyond the electric-dipole approximation based on any truncated multipolar gauge formulation.[28, 29] As indicated in Section 3.6.2 these commutator relations, involving the Hamiltonian, correspond to a gauge transformation from the length to the velocity representation. In other words, gauge-origin independence in multipolar gauge is shown by transforming to another gauge for which origin-independence holds. Thus far, I have not been able to show gauge-origin invariance while staying within multipolar gauge.

4.5 Electronic Circular Dichroism

I have not yet exploited the versatility of the BED implementation to its full extent, since all calculations until this point involved the absorption of linearly polarized light. In this section, I will thus focus on the isotropic and anisotropic ECD calculated using the *full* semi-classical light–matter interaction, as well as the generalized velocity representation. This allows us to investigate the ECD response across the electromagnetic spectrum, from optical to X-ray regimes. So far, previous theoretical studies of the isotropic XNCD of molecules were based on a non-relativistic formulation while only considering the first-order truncated interaction, which is proportional to the dot-product of the electric- and magnetic-dipole moment (Eqn. (3.150)).[228, 229, 230, 231, 232, 233, 234, 235, 236]

A rough estimate of the first-order XNCD can be found by assuming that the transition in question is effectively atomic in nature, which is justified by the atom-like character of core orbitals. Under this assumption, atomic selection rules apply, implying that the electric- and magnetic-dipole moment transition rules dictate whether the XNCD vanishes. However, as demonstrated in Section C.2, the non-relativistic magnetic-dipole selection rules prescribe that atomic transitions can only occur between states that are split by spin-orbit coupling, thus suggesting that the XNCD is zero within this simplified scheme. In more realistic calculations, the core orbitals are polarized away from atomic symmetry, which renders the XNCD non-zero, an effect that was taken into consideration in the above mentioned studies. The current implementation accounts for two additional possible contributions: (*i*) effects of beyond first-order light–matter interactions and (*ii*) inclusion of relativistic effects, notably spin-orbit coupling that modifies selection rules (in particular, the magnetic transition-dipole selection rule, discussed in Section C.2). Consequently, this allows, for the first time, to realistically examine the ECD response of molecules across the valence and X-ray regimes.

However, unlike previous examples, it is not sufficient to use the same atomic target system, which has vanishing ECD due to its high symmetry. Therefore, as test systems, I consider the simplest disulfide chromophore models, dihydrogen disulfide H_2S_2 and dimethyl disulfide $(CH_3S)_2$. Because of the low disulfide torsional barriers (∼6-11 kcal/mol[237, 238, 239, 240]), the two enantiomeric forms (P- and M-helix) cannot be resolved experimentally. However, the disulfide bridge is an important structural element in proteins,[241] where it preferentially occurs in non-planar, chiral conformations (C_2 symmetry) and hence displays structurally-induced axial chirality. An interesting perspective for complex systems (e.g., proteins) is the potential use of XNCD as a local probe of chirality.[235, 230] This could potentially complement the delocalized conformational information encoded in valence ECD. Because of its computational tractability, H_2S_2 has been widely used to benchmark electronic structure methods for the calculation of chiroptical properties.[242, 243, 244, 245, 246, 247, 248] For the same reason, Goulon *et al.* also used it to estimate relative magnitudes of XNCD responses within the first-order truncated interaction and non-relativistic framework, reporting values below the experimental detection limits.[228] Here, I revisit the ECD of the disulfide chromophore across the valence, L- and K-edges, going beyond these approximations.

4.5.1 Computational Details

The geometries of H_2S_2 and $(CH_3S)_2$ were obtained using the B3LYP[249, 250, 251, 252] exchange–correlation functional and the cc-pVTZ[253, 254] basis set. Geometry optimizations were performed in Gaussian 16.[255] To mimic the χ_3 disulfide angle typical for protein structures,[256] a constrained geometry optimization was performed for $\chi_3 = -87°$, corresponding to M-helical chirality.[257] The restricted excitation window approach[215, 216] was used to selectively target the sulfur L- and K-edges. This also eliminates the issue of artificial transitions to quasi-continuum orbitals caused by finite basis set effects that otherwise often interferes simulations at the L-edge.[258, 259] A Gaussian model was employed for the nuclear charge distribution,[115] and an 86-point Lebedev grid ($L_{\max} = 12$) was used for the isotropic averaging of the differential linear absorption based on the full interaction operator. The gauge origin was placed in the center-of-mass (COM) and spatial symmetry was invoked in all cases except for the gauge-origin dependence calculations.

Excitation energies, linear and differential absorption cross sections for the full interaction operator as well as the multipole expansions within the generalized velocity gauge were computed using the PBE0[193, 194] exchange–correlation functional and the uncontracted aug-pcX-3[260] and aug-pc-3[261, 262, 263] basis sets for sulfur and hydrogen, respectively. The pcX-n basis set series was developed for describing core-excitation processes using the ΔSCF (Self-Consistent Field) approach at both the nonrelativistic and relativistic levels. The small component basis sets were generated within the condition of restricted kinetic balance. The relativistic calculations were performed using a Dirac-Coulomb Hamiltonian in which the (SS|SS) integrals are replaced by an interatomic SS energy correction.[195] Gauge-origin invariance of the full semi-classical formulation of the isotropic and anisotropic rotatory strengths (Eqs. (3.20) (3.64) (3.87) (3.134) (3.138)) and its first-order truncated counterpart was confirmed numerically by shifting the gauge-origin (from 0 to 100 a_0) along the C_2 axis. This leads to a redistribution of the E1–E2 and E1–M1 contributions to $R^{[1]}_{xx}$ and $R^{[1]}_{yy}$ (Eqn. (3.153)) for transitions of B symmetry. As expected, the results remained unchanged for both the full and truncated formulations (data not shown). Simulated spectra were obtained by convolving the stick spectrum with Gaussian lineshape functions with full width at half maximum (FWHM) of 0.4 eV, and those for $(CH_3S)_2$ were shifted by different offsets for each absorption edge to match their experimental counterparts.

To assess the effect of increased excitation energies on the differential oscillator strength, the L_1- and K-edge spectra were calculated for the heavier analogues of H_2S_2: H_2X_2, X=Se and Te. In analogy with H_2S_2, the geometries for the two heavier analogous were obtained from a constrained optimization (fixing $\chi_3 = -87°$) using the cc-pVTZ[264] and def2-VTZPP[265] basis sets for X=Se and Te, respectively. Except for the choice of basis set, this series of calculations was carried out at the same level of theory as previously mentioned H_2S_2 calculation. To reduce the computational cost for the heavier analogous, I used the dyall.av3z basis set[266] for all spectral calculations. To make the comparison between the structural analogues more precise, the H_2S_2 calculations were repeated using this basis set.

4.5.2 Results and Discussion

Before considering the ECD response of the disulfides, I assign the linear absorption features across the valence and X-ray regions. I initially focus on $(CH_3S)_2$ for which experimental gas-phase absorption spectra are available.[267, 268, 269, 270, 271] Expectedly, and as shown in Figure D.7 in Section D.3, the spectral profiles for H_2S_2 are similar, and because of its greater computational tractability, I consider this minimal disulfide in subsequent analyses.

Figure 4.17 displays the rotationally averaged linear and differential absorption spectra for valence, sulfur L- and K-edge transitions of $(CH_3S)_2$, computed using the full interaction operator (green shading) with corresponding oscillator strengths indicated as green sticks. Hereafter, I explicitly indicate the results of the full interaction with the superscript "full". For comparison, I also provide the lowest non-vanishing terms in the truncated generalized velocity representation (orange lines) for linear and differential absorption, i.e., zeroth- and first-order in the magnitude of the wave vector, respectively. Black sticks at the top indicate the location of the underlying electronic transitions and black lines (solid and dashed) the experimental absorption spectra.[267, 271, 268, 269, 270] Apart from uniform shifts necessary to align the lowest-energy band to the respective experimental spectrum, the theoretical spectra capture well both relative intensities and peak splittings.

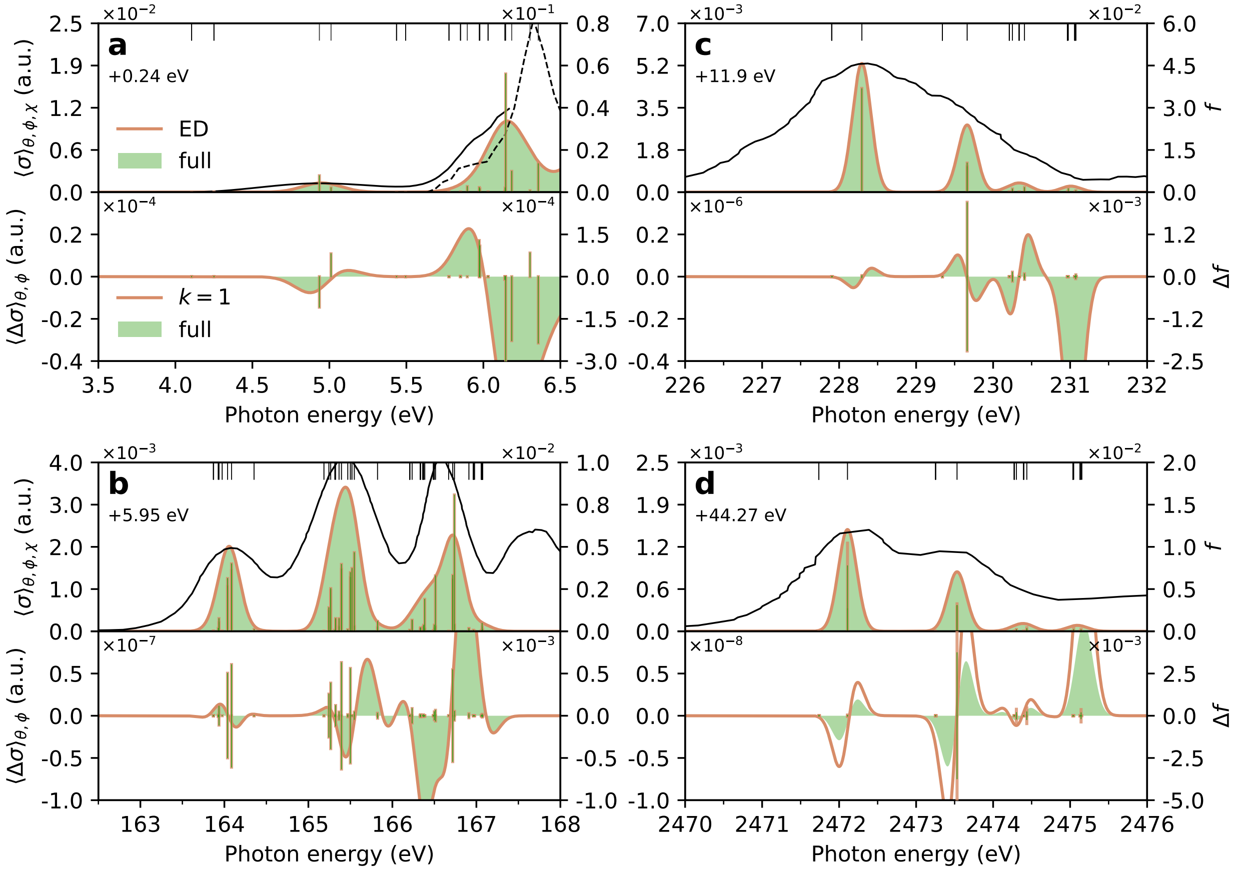

Figure 4.17: Isotropic linear (top) and differential (bottom) absorption spectra of (CH$_3$S)$_2$*: (a) valence, (b)* $L_{2,3}$*-edge, (c)* L_1*-edge and (d) K-edge spectra using the full interaction operator in Eqs. (3.16) (green shadings) or the lowest non-vanishing generalized velocity representation (orange lines). Left axes correspond to (differential) absorption cross-sections, whereas (differential) oscillator strengths (sticks) are shown on the right axes. Black sticks indicate the location of all computed transitions whereas black lines are experimental spectra. [267, 268, 269, 270, 271] The stick spectra were convolved with a Gaussian lineshape with FWHM of 0.4 eV. The theoretical absorption spectra have been uniformly shifted to align with the experimental counterparts (shift values indicated in the top panels). The same shifts were applied to the ECD spectra.*

The first valence band (Figure 4.17a) is dominated by the two excitations from the symmetric and antisymmetric combinations of the non-bonding $3p$ orbital on each sulfur to the lowest unoccupied σ^*_{SS} orbital (b symmetry). This assignment is consistent with the analysis by Linderberg and Michl on H_2S_2.[272] Since the valence orbitals are found to have well-defined spin, I adopt a non-relativistic state notation for the valence states, i.e., 1^1B and 2^1A, respectively. They are separated by ∼0.15 eV. The second valence band originates from transitions into the σ^*_{CS} orbital (3^1A and 2^1B).

Turning to the X-ray region, the first two bands at the sulfur $L_{2,3}$-edge (Figure 4.17b) are dominated by transitions from the symmetric and antisymmetric combinations of the S $2p_{3/2}$ and

$2p_{1/2}$ core orbitals to the σ^*_{SS} orbital. It should be noted that the A/B pair of associated transitions are essentially degenerate (less than 0.1 meV splitting) because of the limited overlap between the core orbitals on each of the sulfur atoms. The calculated spin-orbit splitting of ∼1.35 eV between the L_3- and L_2-branches is comparable to the experimental splitting reported for dihydrogen sulfide (∼1.2 eV[273, 274]). The L_3/L_2 branching ratio of ∼1.4:1 (obtained by summing the underlying oscillator strengths) deviates significantly from its statistical value, which is obtained only in the limit of $j-j$ coupling.[275, 276] The second peak in each branch is dominated by excitations to the σ^*_{CS} orbital and is separated from the first peak by $\sim 1.4-1.5$ eV. Consequently, the second band in the spectrum contains contributions from both branches whereas the third band is associated with the second peak in the L_2 branch. These assignments agree with previous studies.[277, 269] The energy range considered as well as the basis set used in our calculations does not cover the fourth band in the experimental spectrum which, according to previous work,[269] originates from excitations to higher-lying orbitals of mixed σ^*_{CS}/Rydberg character. Not surprisingly, the L_1- and K-edge spectra bear strong resemblance (Figure 4.17c-d): they display two pre-edge features, separated by ∼1.5 eV, which originate from pairs of near-degenerate excitations from the bonding and antibonding combinations of sulfur s-orbitals into the σ^*_{SS} and σ^*_{CS} orbitals, respectively.[278, 279, 270]

A non-vanishing ECD response in these minimal disulfides results from axial chirality caused by trapping the disulfide bridge in a non-planar (i.e., C_2) conformation. As described above, the two lowest-energy transitions in each spectral domain are dominated by an excitation from the bonding or antibonding combinations of the relevant atomic orbitals on the sulfurs into the σ^*_{SS} orbital. This pairing of transitions manifests as bisignate features in the low-energy region of the ECD spectra. On the basis of the simple Bergson model for the low-energy transitions in the disulfide chromophore,[280, 281] Linderberg and Michl[272] formulated a quadrant rule for the optical activity of the two low-energy valence transitions (dominated by excitations from the symmetric and antisymmetric combinations of non-bonding $3p$ orbitals on sulfurs to the σ^*_{SS} orbital) in organic disulfides. This rule relates the sign of the long-wavelength Cotton effect across the four dihedral quadrants and is a specific case of the C_2-rule for general chromophores of effective C_2 symmetry.[282] Woody extended the theoretical analysis to also include the absolute sign of the lowest ECD band within each quadrant,[283] providing predictions in agreement with experimental results across different dihedral angles.[284, 285, 286, 287]

For the M-helical form considered here, a negative-first Cotton effect is observed, consistent with the quadrant rule.[283] The intensity asymmetry of the lowest-energy valence couplet is attributed to different intrafragment (i.e., CH_3S-) contributions to the ECD signal of each transition. At higher energies, the electronic coupling between the (core) orbitals decreases, reducing both their energetic splitting and the intrafragment ECD contributions which become increasingly atomic-like. As a consequence, the paired core transitions become near-degenerate (energy splitting of a few meV or less) with rotational strengths of almost equal magnitudes but opposite signs (see Table 4.8). Hence, after additionally accounting for sources of broadening, including finite core-hole lifetimes (∼0.1 and ∼0.5 eV at the sulfur L- and K-edges,[288, 289] respectively), it may realistically only be possible to resolve the differential contributions with the absolute sign given by the most intense of the transitions. Accordingly, the effective signals are therefore reduced by orders of magnitude in the X-ray region (see accumulated values in Table 4.8).

The linear absorption profiles with the full interaction and the electric-dipole approximation essentially coincide across the four spectral regions. However, as shown by the underlying oscillator

Table 4.8: Beyond first-order effects in the isotropically averaged and anisotropic rotatory strengths for the lowest intense valence, L- and K-edge transitions of $(CH_3S)_2$ *for the full semi-classical light-matter interaction operator and in first-order within the Coulomb gauge, computed at the 4c-TD-PBE0 level of theory and the uncontracted aug-pcx-3/aug-pc3 basis set. For the oriented case,* $\mathbf{k}(\pi/2, \pi/2)$ *for the valence and* $L_{2,3}$*-edge transitions and* $\mathbf{k}(\pi/2, \pi/4)$ *for the* L_1*- and K-edge transitions. For each spectral region, the accumulated (differential) oscillator strength (ac) across the two pairs of transitions (A/B symmetry) is given in the third line. Numbers in parentheses are exponents of 10.*

Transition	ΔE (eV)		$f_{\text{iso}}^{\text{full}}$	$f_{\text{iso}}^{[0]}$	$\Delta f_{\text{iso}}^{\text{full}}$	$\Delta f_{\text{iso}}^{[1]}$	$\Delta f_{\mathbf{k}}^{\text{full}}$	$\Delta f_{\mathbf{k}}^{[1]}$
				valence				
1^1B ($n_\text{S} \rightarrow \sigma^*_\text{SS}$)	4.69514		7.7977(-03)	7.7974(-03)	-1.0856(-04)	-1.0856(-04)	-6.1154(-05)	-6.1147(-05)
2^1A ($n_\text{S} \rightarrow \sigma^*_\text{SS}$)	4.77069		2.0797(-03)	2.0793(-03)	8.1247(-05)	8.1244(-05)	1.1759(-04)	1.1758(-04)
		ac	9.8773(-03)	9.8767(-03)	-2.7316(-05)	-2.7317(-05)	5.6436(-05)	5.6435(-05)
				$L_{2,3}$-edge				
$6B$ ($2p_{3/2} \rightarrow \sigma^*_\text{SS}$)	158.08721		3.1232(-03)	3.1230(-03)	5.0231(-04)	5.0326(-04)	-1.1661(-03)	-1.1692(-03)
$6A$ ($2p_{3/2} \rightarrow \sigma^*_\text{SS}$)	158.08723		2.6587(-03)	2.6566(-03)	-4.9798(-04)	-4.9892(-04)	1.1726(-03)	1.1757(-03)
		ac	5.7818(-03)	5.7796(-03)	4.3272(-06)	4.3363(-06)	6.4960(-06)	6.5232(-06)
$10A$ ($2p_{1/2} \rightarrow \sigma^*_\text{SS}$)	159.29375		1.2239(-03)	1.2227(-03)	-2.5299(-04)	-2.5345(-04)	-5.7854(-04)	-5.7988(-04)
$10B$ ($2p_{1/2} \rightarrow \sigma^*_\text{SS}$)	159.29387		1.3957(-03)	1.3953(-03)	2.5605(-04)	2.5651(-04)	5.8340(-04)	5.8476(-04)
		ac	2.6196(-03)	2.6180(-03)	3.0568(-06)	3.0622(-06)	4.8616(-06)	4.8783(-06)
				L_1-edge				
$4B$ ($2s_{1/2} \rightarrow \sigma^*_\text{SS}$)	216.39399		3.6733(-02)	3.6872(-02)	-3.1538(-05)	-3.1716(-05)	-1.0027(-03)	-1.0085(-03)
$4A$ ($2s_{1/2} \rightarrow \sigma^*_\text{SS}$)	216.39599		2.9891(-04)	1.7881(-04)	3.1469(-05)	3.1646(-05)	1.0279(-03)	1.0338(-03)
		ac	3.7032(-02)	3.7051(-02)	-6.9310(-08)	-6.9637(-08)	2.5196(-05)	2.5212(-05)
				K-edge				
$4B$ ($1s_{1/2} \rightarrow \sigma^*_\text{SS}$)	2427.83334		7.7555(-03)	1.0438(-02)	-2.2670(-05)	-4.6773(-05)	-1.0771(-03)	-1.9842(-03)
$4A$ ($1s_{1/2} \rightarrow \sigma^*_\text{SS}$)	2427.83349		2.6746(-03)	2.4290(-05)	2.2665(-05)	4.6761(-05)	1.0754(-03)	1.9823(-03)
		ac	1.0430(-02)	1.0462(-02)	-5.6000(-09)	-1.1871(-08)	-1.6290(-06)	-1.8216(-06)

strengths in Table 4.8, non-dipolar effects at the K-edge lead to intensity redistribution among the underlying near-degenerate transitions (i.e., unrelated to the arbitrary mixing allowed for degenerate states). Nonetheless, the overall spectral profiles within and beyond the electric-dipole approximation are essentially identical because of the nearly overlapping transitions. This is consistent with our previous findings from Section 4.4. In contrast, the beyond-first-order effects become evident in the differential K-edge absorption profile because of the signed nature of the underlying quantities. This leads to a factor-of-two overestimation of the ECD within the conventional first-order treatment. Introducing third-order contributions largely corrects this discrepancy at the sulfur K-edge but going to higher orders in the expansion is not a general remedy, as will be discussed below.

To better understand the nature of the chiral response across spectral regions, I computed the underlying anisotropic differential oscillator strength distributions, considering now the smaller H_2S_2. Figure 4.18 shows the full ECD distributions (points), compared with the first-order truncated counterparts (surfaces). The solid angle represents the propagation direction, the distance from the origin (COM) indicates the magnitude of the associated signal and the color its sign. Note that different scaling factors have been applied across the transitions (see upper right corner of each subfigure). The C_2-rotation axis coincides with the z-axis, whereas the disulfide bond is along the x-axis. The shapes of the anisotropic distributions can be understood by decomposing the first-order signals into isotropic and d-orbital contributions (Eqn. (3.153)). The resulting orbital weights of the excitations plotted in Figure 4.18 are reported in Table 4.9.

From symmetry considerations detailed in Section D.4, it is found that contributions from d_{xz} and d_{yz} vanish for excitations of both A and B symmetry. In A symmetry, $R_{zz}^{[1]}$ is also zero by symmetry, such that the s- and d_{z^2}- contributions come in a fixed ratio, giving a toroid in the xy-plane. For valence and L_3-edge excitations of A symmetry this shape is modulated by the $d_{x^2-y^2}$-contribution, giving the shape of a biconcave disc elongated along the y- and x-axis, respectively, depending on its relative sign. For the L_1- and K-edge excitations the d_{xy}-contribution completely dominates. This is also the case for the corresponding excitations in B symmetry. It may be noted that in A symmetry the E1–M1 contribution to the d_{xy} term is zero by symmetry, whereas in B symmetry the E1–E2 and E1–M1 contributions are of similar magnitude and the same sign. Continuing to the L_3 excitation of B symmetry, the angular plot resembles that of its counterpart in A symmetry, albeit with opposite overall sign and rotated $\pi/2$ about the molecular axes. The latter can be understood from the relative weights of d_{z^2}- and $d_{x^2-y^2}$- contributions, as seen in Table 4.9. Finally, the angular plot of the valence excitation in B symmetry is a biconcave disc elongated along the z-axis, arising from positive interference between s- and d_{z^2}-contributions contrary to the negative interference observed for its counterpart of A symmetry.

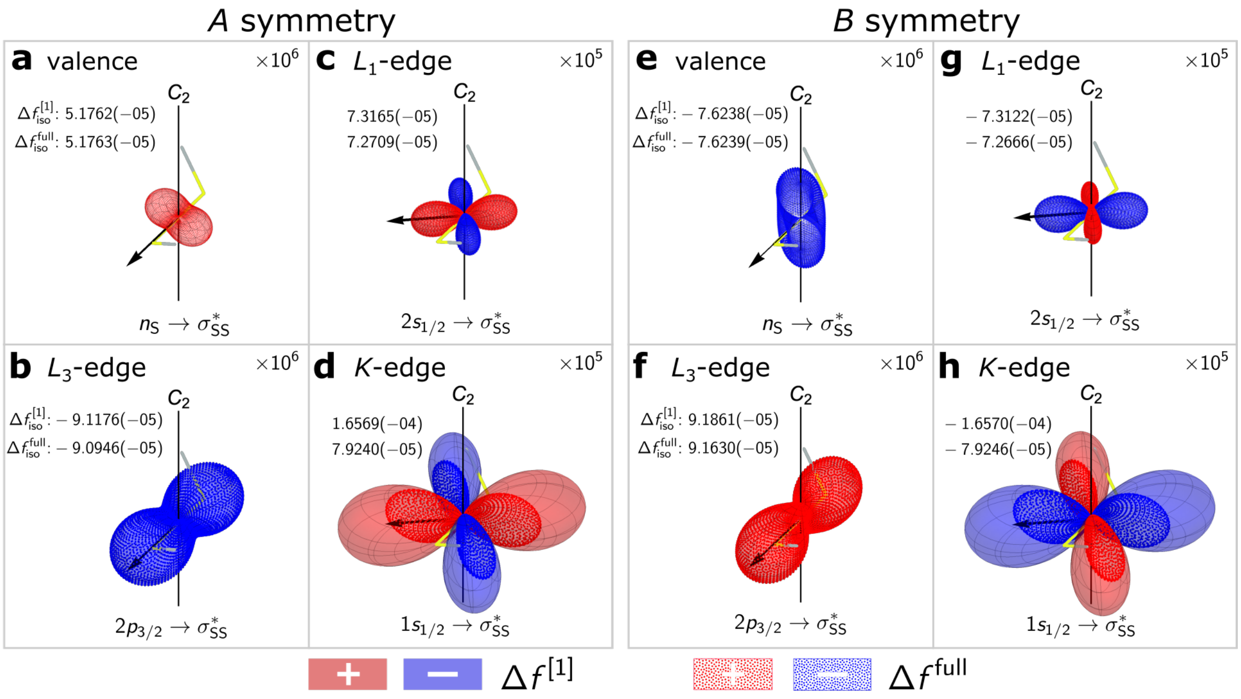

Figure 4.18: Comparison of full and truncated differential oscillator strength $\Delta f(\theta, \phi)$ across the spectral regions (valence, L_3-, L_1- and K-edges). Transitions of (a-d) A and (e-h) B symmetry in H_2S_2. The black arrow points along the direction of the wave vector for the anisotropic ECD intensity given in Table 4.8. The truncated ECD is represented by the smooth surface, whereas the full ECD is shown as individual points generated with a 5810-point Lebedev grid ($L_{max} = 131$). Blue: negative; red: positive ECD signal. Note that different scaling factors (upper right corner) have been applied. The corresponding isotropic differential oscillator strengths are indicated in each subfigure.

Table 4.9: Weights of contributions from solid harmonics (Eqn. (3.153)) to the differential cross section $\Delta f(\theta, \phi)$ of selected transitions in H_2S_2. The weights have been scaled by the absolute value of the s-contribution. Numbers in parentheses are exponents of 10.

Irrep	Excitation	$\Delta f_{\text{iso}}^{[1]}$	s	d_{z^2}	$d_{x^2-y^2}$	d_{xy}
A	Valence	5.176(-05)	1.000	-0.447	0.300	-0.056
	L_3-edge	-9.118(-05)	-1.000	0.447	0.414	-0.031
	L_2-edge	-2.824(-04)	-1.000	0.447	0.408	-0.024
	L_1-edge	7.316(-05)	1.000	-0.447	-0.862	8.817
	K-edge	1.657(-04)	1.000	-0.447	-0.772	9.108
B	Valence	-7.624(-05)	-1.000	-0.328	-0.090	0.314
	L_3-edge	9.186(-05)	1.000	-0.132	-0.592	-0.005
	L_2-edge	2.883(-04)	1.000	-0.128	-0.591	-0.008
	L_1-edge	-7.312(-05)	-1.000	2.503	-0.347	-8.262
	K-edge	-1.657(-04)	-1.000	0.377	0.813	-9.125

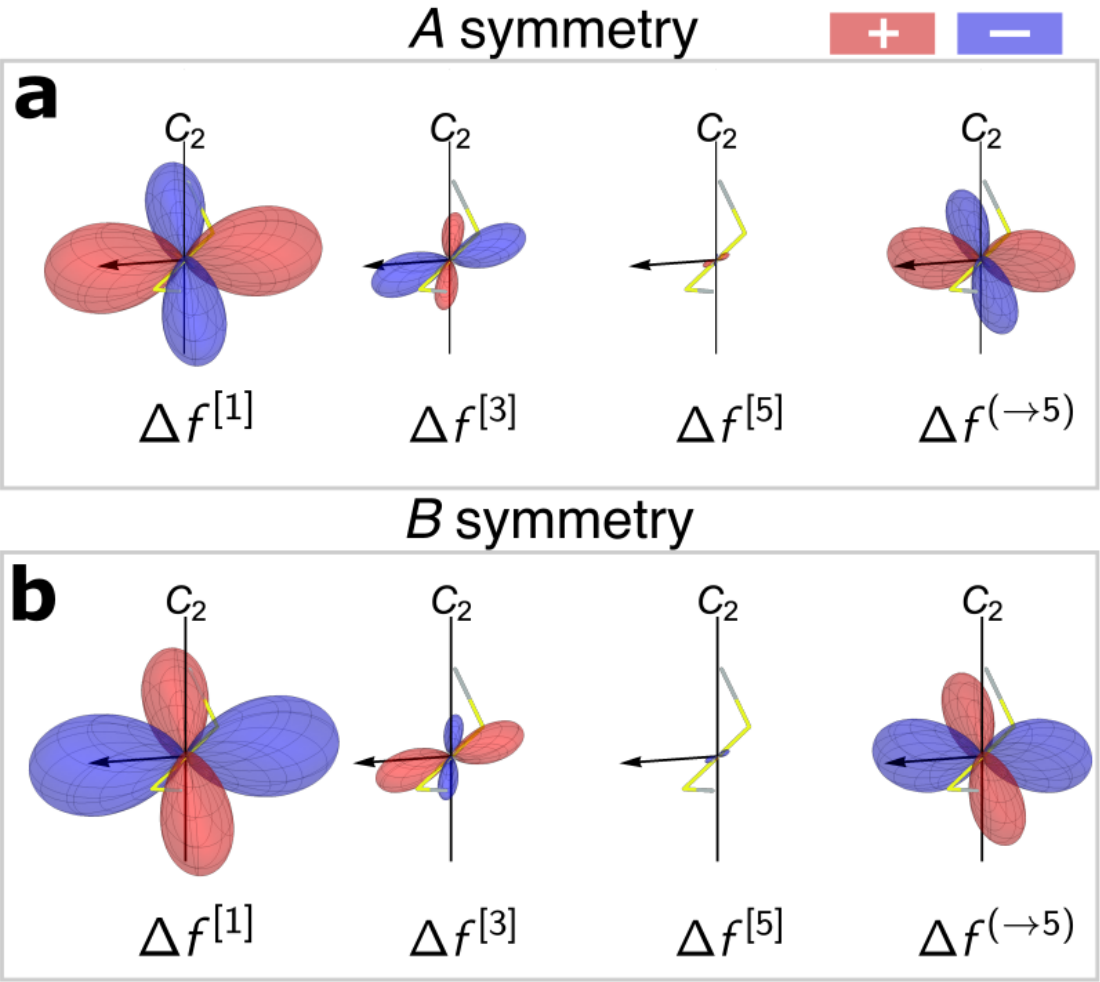

Figure 4.19: Convergence of the truncated anisotropic ECD distributions, i.e., $\Delta f^{[2n+1]}(\theta, \phi)$*, for the* K*-edge transitions in* H_2S_2*. The superscript notation* $\Delta f^{(\rightarrow m)}$ *indicates accumulated contributions up through* m*th order. The black arrows point along the direction of the wave vector for the anisotropic ECD intensity given in Table D.3.*

Next, I compare these conventional first-order truncated ECD distributions with their *full* counterparts. For the valence, L_3- and L_1-edge transitions, the anisotropic distributions virtually coincide, thereby confirming the validity of the first-order truncated description also for the anisotropic signal in these energy regimes. On the other hand, the full and truncated ECD distribution for the K-edge transitions are seen to have the same overall shape, but markedly different size, such that the factor-of-two overestimation at first order of the isotropic response (Table 4.8) arises largely from an overall scaling. Closer inspection of the angular distribution of the full ECD distribution reveals that the lobes are not strictly perpendicular as in a d_{xy}-orbital, hence indicating the contributions from solid harmonics of higher even angular momentum. To investigate this further, the order-by-order contributions are provided together with the full anisotropic ECD distribution in Figure 4.19. Although $\Delta f^{[3]}$ ($\ell = 0, 2, 4$) resembles $\Delta f^{[1]}$, the inclusion of higher-order solid harmonics in the former leads to non-orthogonal lobes. Furthermore, the two distributions differ by an overall sign, such that the inclusion of $\Delta f^{[3]}$ decreases the ECD signal. A possible issue is the rate of convergence of the truncated interaction towards the full one. The BED implementation of truncated interaction for linear absorption allows us to go to arbitrary order, a unique functionality of the DIRAC code. In Section 4.2, it was demonstrated that the truncated treatment converges to the full interaction upon inclusion of higher-order terms, but for higher-energy transitions (photon energies beyond ∼3728 eV) the convergence behavior was too slow for practical applications. In the present case, I assessed the convergence of the isotropic differential oscillator strength expansion at the sulfur K-edge and found that the relative error is below the threshold of 1% at 7th order (Table 4.10). Indeed, as shown in Figure 4.19 the $\Delta f^{[5]}$ distribution ($\ell = 0, 2, 4, 6$) is minute. A similar convergence rate is found for the isotropic linear oscillator strength. From these data, it follows that the rate of convergence is acceptable for the application to the sulfur K-edge, although this conclusion may differ when performing calculations at different energy scales.

To further explore the energy window at which the truncated formalism is functional, I have performed an additional series of the isotropic differential oscillator strength for the heavier H_2X_2 analogues (X=Se and Te). A comparison of the two pre-edge features in the L_1- and K-edge linear and differential absorption spectra with the full and lowest-order truncated interaction across the H_2X_2 (X=S, Se, Te) series is depicted in Figure 4.20. As a consequence of the deeper core levels of the heavier elements, the deficiency of the first-order treatment of the ECD signal now appears also at the L-edge. The discrepancy increases with the transition energy (i.e., Se L_1-edge $<$ S K-edge $<$ Te L_1-edge $<$ Se K-edge $<$ Te K-edge), with the Te K-edge having a vast discrepancy between the full and first-order differential oscillator strength. Similar to the findings of Section 4.2, the convergence of the multipole expansion is met with difficulties for the heavier analogues. Indeed, when considering these structural analogues, only the selenide L-edge converges at a sufficient rate, whereas it is too slow to practically converge for all other edges. In both cases, the first-order treatment not only overestimates the rotatory strengths of individual transitions but most critically it incorrectly predicts the signs of (the intense) pairs of near-degenerate transitions. However, since the relative magnitude of these oppositely signed contributions is preserved, the first-order spectral profile yields the correct overall sign (given sufficiently large Gaussian broadening). By comparing the series of H_2S_2 and its analogues, a trend can be observed between the rate of convergence and excitation energy. Therefore, the breakdown of the first-order description at the sulfur K-edge, and not at the sulfur L-edges, is a consequence of its order-of-magnitude higher transition energy (∼215 and 2427 eV at the L_1 and K-edges).

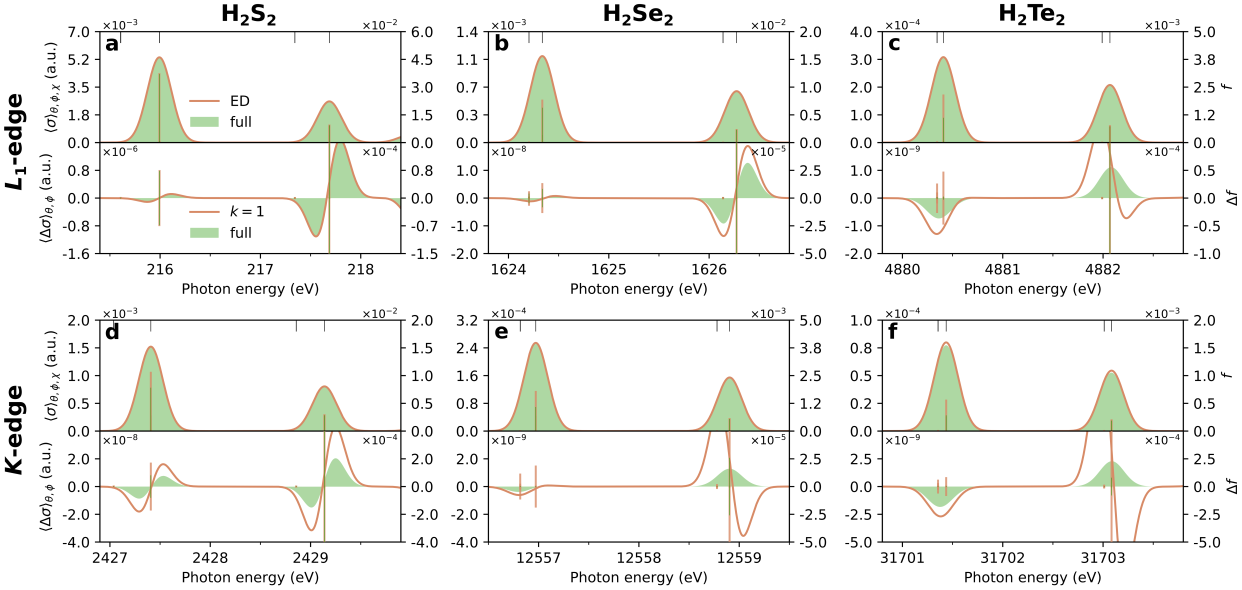

Figure 4.20: Isotropic linear (top) and differential (bottom) absorption spectra of H_2X_2, X=S, Se and Te: (a-c) L_1-edge and (d-f) K-edge spectra using the full interaction operator (green shadings) or the lowest non-vanishing generalized velocity representation (orange lines). Left axes correspond to (differential) absorption cross-sections, whereas (differential) oscillator strengths are shown on the right axes. Black sticks indicate the location of all computed transitions. The stick spectra were convolved with a Gaussian lineshape with FWHM of 0.4 eV. No shifts have been applied to the theoretical spectra.

4.5.3 Conclusion

In this section, I have reported the application of the anisotropic and isotropic ECD signal using the *full*- and truncated semi-classical light–matter interaction operator within a four-component relativistic framework. This simultaneous account of beyond-first-order light–matter interactions and relativistic effects provides two additional sources of ECD which become increasingly important at high photon energies. The linear form of the light–matter interaction operator in the relativistic domain further enabled straightforward extension to a multipole-based scheme in the velocity representation that allows for the traditional (albeit, in general, ambiguous) decomposition into electric and magnetic contributions while retaining order-by-order gauge-origin independence.

The presented approach was used to investigate the ECD response of two prototypical disulfides, H_2S_2 and $(CH_3S)_2$, across the electromagnetic spectrum, from valence to core transitions. To quantify the implications of higher-order effects, I compared the results of the full interaction to those obtained within the traditional lowest-order non-vanishing (i.e., first-order) truncated generalized velocity representation. Going beyond the electric-dipole approximation at the sulfur K-edge leads to non-negligible intensity redistribution among near-degenerate transitions but with no visible implications on the linear absorption profile. On the other hand, the differential absorption profile is not affected by such redistribution, because of its signed nature. This leads to an overall factor-of-two overestimation. By examining the shapes of the underlying anisotropic ECD distributions, this discrepancy is found to largely originate from an overall scaling that is corrected upon introducing third-order contributions.

Critically, the first-order treatment deteriorates at higher transition energies (beyond ω=c~3728 eV), as can be inferred from the additional calculations involving the heavier analogues of H_2S_2. In these cases, this treatment may even fail to predict the sign of individual differential oscillator strengths, although this is partially alleviated if the peaks are broad enough. At such energies, going to higher orders is not a practical remedy because of the slow convergence of the truncated interaction — the full interaction is a must.

Table 4.10: Contributions to the isotropic linear and differential oscillator strength ($\Delta f_{iso}^{[2n+1]}$ *and* $f_{iso}^{[2n]}$*) at various orders for* H_2S_2*,* $n = 0, 1, 2, 3$*, compared to the result of the full interaction for the two* $1s_{1/2} \rightarrow \sigma^*_{SS}$ *transitions of A/B symmetry. The superscript notation* $\square^{(\rightarrow m)}$ *indicates accumulated contributions up through mth order. In particular, the 'ac'-labeled row indicates the (differential) oscillator strengths accumulated through 8th (9th) order. The errors upon truncation are defined as* $\%\delta\Delta f_{iso}^{(\rightarrow 2n+1)} = |(\Delta f_{iso}^{(\rightarrow 2n+1)} - \Delta f_{iso}^{full})/\Delta f_{iso}^{full}|\times 100\%$*. The results were obtained using 4c-TD-PBE0 level of theory and the uncontracted aug-pcx-3/aug-pc3 basis set. Numbers in parentheses are exponents of 10.*

	$4A\ (1s_{1/2} \rightarrow \sigma^*_{\mathrm{SS}})$;	$\omega_A = 2427.88349eV$		
n	$f_{\mathrm{iso}}^{[2n]}$	$\Delta f_{\mathrm{iso}}^{[2n+1]}$	$\%\delta f_{\mathrm{iso}}^{(\rightarrow 2n)}$	$\%\delta\Delta f_{\mathrm{iso}}^{(\rightarrow 2n+1)}$
0	5.5576(-05)	1.6569(-04)	97.99	109.10
1	3.4276(-03)	-1.0818(-04)	26.07	27.42
2	-8.1305(-04)	2.4151(-05)	3.36	3.06
3	9.9900(-05)	-2.2416(-06)	2.57(-1)	2.32(-1)
4	-7.5661(-06)	1.2938(-07)	1.69(-2)	3.96(-1)
ac	2.7625(-03)	7.9240(-05)	-	-
full	2.7630(-03)	7.9240(-05)	-	-
n	$4B\ (1s_{1/2} \rightarrow \sigma^*_{\mathrm{SS}})$;	$\omega_B = 2427.83334eV$		
0	1.0512(-02)	-1.6570(-04)	35.24	109.10
1	-3.4601(-03)	1.0818(-04)	9.27	27.42
2	8.1318(-04)	-2.4153(-05)	1.19	3.06
3	-9.9897(-05)	2.2413(-06)	9.60(-2)	2.24(-1)
4	7.5513(-06)	-1.2878(-07)	1.43(-3)	3.98(-1)
ac	7.7729(-03)	-7.9433(-05)	-	-
full	7.7728(-03)	-7.9246(-05)	-	-

Conclusion

The main goal of this thesis is to assess the validity of the dipole approximation in the simulation of X-ray absorption spectroscopy. Here, the term dipole approximation should be understood as an umbrella term that denotes the first-order truncated multipole expansion corresponding to the absorption of linearly polarized light (electric-dipole approximation) and electronic circular dichroism (rotational strength). To answer this question, I have presented an applied and implementation at the four component relativistic level based on either the full- or truncated light–matter interaction. In addition, it can describe the truncated interaction in two representations, the generalized length- and velocity representation, which become equivalent in the complete basis set limit. In summary, the following conclusions were obtained in previous chapter:

1. At high excitation energies (~ 3728 eV), the truncated interaction converges extremely slowly towards the full interaction, which renders this scheme impractical for simulations in the hard X-ray regime.
2. The truncated interaction is more difficult to converge with respect to the basis set choice than the full interaction. The basis set convergence of the generalized velocity representation is further complicated by problems associated with linear dependence of the small component function.
3. The compactness of the core orbital counteracts the magnitude of non-dipolar effects for transitions arising from a single center, even in the hard X-ray regime. In case of the radium atom, the full interaction provides a correction of approximately ($\sim 13 - 20\%$) compared to the electric-dipole approximation.
4. In general, it seems that non-dipolar effects redistribute the intensities in a near-degenerate manifold of transitions, the effects of which are typically not observable in an absorption spectrum of linearly polarized light due to spectral broadening.
5. In the presence of symmetry equivalent centers, the transitions stemming from these centers have significant non-dipolar corrections, although the validity of this effect can be questioned due to the shortcomings of SCF theory. Furthermore, for the absorption of linearly polarized light, the changes in signal are difficult to observe if spectral broadening is included as a result of the effect outlined in previous point.
6. In case of electronic circular dichroism, non-dipolar effects where already significant for H_2S_2, whereas for the heavier analogues these effects were even more pronounced. Furthermore, the changes in spectral features caused by non-dipolar effects are better preserved after spectral broadening due to the signed nature of circular dichroism.

Taking these points into consideration, we arrive at the general conclusion that at least for the absorption of linearly polarized light, the electric-dipole approximation is an excellent approximation for most systems. Even in the hard X-ray regime, the electric-dipole approximation can capture the overall characteristics of the spectrum. However, to describe the dipole-allowed transitions at high-accuracy and to even include dipole-forbidden transitions, it is mandatory to go beyond the electric-dipole approximation. If this level of accuracy is required, the full interaction operator provides more reliable results than schemes based on a truncated interaction, due to the difficult convergence of the latter with respect to basis set choice and the multipole expansion. Therefore, the full interaction should be the standard in calculations that demand high accuracy.

Another exception where the electric-dipole approximation might be insufficient is given by systems with symmetry equivalent centers, although spectral broadening makes it difficult to observe these effects. Hypothetically, the individual transitions can be resolved if spectral broadening is sufficiently small. However, to the best of my knowledge, the resolution that can be achieved with modern X-ray spectrometers is not enough. Perhaps future X-ray spectrometers will be accurate enough to measure these effects. It may be also worthwhile to simulate the absorption spectra of heavier analogues of $TiCl_4$, e.g. $TiBr_4$ or TiI_4, whose non-dipolar corrections may be so extreme that they can even be observed with significant spectral broadening. In addition, the spin orbit splitting of the Br and I L-edge, may induce interesting effects. However, to rigorously establish the validity of these effects, current implementation needs to be extended to the MCSCF or CC level of theory.

Non-dipolar effects seem to be most relevant for electronic circular dichroism, appearing already for H_2S_2 and being less susceptible to the spectral broadening. For the heavier analogues of H_2S_2, a first-order treatment makes little sense due to the strong non-dipolar effects that are induced by the high excitation energies of the core electrons. Interestingly, non-dipolar effects seem to go hand-in-hand with the effects of relativity, as the heavy atoms in these species demand a fully relativistic treatment. Therefore, the implementation presented in this thesis is ideal to describe these effects. However, to exclude the possibility that these conclusions are system dependent, the ECD of other systems should be studied as well. A particularity of the H_2X_2 series is the near degeneracy of the bonding and anti-bonding core orbitals, giving rise to bidentate signals that are so close that they mostly cancel. Future systems of interest may be chiral metal acetylacetonate complexes, or for that matter any chiral single-centered metal complex.

Chapter 5

Outlook

5.1 MCSCF

In Section 4.4, it is discussed how core transitions stemming from symmetry equivalent centers give rise to elevated non-dipolar effects because the core orbitals are delocalized over these centers. However, improved ionization energies can be obtained by localizing the core orbital, which in principle should decrease non-dipolar effects albeit at the expense of the symmetry of the wave function. At the end of this section, it is also mentioned that this problem is most rigorously solved using wave function methods. Therefore, as a part of this thesis, it was originally envisioned to extend the implementation in DIRAC to the MCSCF level. However, this project has not been finished. In the current Dirac code, energy optimizations at the Kramers-restricted MCSCF level are possible, although only with the inclusion of symmetry. Being based on the quaternion scheme (see Section B.3), this implementation involves more complicated equations without symmetry, explaining why to this day this functionality is not in place. To calculate absorption intensities, two key features need to be implemented: the optimization of excited states and the calculation of transition moments from these states. The former feature can be realized by implementing the NEO algorithm, as described in ref. 290. The implementation of this algorithm heavily benefits from the existing infrastructure for energy optimization. Transition moments at this level of theory are complicated by the fact that the MCSCF wave function contains contributions from multiple determinants. It can be shown that in the corresponding transition moments, the only non-vanishing contributions involve combinations of determinants that differ at most by one orbital. Transition moments at the SCF level do not require these considerations as these methods are based on single determinants.

5.2 Core-Hole Relaxation at the DFT Level

In the introduction of this thesis, it was argued that the description of the core-hole is important for X-ray spectroscopy. Typically, the relaxation effects arising from this hole, may significantly shift the energies in a spectrum. These effects can be taken into account using the static exchange approximation (STEX)[291, 292]. STEX can be thought of as CI singles using a core-hole reference state. In the current state of DIRAC, it is possible to perform calculation of this type using a reference state described at the HF level of theory.[293] However, within this reference, dynamic correlation is not taken into consideration. Furthermore, due to the choice of reference state, the excited state obtained with STEX is not necessarily orthogonal to the HF ground state, making the formalism somewhat more cumbersome.

Therefore, another side project in this thesis was to implement STEX at the DFT level of theory. To avoid the complications associated to non-orthogonality, a scheme was going to be implemented that uses the core-orbitals from the core-hole reference state. The main assumption of this scheme being that the core orbitals are not easily polarizable and thus relatively unchanged in the neutral and core-hole states. The implementation of this scheme heavily leans on the existing Tamm-Dancoff approximation code. However, this project never really took off due to an unresolved bug in this code.

5.3 X-ray Magnetic Circular Dichroism

Knowing that non-dipolar effects play an important role in electronic circular dichoism, it seems straightforward to extend the BED implementation to describe magnetic circular dichroism. This feature has already been implemented by Foglia *et al.*,[34] although in a non-relativistic framework. To generalize it to a relativistic framework, there are two possible routes: either quadratic response is applied, where the static magnetic field is an additional perturbation, or the magnetic field is included during the SCF cycles. Presumably, the isotropic averaging within the latter scheme cannot be carried out in a very elegant manner. The most straightforward method to perform this averaging is to put all possible directions of the magnetic field on a Lebedev grid. However, this requires a separate SCF calculation for every grid point, making the calculation rather expensive. Another challenge associated with this approach is that the magnetic field breaks time-reversal symmetry, implying that the formalism is more involved. Alternatively, this quantity is calculated using quadratic response, which in principle, is possible in DIRAC. The remaining task would then be to identify which response function exactly has to be calculated, making this method the preferred one.

5.4 Full Interaction Operator in the Length Representation

Although the full interaction operator has many advantages, it does not explicitly distinguish between electric- and magnetic interactions. In multipolar gauge, this separation is inherent to the formulation, although it is formulated as a truncated expansion, which is accompanied by a plethora of problems (see Section 3.5). It is possible, however, to get the best of both worlds by utilizing the integral representation of multipolar gauge, where the gauge function is given by[158, 159]

$$\chi_a(\boldsymbol{r},t) = \int_0^1 d\lambda \boldsymbol{\delta}_a \cdot \tilde{\boldsymbol{A}}(\lambda \boldsymbol{\delta}_a + a, t) \tag{5.1}$$

and corresponding potentials

$$\phi_a(\boldsymbol{r}, t) = \tilde{\phi}(\boldsymbol{a}, t) - \boldsymbol{\delta}_a \cdot \int_0^1 d\lambda \boldsymbol{E}(\lambda \boldsymbol{\delta}_a + a, t) \tag{5.2}$$

$$\boldsymbol{A}_a(\boldsymbol{r}, t) = -\int_0^1 d\lambda \lambda \big(\boldsymbol{\delta}_a \times \boldsymbol{B}(\lambda \boldsymbol{\delta}_a + a, t)\big). \tag{5.3}$$

The integral representations of these potentials are completely equivalent to Eqs. (3.71) and (3.77), which can be confirmed by expanding the position argument of above integrands around $\boldsymbol{a}$. An advantageous feature of the integral representation is that it does not involve any truncation, thus being gauge-origin independent, as demonstrated in Section 3.5. The implementation of the absorption intensities derived from these potentials presumably shares some similarities with the implementation of the full interaction, although the integrals are different.

Appendix A

Complements to Chapter 1

A.1 Solving the Generalized Eigenvalue Problem

In this appendix, a possible technique will be discussed to solve the generalized eigenvalue problem from Eqn. (1.114). The derivations provided in this section will mainly follow ref. 294. As discussed in Section 1.3.3, the dimensionality of the problem forms a major obstacle to solve this problem using a numerical scheme. To avoid this issue, the solution vectors will be expressed in a set of trial vectors

$$\tilde{\boldsymbol{X}}_n = \sum_i^N c_i \boldsymbol{B}^i; \quad \boldsymbol{B}^i = \begin{pmatrix} \boldsymbol{b}^i \\ h\boldsymbol{b}^{i*} \end{pmatrix}, \tag{A.1}$$

where h determines the hermiticity of the trial vectors. Accordingly, the electronic Hessian and generalized metric can be projected onto this basis

$$\tilde{E}^{[2]}_{0;ij} = \boldsymbol{B}^{i\dagger} E^{[2]}_0 \boldsymbol{B}^j; \quad \tilde{S}^{[2]}_{ij} = \boldsymbol{B}^{i\dagger} S^{[2]} \boldsymbol{B}^j, \tag{A.2}$$

thus yielding the following reduced problem

$$\tilde{E}^{[2]}_0 \tilde{\boldsymbol{X}}_n = \hbar\tilde{\omega}_{n0} \tilde{S}^{[2]} \tilde{\boldsymbol{X}}_n, \tag{A.3}$$

which can be solved readily using conventional diagonalization packages.

For the full problem, the residual equals zero

$$\tilde{\boldsymbol{R}} = \left(\tilde{E}^{[2]}_0 - \hbar\tilde{\omega}_{n0} \tilde{S}^{[2]} \right) \tilde{\boldsymbol{X}}_n, \tag{A.4}$$

thus forming a suitable diagnostic to assess whether the reduced problem is sufficiently large to yield accurate results. If this is not the case, the residual vector can be used to extend the space of trial vectors. Starting from an initial set of trial vectors, this procedure is repeated iteratively until the residuals fall below a user-defined threshold.

As a main advantage, this procedure avoids explicit storage of the full electronic Hessian. To construct the reduced electronic Hessian from Eqn. (A.3), it suffices to compute the vector quantity $\boldsymbol{\Sigma}^j = E^{[2]} \boldsymbol{B}^j$, which are to be contracted with the trial vectors. Furthermore, since the upper and lower half of $\mathbf{\Sigma}^j$ are related by complex conjugation, I will only compute the upper half in the following

$$\sigma_{ai} = A_{ai,bj}b_{bj} + B_{ai,bj}b_{jb} = \langle 0|\Big[-a_i^\dagger a_a, \big[a_b^\dagger a_j b_{bj}, \hat{H}_0\big]\Big]|0\rangle + \langle 0|\Big[a_i^\dagger a_a, \big[a_j^\dagger a_b b_{jb}, \hat{H}_0\big]\Big]|0\rangle. \tag{A.5}$$

Following a similar procedure as in Section 3.6.2, it can be shown that the inner commutators evaluate to

$$\sigma_{ai} = \langle 0|\Big[-a_i^\dagger a_a, \hat{\tilde{H}}_0\Big]|0\rangle, \tag{A.6}$$

where appears the one-index transformed Hamiltonian

$$\hat{\tilde{H}}_0 = \tilde{h}_{pq}a_p^\dagger a_q + \frac{1}{2}\widetilde{(pq|rs)}a_p^\dagger a_r^\dagger a_s a_q, \tag{A.7}$$

in terms of the one-index transformed integrals

$$\tilde{h}_{pq} = W_{pt}h_{tq} - h_{pt}W_{tq} \tag{A.8}$$

$$\widetilde{(pq|rs)} = W_{pt}(tq|rs) - (pt|rs)W_{tq} + W_{rt}(pq|ts) - (pq|rt)W_{ts}. \tag{A.9}$$

Here, the matrix W is defined in terms of the solution vectors $W_{ai} = b_{ai}$; $W_{ia} = -b_{ia}$; $W_{ij} = W_{ab} = 0$. Alternatively, these vectors can be expressed in terms of the Fock matrix

$$\sigma_{ai} = F_{ab}W_{bi} - W_{aj}F_{ji} + \mathcal{L}_{ai,jb}W_{bj} - W_{jb}\mathcal{L}_{ai,bj}, \tag{A.10}$$

and the anti-symmetrized two-electron integrals (see Eqn. (3.109)).

Solving the reduced problem iteratively thus hinges on the calculation of the sigma vectors, which in turn are obtained from the one-index transformed quantities. Applying this scheme allows us to calculate the lowest few eigenvalues of a matrix which otherwise would be too large to explicitly store. However, being a bottom-up approach, this method is cumbersome to calculate core transitions, requiring us to calculate all lower excitations first. A slight modification to this method that allows the calculation of core excitations is provided in Section C.4.

Appendix B

Complements to Chapter 2

B.1 The Dirac Equation and Spin

In this appendix, I will demonstrate that the Dirac wave function can be expressed as two Pauli spinors (Eqn. (2.84)). To start of, I will express the Dirac equation in this basis

$$\begin{pmatrix} V & c\boldsymbol{\sigma}\cdot\hat{\boldsymbol{\pi}} \\ c\boldsymbol{\sigma}\cdot\hat{\boldsymbol{\pi}} & V-2m_ec^2 \end{pmatrix}\begin{pmatrix} \psi^L(\boldsymbol{r}) \\ \psi^S(\boldsymbol{r}) \end{pmatrix} = E\begin{pmatrix} \psi^L(\boldsymbol{r}) \\ \psi^S(\boldsymbol{r}) \end{pmatrix}, \tag{B.1}$$

where the potential is given by $V = -e\phi$. The Dirac equation is thus constructed from two coupled differential equations, where the second equation has the following solution for the small component

$$\psi^S(\boldsymbol{r}) = \left[2m_ec^2 + E - V\right]^{-1} c(\boldsymbol{\sigma}\cdot\hat{\boldsymbol{p}})\psi^L(\boldsymbol{r}). \tag{B.2}$$

Note that for positive-energy solutions the small component is a factor of $\frac{1}{c}$ smaller than the large component, hence its name. In the non-relativistic limit, it is clear that the small component vanishes, suggesting that we should focus on the large component. Using Eqn. (B.2), we can obtain a single equation for the large component

$$c^2(\boldsymbol{\sigma}\cdot\hat{\boldsymbol{\pi}})\left[2m_ec^2 + E - V\right]^{-1}(\boldsymbol{\sigma}\cdot\hat{\boldsymbol{\pi}})\psi^L(\boldsymbol{r}) + V\psi^L(\boldsymbol{r}) = E\psi^L(\boldsymbol{r}). \tag{B.3}$$

Further applying the identity

$$(A+B)^{-1} = A^{-1} - A^{-1}B(A+B)^{-1}, \tag{B.4}$$

yields the equation

$$\frac{1}{2m_e}(\boldsymbol{\sigma}\cdot\hat{\boldsymbol{\pi}})(\boldsymbol{\sigma}\cdot\hat{\boldsymbol{\pi}})\psi^L(\boldsymbol{r}) + \frac{1}{2m_e}(\boldsymbol{\sigma}\cdot\hat{\boldsymbol{\pi}})\frac{E-V}{2m_ec^2+E-V}(\boldsymbol{\sigma}\cdot\hat{\boldsymbol{\pi}})\psi^L(\boldsymbol{r}) + V\psi^L(\boldsymbol{r}) = E\psi^L(\boldsymbol{r}), \tag{B.5}$$

which gives the Pauli Hamiltonian upon taking the non-relativistic limit. Therefore, it seems only reasonable to identify the first and last two components with a spin degree of freedom. However, it should be stressed that in the Dirac equation, spin appears naturally, contrary to the *ad hoc* treatment of spin in the Pauli equation. In addition, the Dirac equation incorporates non-perturbative spin-orbit coupling in its formalism.

Spin-orbit coupling arises from the relative motion of electrons and nuclei. In the molecular frame, the electrons encircle the (stationary) nuclei, whereas the opposite is true in the rest frame of the electrons. From the viewpoint of the electrons, the moving nuclei induce a magnetic field that interacts with the spin magnetic moment, hence locally steering the direction of electron spin. In Fig. B.1, this effect is represented schematically. Due to this effect, spin- and spatial degrees of freedom become non-separable, which renders the spin density, i.e. the density that integrates up to the spin, position dependent.

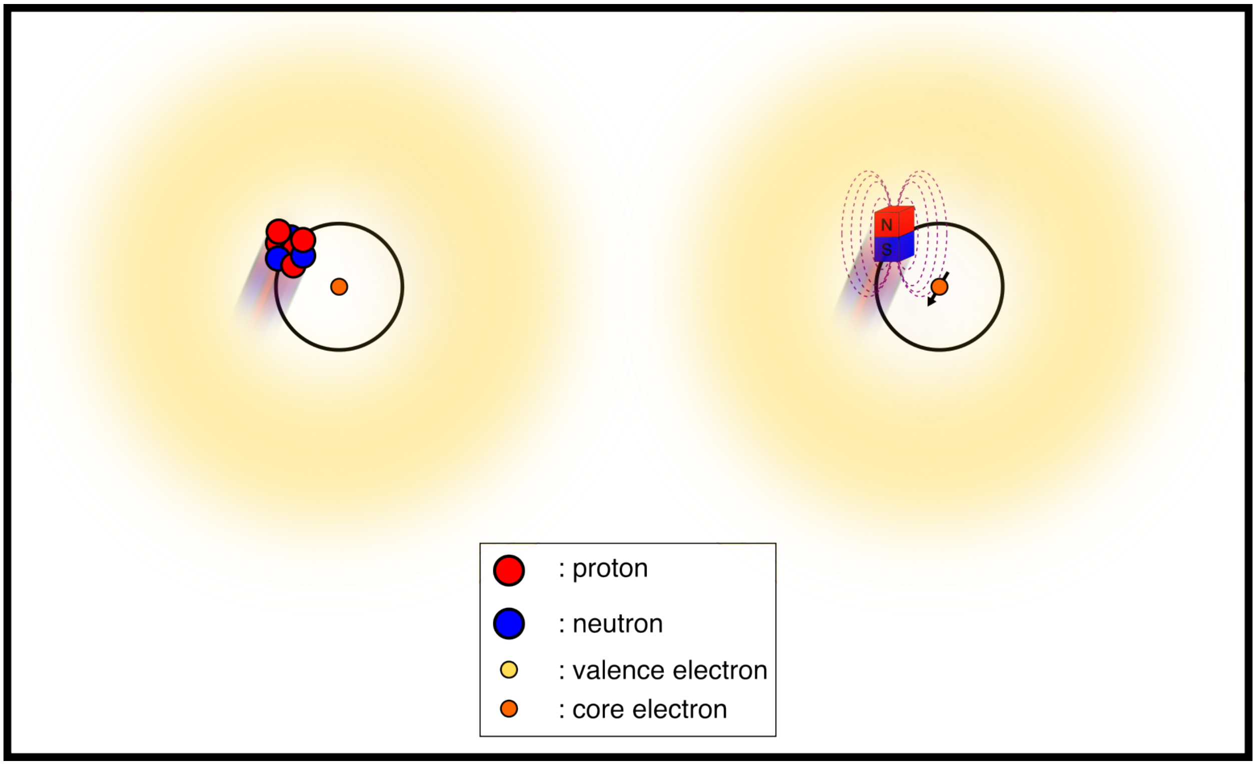

Figure B.1: ***Right:*** *from the perspective of the (core) electron, the nucleus is not stationary, but rather moving (see Fig. 2.1 for a nuclear centric model).* ***Left:*** *this relative motion generates magnetic induction, which couples with the spin magnetic moment of the electron, resulting in an effect more commonly referred to as spin-orbit coupling.*

As pointed out in the work of Thomas, the classical analogue of this effect is magnetic induction.[295] In his work, Thomas considered a charged ball that rotates around its own axis, while simultaneously orbiting around a central potential. Furthermore, he defined a rest frame of the ball by consecutive Lorentz transformations that follow the instantaneous motion of the ball. From the transformations in Eqs. (2.28), it follows that that the magnetic induction is given by

$$\boldsymbol{B} \approx \frac{1}{2}\frac{\boldsymbol{E} \times \boldsymbol{v}}{c^2}, \tag{B.6}$$

where $\boldsymbol{v}$ is the instantaneous velocity of the charged ball. In this expression, it is assumed that the electron moves slow, such that the Lorentz factor is unity. The factor of one half results from the successive Lorentz transformations, also referred to as Thomas precession. The electric field appearing in this expression can be rewritten in terms of the central potential

$$\boldsymbol{E} = -\boldsymbol{\nabla}\phi(r) = -\frac{\boldsymbol{r}}{r}\frac{d\phi(r)}{dr}, \tag{B.7}$$

which gives rise to the following expression for the magnetic field

$$\boldsymbol{B} = -\frac{1}{2m_e c^2}\frac{d\phi(r)}{dr}\boldsymbol{\ell}; \quad \boldsymbol{\ell} = \boldsymbol{r} \times \boldsymbol{p}. \tag{B.8}$$

The interaction between the magnetic field and the magnetic moment of the electron spin, $\hat{\mu}_s = g_e \frac{e}{2m_e}\hat{\boldsymbol{s}}$, are described by the operator

$$\hat{H}_{SO} = -\hat{\boldsymbol{\mu}}_s \cdot \boldsymbol{B} = \xi(r)\hat{\boldsymbol{\ell}} \cdot \hat{\boldsymbol{s}}; \quad \xi(r) = \frac{g_e e}{4m_e^2 c^2}\frac{d\phi(r)}{dr}, \tag{B.9}$$

where $g_e \approx 2$ is the electron g-factor. Typically, these effects can be captured by introducing above operator as a perturbation.

As alluded to before, the Dirac equation already has these effects build in its formulation. To understand this better, consider the time-dependent Dirac equation under the influence of the Coulomb potential from the nuclei. Transforming this equation from the molecular frame to a moving frame yields the following result

$$\big(i\hbar\gamma^\mu\partial_\mu - m_e c + \frac{e}{c}\gamma^0\phi_{nucl}\big)\psi = 0 \xrightarrow{\Lambda} \big(i\hbar\gamma'^\mu\partial'_\mu - m_e c + e\gamma'^\mu A'_\mu\big)\psi' = 0, \tag{B.10}$$

where ψ' is the four-component wave function in the transformed frame. Although this transformation is far from the consecutive transformations as described by Thomas, the above example is sufficient to illustrate that a moving frame introduces magnetic interactions that are absent in the molecular frame. Furthermore, due to its relativistic character, the Dirac equation is equally valid in any inertial frame. Therefore, in the molecular frame, spin-orbit coupling is taken into consideration without introducing any additional perturbing operator.

B.2 Negative Energy Solutions

In this appendix, I will demonstrate that the action of the charge conjugation operator on the four component wave function yields the result provided by Eqn. (2.86). To start off, I will take the complex conjugate of the minimally-coupled time-dependent Dirac equation[89, Section 1.6][90, Chapter 5][110, Section 2.8.1]

$$\big(c\boldsymbol{\alpha}^* \cdot \hat{\boldsymbol{p}}^* + m_e c^2\beta - e\phi + ec\boldsymbol{\alpha}^* \cdot \boldsymbol{A}\big)\psi^*(\boldsymbol{r}, t) = -i\hbar\partial_t\psi^*(\boldsymbol{r}, t). \tag{B.11}$$

Taking the complex conjugate of the Dirac matrices only changes its y-component

$$\alpha_y^* = -\alpha_y, \tag{B.12}$$

whereas all components of the momentum operator change sign due to its imaginary prefactor

$$\hat{\boldsymbol{p}}^* = -\hat{\boldsymbol{p}}. \tag{B.13}$$

Inserting the second relation into Eqn. (B.11), yields the result

$$\big(-c\boldsymbol{\alpha}^* \cdot \hat{\boldsymbol{p}} + m_e c^2\beta - e\phi + ec\boldsymbol{\alpha}^* \cdot \boldsymbol{A}\big)\psi^*(\boldsymbol{r},t) = -i\hbar\partial_t\psi^*(\boldsymbol{r},t). \tag{B.14}$$

The Dirac equation with opposite external charges can be retrieved from this expression by introducing the operator

$$\hat{U}_c = i\beta\alpha_y, \tag{B.15}$$

which has the following commutation relation with the Dirac matrices

$$\hat{U}_c\beta = -\beta\hat{U}_c \quad \hat{U}_c\boldsymbol{\alpha}^* = \boldsymbol{\alpha}\hat{U}_c. \tag{B.16}$$

Application of these relations yields the desired result

$$\big(c\boldsymbol{\alpha} \cdot \hat{\boldsymbol{p}} + m_e c^2\beta + e\phi - ec\boldsymbol{\alpha} \cdot \boldsymbol{A}\big)\hat{U}_c\psi^*(\boldsymbol{r},t) = i\hbar\partial_t\hat{U}_c\psi^*(\boldsymbol{r},t). \tag{B.17}$$

B.3 Quaternion Scheme

The purpose of this appendix is to lay out the fundamental concepts of the quaternion scheme. This derivation closely follows refs. 145, 146, so the reader is referred to these sources for more detail.

In the following, it will be assumed that we have a time-reversal symmetric system, such that the eigenfunctions come in Kramers partners and the matrix representation of time-reversal symmetric operators assume the form in Eqn.(2.132). In most quantum-chemical applications, it is relevant to compute the eigenvectors and - values of such matrices

$$\begin{pmatrix} A & B \\ -B^* & A^* \end{pmatrix}\begin{pmatrix} \boldsymbol{c}^\alpha \\ \boldsymbol{c}^\beta \end{pmatrix} = \epsilon\begin{pmatrix} \boldsymbol{c}^\alpha \\ \boldsymbol{c}^\beta \end{pmatrix}. \tag{B.18}$$

As expected from Kramers theorem, the eigenvectors come in degenerate pairs

$$\begin{pmatrix} A & B \\ -B^* & A^* \end{pmatrix}\begin{pmatrix} -\boldsymbol{c}^{\beta*} \\ \boldsymbol{c}^{\alpha*} \end{pmatrix} = \epsilon\begin{pmatrix} -\boldsymbol{c}^{\beta*} \\ \boldsymbol{c}^{\alpha*} \end{pmatrix} \tag{B.19}$$

that are related by time-reversal. Typically, degeneracies that are related to a symmetry suggest a block-diagonalization of the matrix representations. In our example, this is certainly possible, albeit at the expense of complicating the algebra in these matrices from complex to quaternion.

Before proceeding to demonstrate this transformation explicitly, I will first briefly discuss quaternions. Quaternions can be thought of as generalizations of complex numbers

$$q = a + b\check{i} + c\check{j} + d\check{k}; \quad a, b, c, d \in \mathbb{R} \tag{B.20}$$

constructed from three different types of imaginary units, $\check{i}^2 = \check{j}^2 = \check{k}^2 = \check{i}\check{j}\check{k} = -1$. However, the increase in dimensionality compared to complex algebra comes at the cost of losing commutativity

$$\check{i}\check{j} = -\check{j}\check{i}; \quad \check{i}\check{k} = -\check{k}\check{i}; \quad \check{j}\check{k} = -\check{k}\check{j}. \tag{B.21}$$

Alternatively, quaternions can also be expressed as two complex numbers

$$q = a + b\breve{j}; \quad a, b \in \mathbb{C}, \tag{B.22}$$

where the following relation holds due to the non-commutativity $b\breve{j} = \breve{j}b^*$.

Returning to our eigenvalue problem, the following unitary quaternion matrix ought to be applied

$$U = \frac{1}{\sqrt{2}} \begin{pmatrix} I & \breve{j}I \\ \breve{j}I & I \end{pmatrix}, \tag{B.23}$$

to block-diagonalize our matrix

$$U^\dagger \Omega U = \begin{pmatrix} A + B\breve{j} & 0 \\ 0 & -\breve{k}(A + B\breve{j})\breve{k} \end{pmatrix} \tag{B.24}$$

thereby reducing the eigenvalue problem to the half of its original dimension

$$\big[A + B\breve{j}\big]\big[\boldsymbol{c}^\alpha - \boldsymbol{c}^{\beta *}\breve{j}\big] = \epsilon\big[\boldsymbol{c}^\alpha - \boldsymbol{c}^{\beta *}\breve{j}\big]. \tag{B.25}$$

By using the quaternion scheme, it becomes thus possible to benefit optimally from the reductions provided by time-reversal symmetry. In the quaternion representation the operator associated to this symmetry, can be represented by $\breve{j}$[145]

$$\breve{j}\big[\boldsymbol{c}^\alpha - \boldsymbol{c}^{\beta *}\breve{j}\big] = \big[\boldsymbol{c}^{\alpha *}\breve{j} + \boldsymbol{c}^\beta\big]. \tag{B.26}$$

In the following, it will also be illustrated how the quaternion scheme can be used to introduce point-group symmetry to relativistic calculations.

However, before arriving at that point, let us see how these techniques carry over to the Dirac equation. For these purposes, it proves to be useful to reorder the four-component wave function

$$\begin{pmatrix} \psi^L \\ \psi^S \end{pmatrix} = \begin{pmatrix} \psi^{L\alpha} \\ \psi^{L\beta} \\ \psi^{S\alpha} \\ \psi^{S\beta} \end{pmatrix} \rightarrow \begin{pmatrix} \psi^{L\alpha} \\ \psi^{S\alpha} \\ \psi^{L\beta} \\ \psi^{S\beta} \end{pmatrix} = \begin{pmatrix} \psi^\alpha \\ \psi^\beta \end{pmatrix}. \tag{B.27}$$

In this basis, the time-reversal operator can be represented as

$$\hat{\mathcal{K}} = -i\big[\sigma_y \otimes I_2\big]\hat{\mathcal{K}}_0 \tag{B.28}$$

from which we obtain

$$\hat{\mathcal{K}}\psi = \begin{pmatrix} -\psi^{L\beta *} \\ -\psi^{S\beta *} \\ \psi^{L\alpha *} \\ \psi^{S\alpha *} \end{pmatrix}. \tag{B.29}$$

If we assume the absence of external magnetic fields, the Dirac Hamiltonian in the reordered basis reads

$$\hat{h}_D = \begin{pmatrix} \hat{V} & -ic\partial_z & 0 & -ic\partial_- \\ -ic\partial_z & -2mc^2 + V & -ic\partial_- & 0 \\ 0 & -i\partial_+ & V & ic\partial_z \\ -ic\partial_+ & 0 & ic\partial_z & -2mc^2 + V \end{pmatrix}; \quad \partial_\pm = \partial_x \pm i\partial_y \tag{B.30}$$

where the general structure of Eqn. (B.19) can be recognized. It is thus possible to block diagonalize the Dirac Hamiltonian using the quaternion transformation from Eqn. (B.23), yielding the quaternion Dirac Hamiltonian

$$ {}^{Q}\hat{h}_D = \left\{ \begin{pmatrix} V & 0 \\ 0 & -2mc^2 + V \end{pmatrix} - c\breve{i} \begin{pmatrix} 0 & \partial_z \\ \partial_z & 0 \end{pmatrix} - c\breve{j} \begin{pmatrix} 0 & \partial_y \\ \partial_y & 0 \end{pmatrix} - c\breve{k} \begin{pmatrix} 0 & \partial_z \\ \partial_z & 0 \end{pmatrix} \right\} \tag{B.31} $$

and the quaternion wave function

$$ {}^{Q}\psi = \psi^{\alpha} - \psi^{\beta *}\breve{j}. \tag{B.32} $$

As alluded to before, the quaternion scheme shows its true virtue in combination with point-group symmetry.

However, in a four-component formalism, point-group symmetry deserves special consideration, compared to the more straightforward symmetry considerations of scalar wave functions. After all, the four-component wave function transforms as a fermion function, which have the rather unusual feature of developing a phase of minus one after a rotation of 2π

$$ \hat{R}(2\pi)\psi = -\psi. \tag{B.33} $$

Here, the rotation could be around any axis, so the axis of rotation is left out in the rotation operator, $\hat{R}$. Interestingly, this result implies that a fermion ought to be rotated around an angle of 4π before returning to its initial state. Therefore, in our point-group we should also take this symmetry operation into account. Suppose that we have a point-group, consisting of the symmetry operations $\{\hat{\mathcal{G}}\}$, that preserve the structure of our Hamiltonian, $\left[\hat{h}_D, \hat{\mathcal{G}}\right] = 0$. For every member of this group, we can create a new member by combining it with the operation from Eqn. (B.33), $\hat{\mathcal{G}}' = \hat{R}(2\pi)\hat{\mathcal{G}}$, which results in a group of double dimensions. The amount of irreducible representations (irreps) in this group, however, is not doubled and can generally be divided into bosonic irreps and fermionic irreps, the former is symmetric and the latter is anti-symmetric with respect to $\hat{R}(2\pi)$.

It can be shown, however, that not all of these irreps are unique, because in some cases they are related by time-reversal. Therefore, we may want to include time-reversal into our double groups to obtain a more complete description of the symmetry structure. Including time-reversal turns out to be rather problematic for the group structure, because there is not anymore a one-to-one correspondence between the product of representation matrices and symmetry operations if anti-Hermitian operators are included in the group.[145] It is still possible to construct these matrices, now referred to as a corepresentation, and decompose them into irreducible corepresentations (irrcoreps). However, the symmetry reductions that can be gained from the fermion irr(co)reps is rather limited. More reductions can be gained from symmetry considerations of the individual components.

Although the spinors as a whole generally transform according to the fermion irreps, the real- and imaginary part of each components transform as boson irreps[296]

$$ \Gamma_L = \begin{pmatrix} (\Gamma^R_{L\alpha}, \Gamma^I_{L\alpha}) \\ (\Gamma^R_{L\beta}, \Gamma^I_{L\beta}) \end{pmatrix}; \quad \Gamma_S = \begin{pmatrix} (\Gamma^R_{S\alpha}, \Gamma^I_{S\alpha}) \\ (\Gamma^R_{S\beta}, \Gamma^I_{S\beta}) \end{pmatrix}. \tag{B.34} $$

In the following I will assume that our pointgroup is either D_{2h} or any of its subgroup, implying that at most we have eight irreps: the totally symmetric irrep, Γ_0 the Cartesian coordinates, $(\Gamma_x, \Gamma_y, \Gamma_z)$, the rotations $(\Gamma_{R_x}, \Gamma_{R_y}, \Gamma_{R_z})$ and the function Γ_{xyz}. From the structure of the Dirac equation, in particular Eqn. (B.3), it can be shown that the symmetry content of the large- and small component reads

$$\Gamma_L = \begin{pmatrix} (\Gamma_0, \Gamma_{R_z}) \\ (\Gamma_{R_y}, \Gamma_{R_x}) \end{pmatrix} \otimes \Gamma_\phi; \quad \Gamma_S = \begin{pmatrix} (\Gamma_{xyz}, \Gamma_z) \\ (\Gamma_y, \Gamma_x) \end{pmatrix} \otimes \Gamma_\phi = \Gamma_L \otimes \Gamma_{xyz}, \tag{B.35}$$

where Γ_ϕ corresponds to a phase factor that depends on whether the spinor is gerade/ungerade Γ_0/Γ_{xyz}, or barred/unbarred Γ_0/Γ_{R_y}. This phase can also correspond to the irreps of the rotations or Cartesian coordinates, but in these cases the components in Eqn. (B.35) are merely reordered, thus preserving the overall symmetry structure. By applying this structure to the quaternion wave function, we obtain

$$\Gamma_{Q_\psi} = \begin{pmatrix} \Gamma_{Q_{\psi^L}} \\ \Gamma_{Q_{\psi^S}} \end{pmatrix} = \begin{pmatrix} \left[\Gamma_0, \mathbf{\Gamma}_{R_{\boldsymbol{r}}}\right] \\ \left[\Gamma_{xyz}, \mathbf{\Gamma}_{\boldsymbol{r}}\right] \end{pmatrix} \otimes \Gamma_\phi. \tag{B.36}$$

It can thus be concluded that in this scheme, the function of the quaternions is twofold: it preserves the structure of time-reversal symmetry, while simultaneously each quaternion unit points to a certain boson irrep.

Within the quaternion scheme, the basis set expansion of an orbital can be expressed as

$${}^{Q}\psi_i = \begin{pmatrix} \boldsymbol{\chi}^L & 0 \\ 0 & \boldsymbol{\chi}^S \end{pmatrix} \begin{pmatrix} {}^{Q}\boldsymbol{c}_i^L \\ {}^{Q}\boldsymbol{c}_i^S \end{pmatrix}; \quad {}^{Q}c^X = c_0^X + \breve{i}c_1^X - \breve{j}c_2^X + \breve{k}c_3^X \quad (X = L, S), \tag{B.37}$$

where the coefficients are now given by quaternion numbers. For a symmetry-adapted basis, our orbital is given by the expression

$${}^{Q}\psi_k = \begin{pmatrix} \sum_i \chi_i^L(\Gamma_i)\left[c_{0;i}^L(\Gamma_0) + c_{1;i}^L(\Gamma_{R_z})\breve{i} - c_{2;i}^L(\Gamma_{R_y}) + c_{3;i}^L(\Gamma_{R_x})\breve{k}\right] \\ \sum_j \chi_j^S(\Gamma_j)\left[c_{0;j}^S(\Gamma_{xyz}) + c_{1;j}^S(\Gamma_z)\breve{i} - c_{2;j}^S(\Gamma_y) + c_{3;j}^S(\Gamma_x)\breve{k}\right] \end{pmatrix}, \tag{B.38}$$

where the coefficients vanish if the symmetry of the basis function does not agree with the coefficient, e.g. $c_{0;i}^L(\Gamma_0) = 0$ if $\Gamma_0 \neq \Gamma_i$. For the C_{2v}, D_2 and D_{2h} point groups, this structure implies that the coefficient of each basis function only has contributions from *one* quaternion unit. Following a rather technical procedure that is described with more detail in ref.[145], it can be shown that this single quaternion cancels with the quaternion units in the Dirac Hamiltonian, hence forming a single real matrix. Likewise, for point groups of lower symmetry, such as C_2, C_s and C_{2h}, each coefficient has contributions from *two* quaternion units. From a similar procedure, it follows that we are left with a complex matrix representation of the Dirac Hamiltonian. For the C_1 and C_i point groups, however, the coefficients have contributions from all quaternion units, thus implying that the matrix representation keeps its quaternion structure. Therefore, point-groups of higher symmetries are accompanied by a reduction of the algebra, which simplifies the calculation significantly.

Using this scheme, it is possible to re-express the familiar quantities from chapter 1 in quaternion form. Some examples are: the one-body density matrix

$${}^{Q}D_{pq} = D_{pq} + D_{p\bar{q}}\breve{j}, \tag{B.39}$$

the Fock matrix

$${}^{Q}F_{pq} = F_{pq} + F_{p\bar{q}}\breve{j} \tag{B.40}$$

and even the solution vectors and the property gradient

$$
{}^{Q}Z_{ai} = Z_{ai} + Z_{a\bar{i}}\breve{j}; \quad {}^{Q}g_{A:ai} = g_{A;ai} + g_{A;a\bar{i}}\breve{j}. \tag{B.41}
$$

This composition is particularly useful in the context of selection rules, since the symmetry structure in Eqn. (B.35) implies that each quaternion component of the gradient can be associated with a bosonic irrep[146]

$$
\left[\underbrace{\Gamma_0}_{Re[g_{A;ai}]} + \breve{i} \underbrace{\Gamma_{R_z}}_{Im[g_{A;ai}]} + \breve{j} \underbrace{\Gamma_{R_y}}_{Re[g_{A;a\bar{i}}]} + \breve{k} \underbrace{\Gamma_{R_x}}_{Im[g_{A;a\bar{i}}]} \right] \otimes (\Gamma_{\phi_a} \otimes \Gamma_{\phi_i}) \otimes \Gamma_A. \tag{B.42}
$$

Appendix C

Complements to Chapter 3

C.1 Chirality and ECD Beyond First Order

As alluded to in the introduction of this chapter, there seems to be an intricate relation between ECD and the isotropy of the sample. Contrary to what is mentioned in most textbooks, ECD can yield non-zero signal for achiral molecules under anisotropic conditions. To illustrate this, consider the first-order truncated anisotropic differential oscillator strength

$$\begin{aligned}\Delta f^{[1]} =& \frac{2m_e\omega}{\hbar c^2}\left(\frac{\omega}{c}\right)e_{k;j}e_{k;i}\varepsilon_{ipq}2Re\big\{\langle f|\frac{1}{2}\hat{\mathcal{Q}}^{[2]}_{j;p}|i\rangle\langle f|\hat{\mathcal{Q}}^{[1]}_{q}|i\rangle^*\big\} \\ &+\frac{2m_e\omega}{\hbar c^2}\left(\frac{\omega}{c}\right)e_{k;j}e_{k;i}\varepsilon_{ipq}2Re\big\{\langle f|-\frac{i}{\omega}\hat{m}^{[1]}_{r}\varepsilon_{rjp}|i\rangle\langle f|\hat{\mathcal{Q}}^{[1]}_{q}|i\rangle^*\big\},\end{aligned} \tag{C.1}$$

which is given in terms of the electric-dipole, magnetic-dipole and electric-quadrupole moment. Expressed in the irreps of D_{2h} and subgroups, the electric-dipole moment transforms as the Cartesian coordinates $(\Gamma_x, \Gamma_y, \Gamma_z)$, the magnetic-dipole as the rotations $(\Gamma_{R_x}, \Gamma_{R_y}, \Gamma_{R_z})$ and the electric-quadrupole as the rotations or the totally symmetric irep, Γ_0. To obtain a non-vanishing ECD signal under anisotropic conditions, the transitions must simultaneously have non-vanishing contributions from the electric-dipole and the electric-quadrupole or from the electric-dipole and the magnetic-dipole. Therefore, for a non-vanishing anisotropic ECD, at least one of the Cartesian coordinates must either be totally symmetric $\Gamma_{r_i} = \Gamma_0$, or transform as a rotation $\Gamma_{r_i} = \Gamma_{R_j}$, where the component of the rotation and coordinate do not necessarily have to be equal. Exactly which of these conditions holds true depends on the direction of the wave vector. In general, these conditions can also be met for non-chiral point groups, confirming that non-chiral molecules can have a non-zero ECD signal under anisotropic conditions. Upon taking the isotropic average, the first-order truncated ECD is given by Eqn. (3.150).

Similar to previous example, the minimal condition for non-vanishing ECD is $\Gamma_{r_i} = \Gamma_{R_i}$, for at least one Cartesian coordinate, although in this case, the Cartesian coordinate and the rotation do have to be the same component. This small detail explains why isotropic ECD can only be measured for chiral molecules, since this condition is only met for chiral point groups. However, this derivation leans on the symmetry properties of the lowest-order multipole moments, whereas the full interaction and higher-order terms in the multipole expansion do not generally obey the same selection rules. Therefore, in the following, I will demonstrate that the isotropic ECD is zero for achiral molecules regardless of the order of the multipole expansion.

To start off, suppose that we are considering the isotropic ECD of some achiral molecule, A, consisting of n atoms, whose nuclear coordinates are stored in the matrix

$$R_A = \left(\boldsymbol{R}_{N_1}, \boldsymbol{R}_{N_2}, \cdots \boldsymbol{R}_{N_n}\right) \tag{C.2}$$

In the previous Section, the effects of isotropy where taken into account by fixing the molecule in space and considering all possible propagation- and polarization directions of the incoming light. In this proof, it turns out to be useful to follow the alternative approach: I will fix the incoming light and rotate the coordinates, using the Euler angles θ, ϕ, χ

$$\mathcal{O}(\theta,\phi,\chi)R_A = \left(\mathcal{O}(\theta,\phi,\chi)\boldsymbol{R}_{N_1}, \mathcal{O}(\theta,\phi,\chi)\boldsymbol{R}_{N_2}, \cdots \mathcal{O}(\theta,\phi,\chi)\boldsymbol{R}_{N_n}\right), \tag{C.3}$$

where the matrix $\mathcal{O}(\theta,\phi,\chi)$ is constructed from three orthogonal rotations[32]

$$\mathcal{O}(\theta,\phi,\chi) = O(\phi,\boldsymbol{e}_z)O(\theta,\boldsymbol{e}_y)O(\chi,\boldsymbol{e}_z). \tag{C.4}$$

In this expression, the matrix $O(\alpha,\boldsymbol{e}_n)$ rotates the coordinates with an angle of α around the axis spanned by $\boldsymbol{e}_n$. Starting from R_A, we can thus generate all possible orientations of A by varying the angles ϕ, θ and χ over their respective domains, $[0,2\pi]$, $[0,\pi]$ and $[0,2\pi]$. Let us further denote $\{R_A\}$ as the set of all possible orientation of A.

Because $\{R_A\}$ contains all possible orientations, we can choose any starting geometry from which we generate this set. Furthermore, because A is achiral, we can thus apply any orthogonal transformations to R_A, without changing this set

$$\{R_A\} = \{\hat{U}R_A\}; \quad \hat{U}^T U = I. \tag{C.5}$$

This implies that this set is also invariant under transformations that do not preserve the handedness of the coordinate system, i.e. $det(U) = -1$.

In particular, the parity inversion operator is of great relevance in physics, as it leaves electromagnetic interactions unchanged. Therefore, if we apply this operator to both the nuclear coordinates and the circularly polarized light, the oscillator strength should not change. For these purposes, I will write the anisotropic oscillator strength of circularly polarized light as a function of the wave vector and a parametric function of the nuclear geometry: $f_{L/R}(\boldsymbol{k}; R_A)$. Due to the generality of this proof, this oscillator strength can either be derived from the full interaction operator, or a truncated interaction. The action of parity inversion on the oscillator strength can thus be expressed as

$$f_{L/R}(\boldsymbol{k}; R_A) = \hat{\mathcal{P}}\big(f_{L/R}(\boldsymbol{k}; R_A)\big) = f_{R/L}(-\boldsymbol{k}; \hat{\mathcal{P}}R_A). \tag{C.6}$$

Let us further denote the set of oscillator strengths from all possible orientations of A as $\{f_{L/R}(\boldsymbol{k}; R_A)\}$. The isotropic differential oscillator strength can be obtained as the average of all members in $\{f_{L/R}(\boldsymbol{k}; R_A)\}$. Because $\{f_{L/R}(\boldsymbol{k}; R_A)\}$ is constructed from all possible orientations of A, it is isotropic with respect to $\boldsymbol{k}$. We can thus define $\boldsymbol{k}$ at will, without changing $\{f_{L/R}(\boldsymbol{k}; R_A)\}$, with the only constraint being that $\boldsymbol{k}$ is consistent throughout this set.

I will use this feature, together with Eqn. (C.6), to demonstrate that the isotropic differential oscillator strength is always zero for achiral molecules, regardless of the order in the multipole expansion. For these purposes, I will demonstrate that the sets $\{f_L(\boldsymbol{k}; R_A)\}$ and $\{f_R(\boldsymbol{k}; R_A)\}$

are the same, yielding the same value upon isotropic averaging, which implies that the isotropic differential oscillator strength is zero. Let us start off with the former set and apply parity inversion onto each of its members

$$\{f_L(\boldsymbol{k};R_A)\} = \{\hat{\mathcal{P}}\big(f_L(\boldsymbol{k};R_A)\big)\} = \{f_R(-\boldsymbol{k};\hat{\mathcal{P}}R_A)\}, \tag{C.7}$$

where in the second equality I have inserted Eqn. (C.6). If we further exploit the fact that the set $\{R_A\}$ is invariant under orthogonal transformations and that the set $\{f_{L/R}(\boldsymbol{k};R_A)\}$ does not depend on the choice of $\boldsymbol{k}$, we arrive at the result

$$\{f_L(\boldsymbol{k};R_A)\} = \{f_R(\boldsymbol{k};R_A)\}, \tag{C.8}$$

which thus concludes the proof that isotropic ECD vanishes for achiral molecules.

The situation is different, however, when our molecule is chiral. In this case, we have an enantiomeric pair, that I will label as $\mathcal{L}$ and $\mathcal{R}$. Accordingly, the set of all their possible orientations is given by the sets $\{R_{\mathcal{L}}\}$ and $\{R_{\mathcal{R}}\}$. A defining feature of chiral molecules, is that their point group only contain proper rotations. Any transformation with $det(\hat{U}) = -1$ thus converts between the members of the enantiomeric pair. Unlike previous example, the parity operator thus has the following action on the sets of all orientations

$$\{\hat{\mathcal{P}}R_{\mathcal{L}}\} = \{R_{\mathcal{R}}\}. \tag{C.9}$$

Similar to previous example, we define the collections of oscillator strengths as $\{f_{L/R}(\omega;R_{\mathcal{L}})\}$ and $\{f_{L/R}(\omega;R_{\mathcal{R}})\}$. From this, it follows that it is not possible to recreate the proof given in previous paragraph

$$\begin{aligned}\{f_{L/R}(\boldsymbol{k};R_{\mathcal{L}})\} &= \{\hat{\mathcal{P}}f_{L/R}(\boldsymbol{k};R_{\mathcal{L}})\} = \{f_{R/L}(-\boldsymbol{k};R_{\mathcal{R}})\}\\ \{f_{L/R}(\boldsymbol{k};R_{\mathcal{L}})\} &= \{\hat{\mathcal{P}}f_{L/R}(\boldsymbol{k};R_{\mathcal{L}})\} = \{f_{R/L}(-\boldsymbol{k};R_{\mathcal{R}})\},\end{aligned} \tag{C.10}$$

Therefore, based on these symmetry considerations, there is no *a priori* reason to assume that the isotropic differential oscillator strength vanishes for chiral molecules. I recall that this derivation is entirely based on inversion symmetry, with no reference to selection rules arising from specific operators. Therefore, it is equally valid for the full- and truncated interaction.

C.2 Selection Rules

In this appendix, I will explore the selection rules of multipole moments and the full interaction operator. This section heavily leans on the findings from Appendix B from ref. 113, which, in turn, will be applied to the various interaction operators introduced Chapter 3. Conventional electric-dipole selection rules and those corresponding to higher-order multipole moments are a consequence of spherical symmetry. In the presence of this symmetry, one-electron states can be expressed as eigenfunctions of the total angular momentum (see Section 2.3.3)

$$\hat{j}_z|jm\rangle = \hbar m|jm\rangle; \quad \hat{j}^2|jm\rangle = \hbar^2 j(j+1)|jm\rangle, \tag{C.11}$$

which generally can be understood as irreducible representations of the full rotation group. However, to fully exploit the restrictions imposed by spherical symmetry, we should also express the operator in the transition moment in terms of this symmetry. The irreducible tensor operators generally obey this condition. An irreducible tensor operator of rank k, comes with $2k+1$ components

$$\boldsymbol{T}^k = \{T^k_q \quad | \quad q = k, k-1, \cdots, -k\}, \tag{C.12}$$

where each component obeys the commutator relations

$$[\hat{j}_z, T^k_q] = \hbar m T^k_q; \quad [\hat{j}_\pm, T^k_q] = \hbar\sqrt{k(k+1) - q(q\pm 1)}T^k_{q\pm 1}. \tag{C.13}$$

In this expression, I have introduced the ladder operators $\hat{j}_\pm = \hat{j}_x \pm i\hat{j}_y$, which deserve their name from their action on angular momentum eigenstates

$$\hat{j}_\pm|jm\rangle = \hbar\sqrt{j(j+1) - m(m\pm 1)}|jm\pm 1\rangle. \tag{C.14}$$

The symmetry reductions arising from irreducible tensor operators become manifest in the Wigner-Eckart theorem

$$\langle jm|T^k_q|j'm'\rangle = (-1)^{j-m}\begin{pmatrix} j & k & j' \\ -m & q & m' \end{pmatrix}(j||\boldsymbol{T}^k||j'), \tag{C.15}$$

where the integral on the right-hand-side is independent on the orientation of the system, i.e. the values of m, m' and k. Furthermore, the prefactor of this integral is given by the $3j$-symbol, which can be related to the Clebsch-Gordan coefficients (Eqn. (2.93)) according to

$$\langle j_1m_1j_2m_2|j_1j_2;jm\rangle = (-1)^{j_1-j_2-m}\sqrt{2j+1}\begin{pmatrix} j_1 & j_2 & j \\ m_1 & m_2 & -m \end{pmatrix} = C^{j_1j_2j}_{m_1m_2m}. \tag{C.16}$$

The $3j$-symbol mediates all selection rules, only being non-zero if the following conditions apply

$$\begin{aligned} &m_1 + m_2 = m \\ &|j_1 - j_2| \leq j \leq j_1 + j_2 \\ &j_1 + j_2 + j \in \mathbb{Z}. \end{aligned} \tag{C.17}$$

Typically, the j-dependent integral is found by exploiting the fact that it is the same for all components of $\boldsymbol{T}^k$. For example, by expressing the angular momentum operator as a irreducible tensor operator, $\hat{\boldsymbol{j}}^1 = \{-\frac{1}{\sqrt{2}}\hat{j}_-, \hat{j}_z, \frac{1}{\sqrt{2}}\hat{j}_+\}$, the j-dependent integral can be found from the relation

$$\langle jm|j_z|j'm'\rangle = \hbar m'\delta_{jj'}\delta_{mm'}, \tag{C.18}$$

thus implying

$$(j||\hat{\boldsymbol{j}}^{(1)}||j') = \hbar\sqrt{j(j+1)(2j+1)}\delta_{jj'}. \tag{C.19}$$

In the following, I will be treating operators that are derived from $c\boldsymbol{\alpha}\cdot\boldsymbol{A}$, where $c\boldsymbol{\alpha}$ acts on spin space, whereas $\boldsymbol{A}$ on position space. It will thus be useful to combine two irreducible tensor operators $\boldsymbol{S}^{k_1}$ and $\boldsymbol{T}^{k_2}$, which may act on different spaces, into a new spherical tensor operator

$$[\boldsymbol{S}^{k_1}\otimes\boldsymbol{T}^{k_2}]^k_q = \sum_{q_1=-k_1}^{k_1}\sum_{q_2=-k_2}^{k_2} C^{k_1k_2k}_{q_1q_2q} S^{k_1}_{q_1}\otimes T^{k_2}_{q_2}; \quad q = k, k-1, \cdots, -k; \quad |k_1-k_2| \leq k \leq k_1+k_2. \tag{C.20}$$

As a first example, I will apply this machinery in the derivation of electric-dipole selection rules. For these purposes, I will conveniently express the electric-dipole moment operator in spherical basis

$$\boldsymbol{Q}^{[1]} = -\sqrt{\frac{4\pi}{3}}erY_{10}\boldsymbol{e_0} + \sqrt{\frac{4\pi}{3}}erY_{1-1}\boldsymbol{e}_+ + \sqrt{\frac{4\pi}{3}}erY_{11}\boldsymbol{e}_-; \quad \boldsymbol{e}_\pm = \mp\frac{1}{\sqrt{2}}(\boldsymbol{e}_x \pm i\boldsymbol{e}_y). \tag{C.21}$$

Within this basis, we can rewrite this operator as an irreducible tensor operator of rank 1

$$\boldsymbol{Q}^{[1]} = -er\boldsymbol{C}^1; \quad \boldsymbol{C}^1 = \{\sqrt{\frac{4\pi}{3}}Y_{1-1}, \sqrt{\frac{4\pi}{3}}Y_{10}, \sqrt{\frac{4\pi}{3}}Y_{11}\}, \tag{C.22}$$

which I will insert in Eqn. (C.15)

$$-\langle jm|erC^1_q|j'm'\rangle = (-1)^{j-m}\begin{pmatrix} j & 1 & j' \\ -m & q & m' \end{pmatrix}(j||\boldsymbol{C}^1||j'). \tag{C.23}$$

From Eqn. (C.17), the 3j-symbol yields non-zero results if

$$\begin{aligned} &m' + q = m \\ &|j-1| \leq j' \leq |j+1| \\ &j + j' + j \in \mathbb{Z}. \end{aligned} \tag{C.24}$$

Therefore, the selection rules of electric-dipole transitions are $\Delta j = \pm 1, 0; \quad \Delta m = \pm 1, 0$, with the caveat that any transition of the type $j = 0 \rightarrow j = 0$ are forbidden, as can be inferred from the 3j-symbol. Exactly the same selection rules apply to the velocity representation, as we can express the α matrices in irreducible tensor form as well

$$\boldsymbol{\alpha}^1 = \{-\frac{1}{\sqrt{2}}\alpha_-, \alpha_z, \frac{1}{\sqrt{2}}\alpha_+\}; \quad \alpha_\pm = \alpha_x \pm i\alpha_y, \tag{C.25}$$

which has the same rank as Eqn. (C.22), thus suggesting that the same selection rules apply. Deriving selection rules for magnetic-dipole transitions is more difficult, as this operator has a more complicated structure, being defined as the cross-product between the position and current vector. It is possible, however, to apply the same procedure as the one outlined before. Again, we have to express the relativistic magnetic-dipole moment operator as an irreducible tensor operator. In other words, we first have to express this operator in spherical basis, which can be achieved by evaluating the cross-product of Eqn. (C.22) and (C.25). From [113, Equation B.3.149], it follows that the cross-product of two first rank spherical tensor can be expressed as

$$(\boldsymbol{a}^1 \times \boldsymbol{b}^1)_q = -i\sqrt{2}[\boldsymbol{a}^1 \otimes \boldsymbol{b}^1]^1_q = -i\sqrt{2}\sum_{q_1q_2q} C^{111}_{q_1q_2q} a^1_{q_1} b^1_{q_2}, \tag{C.26}$$

where in the second equality, I have used the composition rule for two spherical tensors (Eqn. (C.20)).

Expressed in spherical basis, the transition moment stemming from the magnetic-dipole moment can be expressed as

$$\langle jm|\hat{m}^{[1]}_q|j'm'\rangle = i\sqrt{2}\langle jm|er[\boldsymbol{C}^1\otimes c\boldsymbol{\alpha}^1]^1_q|j'm'\rangle = (-1)^{j-m}i\sqrt{2}\begin{pmatrix} j & 1 & j' \\ -m & q & m' \end{pmatrix}(j||er[\boldsymbol{C}^1\otimes c\boldsymbol{\alpha}^1]^1||j'). \tag{C.27}$$

Therefore, the magnetic-dipole selection rules are the same as for the electric-dipole: $\Delta j = \pm 1, 0; \quad \Delta m = \pm 1, 0 (j = 0 \nrightarrow j = 0)$. Alternatively, selection rules can be derived in terms of the orbital angular momentum of the large- and small component ($\Delta \ell = 0, 2$). However, this approach will not be pursued here, as the orbital angular momentum is not a good quantum number, which makes these selection rules less useful in current context. For a full derivation, see ref. 297.

It should be noted, however, that these selection rules drastically differ from the ones derived in a non-relativistic framework, where the magnetic-dipole moment assumes the more simple form $\hat{\boldsymbol{m}}^{[1]}_{nr} = \frac{e}{2mc}\hat{\boldsymbol{\ell}}$. Further recalling that the non-relativistic one-electron atomic states can be expressed as $\psi_{n\ell m}(\boldsymbol{r}) = \frac{1}{r}R_{n\ell}(r)Y_{\ell m}(\theta,\phi)$, the selection rules follow from

$$\langle\psi_{n_i\ell_i m_i}|\frac{e}{2mc}\hat{\boldsymbol{\ell}}|\psi_{n_f\ell_f m_f}\rangle = \int_0^\infty dr R_{n_i\ell_i}R_{n_f\ell_f}\int_0^\pi d\theta\sin\theta\int_0^{2\pi} d\phi Y^*_{m_i\ell_i}\frac{e}{2mc}\hat{\boldsymbol{\ell}}Y_{m_f\ell_f}, \tag{C.28}$$

where I have used the fact that the non-relativistic magnetic-dipole moment operator is purely angular. By expressing the angular momentum operator in spherical basis, Eqn. (C.14) can be exploited. Orthogonality relations subsequently give the following selection rules $\Delta n = 0; \quad \Delta \ell = 0$, which suggest that magnetic-dipole transitions can only occur inside the manifold of quasi-degenerate states split by spin-orbit coupling. As noted in Section 4.5, this difference in selection rules can have severe consequences on the magnitude of the first-order isotropic differential oscillator strength.

Although I will not show it explicitly here, the electric-quadrupole selection rules can be derived by expressing this operator in terms of the following irreducible tensor operator of rank 2:

$$\boldsymbol{C}^2 = \{\sqrt{\frac{4\pi}{5}}Y_{2-2}, \sqrt{\frac{4\pi}{5}}Y_{2-1}, \sqrt{\frac{4\pi}{5}}Y_{20}, \sqrt{\frac{4\pi}{5}}Y_{21}, \sqrt{\frac{4\pi}{5}}Y_{22}\}. \tag{C.29}$$

From the Wigner-Eckart theorem it can thus be concluded that its selection rules are given by $\Delta j = \pm 2, \pm 1, 0; \quad \Delta m = \pm 2, \pm 1, 0 (j = 0 \nrightarrow j = 0)$. Using the procedure outlined above, it is in principle possible to find selection rules for multipole moments to arbitrary order.

In the following, however I will use the machinery of irreducible tensor operator to assess the selection rules of the full interaction operator, which I will conveniently expand using a plane-wave expansion

$$\hat{T}_p = \frac{e}{\omega}c\alpha_p e^{i\boldsymbol{k}\cdot\boldsymbol{r}} = 4\pi\frac{e}{\omega}\sum_{\ell=0}^{\infty}\sum_{m=-\ell}^{\ell} i^\ell j_\ell(kr)Y^{m*}_\ell(\boldsymbol{e}_k)c\alpha_p Y^m_\ell(\theta,\phi), \tag{C.30}$$

where the α matrix is expressed in spherical basis. Starting from the irreducible tensor operator

$$X_q^k = [\boldsymbol{\alpha}^{(1)} \otimes \boldsymbol{C}^{(l)}]_q^k = \sum_{q_1=-k_1}^{k_1} \sum_{q_2=-k_2}^{k_2} C_{q_1 q_2 q}^{1lk} \alpha_{q_1} C_{q_2}^{(l)}, \tag{C.31}$$

it can be shown that the full interaction operator can be expressed in terms of this operator by multiplying above operator with $C_{pmq}^{1\ell k}$ and exploiting the orthogonality of the Clebsch-Gordan coefficients

$$\sum_{j_3=|j_1-j_2|}^{|j_1+j_2|} \sum_{m_3=-j_3}^{j_3} C_{m_1 m_2 m_3}^{j_1 j_2 j_3} C_{m_1' m_2' m_3}^{j_1 j_2 j_3} = \delta_{m_1 m_1'} \delta_{m_2 m_2'}, \tag{C.32}$$

where the final result can be identified with the terms appearing in Eqn. (C.30)

$$\begin{aligned} \sum_{k=|\ell-1|}^{|\ell+1|} \sum_{q=-k}^{k} C_{pmq}^{1\ell k} [\boldsymbol{\alpha}^{(1)} \otimes \boldsymbol{C}^{\ell}]_q^k = \sum_{k,q} \sum_{q_1=-k_1}^{k_1} \sum_{q_2=-k_2}^{k_2} C_{pmq}^{1\ell k} C_{q_1 q_2 q}^{1\ell k} \alpha_{q_1} C_{q_2}^{\ell} \\ = \sum_{q_1=-k_1}^{k_1} \sum_{q_2=-k_2}^{k_2} \delta_{p q_1} \delta_{m q_2} \alpha_{q_1} \otimes C_{q_2}^{\ell} = \alpha_p C_m^{\ell}. \end{aligned} \tag{C.33}$$

Therefore, the full interaction operator can be expressed as

$$\hat{T}_p = \frac{e}{\omega} c \alpha_p e^{i \boldsymbol{k} \cdot \boldsymbol{r}} = \sqrt{4\pi} \frac{e}{\omega} \sum_{\ell=0}^{\infty} \sum_{m=-\ell}^{\ell} \sqrt{2\ell+1} i^{\ell} j_{\ell}(kr) Y_{\ell}^{m*}(\boldsymbol{e}_k) \left(\sum_{k=|\ell-1|}^{|\ell+1|} \sum_{q=-k}^{k} C_{pmq}^{1\ell k} X_q^k \right). \tag{C.34}$$

Due to the complexity of this expression, which has contributions from nearly all irreps, it may seem as if there are no selection rules associated to this operator. However, upon closer inspection, it follows that the index k assumes values between 1 and ∞, which in turn implies that a transitions between two states of zero angular momentum always vanishes. Therefore, the selection rules $j = 0 \nrightarrow j = 0$ seems to be a universal rule that applies throughout each order of the multipole expansion.

C.3 Manipulations of Summation Indices

In this appendix, I will illustrate several useful techniques to rewrite summation indices. For these purposes, let A be a square matrix of dimension N and suppose that we want to calculate its sum over all elements

$$\sum_{n=0}^{N} \sum_{m=0}^{N} A_{nm}. \tag{C.35}$$

Written in this form, the summation is carried out row-wise, whereas we could also have defined it column-wise

$$\sum_{m=0}^{N}\sum_{n=0}^{N} A_{nm}. \tag{C.36}$$

Figure C.3 depicts a diagram of both possibilities. In the following example, I will demonstrate all possible ways to sum all terms on the diagonal and lower triangle of this matrix. I will start off with column-wise and row-wise summation, respectively

$$\sum_{m}^{N}\sum_{n=m}^{N} A_{nm} = \sum_{n=0}^{N}\sum_{m=0}^{n} A_{nm}. \tag{C.37}$$

It should be noted that on the diagonal and each sub-diagonal, the index combination $v = n - m$ assumes a constant, distinct and positive value, suggesting that we can use it as a summation index. Summing over v implies that we are summing over the diagonals,

$$\sum_{v=0}^{N}\sum_{m=0}^{N-v} A_{vm} = \sum_{v=0}^{N}\sum_{n=v}^{N} A_{nv}, \tag{C.38}$$

where we have the additional choice to run the second index over the columns or rows. In Figure C.3 a diagram of this type of summations is presented.
In some cases, it may also be useful to constrain our summation over the upper left triangle of the matrix

$$\sum_{m=0}^{N}\sum_{n=0}^{N-m} A_{nm} = \sum_{n=0}^{N}\sum_{m=0}^{n} A_{nm}, \tag{C.39}$$

where the left-hand-side represents column-wise summation and the right-hand-side row-wise summation. Considering that along the any sub anti-diagonal and the anti-diagonal the index $y = n+m$ is constant, distinct and positive, which makes it a suitable summation index. Therefore, it is also possible to carry out the summation over the sub anti-diagonals and the anti-diagonal

$$\sum_{y=0}^{N}\sum_{m=0}^{y} A_{ym} = \sum_{y=0}^{N}\sum_{n=0}^{y} A_{ny}. \tag{C.40}$$

In Figure C.4, this type of summations is depicted diagrammatically.

Another useful technique to manipulate summations involves redefining of summation indices. Similar to previous examples, the main idea is that a summation can be carried out in any order, thus implying that we may shift the summation index, reverse it or even both. For example, suppose we are dealing with a simple row-wise summation and we want to shift the index of the column by a certain amount. This operation can be realized by applying the substitution

$$m \to m' = m + l \tag{C.41}$$

which implies that we have to insert $m = m' - l$ into our summation

$$\sum_{n=0}^{N}\sum_{m'-l=0}^{N} A_{n,m'-l} = \sum_{n=0}^{N}\sum_{m'=l}^{N-l} A_{n,m'-l} \tag{C.42}$$

Typically, once the transformation has been completed, the prime on the index m' is dropped, yielding the relation

$$\sum_{n=0}^{N}\sum_{m=l}^{N-l} A_{n,m-l} \tag{C.43}$$

Another useful example is the reversal of a summation, which can carried out using the substitution

$$m \to m' = N - m, \tag{C.44}$$

and inserting the relation $m = N - m'$

$$\sum_{n=0}^{N}\sum_{N-m'=0}^{N} A_{n,N-m'} = \sum_{n=0}^{N}\sum_{-m'=-N}^{0} A_{n,N-m'} = \sum_{n=0}^{N}\sum_{m'=N}^{0} A_{n,N-m'} = \sum_{n=0}^{N}\sum_{m'=0}^{N} A_{n,N-m'}, \tag{C.45}$$

where the prime on the indices can be dropped afterwards.

C.4 Restricted Excitation-Window Approach

The aim of this appendix is to briefly discuss the restricted excitation-window approach. In Section 3.6.2, the conditions were given that indicate whether the generalized length- and velocity representation are equivalent at the SCF level of theory. As a side note, I argued that this equivalence is broken if the restricted excitation-window approach is applied. Since this approach takes such an important position in this work, I will devote this section to the discussion of its principles.

In Chapter 1, we have learned that solution vectors, and hence transition moments, are obtained by solving the generalized eigenvalue problem from Eqn.(1.114). It was also noted that the Hessian matrix appearing in this problem is typically much too large to store, thus requiring us to project it onto a set of trial vectors and solve it in this reduced basis. In the context of core transitions, such methods are cumbersome because they are generally bottom-up approaches. Therefore, before obtaining the core transition, all transitions of lower excitation energies need to be calculated first.

To solve this problem, the orbital rotation operator (Eqn. (1.85)) is restricted, such that the occupied part only contains contributions from the core orbitals. For example, if we want to study the K-edge of the radium atom, the orbital rotation operator assumes the form

$$\hat{\kappa}(t) = \sum_{a}\left[\kappa_{ai_{1s}}\hat{a}_a^{\dagger}\hat{a}_{i_{1s}} - \kappa_{ai_{1s}}^{*}\hat{a}_{i_{1s}}^{\dagger}\hat{a}_a\right], \tag{C.46}$$

where the Einstein summation convention is *not* applied and i_{1s} is the index corresponding to the $1s_{1/2}$ orbital of the radium atom. This procedure is referred to as the restricted excitation-window approach.[215, 216] Closely related is the core-valence separation scheme, which applies to EOM-CC.[298, 299] Approximation schemes of this type are justified because core transitions typically do not contain significant contributions from occupied valence orbitals. These methods thus allow to selectively study transitions stemming from the core shell. However, due to the nature of the restricted excitation-window approach, the terms appearing in Eqn. (3.107) do not cover all occupied-virtual/virtual-orbital pairs, thus breaking equivalence of the generalized length- and velocity representation.

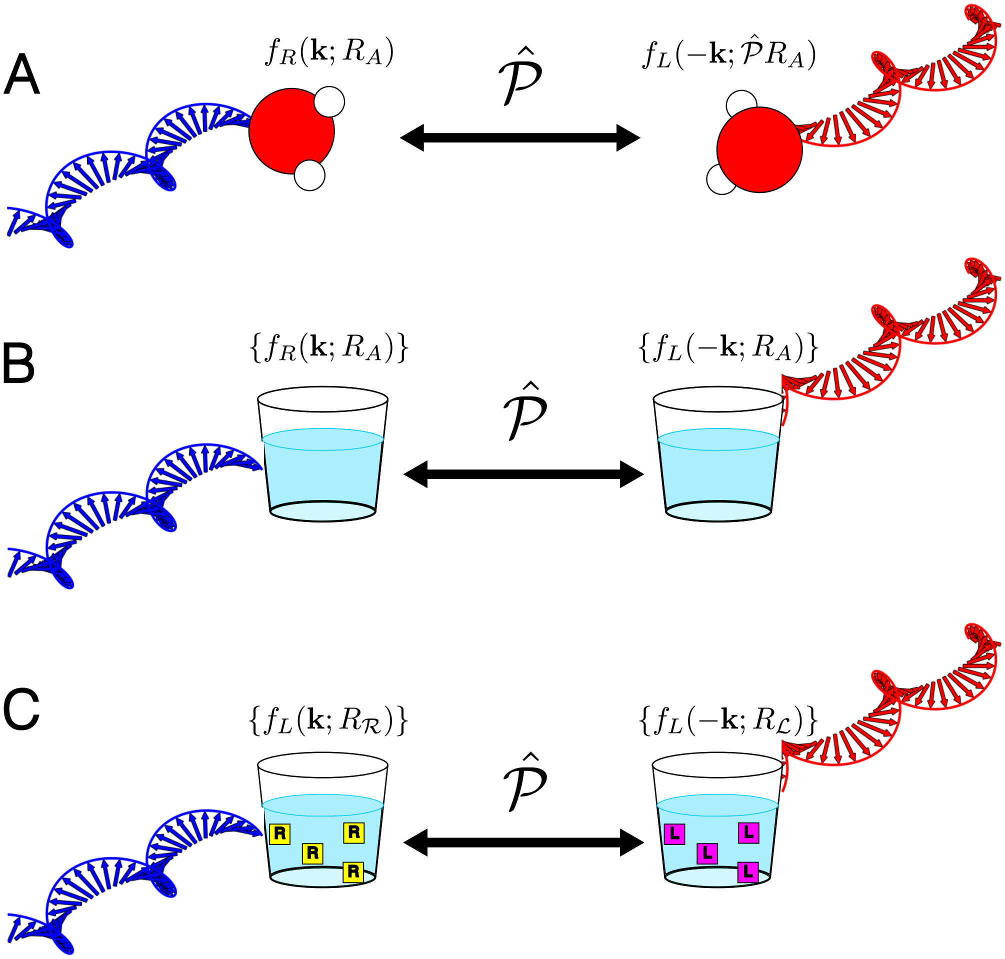

Figure C.1: schematic representation of circularly polarized light interacting with an anisotropic sample (panel A), an isotropic achiral sample (B) and an isotropic chiral sample (C). The corresponding oscillator strengths are shown above. In the isotropic case, the oscillator strength is constructed as an average of the set $\{f_{L/R}(\boldsymbol{k}; R_A\}$.

Figure C.2: diagrammatic representation of column-wise (right) and row-wise (left) summation of the elements of A.

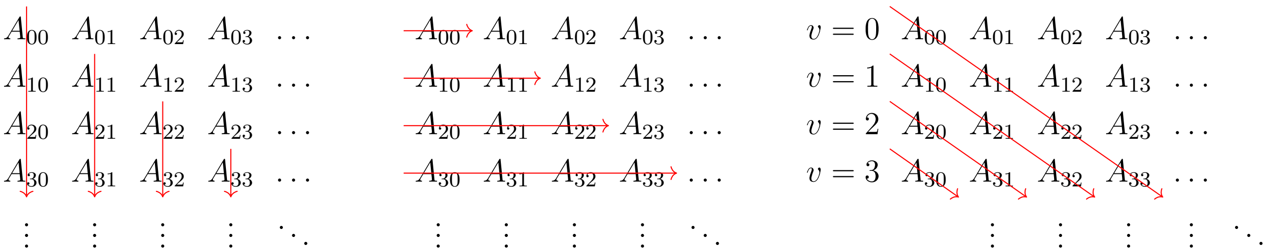

Figure C.3: diagrammatic representation of the column-wise (left), row-wise (middle) and diagonal (right) summation of the lower triangle and main diagonal of a matrix. For the summation on the right, the index $v = n - m$ is given for each (sub) diagonal.

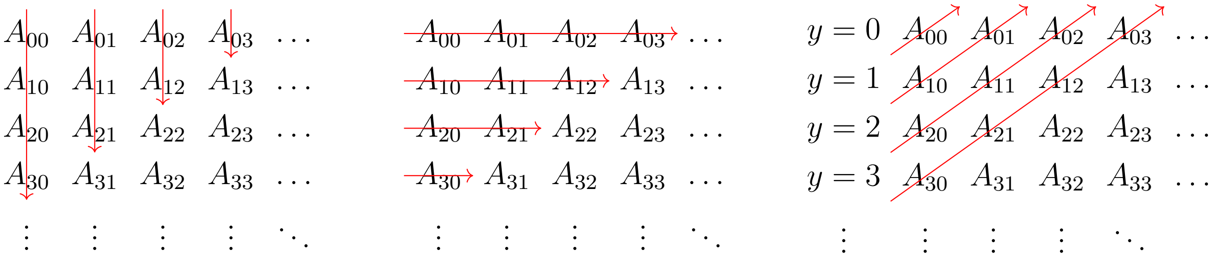

Figure C.4: diagrammatic representation of the column-wise (left), row-wise (middle) and diagonal (right) summation of the sub anti-diagonals and anti-diagonal of a matrix. For the summation on the right, the index $y = n + m$ is given for each (sub) anti-diagonal.

Appendix D

Complements to Chapter 4

D.1 Linear Dependences in Small Component Function

Throughout the main text, it is advocated to use a tight linear dependence threshold, i.e. less functions deleted, for the calculations of radial distributions associated with truncated interaction. In this section, I will demonstrate what happens to the magnetic multipoles if the default linear dependence threshold in the DIRAC code is used (10^{-6} for the large component space and 10^{-8} for the small component space).

Figure D.1 shows the radial distributions of the magnetic multipole moments for the core transition. In these calculations, the default linear dependence threshold is applied, the effects of which are clearly visible: for $1 < n < 5$, the radial distributions of the dyall.ae3z and dyall.ae4z basis sets oscillate considerably around the numerical reference. At higher orders, the oscillations appear to less pronounced because the r-dependent prefactor dominates the characteristics of the curve. Although the oscillations are diminished in these curves, the overall deviations vastly increase. Interestingly, the basis set convergence seems to be inverted: larger basis sets introduce larger deviations from the numerical reference.

To understand the origin of these oscillations, the involved orbitals need to be analyzed (Figure D.2). The $7p_{1/2}$ orbital converges smoothly towards the numerical reference, whereas the error curve of the $1s_{1/2}$ orbital exhibit similar oscillations as the magnetic multipoles. Especially the basis set convergence of the small component of the $1s_{1/2}$ orbital is problematic: instead of reducing the error, the dyall.ae3z and dyall.ae4z deteriorate the description of the small component function. It seems that most of the oscillations in Figure D.1 stem from the small component of the $1s_{1/2}$ orbital. Therefore, in the following, I inspect the $Q_{1,-1}$ function in terms of its basis set expansion.

Ideally, the large and small component are expanded in a two-component basis (Eqn. (2.99))

$$\mathcal{G}_{\alpha\kappa\ell m} = R_{\alpha\ell}(r)\xi_{\kappa m}(\theta,\phi), \tag{D.1}$$

where the radial part is a Gaussian function

$$R_{\alpha\ell} = N_{\alpha\ell} r^{\ell} e^{-\alpha r^2}; \quad N_{\alpha l} = \frac{2(2\alpha)^{3/4}}{\pi^{1/4}}\sqrt{\frac{2^{\ell}}{(2\ell+1)!!}}\left(\sqrt{2\alpha}\right)^{\ell} \tag{D.2}$$

and the angular part a spherical spinor, depending on the angular quantum numbers κ and m. However, in its current form, this basis cannot be used for the small component function, because

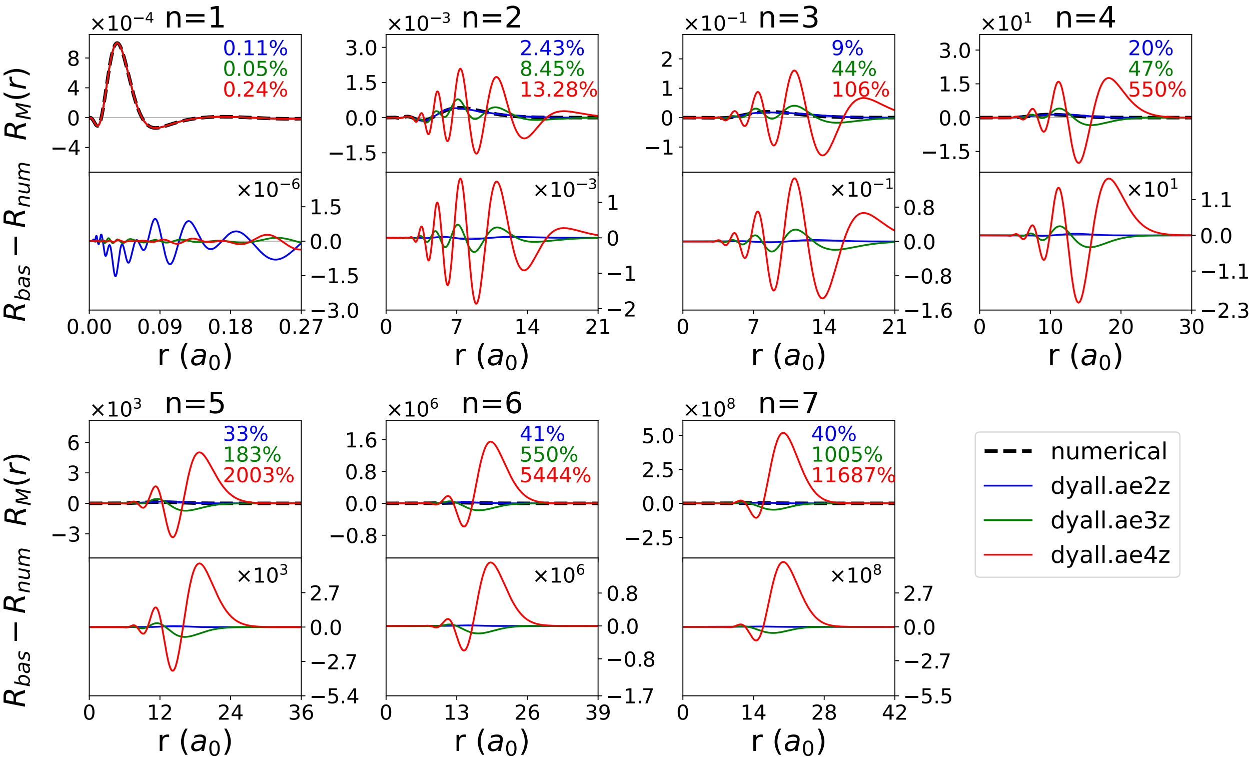

Figure D.1: Core transition ($1s_{1/2} \rightarrow 7p_{1/2}$): radial distributions of magnetic multipole moments $\hat{m}^{[2n]}, n \in [1, 7]$. These distributions are calculated with the default linear dependence thresholds: 10^{-6} and 10^{-8} for the large and small component space. In each box, the upper panel contains the radial distribution, while the lower panel contains error relative to the numerical reference. Note that each box has different scales. The percentages in the upper right corner of each box are the relative errors of the transition moments, i.e. $|\frac{T_{bas}-T_{num}}{T_{num}}|\times 100\%$.

the kinetic balance condition is not met (see Section 2.4.2). In radial form, a kinetically balanced basis assumes the form[90]

$$R^S \propto \begin{cases} \sqrt{2\ell+3}R_{\alpha,\ell^L+1} - 2\sqrt{2\ell+1}R_{\alpha,\ell^L-1} & \text{for } \kappa^L = \ell^L > 0 \\ R_{\alpha,\ell^L+1} & \text{for } \kappa^L = -(\ell^L+1) < 0, \end{cases} \tag{D.3}$$

As an example, the small component $\ell^S = 1$ can be generated either from $\ell^L = 0$ or $\ell^L = 2$, where the latter function is to be used for $p_{1/2}$ and the former for $p_{3/2}$. In the atomic case, the 2-component basis functions do not mix since they have different angular parts, corresponding to $\kappa^S = +1$ and $\kappa^S = -2$, respectively.

However, in the DIRAC code, a scalar basis is employed

$$G_{\alpha\ell m} = R_{\alpha\ell}(r)Y_{\ell m}(\theta, \phi), \tag{D.4}$$

Small component basis functions with radial parts corresponding to both forms of Eqn. (D.3) are generated, hence adhering to kinetic balance. However, now, in the case of e.g. $\ell^S = 1$, basis functions can contribute to both $p_{1/2}$ and $p_{3/2}$, hence possibly amplifying linear dependencies.

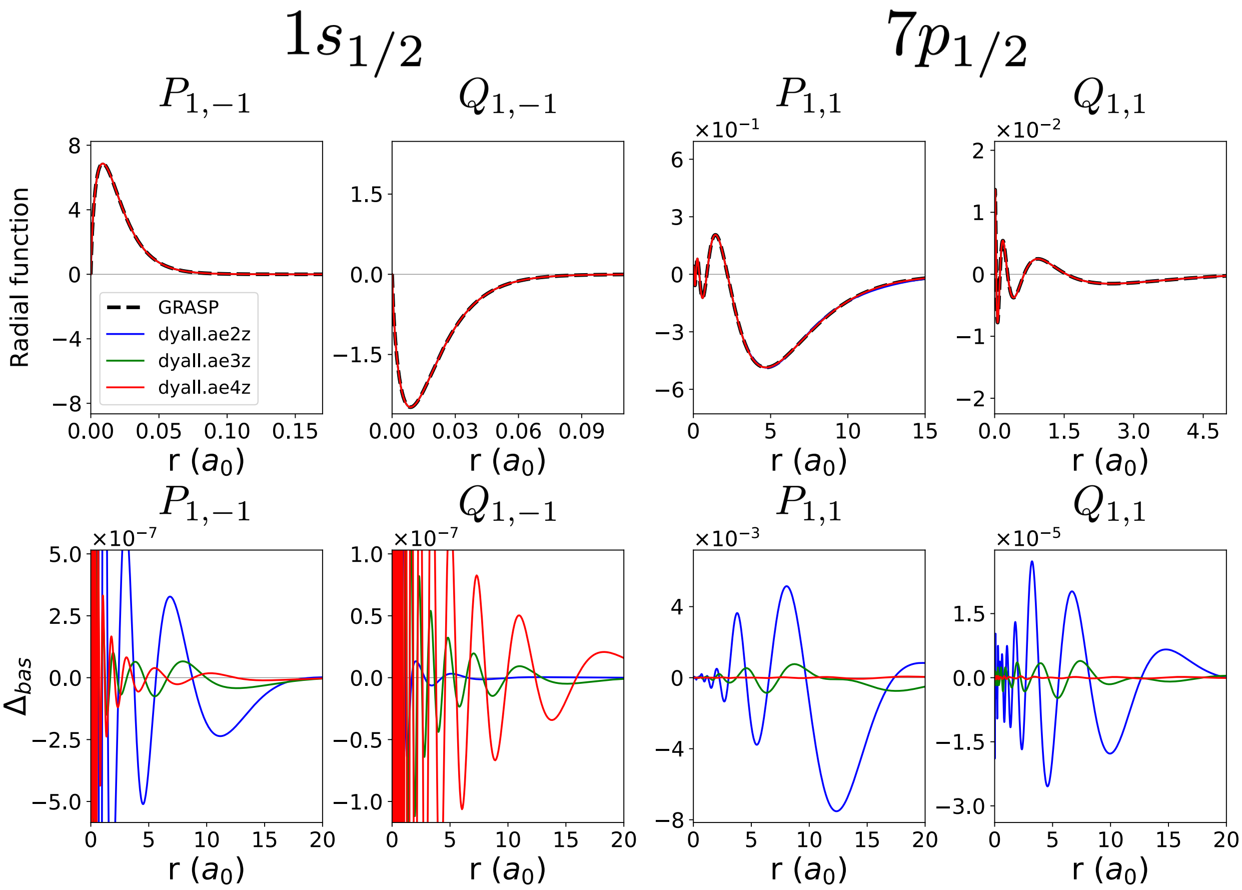

Figure D.2: Radial functions of the large and small component of the $1s_{1/2}$ $(\langle r \rangle = 0.01454\, a_0)$*and* $7p_{1/2}$ *orbital (top row) and their deviations from the numerical reference (bottom row). These orbitals were taken from the radium atom with [Ra]*$1s_{1/2}^{-1}7p_{1/2}^{1}$ *configuration. The basis set orbitals were calculated at the 4c-HF level using* DIRAC*, while the numerical reference was calculated with GRASP. These calculations where carried out using the default linear dependence threshold:* 10^{-6} *and* 10^{-8} *for the large and small component space. Note that the scaling is different for each individual box and that the error curves are plotted in a different range than the radial functions.*

D.2 Augmented Basis Sets

In Section 4.3, I have investigated the absolute basis set convergence of the full interaction operator and the various multipole moments. In general, we have observed that the high-order multipole moments require at least the dyall.ae4z basis set. However, compared to the dyall.ae2z basis set, the dyall.ae4z basis contains additional tight functions, in addition to functions of higher orbital angular momentum, that may not contribute to the high-order multipole moments. Therefore, I investigated the effects of augmenting the dyall.ae2z basis set, such that a better balance could be found between accuracy and basis set size. I have employed two schemes to construct a new basis set:

I Adding diffuse functions to the dyall.ae2z basis set in an even-tempered fashion.

II Replacing the diffuse functions of the dyall.ae2z basis set with the diffuse functions of the larger basis sets. This scheme is inspired by recent work of Jensen and coworkers[219] in which they augmented the cc-pVnZ basis set with the core polarization functions of the cc-pCV(n+1)Z basis set.

In Table D.1, the exponents and the shell of the augmentation functions from Scheme I are depicted. Because the dyall.aeXz basis sets are constructed from uncontracted functions, there is no need to give contraction coefficients in Table D.1. To generate the augmentation functions, the ratio was taken of the two most diffuse exponents. The exponents of the augmentation functions are obtained by multiplying an integer multiple of this ratio with the most diffuse exponent. Table D.2 summarizes the composition of the basis sets from Scheme II. These basis sets are constructed by replacing the N most diffuse functions from the dyall.ae2z basis set with the M most diffuse functions of the dyall.ae3z or dyall.ae4z basis set. Accordingly, these basis sets are named ae2z+dae3z and ae2z+dae4z, respectively. In the construction of these bases, M is always chosen larger than N, hence creating a larger basis set than the original. However, there remains a certain degree of arbitrariness in the construction of the basis sets in Scheme II, because there is not a general method to decide how many functions to remove and introduce. Jensen and coworkers did not face this problem, because the cc-pcVnZ basis sets are constructed by introducing core-polarization functions to the cc-pVnZ basis set. Therefore, the augmentation of the cc-pVnZ basis set with the core polarization functions of the cc-pCV(n+1)Z basis set is unambiguous.

Table D.1: Exponents of the augmentation functions used for the basis sets of Scheme I. The letters s and p denote the shell of the augmentation functions. Numbers in parentheses are exponents of 10.

	s_1	s_2	s_3	p_1	p_2	p_3
Exponent	8.672(−3)	3.669(−3)	1.552(−3)	7.304(−3)	2.821(−3)	1.089(−3)

Table D.2: Composition of the hybrid basis sets from Scheme II. The third column summarizes how many diffuse functions from the dyall.ae2z were removed (N), while the fourth column indicates the number of diffuse functions that were added (M) from the dyall.aeXz ($X = 3, 4$) basis set.

Basis	shell	N	M
ae2z+dae3z	s	9	11
	p	8	10
ae2z+dae4z	s	8	12
	p	8	12

To assess the performance of these composite basis sets, I computed the radial distributions of the length representation electric and magnetic transition multipole moments for the $1s_{1/2} \rightarrow 7p_{1/2}$ transition. The results of Scheme I are depicted in Figures D.3 and D.4, respectively. In both figures, the augmented basis sets have similar performance for the first two orders. For $n = 2$ and $n = 3$, the augmented basis sets seem to induce small oscillations with respect to the numerical reference.

At the three highest orders, the augmented basis sets completely fail to capture the shape of the reference due to severe oscillations, despite the use of tight thresholds for linear dependence. It can thus be concluded that the basis sets from Scheme I are not a proper substitute for the dyall.ae3z and dyall.ae4z basis sets.

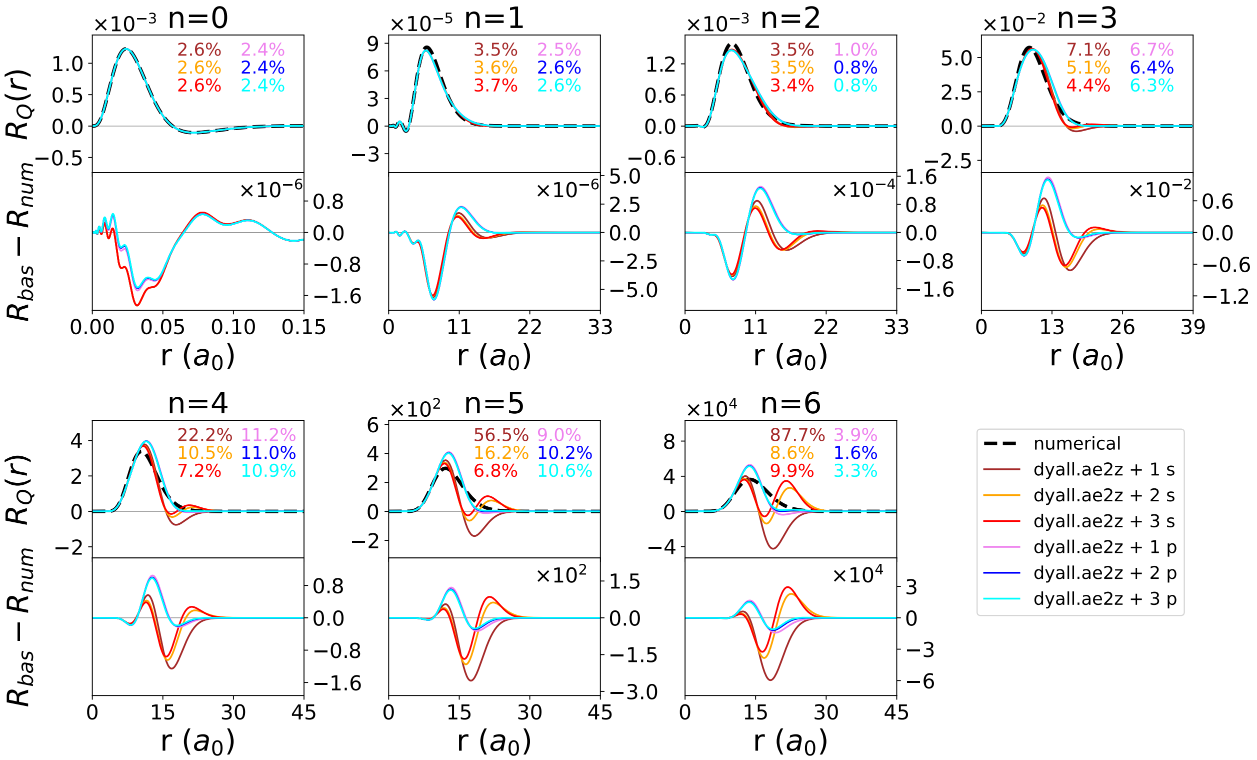

Figure D.3: Scheme I. Radial distributions of electric transition multipole moments in the generalized length representation for the $1s_{1/2} \rightarrow 7p_{1/2}$ transition. The basis sets for these calculations were generated by augmenting the dyall.ae2z basis set with diffuse functions in an even-tempered fashion. The percentages in the upper right corner of each box are the relative errors of the transition moments, i.e. $|\frac{T_{bas}-T_{num}}{T_{num}}|\times 100\%$.

Figures D.5 and D.6 depict the results from Scheme II for the length representation electric and magnetic transition multipole moments, respectively. The basis sets constructed with this scheme provide no obvious improvement over the dyall.ae2z basis sets. Therefore, Scheme II is not a suitable alternative to the dyall.ae3z and dyall.ae4z basis sets.

D.3 H_2S_2

Linear and differential absorption spectra for H_2S_2 are depicted in Figure D.7. Corresponding oscillator strengths are given in Table D.3.

Table D.3: Beyond first-order effects in the isotropically averaged and anisotropic rotatory strengths for the lowest intense valence, L- and K-edge transitions of H_2S_2 for the full semi-classical light–matter interaction operator and in first-order within the Coulomb gauge, computed at the 4c-TD-PBE0 level of theory and the uncontracted aug-pcx-3/aug-pc3 basis set. For the oriented case, $\mathbf{k}(\pi/2, \pi/2)$ for the valence and $L_{2,3}$-edge transitions and $\mathbf{k}(\pi/2, \pi/4)$ for the L_1- and K-edge transitions. For each spectral region, the accumulated (differential) oscillator strength (ac) across the two pairs of transitions (A/B symmetry) is given in the third line. Numbers in parentheses are exponents of 10.

Transition	ΔE (eV)		$f^{\text{full}}_{\text{iso}}$	$f^{(0)}_{\text{iso}}$	$\Delta f^{\text{full}}_{\text{iso}}$	$\Delta f^{[1]}_{\text{iso}}$	$\Delta f^{\text{full}}_{\mathbf{k}}$	$\Delta f^{[1]}_{\mathbf{k}}$
					valence			
1^1B ($n_{\text{S}} \to \sigma^*_{\text{SS}}$)	4.50504		8.6714(-03)	8.6714(-03)	-7.6239(-05)	-7.6238(-05)	-3.4945(-05)	-3.4943(-05)
2^1A ($n_{\text{S}} \to \sigma^*_{\text{SS}}$)	4.65268		3.4838(-03)	3.4838(-03)	5.1763(-05)	5.1762(-05)	4.7569(-05)	4.7567(-05)
		ac	1.2155(-02)	1.2155(-02)	-2.4476(-05)	-2.4476(-05)	1.2625(-05)	1.2624(-05)
					$L_{2,3}$-edge			
$4A$ ($2p_{3/2} \to \sigma^*_{\text{SS}}$)	157.59075		4.5587(-04)	4.5564(-04)	-9.0946(-05)	-9.1176(-05)	-2.0916(-04)	-2.0982(-04)
$4B$ ($2p_{3/2} \to \sigma^*_{\text{SS}}$)	157.59083		5.5139(-04)	5.5160(-04)	9.1630(-05)	9.1861(-05)	2.1009(-04)	2.1076(-04)
		ac	1.0073(-03)	1.0072(-03)	6.8382(-07)	6.8592(-07)	9.3270(-07)	9.4069(-07)
$10A$ ($2p_{1/2} \to \sigma^*_{\text{SS}}$)	158.90894		1.3211(-03)	1.3195(-03)	-2.8191(-04)	-2.8242(-04)	-6.4506(-04)	-6.4652(-04)
$10B$ ($2p_{1/2} \to \sigma^*_{\text{SS}}$)	158.90912		1.5316(-03)	1.5309(-03)	2.8773(-04)	2.8825(-04)	6.5784(-04)	6.5934(-04)
		ac	2.8527(-03)	2.8505(-03)	5.8193(-06)	5.8305(-06)	1.2782(-05)	1.2816(-05)
					L_1-edge			
$4B$ ($2s_{1/2} \to \sigma^*_{\text{SS}}$)	215.99272		3.6930(-02)	3.7070(-02)	-7.2666(-05)	-7.3122(-05)	-1.4390(-03)	-1.4476(-03)
$4A$ ($2s_{1/2} \to \sigma^*_{\text{SS}}$)	215.99487		4.0728(-04)	2.8578(-04)	7.2709(-05)	7.3165(-05)	1.3504(-03)	1.3590(-03)
		ac	3.7337(-02)	3.7356(-02)	4.2890(-08)	4.3175(-08)	-8.8553(-05)	-8.8601(-05)
					K-edge			
$4B$ ($1s_{1/2} \to \sigma^*_{\text{SS}}$)	2427.40755		7.7728(-03)	1.0512(-02)	-7.9246(-05)	-1.6570(-04)	-1.6950(-03)	-3.1637(-03)
$4A$ ($1s_{1/2} \to \sigma^*_{\text{SS}}$)	2427.40769		2.7630(-03)	5.5576(-05)	7.9240(-05)	1.6569(-04)	1.7025(-03)	3.1711(-03)
		ac	1.0536(-02)	1.0568(-02)	-5.3200(-09)	-1.0951(-08)	7.5520(-06)	7.4338(-06)

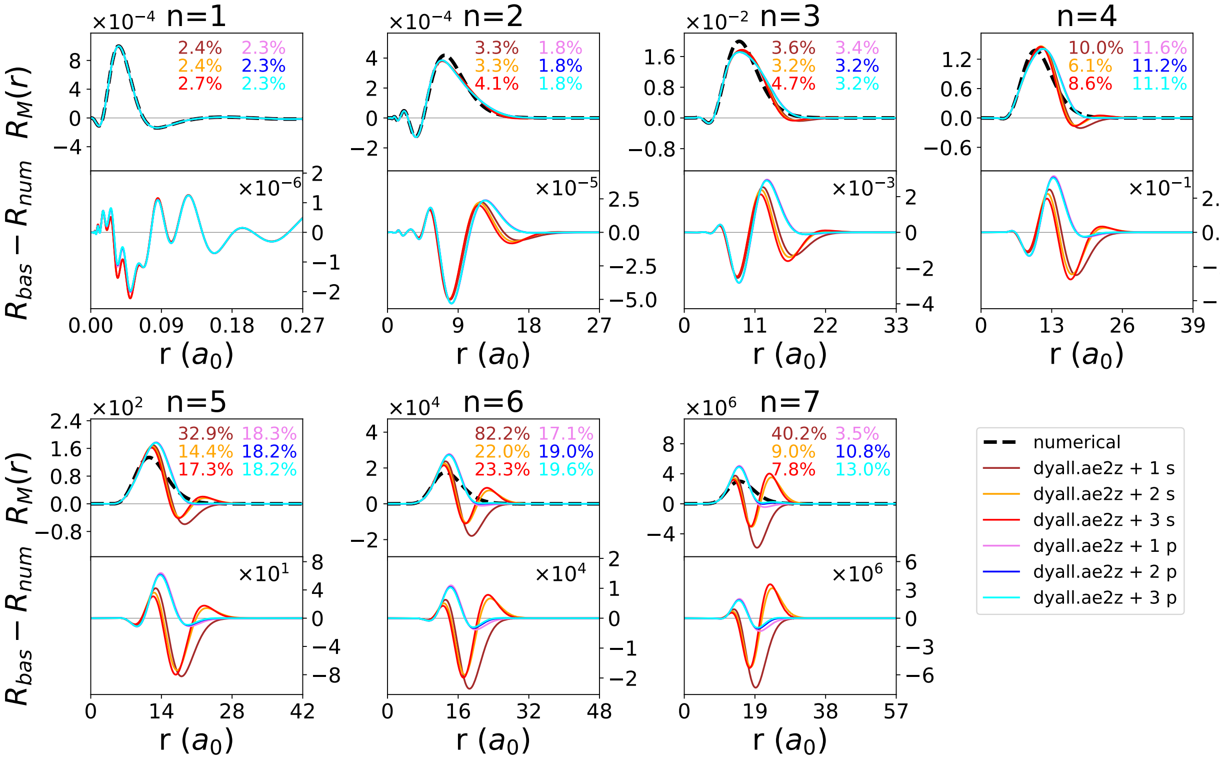

Figure D.4: Scheme I. Radial distributions of magnetic transition multipole moments for the $1s_{1/2} \rightarrow 7p_{1/2}$ *transition. The basis sets were generated by augmenting the dyall.ae2z basis set with diffuse functions in an even-tempered fashion. The percentages in the upper right corner of each box are the relative errors of the transition moments, i.e.* $|\frac{T_{bas}-T_{num}}{T_{num}}|\times 100\%$.

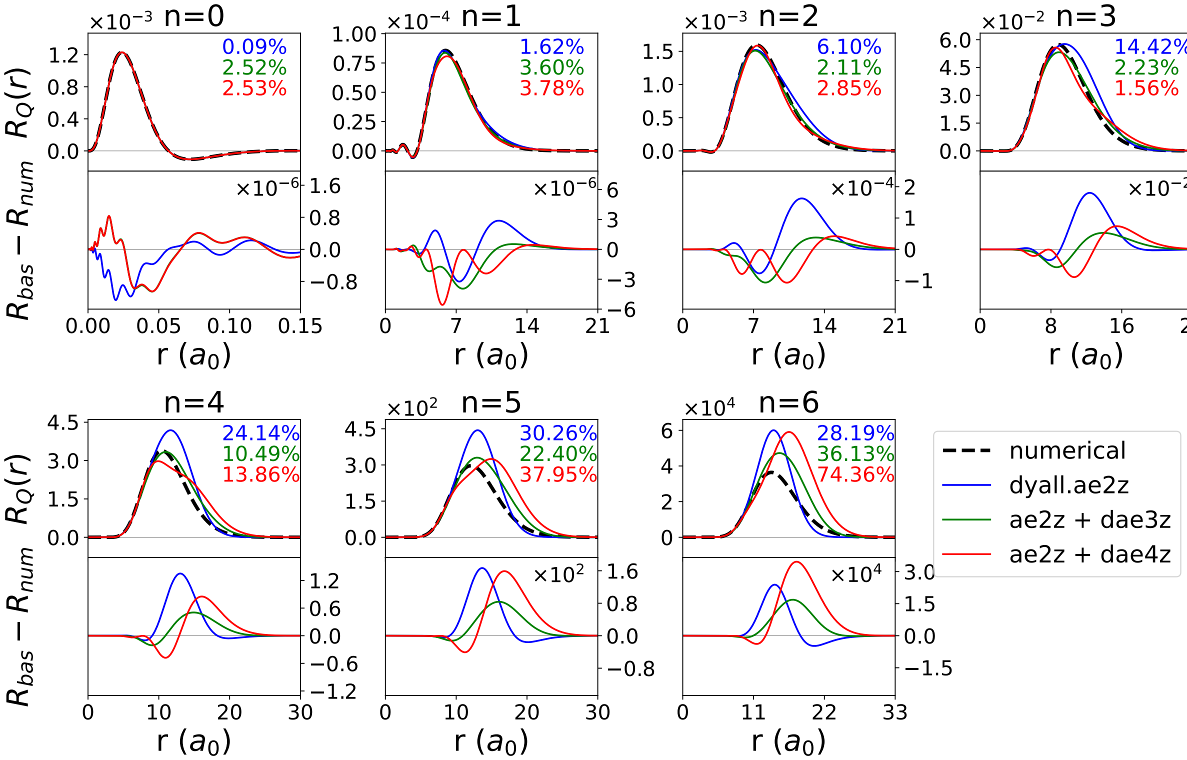

Figure D.5: Scheme II. Radial distributions of electric transition multipole moments in the generalized length representation for the $1s_{1/2} \rightarrow 7p_{1/2}$ *transition. The basis sets for these calculations were generated by augmenting the dyall.ae2z basis set with the diffuse functions of either the dyall.ae3z or dyall.ae4z basis sets. The percentages in the upper right corner of each box are the relative errors of the transition moments, i.e.* $|\frac{T_{bas}-T_{num}}{T_{num}}|\times 100\%$.

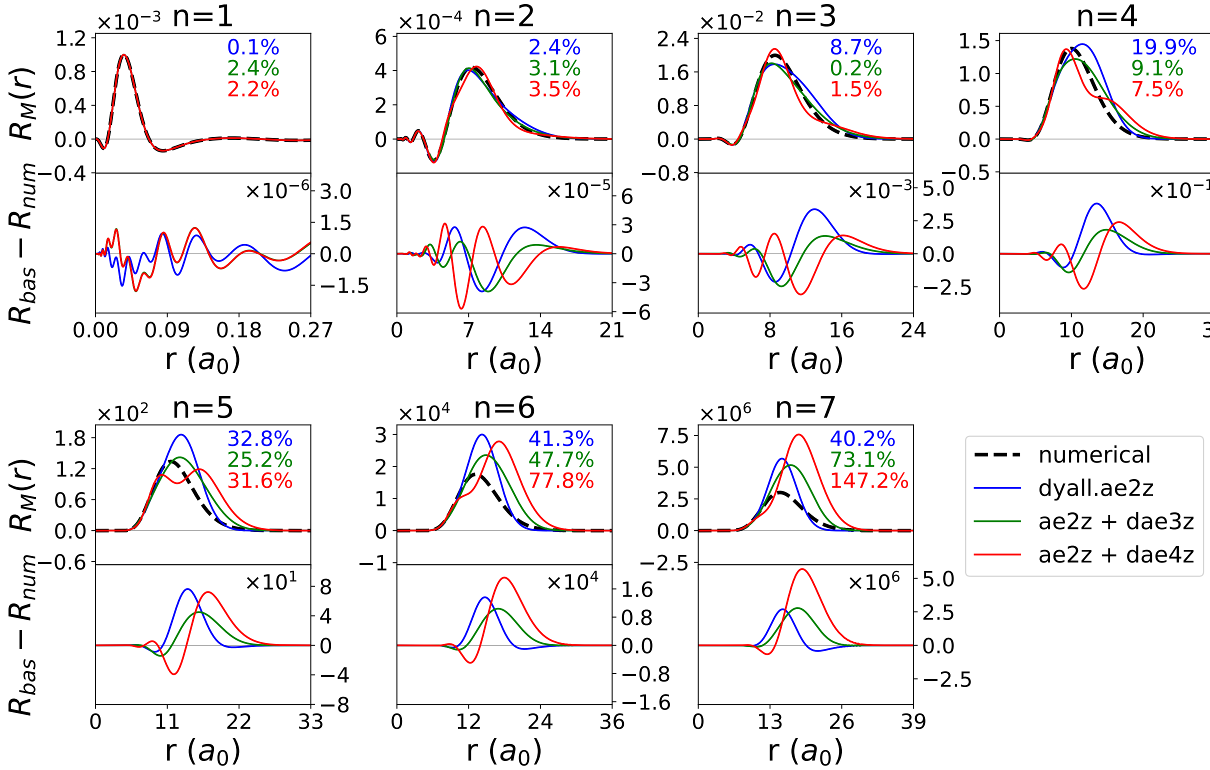

Figure D.6: Scheme II. Radial distributions of magnetic transition multipole moments for the $1s_{1/2} \to 7p_{1/2}$ transition. The basis sets for these calculations were generated by augmenting the dyall.ae2z basis set with the diffuse functions of either the dyall.ae3z or dyall.ae4z basis sets. The percentages in the upper right corner of each box are the relative errors of the transition moments, i.e. $|\frac{T_{bas}-T_{num}}{T_{num}}|\times 100\%$.

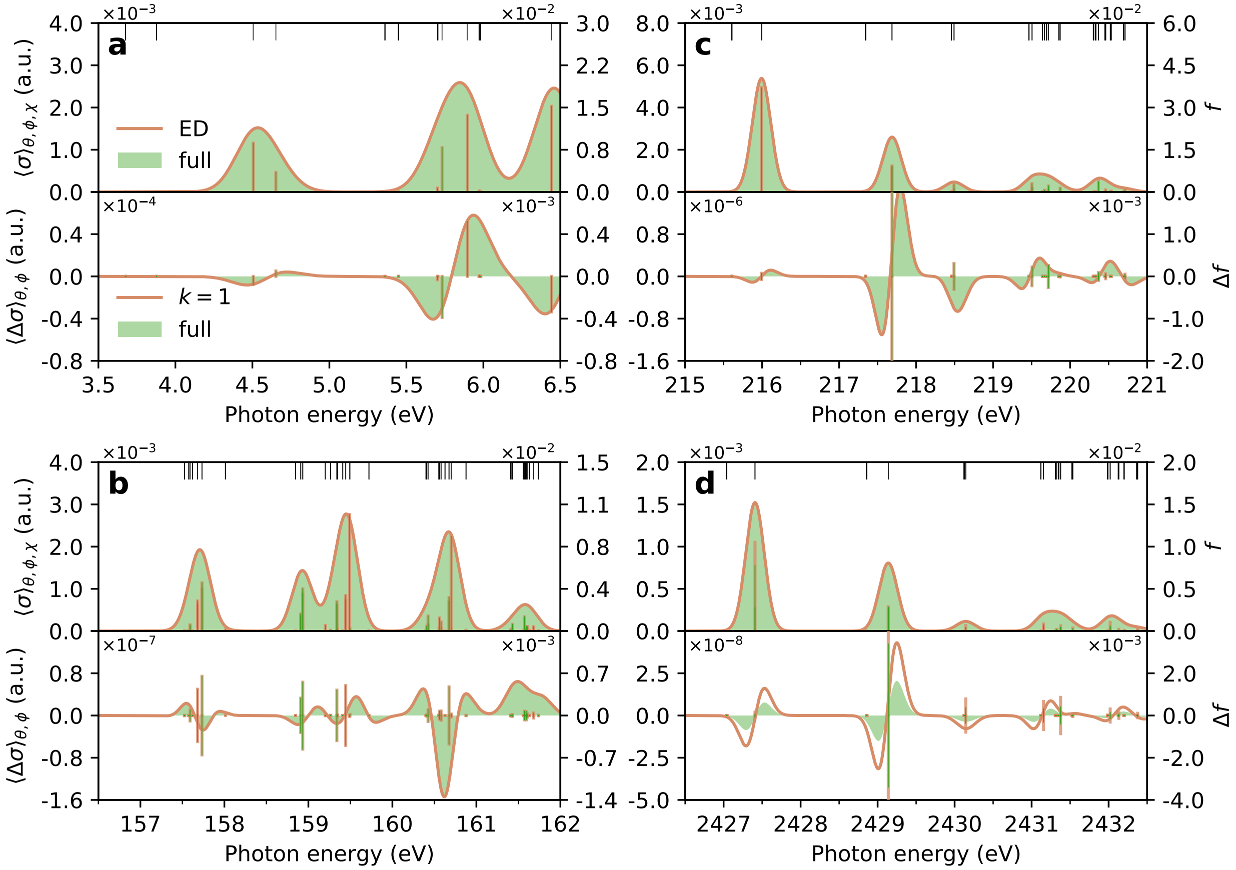

Figure D.7: Isotropic linear (top) and differential (bottom) absorption spectra of H_2S_2: (a) valence, (b) $L_{2,3}$-edge, (c) L_1-edge and (d) K-edge spectra using the full interaction operator (green shadings) or the lowest non-vanishing generalized velocity representation (orange lines). Left axes correspond to (differential) absorption cross-sections, whereas (differential) oscillator strengths are shown on the right axes. Black sticks indicate the location of all computed transitions. The stick spectra were convolved with a Gaussian lineshape with FWHM of 0.4 eV. No shifts have been applied to the theoretical spectra.

D.4 Analysis of the Rotational Strength Tensor

Elements of the rotational strength tensor of Eqn. (3.152) of the main text, using the Einstein summation convention, can be split into the electric-dipole/electric-quadrupole (E1–E2) and electric-dipole/magnetic-dipole (E1–M1) contributions

$$R_{ij}^{\text{E1–E2}} = \frac{4m_e\omega^2}{\hbar c e^2}\varepsilon_{ipq}\langle f|\hat{\mathcal{Q}}_{j;p}^{[2]}|i\rangle\langle f|\hat{\mathcal{Q}}_{q}^{[1]}|i\rangle \tag{D.5}$$

$$R_{ij}^{\text{E1–M1}} = \frac{4m_e\omega^2}{\hbar c e^2}\left(\delta_{ij}\langle f|-\frac{i}{\omega}\hat{m}_q^{[1]}|i\rangle\langle f|\hat{\mathcal{Q}}_{q}^{[1]}|i\rangle - \langle f|-\frac{i}{\omega}\hat{m}_i^{[1]}|i\rangle\langle f|\hat{\mathcal{Q}}_{j}^{[1]}|i\rangle\right) \tag{D.6}$$

and analyzed in terms of symmetry. The target molecules, in the chosen geometries, have C_2 symmetry. Fixing the origin at the center of mass we find that for excitations of irrep A the rotational strength tensor has the structure

$$R_A^{\text{E1–E2}} = \frac{4m_e\omega^2}{e^2\hbar c}\begin{bmatrix} \frac{1}{2}\mathcal{Q}_{xy}^{[2]}\mathcal{Q}_z^{[1]} & \frac{1}{2}\mathcal{Q}_{yy}^{[2]}\mathcal{Q}_z^{[1]} & 0 \\ -\frac{1}{2}\mathcal{Q}_{xx}^{[2]}\mathcal{Q}_z^{[1]} & -\frac{1}{2}\mathcal{Q}_{yx}^{[2]}\mathcal{Q}_z^{[1]} & 0 \\ 0 & 0 & 0 \end{bmatrix} \tag{D.7}$$

$$R_A^{\text{E1–M1}} = \frac{4m_e\omega^2}{e^2\hbar c}\begin{bmatrix} -\frac{i}{\omega}m_z^{[1]}\mathcal{Q}_z^{[1]} & 0 & 0 \\ 0 & -\frac{i}{\omega}m_z^{[1]}\mathcal{Q}_z^{[1]} & 0 \\ 0 & 0 & 0 \end{bmatrix} \tag{D.8}$$

where a shorthand notation is used for transition moments, e.g. $\mathcal{Q}_{xy}^{[2]} = \langle f|\hat{\mathcal{Q}}_{xy}^{[2]}|i\rangle$. For excitations of B symmetry the corresponding matrices are

$$R_B^{\text{E1–E2}} = \frac{4m_e\omega^2}{e^2\hbar c}\begin{bmatrix} -\frac{1}{2}\mathcal{Q}_{xz}^{[2]}\hat{\mathcal{Q}}_y^{[1]} & -\frac{1}{2}\mathcal{Q}_{yz}^{[2]}\mathcal{Q}_y^{[1]} & 0 \\ \frac{1}{2}\mathcal{Q}_{xz}^{[2]}\mathcal{Q}_x^{[1]} & \frac{1}{2}\mathcal{Q}_{yz}^{[2]}\mathcal{Q}_x^{[1]} & 0 \\ 0 & 0 & \frac{1}{2}\mathcal{Q}_{zx}^{[2]}\mathcal{Q}_y^{[1]} - \frac{1}{2}\mathcal{Q}_{zy}^{[2]}\mathcal{Q}_x^{[1]} \end{bmatrix} \tag{D.9}$$

$$R_B^{\text{E1–M1}} = \frac{4m_e\omega^2}{e^2\hbar c}\begin{bmatrix} -\frac{i}{\omega}m_y^{[1]}\mathcal{Q}_y^{[1]} & \frac{i}{\omega}m_x^{[1]}\mathcal{Q}_y^{[1]} & 0 \\ \frac{i}{\omega}m_y^{[1]}\hat{\mathcal{Q}}_x^{[1]} & -\frac{i}{\omega}m_x^{[1]}\mathcal{Q}_x^{[1]} & 0 \\ 0 & 0 & -\frac{i}{\omega}m_x^{[1]}\mathcal{Q}_x^{[1]} - \frac{i}{\omega}m_y^{[1]}\mathcal{Q}_y^{[1]} \end{bmatrix}. \tag{D.10}$$

It should be noted that in both irreps the elements $R_{xz}^{[1]}$, $R_{yz}^{[1]}$, $R_{zx}^{[1]}$, $R_{zy}^{[1]}$ are strictly zero by symmetry; in the A irrep elements $R_{zz}^{[1]}$ are zero as well.

Table D.4: Rotational strength tensors used for the generation of first-order contributions for excitations of A symmetry in Figure 4.18 of the main text. Left: total first-order rotatory strength tensor; middle: E1–E2 contribution and right: E1–M1 contribution, as obtained with the gauge origin in the COM. Numbers in parentheses are exponents of 10.

A valence: total				E1–E2				E1–M1		
1.077(-04)	-1.834(-05)	0.000		3.008(-05)	-1.834(-05)	0.000		7.764(-05)	0.000	0.000
7.175(-06)	4.757(-05)	0.000	=	7.175(-06)	-3.008(-05)	0.000	+	0.000	7.764(-05)	0.000
0.000	0.000	0.000		0.000	0.000	0.000		0.000	0.000	0.000

A L_3-edge										
-6.371(-05)	-1.402(-06)	0.000		7.306(-05)	-1.402(-06)	0.000		-1.368(-04)	0.000	0.000
-9.509(-06)	-2.098(-04)	0.000	=	-9.509(-06)	-7.306(-05)	0.000	+	0.000	-1.368(-04)	0.000
0.000	0.000	0.000		0.000	0.000	0.000		0.000	0.000	0.000

A L_2-edge										
-2.007(-04)	9.546(-06)	0.000		2.229(-04)	9.546(-06)	0.000		-4.236(-04)	0.000	0.000
-3.550(-05)	-6.465(-04)	0.000	=	-3.550(-05)	-2.229(-04)	0.000	+	0.000	-4.236(-04)	0.000
0.000	0.000	0.000		0.000	0.000	0.000		0.000	0.000	0.000

A L_1-edge										
-1.243(-05)	2.264(-03)	0.000		-1.222(-04)	2.264(-03)	0.000		1.097(-04)	0.000	0.000
2.343(-04)	2.319(-04)	0.000	=	2.343(-04)	1.222(-04)	0.000	+	0.000	1.097(-04)	0.000
0.000	0.000	0.000		0.000	0.000	0.000		0.000	0.000	0.000

A K-edge										
8.743(-07)	5.802(-03)	0.000		-2.477(-04)	5.802(-03)	0.000		2.485(-04)	0.000	0.000
4.321(-05)	4.962(-04)	0.000	=	4.321(-05)	2.477(-04)	0.000	+	0.000	2.485(-04)	0.000
0.000	0.000	0.000		0.000	0.000	0.000		0.000	0.000	0.000

Table D.5: Rotational strength tensors used for the generation of first-order contributions for excitations of B symmetry in Figure 4.18 of the main text. Left: total first-order rotatory strength tensor; middle: E1–E2 contribution and right: E1–M1 contribution, as obtained with the gauge origin in the COM. Numbers in parentheses are exponents of 10.

B valence: total				E1–E2				E1–M1		
-6.159(-05)	4.502(-05)	0.000		-6.159(-05)	4.502(-05)	0.000		-5.382(-05)	7.800(-05)	0.000
4.780(-05)	-3.494(-05)	0.000	=	4.780(-05)	-3.494(-05)	0.000	+	4.177(-05)	-6.054(-05)	0.000
0.000	0.000	-1.322(-04)		0.000	0.000	-1.322(-04)		0.000	0.000	-1.144(-04)

B L_3-edge										
-1.124(-08)	-2.632(-06)	0.000		4.131(-08)	-9.106(-07)	0.000		-5.255(-08)	-1.721(-06)	0.000
9.001(-07)	2.108(-04)	0.000	=	-3.308(-06)	7.292(-05)	0.000	+	4.208(-06)	1.378(-04)	0.000
0.000	0.000	6.484(-05)		0.000	0.000	-7.296(-05)		0.000	0.000	1.378(-04)

B L_2-edge										
-5.708(-08)	-1.250(-05)	0.000		1.490(-07)	-4.298(-06)	0.000		-2.060(-07)	-8.199(-06)	0.000
3.011(-06)	6.593(-04)	0.000	=	-7.859(-06)	2.268(-04)	0.000	+	1.087(-05)	4.326(-04)	0.000
0.000	0.000	2.055(-04)		0.000	0.000	-2.269(-04)		0.000	0.000	4.324(-04)

B L_1-edge										
-3.269(-04)	-2.307(-03)	0.000		-3.622(-04)	-8.438(-04)	0.000		3.528(-05)	-1.464(-03)	0.000
-3.238(-05)	-2.285(-04)	0.000	=	-3.588(-05)	-8.358(-05)	0.000	+	3.494(-06)	-1.450(-04)	0.000
0.000	0.000	3.361(-04)		0.000	0.000	4.458(-04)		0.000	0.000	-1.097(-04)

B K-edge										
2.552(-05)	-5.859(-03)	0.000		-7.107(-05)	-1.786(-03)	0.000		9.660(-05)	-4.073(-03)	0.000
2.163(-06)	-4.965(-04)	0.000	=	-6.023(-06)	-1.513(-04)	0.000	+	8.186(-06)	-3.452(-04)	0.000
0.000	0.000	-2.617(-05)		0.000	0.000	2.224(-04)		0.000	0.000	-2.486(-04)

Appendix E

Résumé en Français

Introduction

Au fil des siècles, l'évolution de la chimie se caractérise par l'émergence de sous-disciplines distinctes dont les frontières se sont progressivement estompées au fil du temps. Un exemple notable est l'avènement de la chimie organique au XIXe siècle. Au début, ce domaine était principalement préoccupé par la chimie de la matière vivante, tandis que son cousin plus développé et plus ancien, la chimie inorganique, était plutôt centré sur les sels inorganiques et les acides minéraux. Pour cette raison, une division dichotomique de la chimie prévalait, selon laquelle la chimie organique repose sur des principes fondamentalement différents de la chimie inorganique. Cependant, une découverte clé qui a remis en question ce paradigme est la synthèse de l'urée à partir de matière inorganique par Wöhler en 1828. Associée aux avancées ultérieures de la théorie moléculaire, l'unification des deux domaines était inévitable. Les chimistes au cœur de ces développements peuvent être comparés à des détectives, déduisant méticuleusement les caractéristiques structurelles à l'aide de ressources minimalistes, telles que l'analyse de la décomposition et la réactivité chimique.

Dans la chimie moderne, la résolution de la structure moléculaire est devenue une tâche routinière grâce à l'avènement de la spectroscopie. La spectroscopie mesure généralement les interactions lumière-matière en termes d'absorption, d'émission ou de diffusion en fonction de la longueur d'onde. Cependant, l'utilité de la spectroscopie va au-delà de la simple caractérisation structurale, car elle sert également de technique pour évaluer les propriétés moléculaires, dont la nature dépend généralement de la longueur d'onde de la lumière. Par exemple, dans la plage d'énergie inférieure du spectre, c'est-à-dire les micro-ondes et l'infrarouge (IR), le rayonnement induit des rotations et des vibrations moléculaires, tandis que le régime UV-Vis est associé à des excitations électroniques. En réduisant davantage la longueur d'onde, on obtient des rayons X, dont l'application en spectroscopie moléculaire a été pionnière grâce à de Broglie, Siegbahn et Stenström. Les rayons X ont une énergie suffisante pour révéler la structure des couches d´électrons internes, au coeur des atomes et qui ne sont pas autrement affectés par le rayonnement UV-Vis. De plus, au-dessus d'un certain seuil, les rayons X peuvent même ioniser le système, ce qui se manifeste par des sauts verticaux soudains dans le spectre d'absorption. Les seuils constituent un outil particulièrement utile dans l'analyse structurale, car ils sont centrés sur les énergies d'ionisation des électrons internes, étant ainsi spécifiques aux éléments et bien séparés.

Cependant, les caractéristiques structurales les plus intéressantes ne sont pas facilement déduites des seuils seuls, mais plutôt à partir de leurs régions voisines. Dans la région au-delà du seuil, on peut observer des oscillations subtiles, induits par des interférences de photoélectrons qui sont rétrodiffusés par leur environnement local. La technique de mesure de ces oscillations, également appelée structure fine d'absorption des rayons X étendue (EXAFS), nous fournit des informations sur la structure cristalline de l'échantillon. Cependant, cette thèse sera consacrée plutôt au spectroscopie de structure près du front d´absorption de rayons X, qui peut être sondé à l'aide de la structure fine d'absorption des rayons X en bordure (NEXAFS). Dans cette plage d'énergie, les rayons X ont encore suffisamment d'énergie pour interagir avec les électrons internes, bien qu'ils soient excités vers des niveaux liés et vides. Étant donné que les orbitales internes tendent à être localisées autour des noyaux, le NEXAFS fournit des informations spécifiques au site sur le système à l'étude, formant ainsi un complément à la spectroscopie UV-Vis, qui implique des excitations de valence qui sont délocalisées sur toute la molécule. Dans sa forme la plus simple, le NEXAFS est basé sur la lumière polarisée linéairement, bien que cette procédure ait un point faible critique : elle ne distingue pas entre les membres d'une paire énantiomère. Pour faire cette distinction, il faut mesurer son dichroïsme circulaire électronique (ECD), qui est défini comme la différence d'absorption entre la lumière polarisée circulairement à gauche et à droite. En général, cette quantité est mesurée dans la plage UV-Vis, bien qu'elle se manifeste également dans la gamme des rayons X, où elle est appelée dichroïsme circulaire naturel des rayons X (XNCD) par convention. Le XNCD présente les mêmes avantages que le NEXAFS ordinaire en ce sens qu'il fournit plus d'informations locales par rapport à l'ECD dans la plage UV-Vis.

Cependant, la création de lumière polarisée circulairement à des fréquences élevées peut être assez difficile, car les rayons X sont notoirement difficiles à manipuler à l'aide d'éléments optiques conventionnels. De nos jours, cependant, cet exploit technique peut être réalisé de manière routinière grâce aux récents développements de la radiation synchrotron. Initialement produit en tant que sous-produit de la physique des particules, ces dispositifs sont des accélérateurs de particules circulaires qui utilisent des champs magnétiques pour contraindre les électrons à des orbites circulaires dans leur intérieur creux. Les rayons X peuvent être extraits de ces électrons en appliquant un champ magnétique alternatif supplémentaire qui est perpendiculaire à la trajectoire des électrons. Les oscillations induites des électrons donnent naissance à une source cohérente de rayons X qui permet un contrôle complet de la polarisation. Cela rend la radiation synchrotron particulièrement utile pour effectuer des expériences NEXAFS. D'autres techniques alternatives qui ont gagné en popularité sont basées sur les lasers à électrons libres ou la génération d'harmoniques élevées.

Même si de nombreuses informations utiles peuvent être extraites de ces expériences seules, l'attribution et l'interprétation des spectres nécessitent des apports de la théorie et de la simulation. Par exemple, la stéréochimie absolue des molécules chirales ne peut être déterminée que lorsque le XNCD est comparé à des résultats équivalents issus de simulations chimiques quantiques. De plus, en conjonction avec la théorie, le NEXAFS peut être utilisé pour déterminer l'état d'oxydation et l'environnement de coordination local des complexes métalliques. Par conséquent, les avancées dans les techniques expérimentales doivent aller de pair avec le développement de la théorie et de ses mises en œuvre.

Pour simuler la spectroscopie des rayons X, il semble naturel d'appliquer la théorie bien établie développée pour le régime UV-Vis. Cependant, une grande disparité avec l'expérience est observée si l'on transfère sans réflexion cette théorie au domaine des rayons X. Pour corriger cette disparité, il est donc nécessaire d'inclure plusieurs effets au-delà de ce qui est généralement requis pour la spectroscopie UV-Vis. Tout d'abord, puisque les effets relativistes sont générés dans la région du coeur, ils doivent être pris en compte dans la simulation des excitations du coeur même pour des éléments assez légers. Deuxièmement, après l'excitation de l'électron du coeur, le système est laissé avec un trou qui réduit l´écrántage de la charge nucléaire. En conséquence, la charge nucléaire effective augmente, ce qui équivaut à une stabilisation supplémentaire de l'état excité, appelée relaxation du trou du coeur. Troisièmement, dans le régime UV-Vis, la longueur d'onde est considérablement plus grande que l'étendue de la molécule, ce qui suggère que les champs semblent uniformes du point de vue de la molécule. En raison de cette différence d'échelle, l'interaction lumière-matière peut être effectivement décrite par les premiers termes d'une expansion multipolaire, ce qui donne l'approximation électrique dipolaire pour la lumière polarisée linéaire et la force de rotation pour le dichroïsme circulaire, cette dernière dépendant à la fois du moment dipolaire électrique et magnétique. Dans les deux cas, seules les contributions dipolaires doivent être prises en compte. Il semble donc naturel d'utiliser l'approximation dipolaire comme terme générique pour désigner ces deux schémas. Dans le régime des rayons X, cependant, l'approximation dipolaire est remise en question.

Dans cette thèse, j´étudiais si l'approximation dipolaire est valable dans la simulation de la spectroscopie d'absorption des rayons X.

En général, il existe deux approches possibles pour inclure les effets non dipolaires : soit l'interaction lumière-matière semi-classique est traitée de manière exacte, soit l'expansion multipolaire est tronquée au-delà de l'ordre zéro. Cependant, les expansions tronquées introduisent inévitablement une dépendance à l'origine de jauge dans le calcul, un problème que Bernadotte et al. ont résolu en développant la section efficace d'absorption plutôt que l'interaction lumière-matière elle-même. De plus, des schémas de ce type peuvent également donner de sections efficaces d'absorption négatives et de divergences apparentes, qui sont, en principe, toutes deux atténuées si suffisamment de termes sont inclus dans l'expansion multipolaire, bien que le dernier problème puisse nécessiter une quantité déraisonnablement de termes. Il existe plusieurs autres exemples d'implémentations, en plus de celles des références susmentionnées, qui sont capables de calculer les intensités d'absorption en utilisant soit une interaction tronquée, soit l'interaction complète. Certains de ces schémas ont même été étendus pour modéliser des phénomènes plus complexes tels que le dichroïsme circulaire magnétique des rayons X, la diffusion des rayons X ou l'absorption transitoire. Cependant, toutes ces implémentations ont une plage spectrale d'application limitée, car elles sont dérivées d'un cadre non relativiste, ayant au plus des corrections relativistes perturbatives. Dans le régime des rayons X durs, où les effets non dipolaires sont les plus pertinents, la lumière excite généralement les orbitales du coeur des éléments lourds, ce qui nécessite un traitement entièrement relativiste. Pour répondre à la question principale d'une manière qui s'applique également au régime des rayons X durs, il est donc impératif de travailler dans un cadre relativiste.

Dans cette thèse, je présenterai une implémentation pour simuler les interactions lumière-matière en utilisant à la fois l'interaction complète et tronquée dans un cadre relativiste à quatre composants. Cette implémentation fait partie de Dirac, un code de chimie quantique spécialisé dans les calculs moléculaires relativistes à deux ou quatre composants. Cependant, il convient de noter que même ce niveau de théorie a une portée limitée. À des échelles d'énergie extrêmes, telles que celles rencontrées dans les cations fortement chargés, les effets de l'électrodynamique quantique peuvent jouer un rôle dans les spectres d'absorption des rayons X. De plus, je n'ai pas inclus les effets du trou du coeur, dont l'importance a été évoquée dans le paragraphe précédent. Cependant, l'inclusion de ces effets dépasse le cadre de cette thèse et ne sera pas poursuivie plus avant.

E.1 Chapitre 1

Dans ce chapitre, je vais illustrer les méthodes de chimie quantique conventionnelles pour calculer les spectres d'absorption UV-Vis. Les idées et dérivations exprimées dans ce chapitre suivent généralement le livre *Principes et Pratiques des Propriétés Moléculaires*, auquel il convient de se référer pour plus de détails. Pour classer le type d'approximations généralement effectuées dans la simulation de la spectroscopie UV-Vis, je vais diviser le calcul des intensités d'absorption en trois composantes principales : le calcul de l'état fondamental, le calcul de l'état excité et le traitement de l'interaction lumière-matière.

Pour simplifier le calcul de l'état fondamental, des approximations peuvent être appliquées soit au niveau de la méthode de la structure électronique, soit au niveau de l´Hamiltonien. Par exemple, les orbitales de valence généralement impliquées en spectroscopie UV-Vis sont les moins sensibles aux effets relativistes, suggérant qu'un Hamiltonien non relativiste, tel que l'Hamiltonien de Schrödinger ou l'Hamiltonien de Pauli, est généralement suffisant. Une fois que l´Hamiltonien à utiliser a été décidé, il faut choisir une méthode de structure électronique pour approximer la complexité de la fonction d'onde à plusieurs corps. Il existe une pléthore de méthodes de structure électronique parmi lesquelles choisir, chacune ayant un rapport coût-précision distinct. Par exemple, l'état fondamental peut être obtenu de manière plus fiable à l'aide de méthodes de fonction d'onde telles que le coupled cluster (CC) ou l'interaction de configuration (CI), bien que cela implique des coûts de calcul élevés. Les coûts de calcul sont moindres pour la méthode de Hartree-Fock (HF), bien que sa précision soit plutôt faible. Un rapport coût-précision amélioré peut être obtenu en utilisant la théorie de la fonctionnelle de la densité (DFT), qui se situe généralement entre un calcul HF et peut même approcher la précision des méthodes de fonction d'onde dans certains cas. Dans cette thèse, le HF et la DFT seront les méthodes de choix pour décrire la fonction d'onde de l'état fondamental. Par la suite, le terme "méthodes auto-cohérentes" sera utilisé pour englober les deux approches.

En utilisant la fonction d'onde de l'état fondamental comme point de départ, diverses méthodes sont disponibles pour traiter les états excités, comme cela sera plus clair dans ce chapitre. Pour les états exacts et les fonctions d'onde CI, cette procédure est plutôt simple, car les états excités peuvent être obtenus directement par diagonalisation du Hamiltonien. Suivre cette approche au niveau de la SCF est plus fastidieux, car HF et DFT sont essentiellement des théories de l'état fondamental. Cependant, le calcul explicite des états excités peut être évité en appliquant la théorie de la réponse linéaire. Dans ce chapitre, il sera démontré comment les pôles et les résidus des fonctions de réponse linéaire peuvent être reliés aux énergies d'excitation et aux moments de transition, qui à leur tour peuvent être utilisés pour obtenir les intensités d'absorption. Un inconvénient majeur de cette méthode est qu'elle ne tient pas compte des effets des trous du coeur, ce qui ne devrait pas avoir beaucoup d'importance dans le régime UV-Vis.

Il reste donc à trouver une description adaptée de l'interaction lumière-matière. Dans ce travail, une description semi-classique sera poursuivie, bien qu'il existe des exemples dans la littérature où la nature quantique de la lumière est prise en compte. Une caractéristique particulière du régime UV-Vis est la grande taille de la longueur d'onde par rapport au système moléculaire, ce qui permet l'application de l'approximation du dipôle électrique.

Pour mieux comprendre les origines de cette approximation, considérons l'exemple suivant. Supposons que nous voulons modéliser l'absorption de lumière rouge polarisée linéairement ($\lambda =$ 700 nm) par une molécule de benzène. Les champs électromagnétiques décrivant ce type de lumière sont montrés ci-dessous.

$$\mathbf{E}\left(\mathbf{r},t\right) = E_\omega \boldsymbol{\epsilon} \sin\left[\mathbf{k}\cdot\mathbf{r} - \omega t + \delta\right]; \quad \mathbf{B}\left(\mathbf{r},t\right) = \frac{E_\omega}{\omega}\left(\mathbf{k}\times\boldsymbol{\epsilon}\right)\sin\left[\mathbf{k}\cdot\mathbf{r} - \omega t + \delta\right], \tag{E.1}$$

où apparaît le vecteur d'onde **k** avec magnitude

$$k = \frac{\omega}{c} = \frac{2\pi}{\lambda}, \tag{E.2}$$

le vecteur de polarisation $\boldsymbol{\epsilon}$ et la phase δ. La lumière peut être polarisée sous d'autres formes que celle montrée ci-dessus, mais cette discussion sera reportée au Chapitre 3.

Pour les solutions diluées, l'absorption de la lumière est donnée par la loi de Lambert-Beer.

$$\frac{I}{I_0} = e^{-\mathcal{N}\sigma(\omega)\ell}. \tag{E.3}$$

Dans cette expression, I et I_0 sont les intensités sortantes et incidentes, tandis que l'exposant donne le nombre effectif de molécules absorbantes, exprimé en termes de densité de molécules absorbantes, $\mathcal{N}$, de la longueur parcourue par la lumière, ℓ, et de la section efficace d'absorption, $\sigma(\omega)$. Cette dernière peut être considérée comme une surface couvrant toutes les molécules qui ont absorbé la lumière incidente, formant ainsi une mesure de l'intensité d'absorption. Les quantités exprimées dans la loi de Lambert-Beer sont de nature macroscopique et sont, en principe, uniquement accessibles par l'experience, tandis que les simulations de chimie quantique fournissent généralement des quantités microscopiques. Dans le contexte de l'absorption de la lumière, les deux échelles peuvent être reliées par la relation suivante.

$$I\sigma(\omega_{fi}) = \hbar\omega_{fi} w_{i\rightarrow f}, \tag{E.4}$$

où $w_{i\rightarrow f}$ est le taux de transition et $\hbar\omega_{fi}$ est la différence d'énergie entre l'état initial et final. Les deux côtés de cette équation donnent une mesure de l'énergie absorbée par le système. Le taux de transition peut être calculé à l'aide de méthodes de mécanique quantique, ce qui permet d'éviter de calculer directement la section efficace d'absorption. Avant de procéder au calcul de cette quantité, revenons d'abord en arrière et examinons le système en question (Figure 1.1).

Ce qui ressort, c'est la grande différence d'échelle entre la longueur d'onde et la molécule de benzène, cette dernière ne pouvant être perçue qu'à l'intérieur d'un cadre zoomé. Dans ce cadre, la plupart de la courbure de l'onde plane est perdue, ce qui implique que la molécule ressent effectivement un champ uniforme, dont le composant magnétique peut être négligé en raison de son préfacteur de $1/c$. Formulé de manière plus mathématique, l'interaction lumière-matière est développée en séries de vecteurs d'onde et tronquée à l'ordre zéro, justifiée par la limite $kr \ll 1$. À cet ordre, notre interaction est donnée par l'opérateur de dipôle électrique, correspondant à un champ électrique uniforme. Ces considérations forment la base de l'approximation du dipôle électrique, largement utilisée en spectroscopie UV-Vis. Pour décrire l'ECD, cependant, l'approximation du dipôle électrique ne suffit pas, car cette interaction dépend également de l'opérateur de dipôle magnétique, qui apparaît à un ordre supérieur dans notre expansion.

Tournons maintenant notre attention vers le Hamiltonien qui décrit ce système. Sans perte de généralité, notre Hamiltonien peut être séparé en une partie statique (donnée par un Hamiltonien non relativiste) et un opérateur d'interaction dépendant du temps.

$$\hat{H} = \hat{H}_0 + \hat{V}(t); \quad \hat{V}(t) = \int_{-\infty}^{\infty} dt e^{-i\omega t} \hat{V}(\omega), \tag{E.5}$$

le second étant exprimé de manière pratique sous forme d'une transformée de Fourier. De plus, l'hermiticité de l'opérateur d'interaction implique la relation suivante dans le domaine de fréquence.

$$\hat{V}^{\dagger}(t) = \hat{V}(t) \rightarrow \hat{V}^{\dagger}(\omega) = \hat{V}(-\omega). \tag{E.6}$$

Je vais reporter la construction explicite de cet opérateur au chapitre 3, car il suffit pour le moment de supposer que cet opérateur est périodique. En conséquence, la transformée de Fourier de l'opérateur d'interaction est discrétisée en composantes de fréquence qui sont des multiples entiers d'une fréquence fondamentale.

$$\hat{V}(t) = \hat{V}(t+T) \rightarrow \omega = n\omega_T; \quad \omega_T = \frac{2\pi}{T}, \quad n \in \mathbb{N}. \tag{E.7}$$

Par conséquent, l'opérateur d'interaction peut être exprimé comme suit.

$$\hat{V}(t) = \sum_{y=-N}^{N} \lambda_{\alpha}^{\omega_y} \hat{V}_{\alpha}(\omega_y) e^{-i\omega_y t + \epsilon t}, \tag{E.8}$$

où les indices y et α représentent les composantes de Fourier et cartésiennes. Pour les composantes cartésiennes, la convention de sommation d'Einstein est appliquée, tandis que la somme sur les composantes de fréquence est écrite explicitement. Comme on peut le déduire de l'hermiticité de l'opérateur global, la somme sur les composantes de fréquence contient des indices positifs et négatifs, correspondant à des paires égales mais de signe de fréquences opposées.

$$\omega_0, (\omega_1, -\omega_1), (\omega_2, -\omega_2), (\omega_3, -\omega_3), \cdots . \tag{E.9}$$

Ici, les composantes de fréquence zéro décrivent les contributions statiques, c'est-à-dire $\omega_0 = 0$, à notre perturbation. De plus, dans cette expression, ϵ est un nombre infinitésimal garantissant que la perturbation est activée doucement, c'est-à-dire un commutateur adiabatique.

Dans l'approximation du dipôle électrique, les composantes de fréquence sont données par l'opérateur du moment dipolaire électrique

$$\hat{V}_{\alpha}(\omega_y) = \hat{Q}_{\alpha}^{[1]} = -er_{\alpha}; \quad \lambda_{\alpha}^{\omega_y} = \frac{1}{2} E^{\omega} \epsilon_{\alpha}, \tag{E.10}$$

où $-e$ est la charge de l'électron. Dans notre cas particulier de lumière monochromatique, une seule paire de fréquences contribue, ce qui nous permet d'exprimer notre opérateur d'interaction sous une forme plus simple

$$\hat{V}(t) = E^{\omega} \epsilon_{\alpha} \hat{Q}_{\alpha}^{[1]} \cos(\omega t) e^{\epsilon t}. \tag{E.11}$$

Cependant, dans ce chapitre, la représentation de l'équation (E.8) est préférée pour préserver la généralité du formalisme.

E.2 Chapitre 2

Les électrons de cœur sont généralement pas pris en compte dans la formation de liaisons, car ils ne sont pas facilement polarisés et conservent ainsi largement leur caractère atomique. Cependant, en spectroscopie des rayons X, les électrons de cœur jouent un rôle central, car ces expériences fonctionnent à des énergies suffisamment élevées pour sonder ces électrons. La simulation de la spectroscopie des rayons X est confrontée à des difficultés, car la théorie conventionnelle de la spectroscopie UV-Vis (voir le chapitre 1) ne peut pas reproduire avec précision les expériences des rayons X. Au moins certaines de ces lacunes sont expliqués dans les caractéristiques spéciales des électrons de cœur. En raison de leur proximité avec le noyau, les électrons de cœur subissent une attraction beaucoup plus forte que les électrons de valence, augmentant ainsi considérablement leur vitesse. Un effet analogue se produit dans le système solaire, où la planète Mercure orbite autour du soleil à des vitesses beaucoup plus élevées que les planètes plus éloignées. En général, la vitesse des électrons augmente avec un nombre atomique plus élevé. Déjà pour des éléments de taille modérée, les électrons de cœur se déplacent si rapidement que la mécanique quantique classique échoue à prendre correctement en compte leur mouvement. Cependant, pour les éléments dans la partie basse du tableau périodique, les influences des effets relativistes s'étendent au-delà du cœur, car les orbitales de tous les autres électrons doivent rester orthogonales aux orbitales de cœur, contractant ainsi efficacement la couche de valence. Pour obtenir ne serait-ce qu'une fonction d'onde qualitativement correcte des molécules contenant de tels éléments, les effets relativistes doivent être inclus.

Avec la mécanique quantique, la relativité restreinte a révolutionné le paradigme de la physique moderne. Cette dernière théorie exige une réévaluation drastique des concepts d'espace et de temps, bien qu'elle ne gagne de la pertinence qu'à des échelles d'énergie extrêmement élevées. Cependant, cette théorie est classique dans le sens où elle concerne le mouvement déterministe de particules ponctuelles, tandis que la mécanique quantique est fondamentalement de nature probabiliste. Pour inclure les effets de la relativité dans nos calculs, elle doit être étendue au domaine de la mécanique quantique. Heureusement, ce travail a déjà été fait pour nous par Paul Dirac, qui a formulé une extension relativiste de l'équation de Schrödinger. Les mérites de l'équation de Dirac résident dans ses valeurs d'énergie plus précises, sa description naturelle du spin et du couplage spin-orbite, ainsi que sa prédiction de l'antimatière. Comme mentionné précédemment, l'équation de Dirac est particulièrement utile pour décrire des propriétés qui dépendent des électrons de cœur, telles que la spectroscopie RMN, la spectroscopie Mössbauer ou la spectroscopie des rayons X. Dans ce travail, une approche relativiste sera suivie pour décrire correctement les électrons de cœur. Par conséquent, ce chapitre sera consacré aux méthodes de la chimie quantique relativiste.

E.3 Chapitre 3

Nous avons parcouru un long chemin depuis le début de notre discussion sur les principes de base de la théorie de réponse linéaire de SCF, suivie de la chimie quantique relativiste. Avec les outils théoriques des chapitres précédents en place, nous sommes presque prêts à discuter de quelques exemples pratiques. Cependant, avant de continuer, je dois aborder une hypothèse clé formulée dans le chapitre 1. Je rappelle qu'en régime UV-Vis, l'étendue spatiale de la molécule cible est généralement beaucoup plus petite que la longueur d'onde de la lumière. Pour cette raison, il est justifié d'appliquer l'approximation du dipôle électrique, selon laquelle le champ électromagnétique est approximé comme un champ électrique uniforme. Cependant, en régime X, cette approximation est remise en question car la longueur d'onde est de taille comparable par rapport à la molécule. La Figure 3.1 représente une situation similaire à celle de la Figure 1.1, bien que dans ce cas, la molécule de benzène interagisse avec des rayons X, ayant une longueur d'onde beaucoup plus courte ($\lambda = 2,6$ nm).

Compte tenu du fait que l'approximation du dipôle électrique revient essentiellement à un développement multipolaire à l´ordre zéro, il existe généralement deux méthodes pour corriger les lacunes de cette approximation. La première méthode, la plus directe, évite complètement un développement multipolaire et repose son interaction sur les champs électromagnétiques exacts, conservant ainsi leur caractère sinusoïdal dans l'opérateur d'interaction. En utilisant l'opérateur d'interaction complet, tous les effets non dipolaires sont inclus de manière exacte, bien que le formalisme soit quelque peu plus compliqué en raison de la dépendance en fréquence de cet opérateur.

Alternativement, le développement multipolaire peut être tronqué au-delà de l´ordre zéro, prenant ainsi en compte les moments multipolaires d'ordre supérieur. Les moments multipolaires peuvent être compris comme des idéalisations des distributions de charge et de courant. Par exemple, le moment dipolaire électrique est une quantité vectorielle qui donne la direction globale dans laquelle la distribution de charge est polarisée. Le moment quadrupolaire électrique, en revanche, décrit la largeur globale d'une distribution de charge, semblable à la variance des distributions statistiques. Les inhomogénéités supplémentaires des distributions sont décrites par des moments multipolaires d'ordre supérieur, qui, sous forme cartésienne, sont définis comme suit :

$$Q^{[n]}_{j_1\cdots j_n} = \int d^3\boldsymbol{r}\, r_{j_1} r_{j_2}\cdots r_{j_n}\rho(\boldsymbol{r},t); \quad m^{[n]}_{j_1\cdots j_{n-1};i} = \frac{n}{n+1}\int d^3\boldsymbol{r}\, r_{j_1} r_{j_2}\cdots r_{j_{n-1}}\big(\boldsymbol{r}\times\boldsymbol{j}(\boldsymbol{r},t)\big)_i. \tag{E.12}$$

En incluant les contributions de tous les moments multipolaires, les distributions de charge ou de courant peuvent être récupérées exactement. Cependant, en pratique, cela n'est souvent pas nécessaire, car généralement, les contributions les plus dominantes proviennent des moments multipolaires d'ordre le plus bas. Les distributions de charge ou de courant compliquées peuvent donc être simplifiées en ne considérant que ces contributions dominantes. Cette approche se révèle particulièrement utile lors de la description des interactions intermoléculaires. Dans ce contexte, cependant, j'utiliserai cette méthode pour approximer les interactions lumière-matière.

En utilisant soit l'interaction lumière-matière complète, soit l'interaction tronquée, je décrirai deux types de spectroscopie : près du front d´absorption de rayons X (NEXAFS) et le dichroïsme circulaire naturel des rayons X (XNCD). La NEXAFS peut être calculée directement à partir de la section efficace d'absorption dérivée de la lumière polarisée linéairement. Le calcul du XNCD, cependant, est un peu plus compliqué, car il implique la différence entre la section efficace d'absorption de la lumière polarisée circulairement à gauche et à droite :

$$\Delta\sigma(\omega) = \sigma_L(\omega) - \sigma_R(\omega). \tag{E.13}$$

En tenant compte de la parité, on peut faire valoir que le dichroïsme circulaire des échantillons isotropes, par exemple les gaz et les solutions, n'est différent de zéro que pour les molécules chirales. En fait, pour les énantiomères, le dichroïsme circulaire est égal mais du signe opposé, ce qui en fait l'une des rares techniques pour distinguer les énantiomères. Des effets similaires peuvent être obtenus pour les systèmes non chiraux en imposant des conditions anisotropes, comme dans les cristaux, ou en appliquant un champ magnétique externe supplémentaire. Cependant, cette dernière suggestion crée un type d'interaction différent, également appelé dichroïsme circulaire magnétique des rayons X.

S'appuyant sur les résultats du chapitre précédent, toutes les dérivations seront effectuées dans un cadre relativiste à quatre composantes. Ces dérivations reposent principalement sur des articles dont je suis co-auteur. Alternativement, il est également possible de dériver un formalisme similaire dans un cadre non relativiste, bien qu'il soit plus compliqué en raison du grand nombre de termes nécessaires pour décrire l'interaction lumière-matière. Par conséquent, le formalisme non relativiste ne sera pas poursuivi ici, sauf indication contraire. En outre, sauf indication contraire, j'utiliserai la notation de la théorie de l'état exact tout au long de mes dérivations, car la généralisation à la théorie SCF découle directement de la procédure décrite au chapitre 1.

E.4 Chapitre 4

E.4.1 Implémentation

Dans la chimie quantique contemporaine, la formulation de la théorie n'est que la moitié du travail, car une implémentation efficace est cruciale pour rendre les calculs chimiques quantiques réalisables, ce qui impliquent souvent de nombreuses opérations mathématiques fastidieuses. Pour cette raison, cette section sera consacrée à l'implémentation de l'opérateur d'interaction lumière-matière complet et tronqué. Ces deux développements ont été réalisés dans DIRAC, qui est un code chimique quantique adapté aux calculs relativistes à quatre composantes. L'implémentation de ces interactions est encore en cours, donc ce qui suit est une invertoire de toutes les fonctionnalités disponibles. Il est possible d'effectuer des calculs d'intensité à l'aide des opérateurs d'interaction complets et tronqués, à la fois dans des conditions isotropes et anisotropes. Cependant, dans l'implémentation actuelle, les calculs ECD ne peuvent être effectués qu'à l'aide de l'opérateur d'interaction complet, tandis que l'ECD tronqué est encore en développement. L'ECD tronqué rapporté plus loin dans ce chapitre a été calculé à l'aide d'un script externe avec les moments de transition de DIRAC en entrée. Dans ce qui suit, je donnerai un bref aperçu de l'implémentation de l'interaction complète et tronquée, en mettant en évidence leurs caractéristiques uniques. Dans la section à venir et les suivantes, cette partie du code sera désignée sous le nom d'implémentation BED, l'abréviation signifiant au-delà de l'approximation électro-dipolaire. Bien que cette abréviation ne s'applique pas nécessairement à l'ECD, qui est déjà au-delà de cette approximation au premier ordre, elle sera quand même utilisée par souci de cohérence.

E.4.2 Convergence de l'Expansion Multipolaire

Avoir une implémentation entièrement fonctionnelle à notre disposition qui peut calculer des forces d'oscillateur au-delà de l'approximation électro-dipolaire nous permet de procéder à nos premiers calculs. Pour toute nouvelle fonctionnalité développée, il est toujours bon de procéder avec prudence et de commencer par des calculs sur des systèmes de test simples, ce qui facilite l'identification des erreurs et des résultats inattendus. Par conséquent, cette section se concentrera principalement sur les spectres d'absorption UV-Vis et absorption des rayons X de l'atome de radium, dont la symétrie sphérique simplifiera considérablement le problème à portée de main. De plus, cette symétrie induit des règles de sélection pour les transitions multipolaires. Il est probable que les principales caractéristiques des spectres seront décrites par la force d'oscillateur électrique-dipolaire, tandis que les détails plus fins seront donnés par des contributions dépendant du moment magnétique-dipolaire et du quadrupôle électrique. Les règles de sélection pertinentes sont les suivantes :

- dipolaire-électrique: $\Delta j = 0, \pm 1; \quad \Delta m = 0, \pm 1; \quad (j = 0 \nrightarrow j = 0)$
- dipolaire-magnétique : $\Delta j = 0, \pm 1; \quad \Delta m = 0, \pm 1; \quad (j = 0 \nrightarrow j = 0)$
- quadrupôle électrique : $\Delta j = 0, \pm 1, \pm 2; \quad \Delta m = 0, \pm 1, \pm 2; \quad (j = 0 \nrightarrow j = 0)$
- interaction complète : $(j = 0 \nrightarrow j = 0)$.

Dans ce chapitre, je vais mettre en pratique ces règles et calculer les intensités d'absorption de l'atome de radium à la fois dans les régions centrale et de valence.

Sauf indication contraire, les données rapportées dans cette section ont été obtenues avec une version en développement du code de structure électronique DIRAC. En utilisant l'interaction complète, le spectre de valence et de cœur de l'atome de radium a été calculé au niveau de la théorie TDDFT en utilisant la fonction d'échange-corrélation PBE0, basée sur l'hamiltonien de Dirac-Coulomb et dans le cadre de la méthode de fenêtre d'excitation restreinte (REW). Dans ces calculs, les intégrales biéléctronique ont été remplacées par une correction d'énergie SS interatomique. Pour des raisons techniques qui deviennent plus claires par la suite, les calculs impliquant des interactions tronquées ont été limités aux excitations $ns_{1/2} \rightarrow 7p_{1/2}; \quad n = 1, 2, \cdots, 7$ de l'atome de radium et effectués au niveau de la théorie TD-HF. De plus, dans ces calculs, le criblage des intégrales $(SS|SS)$ a été désactivé et les intégrales $(SS|SS)$ ont été incluses. Pour les deux séries de calculs, l'ensemble de base dyall.ae3z a été utilisé.

Il a été constaté que pour des énergies d'excitation croissantes, l'utilisation de l'interaction tronquée lumière-matière devient de plus en plus problématique en raison de la convergence lente de ces expansions. Il ne s'agit pas d'un problème de base qui peut être atténué en augmentant la base, car cette lente convergence a été observée au niveau des intégrales atomiques sous-jacentes OA. En particulier, pour les excitations de cœur, une convergence extrêmement lente a été observée pour les intégrales impliquant des orbitales gaussiennes cartésiennes avec des exposants diffus. Cela peut s'expliquer par le fait que de telles fonctions diffuses sont moins efficaces que les fonctions serrées pour amortir les puissances cartésiennes croissantes apparaissant dans une expansion de l'interaction lumière-matière complète en fonction de la norme du vecteur d'onde. Cela suggère à son tour que l'utilisation d'orbitales de type Slater, qui ont une décroissance plus lente que les orbitales gaussiennes, sera encore plus problématique.

E.4.3 Convergence de la base

Le choix approprié de la base est essentiel pour atteindre une précision quantitative dans les calculs chimiques quantiques. Surtout dans le contexte actuel, où des opérateurs d'interaction non conventionnels sont utilisés, il est important de tenir compte spécialement du choix de la base. Par conséquent, dans cette section, il sera évalué si les bases conventionnelles sont suffisamment flexibles pour satisfaire les exigences de ces opérateurs d'interaction.

Les bases conventionnelles sont construites en choisissant un ensemble de fonctions qui minimisent l'énergie. En général, on gagne plus d'énergie en ajoutant des fonctions serrées qu'en ajoutant des fonctions diffuses. En raison de cela, les bases optimisées en termes d'énergie saturent plus rapidement la région du coeur que la région au-délà du valence. L'interaction lumière-matière complète et tronquée peut nécessiter l'ajout de fonctions de base supplémentaires. Un problème à cet égard est l'absence d'un principe variationnel pour les moments de transition. Alternativement, des bases pour une utilisation au-delà des énergies peuvent être construites en utilisant l'approximation du cœur équivalent, la règle de Slater ou le schéma d'optimisation de la complétude. Une autre stratégie consiste à augmenter systématiquement la taille de la base jusqu'à ce que la propriété d'intérêt soit stabilisée.

Sørensen *et al.* ont réalisé une série de calculs dans un cadre non relativiste en utilisant l'opérateur d'interaction complet et tronqué, ce dernier étant limité à l'ordre deux, exprimé avec les bases ANO-RCC. Bien que la série n'ait pas complètement convergé pour les bases plus grandes, leurs résultats indiquent que l'opérateur d'interaction complet est plus stable en ce qui concerne le choix de la base. De plus, Sørensen *et al.* ont fait valoir que chaque moment multipolaire nécessite des bases différentes, ce qui rend extrêmement difficile la construction de bases pouvant décrire l'interaction tronquée à des ordres plus élevés. Ils ont conclu que l'opérateur d'interaction complet devrait être la norme pour les calculs impliquant des effets non dipolaires. Pour les interactions d´ordre zéro et de premier ordre, la représentation en longueur semble être le choix privilégié dans la littérature, bien qu'il n'y ait pas de réponse concise quant à la supériorité de la convergence de la base dans une représentation donnée.

Une autre stratégie pour évaluer la qualité d'une base consiste à la comparer à une valeur de référence. Dans cette section, les besoins en termes de base pour les effets non dipolaires sont évalués en comparant des calculs utilisant des bases gaussiennes avec le code moléculaire DIRAC à des calculs de différences finies équivalents avec le code atomique GRASP. Si la taille de la grille de ce dernier est suffisamment grande, les résultats correspondent effectivement à la limite de la base complète, ce qui en fait une référence appropriée pour les calculs de base. À cette fin, j'étudierai les transitions $1s_{1/2} \rightarrow 7p_{1/2}$ et $7s_{1/2} \rightarrow 7p_{1/2}$ dans l'atome de radium, qui sont représentatives des excitations de cœur et de valence, respectivement.

Pour comparer les effets de la base dans les régions de valence et de cœur, j'ai étudié les transitions $7s_{1/2} \rightarrow 7p_{1/2}$ et $1s_{1/2} \rightarrow 7p_{1/2}$ de l'atome de radium. Les transitions étaient contraintes à se produire entre des orbitales simples pour faciliter la comparaison entre les calculs utilisant des orbitales de type gaussien dans DIRAC et les calculs de référence numériques dans GRASP. Comme GRASP ne calcule que les orbitales *occupées*, les orbitales ont été optimisées en utilisant la méthode de Hartree-Fock avec moyenne des configurations (AOC) par rapport à des déterminants *d'états excités*, c'est-à-dire $[\mathrm{Rn}]7s^1_{1/2}7p^1_{1/2}$ pour la transition de valence et $[\mathrm{Ra}]1s^{-1}_{1/2}7p^1_{1/2}$ pour la transition de cœur. Même si l'orbitale $7p_{1/2}$ est formellement occupée dans ces configurations, je la traite comme une orbitale virtuelle pour construire les moments de transition. Dans le cas de GRASP, ceux-ci ont été obtenus en insérant les fonctions radiales $P_{n\kappa}$ et $Q_{n\kappa}$ dans les équations décrivant les distributions radiales. Comme les moments de transition sont déterminés jusqu'à une phase complexe, je les ai définis de manière à ce que toutes les distributions radiales soient réelles et aient une valeur maximale positive. Étant donné que les fonctions radiales de GRASP sont calculées sur une grille numérique et correspondent ainsi effectivement à la limite de la base complète, les moments de transition de GRASP ont été utilisés comme référence. Dans le cas de DIRAC, j'ai appliqué la sélection par recourrement pour éviter que l'état excité de cœur ne s'effondre pendant les cycles SCF. J'ai ensuite utilisé les orbitales des calculs de l'état excité dans un calcul d'état fondamental de Hartree-Fock dépendant du temps à quatre composantes (4c-TD-HF) dans le cadre de la réponse linéaire. La méthode de la fenêtre d'excitation restreinte a été invoquée pour ne considérer qu'une seule amplitude. Les distributions radiales ont ensuite été divisées par cette amplitude restante pour comparer les résultats des calculs de base avec les valeurs de référence numériques. Dans DIRAC, les distributions radiales ont été calculées sur une grille radiale avec le module de visualisation, qui effectue l'intégration angulaire sur une grille de Lebedev ($L_{\mathrm{max}} = 64$). En raison du schéma de symétrie quaternion dans DIRAC, tous les moments de transition sont par défaut réels.

Les calculs de base ont été effectués au niveau de la théorie de Hartree-Fock en utilisant le Hamiltonien de Dirac-Coulomb et les bases dyall.aeXz (X=2,3,4). Ces bases sont construites à partir de fonctions de base gaussiennes cartésiennes non contractées qui sont conçues pour les calculs corrélés et contiennent donc des fonctions de base de grand moment cinétique orbital. J'ai supprimé les fonctions g, h et i car, pour les systèmes atomiques, elles ne contribuent qu'à l'espace des orbitales virtuelles. Les bases des petites composantes ont été générées en respectant la condition de l'équilibre cinétique restreint et les intégrales $(SS|SS)$ ont été traitées exactement, pour une cohérence avec les calculs numériques. De plus, j'ai constaté qu'avec le seuil de dépendance linéaire par défaut (10^{-6} et 10^{-8} pour les espaces des grandes et petites composantes, respectivement), plusieurs fonctions de base étaient supprimées. Surtout, la petite composante du $1s_{1/2}$ était susceptible d'être supprimée. Cela nuit à la qualité des résultats, donc pour toutes les calculs, j'ai réglé le seuil de dépendance linéaire à 10^{-9} et 10^{-10} pour les espaces des grandes et petites composantes, respectivement.

Pour les ordres les plus bas, la base dyall.ae2z était suffisante pour converger les moments multipolaires électriques en représentation de longueur pour les deux transitions. À des ordres plus élevés, la base dyall.ae4z était nécessaire. Il a été couramment observé que la transition de cœur a tendance à être plus difficile à converger que la transition de valence. La convergence de la base des moments multipolaires magnétiques suit également ces tendances, bien qu'elle semble être encore plus difficile à converger pour la transition de cœur. Par conséquent, pour la représentation de la longueur généralisée, la base dyall.ae4z suffit pour décrire correctement les multipôles d'ordre supérieur, bien que le seuil de dépendance linéaire doive être ajusté.

De tous les types de multipôles, il semble que les multipôles électriques en représentation de vitesse soient les plus problématiques à converger. Même si les multipôles de valence convergent vers la référence numérique, les multipôles de cœur présentent des écarts par rapport à la référence sous forme d'oscillations et de pics supplémentaires. En raison de ces artefacts, la convergence de la base semble inversée : les bases plus grandes s'éloignent davantage de la référence. Cela suggère que la représentation de la vitesse généralisée doit être utilisée avec prudence pour $n > 3$. Pour la représentation de la vitesse généralisée, je recommande d'utiliser la base dyall.ae3z, qui ne semble pas souffrir autant des artefacts que la base dyall.ae4z. De plus, je recommande de ne pas aller au-delà de $n = 3$, car après cet ordre, la fiabilité de ce schéma devient douteuse.

L'opérateur d'interaction complet ne souffre pas de ces problèmes et est déjà convergé avec la base dyall.ae2z. Étant donné que l'interaction tronquée souffre également d'une convergence lente par rapport à l'expansion multipolaire, je recommande d'appliquer l'interaction complète lors du calcul des transitions aux rayons X.

Ces conclusions sont potentiellement moins évidentes pour le niveau relativiste à 2 composantes intermédiaire. L'approche actuelle exigerait formellement la génération de distributions radiales en utilisant des opérateurs d'interaction transformés correctement, et ceux-ci ne sont par exemple pas disponibles pour le Hamiltonien à 2 composantes eXact (X2C), pour lequel en général seule une représentation matricielle, et non une représentation en espace réel, est disponible. Cependant, l'élimination des petites composantes suggère à nouveau que la convergence de la base devrait s'améliorer.

E.4.4 Systèmes avec des Centres de Symétrie Équivalents

Pour les calculs sur l'atome de radium, on a observé que les transitions permises par le dipôle ne gagnaient que des corrections modestes lorsqu'on incluait des effets non dipolaires, l'explication étant que la compacité des orbitales du cœur annule ces effets. Cependant, si le système en question contient des centres de symétrie équivalents, les transitions du cœur qui en découlent sont délocalisées, ce qui, en principe, devrait renforcer les effets non dipolaires. À cette fin, je considérerai le seuil K du Cl dans $TiCl_4$. De plus, ce système représente un cas où il n'y a pas de choix naturel d'origine du jauge, formant ainsi un système approprié pour tester l'indépendance de l'origine du jauge des deux représentations. Ce système a déjà été étudié dans le contexte des effets non dipolaires dans l'absorption des rayons X linéaires en utilisant des expansions multipolaires de faible ordre. En particulier, il a été utilisé pour démontrer l'apparition de forces oscillatoires négatives lors de la troncature de l'interaction lumière-matière dans la représentation de la vitesse généralisée dans un cadre non relativiste. Ci-dessous, je revisiterai ce cas et évaluerai la nécessité d'aller au-delà de l'approximation électrique-dipolaire. J'étudie également numériquement l'indépendance de l'origine du jauge des trois schémas dans le cas de l'absorption des rayons X mous. La spectroscopie d'absorption de le seuil K du ligand suppose fournir des informations directes sur la covalence des liaisons métal–ligand en raison du mélange des orbitales p du ligand avec les orbitales d du métal. L'absorption de Cl K-edge de $TiCl_4$ a été étudiée à la fois expérimentalement et théoriquement dans le cadre et au-delà de l'approximation électrique-dipolaire en utilisant des expressions tronquées d'expansions multipolaires. Son spectre expérimental présente un pic pré-edge large qui nécessite un ajustement à deux pics (dans le toluène : à 2821,58 et 2822,32 eV avec un rapport d'intensité approximatif de 0,84). Dans la symétrie T_d, les cinq orbitales $3d$ de Ti appartiennent aux représentations irréductibles e et t_2, et les bandes pré-edge peuvent être attribuées à des excitations des orbitales $1s$ du Cl a_1 et t_2 vers les ensembles e et t_2 des orbitales $3d$ sur Ti, respectivement. Ici, je me concentre sur les huit transitions les plus basses $(a_1, t_2 \rightarrow e)$ qui donnent naissance à trois ensembles dégénérés (E, T_1 et T_2), dont le dernier est permis en ED.

Les données rapportées dans cette section ont été obtenues avec une version de développement du code de structure électronique .

Les résultats calculés présentés dans cette section ont été obtenus par des calculs de théorie de la fonctionnelle de la densité dépendante du temps (TD-DFT), basés sur le Hamiltonien de Dirac–Coulomb et dans le cadre de la fenêtre d'excitation restreinte (REW) en utilisant la fonctionnelle d'échange-corrélation PBE0 et les bases dyall.ae3z. Les bases des petites composantes ont été générées en respectant la condition de l'équilibre cinétique restreint, et les intégrales (SS|SS) ont été remplacées par une correction SS interatomique. Un modèle gaussien a été utilisé pour la distribution des charges nucléaires. Une grille Lebedev à 86 points ($L_{\max} = 12$) a été utilisée pour la moyenne isotropique des forces oscillatoires basées sur l'opérateur complet de l'interaction lumière-matière. L'origine du jauge a été placée au centre de masse et la symétrie spatiale a été invoquée dans tous les cas, sauf pour les calculs de l'indépendance de l'origine du jauge.

Deux conclusions clés importantes découlent de ces calculs :

- Les transitions étudiées issues du seuil K du Cl dans $TiCl_4$ ont d'importantes corrections non dipolaires, principalement induites par la délocalisation des orbitales du cœur du Cl. Cependant, en raison de la proximité des transitions, la valeur cumulative de ces transitions est à peine affectée. Même dans le cas contraire, on peut remettre en question si la délocalisation de l'orbite du cœur est un effet physique réel. Pour l'évaluer correctement, il est nécessaire d'aller au-delà de la théorie SCF.

- L'invariance formelle de l'origine du jauge des forces oscillatoires en jauge multipolaire repose sur des expressions de commutateur qui ne tiennent pas nécessairement dans une base finie. Cela explique le manque notoire d'indépendance de l'origine du jauge d'ordre en ordre dans les calculs pratiques au-delà de l'approximation électrique-dipolaire basée sur n'importe quelle formulation tronquée du jauge multipolaire. Comme indiqué au chapitre 3, ces relations de commutateur, impliquant le Hamiltonien, correspondent à une transformation du jauge de la représentation de la longueur à la représentation de la vitesse. En d'autres termes, l'indépendance de l'origine du jauge en jauge multipolaire est démontrée en se transformant en une autre jauge pour laquelle l'indépendance de l'origine est maintenue. Jusqu'à présent, je n'ai pas été en mesure de démontrer l'invariance de l'origine du jauge tout en restant dans le jauge multipolaire.

E.4.5 Dichroïsme Circulaire Électronique

Jusqu'à présent, je n'ai pas encore exploité pleinement la polyvalence de la mise en œuvre BED, car toutes les calculs jusqu'à présent portaient sur l'absorption de lumière polarisée linéairement. Dans cette section, je me concentrerai donc sur le ECD isotrope et anisotrope calculé en utilisant l'interaction lumière–matière semi-classique *complète*, ainsi que la représentation de la vitesse généralisée. Cela nous permet d'étudier la réponse ECD sur l'ensemble du spectre électromagnétique, de l'optique aux régimes des rayons X. Jusqu'à présent, les études théoriques précédentes sur le XNCD isotrope des molécules étaient basées sur une formulation non relativiste tout en ne considérant que l'interaction tronquée du premier ordre, qui est proportionnelle au produit scalaire du moment dipolaire électrique et magnétique).

Une estimation sommaire du XNCD du premier ordre peut être trouvée en supposant que la transition en question est effectivement de nature atomique, ce qui est justifié par le caractère de type atomique des orbitales du cœur. Dans cette hypothèse, les règles de sélection atomiques s'appliquent, ce qui signifie que les règles de transition des moments dipolaires électriques et magnétiques dictent si le XNCD s'annule. Cependant, les règles de sélection des moments dipolaires magnétiques non relativistes prescrivent que les transitions atomiques ne peuvent se produire qu'entre des états qui sont séparés par un couplage spin-orbite, suggérant ainsi que le XNCD est nul dans ce schéma simplifié. Dans des calculs plus réalistes, les orbitales du cœur sont polarisées hors de la symétrie atomique, ce qui rend le XNCD non nul, un effet pris en compte dans les études mentionnées ci-dessus. La mise en œuvre actuelle tient compte de deux contributions possibles supplémentaires : (*i*) les effets des interactions lumière–matière au-delà du premier ordre et (*ii*) l'inclusion d'effets relativistes, notamment le couplage spin-orbite qui modifie les règles de sélection. Par conséquent, cela permet, pour la première fois, d'examiner de manière réaliste la réponse ECD des molécules sur l'ensemble des régimes de valence et des rayons X.

Cependant, contrairement aux exemples précédents, il n'est pas suffisant d'utiliser le même système cible atomique, qui a une ECD nulle en raison de sa grande symétrie. Par conséquent, en tant que systèmes de test, je considère les modèles chromophores les plus simples de disulfure, le dihydrogène disulfure H_2S_2 et le diméthyl disulfure $(CH_3S)_2$. En raison des barrières de torsion faibles du disulfure (∼6-11 kcal/mol, les deux formes énantiomères (P- et M-hélice) ne peuvent pas être résolues expérimentalement. Cependant, le pont disulfure est un élément structural important dans les protéines, où il se produit de préférence dans des conformations non planes, chirales (de symétrie C_2) et affiche donc une chiralté axiale induite structuralement. Une perspective intéressante pour les systèmes complexes (par exemple, les protéines) est l'utilisation potentielle du XNCD comme une sonde locale de la chiralté. Cela pourrait éventuellement compléter les informations de conformation délocalisées encodées dans l'ECD de valence. En raison de sa facilité de calcul, H_2S_2 a été largement utilisé pour évaluer les méthodes de structure électronique pour le calcul des propriétés chiroptiques. Pour la même raison, Goulon *et al.* l'ont également utilisé pour estimer les magnitudes relatives des réponses XNCD dans le cadre de l'interaction tronquée du premier ordre et du cadre non relativiste, en signalant des valeurs en dessous des limites de détection expérimentales. Ici, je revisite l'ECD du chromophore disulfure sur toute l'échelle de valence, les seuils L- et K, allant au-delà de ces approximations.

Les géométries de H_2S_2 et $(CH_3S)_2$ ont été obtenues en utilisant la fonctionnelle d'échange-corrélation B3LYP et l'ensemble de bases cc-pVTZ. Les optimisations de géométrie ont été effectuées dans Gaussian 16. Pour imiter l'angle de disulfure χ_3 typique des structures protéiques, une optimisation de géométrie contrainte a été réalisée pour $\chi_3 = -87°$, correspondant à la chiralté M-hélicoïdale. L'approche de fenêtre d'excitation restreinte a été utilisée pour cibler sélectivement les seuils du soufre L- et K. Cela élimine également le problème des transitions artificielles vers les orbitales quasi-continues causé par les effets du jeu de bases finies, qui interfèrent souvent avec les simulations au bord L. Un modèle gaussien a été utilisé pour la distribution de charges nucléaire, et une grille Lebedev à 86 points ($L_{\text{max}} = 12$) a été utilisée pour la moyenne isotropique de l'absorption linéaire différentielle basée sur l'opérateur complet de l'interaction. L'origine du jauge a été placée au centre de masse (CM) et la symétrie spatiale est pris en compte dans tous les cas, sauf pour les calculs de dépendance à l'origine du jauge.

Les énergies d'excitation, les sections efficaces d'absorption linéaire et différentielle pour l'opérateur complet d'interaction ainsi que les expansions multipolaires dans le jauge de vitesse généralisée ont été calculées en utilisant la fonctionnelle d'échange-corrélation PBE0 et les ensembles de bases non contractés aug-pcX-3 et aug-pc-3 pour le soufre et l'hydrogène, respectivement. La série de jeux de bases pcX-n a été développée pour décrire les processus d'excitation du cœur en utilisant l'approche ΔSCF (Self-Consistent Field) aux niveaux non relativiste et relativiste. Les jeux de bases des petites composantes ont été générés dans le cadre de l'équilibre cinétique restreint. Les calculs relativistes ont été effectués en utilisant un Hamiltonien Dirac-Coulomb dans lequel les intégrales (SS|SS) ont été remplacées par une correction d'énergie (SS–SS). L'invariance de l'origine du jauge de la formulation semi-classique complète des intensités rotatoires isotropes et anisotropes et de sa forme tronquée du premier ordre a été confirmée numériquement en déplaçant l'origine du jauge (de 0 à 100 a_0) le long de l'axe C_2. Cela conduit à une redistribution des contributions E1–E2 et E1–M1 à $R_{xx}^{[1]}$ et $R_{yy}^{[1]}$ pour les transitions de symétrie B. Comme prévu, les résultats sont restés inchangés à la fois pour les formulations complètes et tronquées (données non présentées). Les spectres simulés ont été obtenus en convoluant le spectre à bâtonnets avec des fonctions de forme gaussienne avec une largeur totale à mi-hauteur (FWHM) de 0,4 eV, et ceux de $(CH_3S)_2$ ont été décalés par des décalages différents pour chaque bord d'absorption afin de correspondre à leurs homologues expérimentaux.

Pour évaluer l'effet de l'augmentation des énergies d'excitation sur la force oscillatrice différentielle, les spectres des seuils L_1 et K ont été calculés pour les analogues plus lourds de H_2S_2 : H_2X_2, X=Se et Te. En analogie avec H_2S_2, les géométries des deux analogues plus lourds ont été obtenues à partir d'une optimisation contrainte (fixant $\chi_3 = -87°$) en utilisant les ensembles de bases cc-pVTZ et def2-VTZPP pour X=Se et Te, respectivement. À l'exception du choix du jeu de bases, cette série de calculs a été réalisée au même niveau de théorie que les calculs précédemment mentionnés pour H_2S_2. Pour réduire le coût du calcul des analogues plus lourds, j'ai utilisé le jeu de bases dyall.av3z pour toutes les simulations spectrales. Pour rendre la comparaison entre les analogues structuraux plus précise, les calculs de H_2S_2 ont été répétés en utilisant ce jeu de bases.

Aller au-delà de l'approximation du dipôle électrique au seuil K du soufre entraîne une redistribution non négligeable de l'intensité parmi les transitions presque dégénérées, mais sans implications visibles sur le profil d'absorption linéaire. En revanche, le profil d'absorption différentielle n'est pas affecté par une telle redistribution, en raison de sa nature signée. Cela entraîne une surestimation globale d'un facteur deux. En examinant les formes des distributions ECD anisotropes sous-jacentes, on constate que cette disparité provient en grande partie d'une mise à l'échelle globale corrigée en introduisant des contributions du troisième ordre.

De manière critique, le traitement du premier ordre se détériore à des énergies de transition plus élevées (au-delà de ω=c∼3728 eV), comme cela peut être déduit des calculs supplémentaires impliquant les analogues plus lourds de H_2S_2. Dans ces cas, ce traitement peut même pas réussir à prédire le signe des intensités de force oscillatrice individuelles, bien que cela soit partiellement atténué si les pics sont suffisamment larges. À de telles énergies, passer à des ordres supérieurs n'est pas une solution pratique en raison de la convergence lente de l'interaction tronquée - l'interaction complète est incontournable.

E.5 Conclusion et Perspectives

Nous parvenons à la conclusion générale qu'au moins pour l'absorption de la lumière polarisée linéairement, l'approximation du dipôle électrique est une excellente approximation pour la plupart des systèmes. Même dans le régime des rayons X durs, l'approximation du dipôle électrique peut capturer les caractéristiques générales du spectre. Cependant, pour décrire avec précision les transitions autorisées par le dipôle et même inclure les transitions interdites par le dipôle, il est impératif d'aller au-delà de l'approximation du dipôle électrique. Une autre exception où l'approximation du dipôle électrique pourrait être insuffisante est donnée par des systèmes avec des centres symétriques équivalents, bien que l'élargissement spectral rende difficile d'observer ces effets. Les effets non dipolaires semblent être les plus pertinents pour le dichroïsme circulaire électronique, apparaissant déjà pour H2S2 et étant moins sensibles à l'élargissement spectral. Deux exemples de projets futurs sont l'extension au dichroïsme circulaire magnétique et la mise en œuvre de la relaxation des trous de cœur.

Bibliography

[1] Nanna Holmgaard List, Timothé Romain Léo Melin, Martin van Horn, and Trond Saue. Beyond the electric-dipole approximation in simulations of x-ray absorption spectroscopy: Lessons from relativistic theory. *The Journal of chemical physics*, 152(18):184110, 2020. doi:10.1063/5.0003103.

[2] Martin van Horn, Trond Saue, and Nanna Holmgaard List. Probing chirality across the electromagnetic spectrum with the full semi-classical light–matter interaction. *The Journal of Chemical Physics*, 156(5):054113, 2022. doi:10.1063/5.0077502.

[3] Martin van Horn, Nanna Holmgaard List, and Trond Saue. Transition moments beyond the electric-dipole approximation: Visualization and basis set requirements. *The Journal of Chemical Physics*, 158(18):184103, 05 2023. doi:10.1063/5.0147105.

[4] Yuval N. Harari. *21 lessons for the 21st century*. Jonathan Cape, London, 2018. URL `https://www.ynharari.com/book/21-lessons-book/`.

[5] Trevor H Levere. *Transforming matter: a history of chemistry from alchemy to the buckyball*. JHU Press, 2001. URL `https://www.press.jhu.edu/books/title/2940/transforming-matter`.

[6] F. Wöhler. Ueber künstliche Bildung des Harnstoffs. *Annalen der Physik*, 88(2):253–256, 1828. doi:10.1002/andp.18280880206.

[7] Patrick Norman and Kenneth Ruud and Trond Saue. *Principles and Practices of Molecular Properties: Theory, Modeling and Simulations*. Wiley, Hoboken, NJ, 2018. doi:10.1002/9781118794821.

[8] P. W. (Peter William) Atkins and Ronald Friedman. *Molecular quantum mechanics*. Oxford University Press, Oxford ; New York, 5th ed edition, 2011. URL `https://global.oup.com/academic/product/molecular-quantum-mechanics-9780199541423?cc=fr&lang=en&`.

[9] Maurice de Broglie. Sur une nouveau procédé permettant d'obtenir la photographie des spectres de raies des rayons Röntgen. *Acad'emie des sciences*, 157:924–926, 1913. URL `https://gallica.bnf.fr/ark:/12148/bpt6k31103/f924`.

[10] H. G. J. Moseley. XCIII. The high-frequency spectra of the elements . *The London, Edinburgh, and Dublin Philosophical Magazine and Journal of Science*, 26(156):1024–1034, 1913. doi:10.1080/14786441308635052.

[11] Manne Siegbahn. Röntgenspektroskopische Präzisionsmessungen. *Annalen der Physik*, 364 (9):56–72, 1919. doi:10.1002/andp.19193640906.

[12] Manne Siegbahn. LVIII. Precision-measurements in the X-ray spectra. *The London, Edinburgh, and Dublin Philosophical Magazine and Journal of Science*, 37(222):601–612, 1919. doi:10.1080/14786440608635923.

[13] W. Stenström. Experimentelle Untersuchungen der Röntgenspektra. M-Reihe. *Annalen der Physik*, 362(21):347–375, 1918. doi:10.1002/andp.19183622103.

[14] Antonio Bianconi. Surface X-ray absorption spectroscopy: Surface EXAFS and surface XANES. *Applications of Surface Science*, 6(3-4):392–418, nov 1980. doi:10.1016/0378-5963(80)90024-0.

[15] Stumm von Bordwehr. A History of X-ray absorption fine structure. *Annales de Physique*, 14 (4):377–465, jun 1989. doi:10.1051/anphys:01989001404037700.

[16] Carlo Lamberti and Jeroen A. van Bokhoven. Introduction: Historical Perspective on XAS. In *X-Ray Absorption and X-Ray Emission Spectroscopy*, chapter 1, pages 1–21. John Wiley & Sons, Ltd, 2016. doi:10.1002/9781118844243.ch1.

[17] S. Doniach, K. Hodgson, I. Lindau, P. Pianetta, and H. Winick. Early Work with Synchrotron Radiation at Stanford. *Journal of Synchrotron Radiation*, 4(6):380–395, Nov 1997. doi:10.1107/S0909049597012235.

[18] Kwang-Je Kim. Characteristics of synchrotron radiation. *AIP Conference Proceedings*, 184 (1):565–632, 04 1989. doi:10.1063/1.38046.

[19] B. D. Patterson. A simplified approach to synchrotron radiation. *American Journal of Physics*, 79(10):1046–1052, 10 2011. doi:10.1119/1.3614033.

[20] Paul Emma, R Akre, J Arthur, R Bionta, C Bostedt, J Bozek, A Brachmann, P Bucksbaum, Ryan Coffee, F-J Decker, et al. First lasing and operation of an ångstrom-wavelength free-electron laser. *nature photonics*, 4(9):641–647, 2010. doi:10.1038/nphoton.2010.176.

[21] Ofer Kfir, Eliyahu Bordo, Gil Ilan Haham, Oren Lahav, Avner Fleischer, and Oren Cohen. In-line production of a bi-circular field for generation of helically polarized high-order harmonics. *Applied Physics Letters*, 108(21):211106, 05 2016. doi:10.1063/1.4952436.

[22] Tami E. Westre, Pierre Kennepohl, Jane G. DeWitt, Britt Hedman, Keith O. Hodgson, and Edward I. Solomon. A Multiplet Analysis of Fe K-Edge 1s → 3d Pre-Edge Features of Iron Complexes. *Journal of the American Chemical Society*, 119(27):6297–6314, 1997. doi:10.1021/ja964352a.

[23] Pekka Pyykko. Relativistic effects in structural chemistry. *Chemical Reviews*, 88(3):563–594, 1988. doi:10.1021/cr00085a006.

[24] Thomas Fransson, Sonia Coriani, Ove Christiansen, and Patrick Norman. Carbon X-ray absorption spectra of fluoroethenes and acetone: A study at the coupled cluster, density functional, and static-exchange levels of theory. *The Journal of Chemical Physics*, 138(12): 124311, 2013. doi:10.1063/1.4795835.

[25] Kai Siegbahn. Electron spectroscopy for atoms, molecules, and condensed matter. *Reviews of Modern Physics*, 54(3):709, 1982. doi:10.1103/RevModPhys.54.709.

[26] Markus Drescher, Michael Hentschel, R Kienberger, Matthias Uiberacker, Vladislav Yakovlev, Armin Scrinzi, Th Westerwalbesloh, U Kleineberg, Ulrich Heinzmann, and Ferenc Krausz. Time-resolved atomic inner-shell spectroscopy. *Nature*, 419(6909):803–807, 2002. doi:10.1038/nature01143.

[27] Stephan Bernadotte, Andrew J Atkins, and Christoph R Jacob. Origin-independent calculation of quadrupole intensities in X-ray spectroscopy. *The Journal of chemical physics*, 137 (20):204106, 2012. doi:10.1063/1.4766359.

[28] Patrick J. Lestrange, Franco Egidi, and Xiaosong Li. The consequences of improperly describing oscillator strengths beyond the electric dipole approximation. *The Journal of Chemical Physics*, 143(23):234103, dec 2015. doi:10.1063/1.4937410.

[29] Lasse Kragh Sørensen, Meiyuan Guo, Roland Lindh, and Marcus Lundberg. Applications to metal K pre-edges of transition metal dimers illustrate the approximate origin independence for the intensities in the length representation. *Molecular Physics*, 115(1-2):174–189, 2017. doi:10.1080/00268976.2016.1225993.

[30] Lasse Kragh Sørensen, Roland Lindh, and Marcus Lundberg. Gauge origin independence in finite basis sets and perturbation theory. *Chemical Physics Letters*, 683:536–542, 2017. doi:10.1016/j.cplett.2017.05.003.

[31] Nanna Holmgaard List, Joanna Kauczor, Trond Saue, Hans Jørgen Aa. Jensen, and Patrick Norman. Beyond the electric-dipole approximation: A formulation and implementation of molecular response theory for the description of absorption of electromagnetic field radiation. *The Journal of chemical physics*, 142(24):244111, 2015. doi:10.1063/1.4922697.

[32] Nanna Holmgaard List, Trond Saue, and Patrick Norman. Rotationally averaged linear absorption spectra beyond the electric-dipole approximation. *Molecular Physics*, 115(1-2):63–74, 2017. doi:10.1080/00268976.2016.1187773.

[33] Lasse Kragh Sørensen, Emil Kieri, Shruti Srivastav, Marcus Lundberg, and Roland Lindh. Implementation of a semiclassical light-matter interaction using the Gauss-Hermite quadrature: A simple alternative to the multipole expansion. *Physical Review A*, 99(1):013419, 2019. doi:10.1103/PhysRevA.99.013419.

[34] Nicolás O. Foglia, Dimitrios Maganas, and Frank Neese. Going beyond the electric-dipole approximation in the calculation of absorption and (magnetic) circular dichroism spectra including scalar relativistic and spin–orbit coupling effects. *The Journal of Chemical Physics*, 157(8):084120, 08 2022. doi:10.1063/5.0094709.

[35] Mickaël G Delcey, Rafael Carvalho Couto, Lasse Kragh Sørensen, Ignacio Fdez. Galván, Meiyuan Guo, Roland Lindh, and Marcus Lundberg. Exact semi-classical light–matter interaction operator applied to two-photon processes with strong relativistic effects. *The Journal of Chemical Physics*, 153(2):024114, 2020. doi:10.1063/5.0007833.

[36] Einar Aurbakken, Benedicte Sverdrup Ofstad, Håkon Emil Kristiansen, Øyvind Sigmundson Schøyen, Simen Kvaal, Lasse Kragh Sørensen, Roland Lindh, and Thomas Bondo Pedersen. Transient spectroscopy from time-dependent electronic-structure theory without multipole expansions. 2023. doi:10.48550/arXiv.2307.02519.

[37] Trond Saue, Radovan Bast, André Severo Pereira Gomes, Hans Jørgen Aa. Jensen, Lucas Visscher, Ignacio Agustín Aucar, Roberto Di Remigio, Kenneth G Dyall, Ephraim Eliav, Elke Fasshauer, et al. The DIRAC code for relativistic molecular calculations. *The Journal of chemical physics*, 152(20):204104, 2020. doi:10.1063/5.0004844.

[38] Johannes Flick, Michael Ruggenthaler, Heiko Appel, and Angel Rubio. Atoms and molecules in cavities, from weak to strong coupling in quantum-electrodynamics (QED) chemistry. *Proceedings of the National Academy of Sciences*, 114(12):3026–3034, 2017. doi:10.1073/pnas.1615509114.

[39] Rosario R Riso, Tor S Haugland, Enrico Ronca, and Henrik Koch. Molecular orbital theory in cavity QED environments. *Nature Communications*, 13(1):1368, 2022. doi:10.1038/s41467-022-29003-2.

[40] David J Griffiths. *Introduction to electrodynamics; 3rd ed.* Prentice-Hall, Upper Saddle River, NJ, 1999. URL `https://cds.cern.ch/record/611579`.

[41] John David Jackson. *Classical electrodynamics.* Wiley, New York, NY, 3rd ed. edition, 1999. URL `http://cdsweb.cern.ch/record/490457`.

[42] Viktor Weisskopf. Probleme der neueren Quantentheorie des Elektrons. *Naturwissenschaften*, 23(37):631–637, 1935. doi:10.1007/BF01491091.

[43] Paul Adrien Maurice Dirac. The quantum theory of the emission and absorption of radiation. *Proceedings of the Royal Society of London. Series A, Containing Papers of a Mathematical and Physical Character*, 114(767):243–265, 1927. doi:10.1098/rspa.1927.0039.

[44] Enrico Fermi. *Nuclear physics: a course given by Enrico Fermi at the University of Chicago.* University of Chicago Press, 1950.

[45] Jens Oddershede, Poul Jørgensen, and Danny L. Yeager. Polarization propagator methods in atomic and molecular calculations. *Computer Physics Reports*, 2(2):33–92, 1984. doi:10.1016/0167-7977(84)90003-0.

[46] Jan Linderberg and Yngve Öhrn. *Propagators in quantum chemistry.* John Wiley & Sons, 2nd edition, 2004. doi:10.1002/0471721549.

[47] Patrick Norman, David M. Bishop, Hans Jørgen Aa. Jensen, and Jens Oddershede. Near-resonant absorption in the time-dependent self-consistent field and multiconfigurational self-consistent field approximations. *The Journal of Chemical Physics*, 115(22):10323–10334, 12 2001. doi:10.1063/1.1415081.

[48] B.J. Orr and J.F. Ward. Perturbation theory of the non-linear optical polarization of an isolated system. *Molecular Physics*, 20(3):513–526, 1971. doi:10.1080/00268977100100481.

[49] Auayporn Jiemchooroj and Patrick Norman. Electronic circular dichroism spectra from the complex polarization propagator. *The Journal of Chemical Physics*, 126(13):134102, 04 2007. doi:10.1063/1.2716660.

[50] Auayporn Jiemchooroj, Ulf Ekström, and Patrick Norman. Near-edge x-ray absorption and natural circular dichroism spectra of L-alanine: A theoretical study based on the complex polarization propagator approach. *The Journal of Chemical Physics*, 127(16):165104, 10 2007. doi:10.1063/1.2800024.

[51] Ulf Ekström and Patrick Norman. X-ray absorption spectra from the resonant-convergent first-order polarization propagator approach. *Phys. Rev. A*, 74:042722, Oct 2006. doi:10.1103/PhysRevA.74.042722.

[52] Ulf Ekström, Patrick Norman, Vincenzo Carravetta, and Hans Ågren. Polarization propagator for x-ray spectra. *Phys. Rev. Lett.*, 97:143001, Oct 2006. doi:10.1103/PhysRevLett.97.143001.

[53] P. Hohenberg and W. Kohn. Inhomogeneous Electron Gas. *Phys. Rev.*, 136:B864–B871, Nov 1964. doi:10.1103/PhysRev.136.B864.

[54] W. Kohn and L. J. Sham. Self-Consistent Equations Including Exchange and Correlation Effects. *Phys. Rev.*, 140:A1133–A1138, Nov 1965. doi:10.1103/PhysRev.140.A1133.

[55] Helgaker, Trygve and Jørgensen, Poul and Olsen, Jeppe. Second quantization. In *Molecular Electronic-Structure Theory*, chapter 1, pages 1–33. John Wiley & Sons, Ltd, 2000. doi:10.1002/9781119019572.ch1.

[56] Trond Saue and Trygve Helgaker. Four-component relativistic Kohn–Sham theory. *Journal of computational chemistry*, 23(8):814–823, 2002. doi:10.1002/jcc.10066.

[57] Axel D. Becke. A new mixing of Hartree–Fock and local density-functional theories. *The Journal of Chemical Physics*, 98(2):1372–1377, 01 1993. doi:10.1063/1.464304.

[58] J. H. Van Lenthe, R. Zwaans, H. J. J. Van Dam, and M. F. Guest. Starting SCF calculations by superposition of atomic densities. *Journal of Computational Chemistry*, 27(8):926–932, 2006. doi:10.1002/jcc.20393.

[59] Patrick Norman and Hans Jørgen Aa. Jensen. Phosphorescence parameters for platinum (II) organometallic chromophores: A study at the non-collinear four-component Kohn–Sham level of theory. *Chemical Physics Letters*, 531:229–235, 2012. doi:10.1016/j.cplett.2012.02.012.

[60] Susi Lehtola, Lucas Visscher, and Eberhard Engel. Efficient implementation of the superposition of atomic potentials initial guess for electronic structure calculations in Gaussian basis sets. *The Journal of Chemical Physics*, 152(14):144105, 04 2020. doi:10.1063/5.0004046.

[61] C. C. J. Roothaan. New Developments in Molecular Orbital Theory. *Rev. Mod. Phys.*, 23: 69–89, Apr 1951. doi:10.1103/RevModPhys.23.69.

[62] Frank Jensen. *Introduction to computational chemistry*. John wiley & sons, second edition, 2017. URL `https://www.wiley.com/en-us/Introduction+to+Computational+Chemistry,+2nd+Edition-p-9780470058046`.

[63] Charlotte Froese-Fischer, Tomas Brage, and P Johnsson. *Computational atomic structure: an MCHF approach*. CRC press, 1997. doi:10.1201/9781315139982.

[64] Hans Hellmann. Einführung in die Quantenchemie. In Dirk Andrae, editor, *Hans Hellmann: Einführung in die Quantenchemie: Mit biografischen Notizen von Hans Hellmann jr.*, page 285. Springer Berlin Heidelberg, Berlin, Heidelberg, 2015. doi:10.1007/978-3-662-45967-6_2.

[65] R. P. Feynman. Forces in molecules. *Phys. Rev.*, 56:340–343, Aug 1939. doi:10.1103/PhysRev.56.340.

[66] Frédéric London. Théorie quantique des courants interatomiques dans les combinaisons aromatiques. *Journal De Physique Et Le Radium*, 8:397–409, 1937. doi:10.1051/jphysrad:01937008010039700.

[67] Jon H. Shirley. Solution of the schrödinger equation with a hamiltonian periodic in time. *Phys. Rev.*, 138:B979–B987, May 1965. doi:10.1103/PhysRev.138.B979.

[68] Ralph H. Young, Walter J. Deal Jr., and Neil R. Kestner. Quasi-periodic states of an oscillatory hamiltonian. *Molecular Physics*, 17(4):369–376, 1969. doi:10.1080/00268976900101141.

[69] Hideo Sambe. Steady States and Quasienergies of a Quantum-Mechanical System in an Oscillating Field. *Phys. Rev. A*, 7:2203–2213, Jun 1973. doi:10.1103/PhysRevA.7.2203.

[70] P. W. Langhoff, S. T. Epstein, and M. Karplus. Aspects of Time-Dependent Perturbation Theory. *Rev. Mod. Phys.*, 44:602–644, Jul 1972. doi:10.1103/RevModPhys.44.602.

[71] O. Christiansen, P. Jørgensen, and C. Hättig. Response Functions from Fourier Component Variational Perturbation Theory Applied to a Time-Averaged Quasienergy. *Int. J. Quant. Chem.*, 68:1–52, 1998. doi:10.1002/(SICI)1097-461X(1998)68:1<1::AID-QUA1>3.0.CO;2-Z.

[72] Erich Runge and Eberhard KU Gross. Density-functional theory for time-dependent systems. *Physical review letters*, 52(12):997, 1984. doi:10.1103/PhysRevLett.52.997.

[73] B. M. Deb and Swapan K. Ghosh. Schrödinger fluid dynamics of many-electron systems in a time-dependent density-functional framework. *Journal of Chemical Physics*, 77:342–348, 1982. doi:10.1063/1.443611.

[74] Fumihiko Aiga, Tsukasa Tada, and Reiko Yoshimura. Frequency-dependent polarizabilities, hyperpolarizabilities, and excitation energies from time-dependent density-functional theory based on the quasienergy derivative method. *The Journal of chemical physics*, 111(7):2878–2888, 1999. doi:10.1063/1.479570.

[75] Pawel Salek, Trygve Helgaker, and Trond Saue. Linear response at the 4-component relativistic density-functional level: application to the frequency-dependent dipole polarizability of Hg, AuH and PtH2. *Chemical Physics*, 311(1):187–201, 2005. doi:10.1016/j.chemphys.2004.10.011.

[76] E. K. U. Gross and Walter Kohn. Local density-functional theory of frequency-dependent linear response. *Phys. Rev. Lett.*, 55:2850–2852, Dec 1985. doi:10.1103/PhysRevLett.55.2850.

[77] T. H. Dunning and V. McKoy. Nonempirical Calculations on Excited States: The Ethylene Molecule. *J. Chem. Phys.*, 47:1735, 1967. doi:10.1063/1.1712158.

[78] Casida Mark E. Time-Dependent Density Functional Response Theory for Molecules. In *Recent Advances in Density Functional Methods*, pages 155–192. doi:10.1142/9789812830586_0005.

[79] Radovan Bast, Hans Jørgen Aa. Jensen, and Trond Saue. Relativistic adiabatic time-dependent density functional theory using hybrid functionals and noncollinear spin magnetization. *International Journal of Quantum Chemistry*, 109(10):2091–2112, 2009. doi:10.1002/qua.22065.

[80] D. J. Rowe. Equations-of-motion method and the extended shell model. *Rev. Mod. Phys.*, 40:153–166, Jan 1968. doi:10.1103/RevModPhys.40.153.

[81] Paul Adrien Maurice Dirac and Ralph Howard Fowler. A theory of electrons and protons. *Proceedings of the Royal Society of London. Series A, Containing Papers of a Mathematical and Physical Character*, 126(801):360–365, 1930. doi:10.1098/rspa.1930.0013.

[82] P. Pyykkö. On the relativistic theory of NMR chemical shifts. *Chemical Physics*, 74(1):1–7, 1983. doi:10.1016/0301-0104(83)80001-9.

[83] Proton, carbon, and cadmium nmr measurements and relativistic calculation of the cadmium-carbon coin tensor in dimethyl cadmium. *Journal of Magnetic Resonance*, 31(1):121–132, 1978. doi:10.1016/0022-2364(78)90175-0.

[84] J. Jokisaari, K. Räisänen, J. Kuonanoja, P. Pyykkö, and L. Lajunen. The r_α-structure and anisotropy of the Hg-C indirect coupling constant of methylmercury nitrate dissolved in nematic and lyotropic liquid crystals. *Molecular Physics*, 39(3):715–723, 1980. doi:10.1080/00268978000100611.

[85] S. Knecht, S. Fux, R. van Meer, L. Visscher, M. Reiher, and T. Saue. Mössbauer spectroscopy for heavy elements: a relativistic benchmark study of mercury. *Theoretical Chemistry Accounts*, 2011(129):631, 2011. doi:10.1007/s00214-011-0911-2.

[86] Erik Donovan Hedegård, Stefan Knecht, Ulf Ryde, Jacob Kongsted, and Trond Saue. Theoretical ^{57}Fe Mössbauer spectroscopy: isomer shifts of [Fe]-hydrogenase intermediates. *Physical Chemistry Chemical Physics*, 16(10):4853–4863, 2014. doi:10.1039/C3CP54393E.

[87] Tamar Zelovich, Anastasia Borschevsky, Ephraim Eliav, and Uzi Kaldor. Relativistic coupled cluster calculation of Mössbauer isomer shifts of iodine compounds. *Molecular Physics*, 115: 138 – 143, 2017. doi:10.1080/00268976.2016.1203036.

[88] Albert Einstein. Zur elektrodynamik bewegter körper. *Annalen der physik*, 4, 1905. doi:10.1002/andp.19053221004.

[89] Trond Saue. *Principles and applications of relativistic molecular calculations*. PhD thesis, University of Oslo, 1996. URL `https://diracprogram.org/lib/exe/fetch.php?media=dissertations:trond_saue.pdf`.

[90] Kenneth G Dyall and Knut Fægri Jr. *Introduction to relativistic quantum chemistry*. Oxford University Press, 2007. doi:10.1093/oso/9780195140866.001.0001.

[91] Hendrik Antoon Lorentz. De relatieve beweging van de aarde en den aether. *Zittingsverlag Akad. V. Wet.*, 1:74–79, 1892. URL `https://www.lorentz.leidenuniv.nl/IL-publications/sources/Lorentz_KNAW_1892b.pdf`.

[92] George Franscis FitzGerald. The Ether and the Earth's Atmosphere. *Science*, ns-13(328): 390–390, 1889. doi:10.1126/science.ns-13.328.390.a.

[93] Joseph Larmor. A dynamical theory of the electric and luminiferous medium. *Proceedings of the Royal Society of London*, 54:438–461, 1893. URL `http://www.jstor.org/stable/115551`.

[94] Emil Cohn. *Zur Elektrodynamik bewegter Systeme I*. Deutsche Akademie der Wissenschaften zu Berlin, 1904. URL `https://archive.org/details/sitzungsberichte1904deut`.

[95] Hermann Minkowski. Die Grundgleichungen für die elektromagnetischen Vorgänge in bewegten Körpern. *Nachrichten von der Gesellschaft der Wissenschaften zu Göttingen, Mathematisch-Physikalische Klasse*, 1908:53–111, 1908. doi:10.1007/BF01455871.

[96] Hendrik Antoon Lorentz. Electromagnetic Phenomena in a System Moving with any Velocity Smaller than that of Light. In *Collected Papers: Volume V*, pages 172–197. Springer Netherlands, Dordrecht, 1937. doi:10.1007/978-94-015-3445-1_5.

[97] H. Helmholtz. Über Integrale der hydrodynamischen Gleichungen, welche den Wirbelbewegungen entsprechen. 1858(55):25–55, 1858. doi:doi:10.1515/crll.1858.55.25.

[98] George Gabriel Stokes. On the dynamical theory of diffraction. In *Mathematical and Physical Papers*, volume 2 of *Cambridge Library Collection - Mathematics*, page 243–328. Cambridge University Press, 2009. doi:10.1017/CBO9780511702259.015.

[99] J. D. Jackson and L. B. Okun. Historical roots of gauge invariance. *Rev. Mod. Phys.*, 73: 663–680, Sep 2001. doi:10.1103/RevModPhys.73.663.

[100] J. D. Jackson. From Lorenz to Coulomb and other explicit gauge transformations. *American Journal of Physics*, 70(9):917–928, aug 2002. doi:10.1119/1.1491265.

[101] Albert Einstein. Ist die Trägheit eines Körpers von seinem Energieinhalt abhängig? *Annalen der Physik*, 323(13):639–641, 1905. doi:10.1002/andp.19053231314.

[102] K. Schwarzschild. Zur Elektrodynamik: I. Zwei Formen des Princips der kleinsten Action in der Elektrontheorie. *Gött. Nach., Math.-Phys. Kl.*, page 126, 1903. URL `http://www.digizeitschriften.de/dms/resolveppn/?PID=GDZPPN002499665`.

[103] Murray Gell-Mann. The interpretation of the new particles as displaced charge multiplets. *Il Nuovo Cimento (1955-1965)*, 4:848–866, 1956. doi:10.1007/BF02748000.

[104] T. Saue. Post Dirac-Hartree-Fock Methods - Properties. In P. Schwerdtfeger, editor, *Relativistic Electronic Structure Theory. Part 1. Fundamentals*, page 332. Elsevier, Amsterdam, 2002. doi:10.1016/S1380-7323(02)80033-4.

[105] Walter Gordon. Der comptoneffekt nach der schrödingerschen theorie. *Zeitschrift für Physik*, 40(1-2):117–133, 1926. doi:10.1007/BF01390840.

[106] Helge Kragh. Equation with the many fathers. The Klein–Gordon equation in 1926. *American Journal of Physics*, 52(11):1024–1033, 11 1984. doi:10.1119/1.13782.

[107] Paul Adrien Maurice Dirac. The quantum theory of the electron. *Proceedings of the Royal Society of London. Series A, Containing Papers of a Mathematical and Physical Character*, 117(778):610–624, 1928. doi:10.1098/rspa.1928.0023.

[108] Erwin Schrödinger. Über die kräftefreie bewegung in der relativistischen quantenmechanik. 1930.

[109] Paul Strange. *Separating Particles from Antiparticles*, page 199–226. Cambridge University Press, 1998. doi:10.1017/CBO9780511622755.008.

[110] Maen Salman. *Quantum electrodynamic corrections in quantum chemistry.* PhD thesis, Université Paul Sabatier-Toulouse III, 2022. URL `https://www.theses.fr/2022TOU30032`.

[111] Carl D. Anderson. The Positive Electron. *Phys. Rev.*, 43:491–494, Mar 1933. doi:10.1103/PhysRev.43.491.

[112] Radosław Szmytkowski. Recurrence and Differential Relations for Spherical Spinors. *Journal of Mathematical Chemistry*, 42(3):397–413, may 2006. doi:10.1007/s10910-006-9110-0.

[113] I. P. Grant. The Dirac Equation. In *Relativistic Quantum Theory of Atoms and Molecules: Theory and Computation*, pages 121–179. Springer New York, New York, NY, 2007. doi:10.1007/978-0-387-35069-1_3.

[114] Markus Reiher and Alexander Wolf. The Dirac Hydrogen Atom. In *Relativistic Quantum Chemistry*, chapter 6, pages 193–234. John Wiley & Sons, Ltd, 2014. doi:10.1002/9783527667550.ch6.

[115] L. Visscher and K.G. Dyall. Dirac–Fock atomic electronic structure calculations using different nuclear charge distributions. *Atomic Data and Nuclear Data Tables*, 67(2):207–224, 1997. doi:10.1006/adnd.1997.0751.

[116] F. A. Parpia and A. K. Mohanty. Relativistic basis-set calculations for atoms with Fermi nuclei. *Phys. Rev. A*, 46:3735–3745, Oct 1992. doi:10.1103/PhysRevA.46.3735.

[117] Trond Saue. Relativistic Hamiltonians for Chemistry: A Primer. *ChemPhysChem*, 12(17): 3077–3094, 2011. doi:10.1002/cphc.201100682.

[118] G. Breit. The Effect of Retardation on the Interaction of Two Electrons. *Phys. Rev.*, 34: 553–573, Aug 1929. doi:10.1103/PhysRev.34.553.

[119] J. A. Gaunt. IV. The triplets of helium. *Philosophical Transactions of the Royal Society of London. Series A, Containing Papers of a Mathematical or Physical Character*, 228(659-669): 151–196, 1929. doi:10.1098/rsta.1929.0004.

[120] Keh-Ning Huang. Orbit–orbit interaction. *The Journal of Chemical Physics*, 71(9):3830–3836, 07 2008. doi:10.1063/1.438792.

[121] E. Engel and R. M. Dreizler. Relativistic density functional theory. In R. F. Nalewajski, editor, *Density Functional Theory II: Relativistic and Time Dependent Extensions*, pages 1–80. Springer Berlin Heidelberg, Berlin, Heidelberg, 1996. doi:10.1007/BFb0016642.

[122] G. A. Aucar, T. Saue, L. Visscher, and H. J. Aa. Jensen. On the origin and contribution of the diamagnetic term in four-component relativistic calculations of magnetic properties. *The Journal of Chemical Physics*, 110(13):6208–6218, 04 1999. doi:10.1063/1.479181.

[123] James D. Talman. Minimax Principle for the Dirac Equation. *Phys. Rev. Lett.*, 57:1091–1094, Sep 1986. doi:10.1103/PhysRevLett.57.1091.

[124] Knut Faegri Jr. Relativistic Gaussian basis sets for the elements K–Uuo. *Theoretical Chemistry Accounts*, 105:252–258, 2001. doi:10.1007/s002140000209.

[125] Yong-Ki Kim. Relativistic Self-Consistent-Field Theory for Closed-Shell Atoms. *Phys. Rev.*, 154:17–39, Feb 1967. doi:10.1103/PhysRev.154.17.

[126] W. N. Asaad. Relativistic K Electron Wave Functions by the Variational Principle. *Proceedings of the Physical Society*, 76(5):641, nov 1960. doi:10.1088/0370-1328/76/5/304.

[127] W.H.E. Schwarz and H. Wallmeier. Basis set expansions of relativistic molecular wave equations. *Molecular Physics*, 46(5):1045–1061, 1982. doi:10.1080/00268978200101771.

[128] Ian P Grant. Conditions for convergence of variational solutions of Dirac's equation in a finite basis. *Physical Review A*, 25(2):1230, 1982. doi:10.1103/PhysRevA.25.1230.

[129] Holger Wallmeier and Werner Kutzelnigg. Basis-set expansion of the Dirac equation without variational collapse: Numerical test of the forth-back free-particle Foldy-Wouthuysen transformation. *Phys. Rev. A*, 28:3092–3094, Nov 1983. doi:10.1103/PhysRevA.28.3092.

[130] K G Dyall, I P Grant, and S Wilson. Matrix representation of operator products. *Journal of Physics B: Atomic and Molecular Physics*, 17(4):493, feb 1984. doi:10.1088/0022-3700/17/4/006.

[131] Richard E. Stanton and Stephen Havriliak. Kinetic balance: A partial solution to the problem of variational safety in Dirac calculations. *The Journal of chemical physics*, 81(4):1910–1918, 1984. doi:10.1063/1.447865.

[132] Kenneth G. Dyall. An exact separation of the spin-free and spin-dependent terms of the Dirac–Coulomb–Breit Hamiltonian. *The Journal of Chemical Physics*, 100(3):2118–2127, 02 1994. doi:10.1063/1.466508.

[133] Hans Jørgen Aagaard Jensen and Miroslav Iliaš. BSS / DKH infinite order the easy way ! (Talk from REHE 2005). 3 2020. doi:10.6084/m9.figshare.12046158.v3.

[134] Miroslav Iliaš, Hans Jørgen Aa. Jensen, Vladimir Kellö, Björn O. Roos, and Miroslav Urban. Theoretical study of PbO and the PbO anion. *Chemical Physics Letters*, 408(4):210–215, 2005. doi:10.1016/j.cplett.2005.04.027.

[135] Werner Kutzelnigg and Wenjian Liu. Quasirelativistic theory equivalent to fully relativistic theory. *The Journal of Chemical Physics*, 123(24):241102, 12 2005. doi:10.1063/1.2137315.

[136] Miroslav Iliaš and Trond Saue. An infinite-order two-component relativistic Hamiltonian by a simple one-step transformation. *The Journal of Chemical Physics*, 126(6):064102, 02 2007. doi:10.1063/1.2436882.

[137] Ch Chang, M Pelissier, and Ph Durand. Regular Two-Component Pauli-Like Effective Hamiltonians in Dirac Theory. *Physica Scripta*, 34(5):394, nov 1986. doi:10.1088/0031-8949/34/5/007.

[138] E. van Lenthe, E. J. Baerends, and J. G. Snijders. Relativistic regular two-component Hamiltonians. *The Journal of Chemical Physics*, 99(6):4597–4610, 09 1993. doi:10.1063/1.466059.

[139] E. van Lenthe, J. G. Snijders, and E. J. Baerends. The zero-order regular approximation for relativistic effects: The effect of spin–orbit coupling in closed shell molecules. *The Journal of Chemical Physics*, 105(15):6505–6516, 10 1996. doi:10.1063/1.472460.

[140] Marvin Douglas and Norman M Kroll. Quantum electrodynamical corrections to the fine structure of helium. *Annals of Physics*, 82(1):89–155, 1974. doi:10.1016/0003-4916(74)90333-9.

[141] Bernd A. Hess. Applicability of the no-pair equation with free-particle projection operators to atomic and molecular structure calculations. *Phys. Rev. A*, 32:756–763, Aug 1985. doi:10.1103/PhysRevA.32.756.

[142] Bernd A. Hess. Relativistic electronic-structure calculations employing a two-component no-pair formalism with external-field projection operators. *Phys. Rev. A*, 33:3742–3748, Jun 1986. doi:10.1103/PhysRevA.33.3742.

[143] Hendrik Antoon Kramers. Théorie générale de la rotation paramagnétique dans les cristaux. *Proc. Acad. Amst*, 33(6), 1930. URL `https://dwc.knaw.nl/DL/publications/PU00015981.pdf`.

[144] GA Aucar, HJ Aa Jensen, and J Oddershede. Operator representations in kramers bases. *Chemical physics letters*, 232(1-2):47–53, 1995. doi:10.1016/0009-2614(94)01332-p.

[145] Trond Saue and HJ Aa Jensen. Quaternion symmetry in relativistic molecular calculations: The Dirac–Hartree–Fock method. *The Journal of chemical physics*, 111(14):6211–6222, 1999. doi:10.1063/1.479958.

[146] T. Saue and H. J. Aa. Jensen. Linear response at the 4-component relativistic level: Application to the frequency-dependent dipole polarizabilities of the coinage metal dimers. *The Journal of Chemical Physics*, 118(2):522–536, 12 2002. doi:10.1063/1.1522407.

[147] Anthony Stone. *The Theory of Intermolecular Forces*. Oxford University Press, 01 2013. doi:10.1093/acprof:oso/9780199672394.001.0001.

[148] Laurence D. Barron. A historical review of optical activity phenomena. In *Molecular Light Scattering and Optical Activity*, page 1–52. Cambridge University Press, 2 edition, 2004. doi:10.1017/CBO9780511535468.003.

[149] Christine Isborn, Kacey Claborn, and Bart Kahr. The optical rotatory power of water. *The Journal of Physical Chemistry A*, 111(32):7800–7804, 2007. doi:10.1021/jp073439n.

[150] Marjan Khamesian, Ignacio Fdez Galván, Mickaël G Delcey, Lasse Kragh Sørensen, and Roland Lindh. Spectroscopy of linear and circular polarized light with the exact semiclassical light–matter interaction. In *Annual Reports in Computational Chemistry*, volume 15, pages 39–76. Elsevier, 2019. doi:10.1016/bs.arcc.2019.08.004.

[151] Nan Yang, Yiqiao Tang, and Adam E Cohen. Spectroscopy in sculpted fields. *Nano Today*, 4 (3):269–279, 2009. doi:10.1016/j.nantod.2009.05.001.

[152] S. E. Braslavsky. Glossary of terms used in photochemistry, 3rd edition (IUPAC Recommendations 2006). *Pure and Applied Chemistry*, 79(3):293 – 465, 2007. doi:10.1351/pac200779030293.

[153] A.E. Hansen and J. Avery. A fully retarded expression for the rotatory strength. *Chemical Physics Letters*, 13(4):396 – 398, 1972. doi:10.1016/0009-2614(72)80109-X.

[154] Paolo Lazzeretti, Massimo Malagoli, and Riccardo Zanasi. Computational approach to molecular magnetic properties by continuous transformation of the origin of the current density. *Chemical Physics Letters*, 220(3):299–304, 1994. doi:10.1016/0009-2614(94)00158-8.

[155] Francesco Ferdinando Summa, Riccardo Zanasi, and Paolo Lazzeretti. On the computation of frequency-dependent molecular magnetizabilities via dynamical charge and current electron densities. *Journal of Computational Chemistry*, 44(16):1517–1530, 2023. doi:10.1002/jcc.27106.

[156] F. Bloch. Zur Wirkung äußerer elektromagnetischer Felder auf kleine Systeme. In Fritz Bopp, editor, *Werner Heisenberg und die Physik unserer Zeit*, pages 93–102. Vieweg+Teubner Verlag, Wiesbaden, 1961. doi:10.1007/978-3-663-05439-9_9.

[157] L. D. Barron and C. G. Gray. The multipole interaction Hamiltonian for time dependent fields. *Journal of Physics A: Mathematical, Nuclear and General*, 6(1):59, jan 1973. doi:10.1088/0305-4470/6/1/006.

[158] Wesley E. Brittin, W. Rodman Smythe, and Walter Wyss. Poincaré gauge in electrodynamics. *American Journal of Physics*, 50(8):693–696, 08 1982. doi:10.1119/1.12731.

[159] Donald H. Kobe. Gauge transformations and the electric dipole approximation. *American Journal of Physics*, 50(2):128–133, 02 1982. doi:10.1119/1.13029.

[160] V. Fock. Über die invariante Form der Wellen- under Bewegungsgleichungen für einen geladenen Massenpunkt. *Z. Phys.*, 39:226–232, 1926. doi:10.1007/BF01321989.

[161] L.D. Faddeev, L.A. Khalfin, and I.V. Komarov, editors. *V.A. Fock - Selected Works: Quantum Mechanics and Quantum Field Theory*. CRC Press, 2019. URL `https://www.routledge.com/VA-Fock---Selected-Works-Quantum-Mechanics-and-Quantum-Field-Theory/Faddeev-Khalfin-Komarov/p/book/9780367394301`.

[162] Filipp Furche. On the density matrix based approach to time-dependent density functional response theory. *The Journal of Chemical Physics*, 114(14):5982–5992, 2001. doi:10.1063/1.1353585.

[163] Thomas Bondo Pedersen and Henrik Koch. Coupled cluster response functions revisited. *The Journal of Chemical Physics*, 106(19):8059–8072, 05 1997. doi:10.1063/1.473814.

[164] Jeppe Olsen and Poul Jørgensen. Linear and nonlinear response functions for an exact state and for an MCSCF state. *The Journal of chemical physics*, 82(7):3235–3264, 1985. doi:10.1063/1.448223.

[165] K. G. Dyall, I. P. Grant, and S. Wilson. Matrix representation of operator products. *J. Phys. B*, 17:493, 1984. doi:10.1088/0022-3700/17/4/006.

[166] V. Fock. Über die Anwendbarkeit des quantenmechanischen Summensatzes. *Zeitschrift für Physik*, 89(11):744–749, Nov 1934. doi:10.1007/BF01341387.

[167] Anthony F. Starace. Length and Velocity Formulas in Approximate Oscillator-Strength Calculations. *Phys. Rev. A*, 3:1242–1245, Apr 1971. doi:10.1103/PhysRevA.3.1242.

[168] Robert A. Harris. Oscillator Strengths and Rotational Strengths in Hartree–Fock Theory. *The Journal of Chemical Physics*, 50(9):3947–3951, 1969. doi:10.1063/1.1671653.

[169] Keld L Bak, Aage E Hansen, Kenneth Ruud, Trygve Helgaker, Jeppe Olsen, and Poul Jørgensen. Ab initio calculation of electronic circular dichroism fortrans-cyclooctene using London atomic orbitals. *Theoretica chimica acta*, 90(5):441–458, 1995. doi:10.1007/BF01113546.

[170] Marco Caricato. Origin invariant optical rotation in the length dipole gauge without London atomic orbitals. *The Journal of Chemical Physics*, 153(15):151101, 2020. doi:10.1063/5.0028849.

[171] Niklas Niemeyer, Marco Caricato, and Johannes Neugebauer. Origin invariant electronic circular dichroism in the length dipole gauge without London atomic orbitals. *The Journal of Chemical Physics*, 156(15):154114, 2022. doi:10.1063/5.0088922.

[172] V. I. Lebedev. Values of the Nodes and Weights of Ninth to Seventeenth Order Gauss-Markov Quadrature Formulae Invariant under the Octahedron Group with Inversion. *USSR Comput. Math. Math. Phys.*, 15(1):44–51, 1975. doi:10.1016/0041-5553(75)90133-0.

[173] V. I. Lebedev. Quadratures on a Sphere. *USSR Comput. Math. Math. Phys.*, 16(2):10–24, 1976. doi:10.1016/0041-5553(76)90100-2.

[174] V. I. Lebedev. Spherical Quadrature Formulas Exact to Orders 25–29. *Sib. Math. J.*, 18(1): 99–107, 1977. doi:10.1007/BF00966954.

[175] V. I. Lebedev and A. L. Skorokhodov. quadrature formulas of orders 41, 47, and 53 for the sphere. *Russ. Acad. Sci. Dokl. Math.*, 45(2):587–592, 1992. URL `https://zbmath.org/?q=an%3A0795.41026`.

[176] V. I. Lebedev. a quadrature formula for the sphere of 59th algebraic order of accuracy. *Russ. Acad. Sci. Dokl. Math.*, 50(2):283–286, 1995. URL `https://zbmath.org/?q=an%3A0863.41018`.

[177] V. I. Lebedev and D. N. Laikov. A Quadrature Formula for the Sphere of the 131st Algebraic Order of Accuracy. In *Dokl. Math.*, volume 59, pages 477–481. MAIK Nauka/Interperiodica, 1999. Angular quadrature parameters available from: `http://server.ccl.net/cca/software/SOURCES/FORTRAN/Lebedev-Laikov-Grids/index.shtml`.

[178] E. A. Kearsley and J. T. Fong. Linearly independent sets of isotropic Cartesian tensors of ranks up to eight. *J. Res. Nat. Bur. Stand. B. Math. Sci.*, 79B:49–58, 1975. doi:10.6028/jres.079B.005.

[179] D. L. Andrews and N. P. Blake. Three-dimensional rotational averages in radiation-molecule interactions: an irreducible cartesian tensor formulation. *Journal of Physics A: Mathematical and General*, 22(1):49, 1989. URL `http://stacks.iop.org/0305-4470/22/i=1/a=011`.

[180] D. L. Andrews and T. Thirunamachandran. On three-dimensional rotational averages. *J. Chem. Phys.*, 67(11):5026–5033, 1977. doi:10.1063/1.434725.

[181] D L Andrews and W A Ghoul. Eighth rank isotropic tensors and rotational averages. *Journal of Physics A: Mathematical and General*, 14(6):1281, 1981. URL `http://stacks.iop.org/0305-4470/14/i=6/a=008`.

[182] Daniel H. Friese, Maarten T. P. Beerepoot, and Kenneth Ruud. Rotational averaging of multiphoton absorption cross sections. *The Journal of Chemical Physics*, 141(20):204103, 2014. doi:10.1063/1.4901563.

[183] June-Haak Ee, Dong-Won Jung, U-Rae Kim, and Jungil Lee. Combinatorics in tensor-integral reduction. *European Journal of Physics*, 38(2):025801, 2017. doi:10.1088/1361-6404/aa54ce.

[184] W. Thomas. Über die zahl der dispersionselektronen, die einem stationären zustande zugeordnet sind. (vorläufige mitteilung). *Naturwissenschaften*, 13(28):627–627, Jul 1925. doi:10.1007/BF01558908.

[185] F. Reiche and W. Thomas. Über die Zahl der Dispersionselektronen, die einem stationären Zustand zugeordnet sind. *Zeitschrift für Physik*, 34(1):510–525, dec 1925. doi:10.1007/BF01328494.

[186] W. Kuhn. Über die gesamtstärke der von einem zustande ausgehenden absorptionslinien. *Zeitschrift für Physik*, 33(1):408–412, Dec 1925. doi:10.1007/BF01328322.

[187] E. U. Condon, William Altar, and Henry Eyring. One-Electron Rotatory Power. *The Journal of Chemical Physics*, 5(10):753–775, 12 2004. doi:10.1063/1.1749938.

[188] Edward U Condon. Theories of optical rotatory power. *Reviews of modern physics*, 9(4):432, 1937. doi:10.1103/RevModPhys.9.432.

[189] Thomas Bondo Pedersen and Aage E Hansen. Ab initio calculation and display of the rotary strength tensor in the random phase approximation. Method and model studies. *Chemical Physics Letters*, 246(1-2):1–8, 1995. doi:10.1016/0009-2614(95)01036-9.

[190] DIRAC, a relativistic ab initio electronic structure program, Release DIRAC22 (2022), written by H. J. Aa. Jensen, R. Bast, A. S. P. Gomes, T. Saue and L. Visscher, with contributions from I. A. Aucar, V. Bakken, C. Chibueze, J. Creutzberg, K. G. Dyall, S. Dubillard, U. Ekström, E. Eliav, T. Enevoldsen, E. Faßhauer, T. Fleig, O. Fossgaard, L. Halbert, E. D. Hedegård, T. Helgaker, B. Helmich–Paris, J. Henriksson, M. van Horn, M. Iliaš, Ch. R. Jacob, S. Knecht, S. Komorovský, O. Kullie, J. K. Lærdahl, C. V. Larsen, Y. S. Lee, N. H. List, H. S. Nataraj, M. K. Nayak, P. Norman, G. Olejniczak, J. Olsen, J. M. H. Olsen, A. Papadopoulos, Y. C. Park, J. K. Pedersen, M. Pernpointner, J. V. Pototschnig, R. di Remigio, M. Repisky, K. Ruud, P. Sałek, B. Schimmelpfennig, B. Senjean, A. Shee, J. Sikkema, A. Sunaga, A. J. Thorvaldsen, J. Thyssen, J. van Stralen, M. L. Vidal, S. Villaume, O. Visser, T. Winther, S. Yamamoto and X. Yuan (available at `http://dx.doi.org/10.5281/zenodo.6010450`, see also `http://www.diracprogram.org`).

[191] T Helgaker and PR Taylor. Hermit, a molecular integral code. *Oslo, Norway: University of Oslo*, 1986.

[192] Jussi Lehtola, Mikko Hakala, Arto Sakko, and Keijo Hämäläinen. ERKALE—A flexible program package for X-ray properties of atoms and molecules. *Journal of computational chemistry*, 33(18):1572–1585, 2012. doi:10.1002/jcc.22987.

[193] John P Perdew, Kieron Burke, and Matthias Ernzerhof. Generalized gradient approximation made simple. *Physical Review Letters*, 77(18):3865, 1996. doi:10.1103/PhysRevLett.77.3865.

[194] Carlo Adamo and Vincenzo Barone. Toward reliable density functional methods without adjustable parameters: The PBE0 model. *The Journal of chemical physics*, 110(13):6158–6170, 1999. doi:10.1063/1.478522.

[195] Lucas Visscher. Approximate molecular relativistic Dirac-Coulomb calculations using a simple Coulombic correction. *Theoretical Chemistry Accounts*, 98(2):68–70, 1997. doi:10.1007/s002140050280.

[196] Kenneth G Dyall. Relativistic double-zeta, triple-zeta, and quadruple-zeta basis sets for the 4s, 5s, 6s, and 7s elements. *The Journal of Physical Chemistry A*, 113(45):12638–12644, 2009. doi:10.1021/jp905057q.

[197] Kenneth G Dyall. Core correlating basis functions for elements 31–118. *Theoretical Chemistry Accounts*, 131(5):1217, 2012. doi:10.1007/s00214-012-1217-8.

[198] J A Bearden and A F Burr. Reevaluation of X-ray atomic energy levels. *Reviews of Modern Physics*, 39(1):125, 1967. doi:10.1103/RevModPhys.39.125.

[199] Wolfram Research, Inc. Mathematica, Version 11.3. Champaign, IL, 2018.

[200] William L Jolly and David N Hendrickson. Thermodynamic interpretation of chemical shifts in core-electron binding energies. *Journal of the American Chemical Society*, 92(7):1863–1871, 1970. doi:10.1021/ja00710a012.

[201] Hans Ågren, Carmen Medina-Llanos, Kurt V Mikkelsen, and Hans Jørgen Aa. Jensen. On the validity of the equivalent core approximation in Born-Haber analyses of liquids and solutions. *Chemical physics letters*, 153(4):322–327, 1988. doi:10.1016/0009-2614(88)80149-0.

[202] John C Slater. Atomic shielding constants. *Physical Review*, 36(1):57, 1930. doi:10.1103/PhysRev.36.57.

[203] Jin Qian, Ethan J Crumlin, and David Prendergast. Efficient basis sets for core-excited states motivated by Slater's rules. *Physical Chemistry Chemical Physics*, 24(4):2243–2250, 2022. doi:10.1039/D1CP03931H.

[204] Delano P Chong. Completeness profiles of one-electron basis sets. *Canadian journal of chemistry*, 73(1):79–83, 1995. doi:10.1139/v95-011.

[205] Pekka Manninen and Juha Vaara. Systematic Gaussian basis-set limit using completeness-optimized primitive sets. A case for magnetic properties. *Journal of computational chemistry*, 27(4):434–445, 2006. doi:10.1002/jcc.20358.

[206] Magdalena Pecul, Kenneth Ruud, and Trygve Helgaker. Density functional theory calculation of electronic circular dichroism using London orbitals. *Chemical physics letters*, 388(1-3):110–119, 2004. doi:10.1016/j.cplett.2004.03.008.

[207] Milan Šindelka and Nimrod Moiseyev. Floquet perturbation theory: Applicability of the finite level approximation in different gauges. *Physical Review A*, 76(4):043844, 2007. doi:10.1103/PhysRevA.76.043844.

[208] RJS Crossley. The Calculation of Atomic Transition Probabilities. In *Advances in atomic and molecular physics*, volume 5, pages 237–296. Elsevier, 1969. doi:10.1016/S0065-2199(08)60159-1.

[209] KG Dyall, IP Grant, CT Johnson, FA Parpia, and EP Plummer. GRASP: A general-purpose relativistic atomic structure program. *Computer Physics Communications*, 55(3):425–456, 1989. doi:10.1016/0010-4655(89)90136-7.

[210] Frank WJ Olver, Daniel W Lozier, Ronald F Boisvert, and Charles W Clark. *NIST handbook of mathematical functions hardback and CD-ROM*. Cambridge university press, 2010.

[211] Jørn Thyssen. *Development and Applications of Methods for Correlated Relativistic Calculations of Molecular Properties*. PhD thesis, 2001. URL `http://dirac.chem.sdu.dk/thesis/thesis-jth2001.pdf`.

[212] Helene Lefebvre-Brion. CECAM-ORSAY Documentation for Molecular Calculations – 1970, feb 2021. URL `https://doi.org/10.5281/zenodo.4527848`.

[213] Paul S Bagus and Henry F Schaefer III. Direct Near-Hartree–Fock Calculations on the 1s Hole States of NO^+. *The Journal of Chemical Physics*, 55(3):1474–1475, 1971. doi:10.1063/1.1676248. This paper employs overlap selection, but does not write it explicitly. The proper keyword MOORDR is found on page 9 of Ref. 212.

[214] Andrew TB Gilbert, Nicholas A Besley, and Peter MW Gill. Self-consistent field calculations of excited states using the maximum overlap method (MOM). *The Journal of Physical Chemistry A*, 112(50):13164–13171, 2008. doi:10.1021/jp801738f.

[215] Mauro Stener, Giovanna Fronzoni, and Monica de Simone. Time dependent density functional theory of core electrons excitations. *Chemical physics letters*, 373(1-2):115–123, 2003. doi:10.1016/S0009-2614(03)00543-8.

[216] Christopher South, Avijit Shee, Debashis Mukherjee, Angela K Wilson, and Trond Saue. 4-Component relativistic calculations of L_3 ionization and excitations for the isoelectronic species ${UO_2}^{2+}$, OUN^+ and UN_2. *Physical Chemistry Chemical Physics*, 18(31):21010–21023, 2016. doi:10.1039/C6CP00262E.

[217] Kenneth G Dyall. Dyall double-zeta, triple-zeta, and quadruple-zeta basis set archive files, feb 2023. URL `https://doi.org/10.5281/zenodo.7606547`.

[218] Kenneth G Dyall and Knut Fægri Jr. Kinetic balance and variational bounds failure in the solution of the Dirac equation in a finite Gaussian basis set. *Chemical physics letters*, 174(1): 25–32, 1990. doi:10.1016/0009-2614(90)85321-3.

[219] Maximilien A Ambroise, Andreas Dreuw, and Frank Jensen. Probing basis set requirements for calculating core ionization and core excitation spectra using correlated wave function methods. *Journal of Chemical Theory and Computation*, 17(5):2832–2842, 2021. doi:10.1021/acs.jctc.1c00042.

[220] Thorsten Glaser, Britt Hedman, Keith O Hodgson, and Edward I Solomon. Ligand k-edge x-ray absorption spectroscopy: a direct probe of ligand- metal covalency. *Accounts of chemical research*, 33(12):859–868, 2000. doi:10.1021/ar990125c.

[221] Edward I Solomon, Britt Hedman, Keith O Hodgson, Abhishek Dey, and Robert K Szilagyi. Ligand k-edge x-ray absorption spectroscopy: covalency of ligand–metal bonds. *Coordination Chemistry Reviews*, 249(1-2):97–129, 2005. doi:10.1016/j.ccr.2004.03.020.

[222] Serena DeBeer George, Patrick Brant, and Edward I Solomon. Metal and ligand k-edge xas of organotitanium complexes: Metal 4p and 3d contributions to pre-edge intensity and their contributions to bonding. *Journal of the American Chemical Society*, 127(2):667–674, 2005. doi:10.1021/ja044827v.

[223] A. D. Becke. Density-functional exchange-energy approximation with correct asymptotic behavior. *Phys. Rev. A*, 38:3098–3100, Sep 1988. doi:10.1103/PhysRevA.38.3098.

[224] John P. Perdew. Erratum: Density-functional approximation for the correlation energy of the inhomogeneous electron gas. *Phys. Rev. B*, 34:7406–7406, Nov 1986. doi:10.1103/PhysRevB.34.7406. (erratum).

[225] Van Lenthe, E. and Baerends, E. J. Optimized slater-type basis sets for the elements 1–118. *Journal of Computational Chemistry*, 24(9):1142–1156, 2003. doi:10.1002/jcc.10255.

[226] Hans Agren, Paul S. Bagus, and Björn O. Roos. Symmetry adapted versus symmetry broken wavefunctions: the 1s core level ions of O^{+2}. *Chemical Physics Letters*, 82(3):505–510, 1981. doi:10.1016/0009-2614(81)85429-2.

[227] John F. Stanton, Jürgen Gauss, and Rodney J. Bartlett. On the choice of orbitals for symmetry breaking problems with application to NO_3. *The Journal of chemical physics*, 97(8):5554–5559, 1992. doi:10.1063/1.463762.

[228] José Goulon, Francesco Sette, Claude Moise, Alain Fontaine, Dantele Perey, Petra Rudolf, and Francois Baudelet. Detection limits for natural circular dichroism of chiral complexes in the x-ray range. *Japanese Journal of Applied Physics*, 32(S2):284, jan 1993. doi:10.7567/jjaps.32s2.284.

[229] Sebastien Villaume and Patrick Norman. On circular dichroism and the separation between chromophore and chiral center: The near carbon k-edge x-ray absorption and circular dichroism spectra of noradrenaline and l-dopa. *Chirality*, 21(1E):E13–E19, 2009. doi:10.1002/chir.20763.

[230] Yu Zhang, Jérémy R Rouxel, Jochen Autschbach, Niranjan Govind, and Shaul Mukamel. X-ray circular dichroism signals: a unique probe of local molecular chirality. *Chemical science*, 8(9):5969–5978, 2017. doi:10.1039/C7SC01347G.

[231] Osamu Takahashi, Mai Kimoto, and Lars GM Pettersson. Theoretical study of the x-ray natural circular dichroism of some crystalline amino acids. *Chemical Physics*, 450:109–114, 2015. doi:10.1016/j.chemphys.2015.01.012.

[232] Victor Kimberg and Nobuhiro Kosugi. Calculation of K-edge circular dichroism of amino acids: Comparison of random phase approximation with other methods. *The Journal of Chemical Physics*, 126(24):06B612, 2007. doi:10.1063/1.2743010.

[233] Auayporn Jiemchooroj, Ulf Ekström, and Patrick Norman. Near-edge x-ray absorption and natural circular dichroism spectra of L-alanine: A theoretical study based on the complex polarization propagator approach. *The Journal of Chemical Physics*, 127(16):165104, 2007. doi:10.1063/1.2800024.

[234] Vincenzo Carravetta, Olexandre Plachkevytch, Olav Vahtras, and Hans Ågren. Ordinary and rotatory intensities for X-ray absorption at the C-1s edge of organic chiral molecules: propylene oxide and trans-1,2-dimethylcyclopropane. *Chemical Physics Letters*, 275(1):70 – 78, 1997. doi:10.1016/S0009-2614(97)00687-8.

[235] Oleksandr Plashkevych, Vincenzo Carravetta, Olav Vahtras, and Hans Ågren. Theoretical study of x-ray circular dichroism of amino acids. *Chemical Physics*, 232(1):49 – 62, 1998. doi:10.1016/S0301-0104(98)00055-X.

[236] Stefano Turchini, Nicola Zema, Stefano Zennaro, Lucilla Alagna, Brian Stewart, Robert D. Peacock, and Tommaso Prosperi. Core Electron Transitions as a Probe for Molecular Chirality: Natural Circular Dichroism at the Carbon K-edge of Methyloxirane. *Journal of the American Chemical Society*, 126(14):4532–4533, 2004. doi:10.1021/ja039348v.

[237] Stepan Urban, Eric Herbst, Petra Mittler, Gisbert Winnewisser, Koichi M.T. Yamada, and Manfred Winnewisser. The high-resolution rotational and torsional spectra of HSSH. *Journal of Molecular Spectroscopy*, 137(2):327–353, 1989. doi:10.1016/0022-2852(89)90177-X.

[238] Eric Herbst and Gisbert Winnewisser. An experimentally derived torsional potential function for HSSH. *Chemical Physics Letters*, 155(6):572–575, 1989. doi:10.1016/0009-2614(89)87475-5.

[239] Glauciete S. Maciel, Patricia R. P. Barreto, Federico Palazzetti, Andrea Lombardi, and Vincenzo Aquilanti. A quantum chemical study of H_2S_2: Intramolecular torsional mode and intermolecular interactions with rare gases. *The Journal of Chemical Physics*, 129(16):164302, 2008. doi:10.1063/1.2994732.

[240] Vincenzo Aquilanti, Mirco Ragni, Ana C. P. Bitencourt, Glauciete S. Maciel, and Frederico V. Prudente. Intramolecular Dynamics of RS–SR' Systems (R, R' = H, F, Cl, CH_3, C_2H_5): Torsional Potentials, Energy Levels, Partition Functions. *The Journal of Physical Chemistry A*, 113(16):3804–3813, 2009. doi:10.1021/jp8094215.

[241] J.M. Thornton. Disulphide bridges in globular proteins. *Journal of Molecular Biology*, 151 (2):261–287, 1981. doi:10.1016/0022-2836(81)90515-5.

[242] Arvi Rauk. Chiroptical properties of disulfides. Ab initio studies of dihydrogen disulfide and dimethyl disulfide. *Journal of the American Chemical Society*, 106(22):6517–6524, 1984. doi:10.1021/ja00334a010.

[243] Tae-Kyu Ha and W. Cencek. Ab initio CI study of the optical rotatory strengths of HSSH. *Chemical Physics Letters*, 182(5):519–523, 1991. doi:https://doi.org/10.1016/0009-2614(91)90117-R.

[244] Marjorie Pericou-Cayere, Michel Rerat, and Alain Dargelos. Theoretical treatment of the electronic circular dichroism spectrum and the optical rotatory power of H_2S_2. *Chemical Physics*, 226(3):297 – 306, 1998. doi:10.1016/S0301-0104(97)00285-1.

[245] Christian Diedrich and Stefan Grimme. Systematic Investigation of Modern Quantum Chemical Methods to Predict Electronic Circular Dichroism Spectra. *The Journal of Physical Chemistry A*, 107(14):2524–2539, 2003. doi:10.1021/jp0275802.

[246] Magdalena Pecul and Kenneth Ruud. The ab initio calculation of optical rotation and electronic circular dichroism. In H. J. Aa. Jensen, editor, *Response Theory and Molecular Properties (A Tribute to Jan Linderberg and Poul Jørgensen)*, volume 50 of *Advances in Quantum Chemistry*, pages 185–212. Academic Press, 2005. doi:10.1016/S0065-3276(05)50009-1.

[247] Lucie Bednárová, Petr Bouř, and Petr Maloň. Vibrational and electronic optical activity of the chiral disulphide group: Implications for disulphide bridge conformation. *Chirality*, 22(5): 514–526, 2010. doi:10.1002/chir.20772.

[248] Mikael Scott, Dirk R. Rehn, Sonia Coriani, Patrick Norman, and Andreas Dreuw. Electronic circular dichroism spectra using the algebraic diagrammatic construction schemes of the polarization propagator up to third order. *The Journal of Chemical Physics*, 154(6):064107, 2021. doi:10.1063/5.0038315.

[249] P. J. Stephens, F. J. Devlin, C. F. Chabalowski, and M. J. Frisch. Ab Initio Calculation of Vibrational Absorption and Circular Dichroism Spectra Using Density Functional Force Fields. *J. Phys. Chem.*, 98:11623–11627, 1994. doi:10.1021/j100096a001.

[250] A. D. Becke. Density-Functional Thermochemistry. III. The Role of Exact Exchange. *J. Chem. Phys.*, 98:5648–5652, 1993. doi:10.1063/1.464913.

[251] S. H. Vosko, L. Wilk, and M. Nusair. Accurate Spin-Dependent Electron Liquid Correlation Energies for Local Spin Density Calculations: A Critical Analysis. *Can. J. Phys.*, 58:1200–1211, 1980. doi:10.1139/p80-159.

[252] C. Lee, W. Yang, and R. G. Parr. Development of the Colle-Salvetti Correlation-Energy Formula Into a Functional of the Electron Density. *Phys. Rev. B*, 37:785–789, 1988. doi:10.1103/PhysRevB.37.785.

[253] T. H. Dunning. Gaussian Basis Sets for Use in Correlated Molecular Calculations. I. The Atoms Boron through Neon and Hydrogen. *J. Chem. Phys.*, 90:1007–1023, 1989. doi:10.1063/1.456153.

[254] David E. Woon and Thom H. Dunning. Gaussian basis sets for use in correlated molecular calculations. iii. the atoms aluminum through argon. *The Journal of Chemical Physics*, 98 (2):1358–1371, 1993. doi:10.1063/1.464303.

[255] M. J. Frisch, G. W. Trucks, H. B. Schlegel, G. E. Scuseria, M. A. Robb, J. R. Cheeseman, G. Scalmani, V. Barone, G. A. Petersson, H. Nakatsuji, X. Li, M. Caricato, A. V. Marenich, J. Bloino, B. G. Janesko, R. Gomperts, B. Mennucci, H. P. Hratchian, J. V. Ortiz, A. F. Izmaylov, J. L. Sonnenberg, D. Williams-Young, F. Ding, F. Lipparini, F. Egidi, J. Goings, B. Peng, A. Petrone, T. Henderson, D. Ranasinghe, V. G. Zakrzewski, J. Gao, N. Rega, G. Zheng, W. Liang, M. Hada, M. Ehara, K. Toyota, R. Fukuda, J. Hasegawa, M. Ishida, T. Nakajima, Y. Honda, O. Kitao, H. Nakai, T. Vreven, K. Throssell, J. A. Montgomery, Jr., J. E. Peralta, F. Ogliaro, M. J. Bearpark, J. J. Heyd, E. N. Brothers, K. N. Kudin, V. N. Staroverov, T. A. Keith, R. Kobayashi, J. Normand, K. Raghavachari, A. P. Rendell, J. C. Burant, S. S. Iyengar, J. Tomasi, M. Cossi, J. M. Millam, M. Klene, C. Adamo, R. Cammi, J. W. Ochterski, R. L. Martin, K. Morokuma, O. Farkas, J. B. Foresman, and D. J. Fox. Gaussian16 Revision C.01, 2016. Gaussian Inc. Wallingford CT.

[256] Douglas B Craig and Alan A Dombkowski. Disulfide by design 2.0: a web-based tool for disulfide engineering in proteins. *BMC bioinformatics*, 14(1):346, 2013. doi:10.1186/1471-2105-14-346.

[257] Gennaro Pescitelli, Lorenzo Di Bari, and Nina Berova. Conformational aspects in the studies of organic compounds by electronic circular dichroism. *Chem. Soc. Rev.*, 40:4603–4625, 2011. doi:10.1039/C1CS15036G.

[258] Marius Kadek, Lukas Konecny, Bin Gao, Michal Repisky, and Kenneth Ruud. X-ray absorption resonances near $L_{2,3}$-edges from real-time propagation of the Dirac–Kohn–Sham density matrix. *Phys. Chem. Chem. Phys.*, 17:22566–22570, 2015. doi:10.1039/C5CP03712C.

[259] Thomas Fransson, Daria Burdakova, and Patrick Norman. K- and L-edge X-ray absorption spectrum calculations of closed-shell carbon, silicon, germanium, and sulfur compounds using damped four-component density functional response theory. *Phys. Chem. Chem. Phys.*, 18: 13591–13603, 2016. doi:10.1039/C6CP00561F.

[260] Maximilien A. Ambroise and Frank Jensen. Probing Basis Set Requirements for Calculating Core Ionization and Core Excitation Spectroscopy by the Δ Self-Consistent-Field Approach. *Journal of Chemical Theory and Computation*, 15(1):325–337, 2019. doi:10.1021/acs.jctc.8b01071.

[261] Frank Jensen. Polarization consistent basis sets: Principles. *The Journal of Chemical Physics*, 115(20):9113–9125, 2001. doi:10.1063/1.1413524.

[262] Frank Jensen. Polarization consistent basis sets. II. Estimating the Kohn–Sham basis set limit. *The Journal of Chemical Physics*, 116(17):7372–7379, 2002. doi:10.1063/1.1465405.

[263] Frank Jensen. Polarization consistent basis sets. III. The importance of diffuse functions. *The Journal of Chemical Physics*, 117(20):9234–9240, 2002. doi:10.1063/1.1515484.

[264] Angela K. Wilson, David E. Woon, Kirk A. Peterson, and Jr. Dunning, Thom H. Gaussian basis sets for use in correlated molecular calculations. IX. The atoms gallium through krypton. *The Journal of Chemical Physics*, 110(16):7667–7676, 04 1999. doi:10.1063/1.478678.

[265] Florian Weigend and Reinhart Ahlrichs. Balanced basis sets of split valence, triple zeta valence and quadruple zeta valence quality for H to Rn: Design and assessment of accuracy. *Physical Chemistry Chemical Physics*, 7(18):3297–3305, 2005. doi:10.1039/B508541A.

[266] Kenneth G Dyall. Relativistic double-zeta, triple-zeta, and quadruple-zeta basis sets for the light elements H–Ar. *Theoretical Chemistry Accounts*, 135(5):128, 2016. doi:10.1007/s00214-016-1884-y.

[267] Ikuo Tokue, Atsunari Hiraya, and Kosuke Shobatake. Photoexcitation of dimethyl sulfide and dimethyl disulfide in the vacuum ultraviolet region: Rydberg states and photofragment emissions. *Chemical Physics*, 130(1):401–408, 1989. doi:10.1016/0301-0104(89)87069-7.

[268] Christine H Hearn, Elena Turcu, and Jeffrey A Joens. The near U.V. absorption spectra of dimethyl sulfide, diethyl sulfide and dimethyl disulfide at T=300 K. *Atmospheric Environment. Part A. General Topics*, 24(7):1939–1944, 1990. doi:10.1016/0960-1686(90)90527-T.

[269] Kirsten Schnorr, Aditi Bhattacherjee, Katherine J. Oosterbaan, Mickaël G. Delcey, Zheyue Yang, Tian Xue, Andrew R. Attar, Adam S. Chatterley, Martin Head-Gordon, Stephen R. Leone, and Oliver Gessner. Tracing the 267 nm-Induced Radical Formation in Dimethyl Disulfide Using Time-Resolved X-ray Absorption Spectroscopy. *The Journal of Physical Chemistry Letters*, 10(6):1382–1387, 2019. doi:10.1021/acs.jpclett.9b00159.

[270] Miguel Ochmann, Abid Hussain, Inga von Ahnen, Amy A. Cordones, Kiryong Hong, Jae Hyuk Lee, Rory Ma, Katrin Adamczyk, Tae Kyu Kim, Robert W. Schoenlein, Oriol Vendrell, and Nils Huse. UV-Photochemistry of the Disulfide Bond: Evolution of Early Photoproducts from Picosecond X-ray Absorption Spectroscopy at the Sulfur K-Edge. *Journal of the American Chemical Society*, 140(21):6554–6561, 2018. doi:10.1021/jacs.7b13455.

[271] A.P. Hitchcock, S. Bodeur, and M. Tronc. Sulfur and Chlorine K-shell spectra of gases. *Physica B: Condensed Matter*, 158(1):257–258, 1989. doi:10.1016/0921-4526(89)90279-2.

[272] Jan Linderberg and Josef Michl. Inherent optical activity of organic disulfides. *J. Am. Chem. Soc.*, 92(9):2619–2625, 1970. doi:10.1021/ja00712a005.

[273] S. Svensson, A. Naves de Brito, M. P. Keane, N. Correia, and L. Karlsson. Observation of an energy shift in the S2$p_{3/2}$–S2$p_{1/2}$ spin-orbit splitting between x-ray photoelectron and Auger-electron spectra for the H_2S molecule. *Phys. Rev. A*, 43:6441–6443, Jun 1991. doi:10.1103/PhysRevA.43.6441.

[274] S. Svensson, A. Ausmees, S. J. Osborne, G. Bray, F. Gel'mukhanov, H. Ågren, A. Naves de Brito, O.-P. Sairanen, A. Kivimäki, E. Nõmmiste, H. Aksela, and S. Aksela. Observation of an anomalous decay ratio between the molecular field split levels in the S 2p core photoelectron and LVV Auger spectrum of H_2S. *Phys. Rev. Lett.*, 72:3021–3024, May 1994. doi:10.1103/PhysRevLett.72.3021.

[275] B. T. Thole and G. van der Laan. Linear relation between x-ray absorption branching ratio and valence-band spin-orbit expectation value. *Phys. Rev. A*, 38:1943–1947, Aug 1988. doi:10.1103/PhysRevA.38.1943.

[276] Paul S. Bagus, Hajo Freund, Helmut Kuhlenbeck, and Eugene S. Ilton. A new analysis of X-ray adsorption branching ratios: Use of Russell–Saunders coupling. *Chemical Physics Letters*, 455(4):331–334, 2008. doi:10.1016/j.cplett.2008.02.085.

[277] R. B. Bernini, L. B. G. da Silva, F. N. Rodrigues, L. H. Coutinho, A. B. Rocha, and G. G. B. de Souza. Core level (S 2p) excitation and fragmentation of the dimethyl sulfide and dimethyldisulfide molecules. *The Journal of Chemical Physics*, 136(14):144307, 2012. doi:10.1063/1.3701567.

[278] Y. Baba, K. Yoshii, and T. A. Sasaki. Site-specific fragmentation in condensed $(CH_3S)_2$ by sulfur K-edge photoexcitation. *The Journal of Chemical Physics*, 105(19):8858–8864, 1996. doi:10.1063/1.472615.

[279] Ingrid J. Pickering, Monica Barney, Julien J. H. Cotelesage, Linda Vogt, M. Jake Pushie, Andrew Nissan, Roger C. Prince, and Graham N. George. Chemical Sensitivity of the Sulfur K-Edge X-ray Absorption Spectra of Organic Disulfides. *The Journal of Physical Chemistry A*, 120(37):7279–7286, 2016. doi:10.1021/acs.jpca.6b06790.

[280] G. Bergson. Molecular orbital treatment of the $3p\pi$ interaction in five-membered cyclic disulphides. *Ark. Kemi*, 12:233, 1958.

[281] G. Bergson. A semi-empirical study of the interaction between lone-pair electrons with special reference to the problem of hybridization and the theory of restricted rotation about single bonds. *Ark. Kemi*, 18:409, 1961.

[282] G. Wagnière and W. Hug. Polarization and the sign of the long-wavelength cotton-effects in chromophores of symmetry C_2. *Tetrahedron Letters*, 11(55):4765–4768, 1970. doi:10.1016/S0040-4039(00)89340-5.

[283] R.W. Woody. Application of the Bergson model to the optical properties of chiral disulfides. *Tetrahedron*, 29(10):1273–1283, 1973. doi:10.1016/S0040-4020(01)83144-6.

[284] Marvin. Carmack and Leonard A. Neubert. Circular dichroism and the absolute configuration of the chiral disulfide group. *Journal of the American Chemical Society*, 89(26):7134–7136, 1967. doi:10.1021/ja01002a064.

[285] Raymond M. Dodson and Victor C. Nelson. Correlation of the chirality of the disulfide group with its molecular ellipticity. *The Journal of Organic Chemistry*, 33(10):3966–3968, 1968. doi:10.1021/jo01274a070.

[286] Göran Claeson, U. Anthoni, C. Larsen, and P. Nielsen. Temperature-Dependent Optical Rotatory Dispersion Measurements of Methyl (R)(-)-1,2-Dithiane-4-carboxylate. The Absolute Configuration of the Disulphide Group. *Acta Chemica Scandinavica*, 22:2429–2437, 1968. doi:10.1002/bip.360240902.

[287] Urs Ludescher and Robert Schwyzer. On the chirality of the cystine disulfide group: Assignment of helical sense in a model compound with a dihedral angle greater than ninety degrees using NMR. and CD. *Helvetica Chimica Acta*, 54(6):1637–1644, 1971. doi:10.1002/hlca.19710540615.

[288] J.L. Campbell and Tibor Papp. Widths of the atomic K-N7 levels. *Atomic Data and Nuclear Data Tables*, 77(1):1–56, 2001. doi:10.1006/adnd.2000.0848.

[289] Christophe Nicolas and Catalin Miron. Lifetime broadening of core-excited and -ionized states. *Journal of Electron Spectroscopy and Related Phenomena*, 185(8):267–272, 2012. doi:10.1016/j.elspec.2012.05.008.

[290] Hans Jørgen Aa. Jensen and Hans Ågren. A direct, restricted-step, second-order MC SCF program for large scale ab initio calculations. *Chemical Physics*, 104(2):229–250, 1986. doi:10.1016/0301-0104(86)80169-0.

[291] Hans Ågren, Vincenzo Carravetta, Olav Vahtras, and Lars GM Pettersson. Direct, atomic orbital, static exchange calculations of photoabsorption spectra of large molecules and clusters. *Chemical physics letters*, 222(1-2):75–81, 1994. doi:10.1016/0009-2614(94)00318-1.

[292] Hans Ågren, Vincenzo Carravetta, Olav Vahtras, and Lars GM Pettersson. Direct SCF direct static-exchange calculations of electronic spectra. *Theoretical Chemistry Accounts*, 97:14–40, 1997. doi:10.1007/s002140050234.

[293] Ulf Ekström, Patrick Norman, and Vincenzo Carravetta. Relativistic four-component static-exchange approximation for core-excitation processes in molecules. *Phys. Rev. A*, 73:022501, Feb 2006. doi:10.1103/PhysRevA.73.022501.

[294] T. Saue and H. J. Aa. Jensen. Linear response at the 4-component relativistic level: Application to the frequency-dependent dipole polarizabilities of the coinage metal dimers. *The Journal of Chemical Physics*, 118(2):522–536, 2003. doi:10.1063/1.1522407.

[295] L.H. Thomas. I. The kinematics of an electron with an axis . *The London, Edinburgh, and Dublin Philosophical Magazine and Journal of Science*, 3(13):1–22, 1927. doi:10.1080/14786440108564170.

[296] Eugene P. Wigner. 26 - time inversion. In *Group Theory*, volume 5 of *Pure and Applied Physics*, pages 325–348. Elsevier, 1959. doi:10.1016/B978-0-12-750550-3.50031-8.

[297] J. Kaniauskas. Relativistic investigation of electronic transitions in many-electron atoms. *Liet. Fiz. Rink*, XIV(3):463–475, 1974.

[298] L. S. Cederbaum, W. Domcke, and J. Schirmer. Many-body theory of core holes. *Phys. Rev. A*, 22:206–222, Jul 1980. doi:10.1103/PhysRevA.22.206.

[299] Loïc Halbert, Marta L Vidal, Avijit Shee, Sonia Coriani, and André Severo Pereira Gomes. Relativistic EOM-CCSD for Core-Excited and Core-Ionized State Energies Based on the Four-Component Dirac–Coulomb (- Gaunt) Hamiltonian. *Journal of Chemical Theory and Computation*, 17(6):3583–3598, 2021. doi:10.1021/acs.jctc.0c01203.